

DOE/ET-53088-178

IFSR #178

**PARTICLE SIMULATION OF
LOW FREQUENCY FLUCTUATIONS
IN A SHEARED MAGNETIC FIELD**

Richard D. Sydora
Institute for Fusion Studies
The University of Texas at Austin
Austin, Texas 78712

April 1985

PARTICLE SIMULATION OF LOW FREQUENCY
FLUCTUATIONS IN A SHEARED MAGNETIC FIELD

Publication No. _____

Richard Dwayne Sydora, Ph.D.
The University of Texas at Austin, 1985

Supervising Professors: Jean-Noel Leboeuf
Toshiki Tajima
Patrick H. Diamond

The tools of particle simulation are used to investigate the physics of density gradient-driven low frequency fluctuations in a sheared magnetic field. This is important for the understanding of anomalous plasma losses in toroidal confinement devices. Two types of fluctuations are studied.

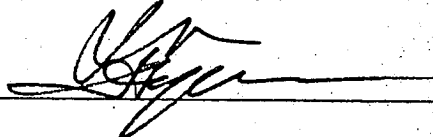
The first is the electrostatic drift wave in a sheared magnetic field. The existence of absolutely stable drift wave eigenmodes, localized about a single mode rational surface, is established in the sheared slab geometry. From the simulation results in the strong shear limit the eigenmode frequency and mode structure agree with the linear theory. In the weak shear regime localized, convective transient growths are observed before the

eigenmodes have developed. An extension of the strong shear case to three dimensions is made and the eigenmode stability is examined. The modification of the electron dynamics due to the presence of multiple rational surfaces and thermal noise is shown to affect the eigenmode stability. Enhancements above the thermal level are observed in certain parameter regimes.

The second kind of fluctuation studied is the resistive interchange (g) mode in a sheared magnetic field. The saturation and nonlinear evolution of the instability is compared in single and multiple rational surface configurations. It is found that in the single rational surface case the unstable g-modes saturate by density flattening over the eigenmode width. In the presence of multiple rational surfaces localized profile modification is absent and the convective nonlinearities dominate. It is shown that a mixing length theory is adequate to describe the saturated potential fluctuations. The density fluctuations saturate by coupling to small scales.

PARTICLE SIMULATION OF LOW FREQUENCY FLUCTUATIONS
IN A SHEARED MAGNETIC FIELD

APPROVED BY SUPERVISORY COMMITTEE:



Libby J...

Patric H. Diamond

Marshall M. R. Bloch

Samuel J. Pinner

Copyright, 1985

by

Richard Dwayne Sydora.

All rights reserved.

Dedicated to my parents
and brothers
for the many good years

PARTICLE SIMULATION OF LOW FREQUENCY FLUCTUATIONS
IN A SHEARED MAGNETIC FIELD

by

RICHARD DWAYNE SYDORA, B.Sc., M.S.

DISSERTATION

Presented to the Faculty of the Graduate School of

The University of Texas at Austin

in Partial Fulfillment

of the Requirements

for the Degree of

DOCTOR OF PHILOSOPHY

THE UNIVERSITY OF TEXAS AT AUSTIN

May, 1985

A C K N O W L E D G M E N T S

It has been a great privilege to work with and learn from Dr. Jean-Noel Leboeuf. I wish to express my deepest appreciation to him for his insightful comments, availability and enthusiasm. I would like to thank Dr. Patrick H. Diamond for his deep interest in my research and education as a plasma physicist as well as the many late nights of stimulating discussions.

I am indebted to Professor Toshiki Tajima and Professor Marshall Rosenbluth for providing an exciting atmosphere to do research and for their advice during the course of this project. I wish to thank my officemates, Nicolas Dominguez and Tzihong Chiueh, for their warm friendship, as well as Gyung Su Lee, G. Craddock, Dr. Y. M. Li, and Dr. Cliff Burgess. I have benefited from many discussions with Dr. P. W. Terry, Dr. Z. G. An, Dr. T. S. Hahn, Dr. D. Thayer, and Dr. Jim Van Dam.

My special thanks go to Patricia Schoirfer-Leboeuf for strong words of encouragement. I also wish to express gratitude towards the Institute for Fusion Studies technical staff members for all the assistance they have given me. In particular, I thank Carolyn Valentine,

Saralyn Stewart, Suzy Crumley, and Dawn East. Finally, I thank Sergeant C. Kent for helping me put it all in perspective.

Richard Dwayne Sydora

The University of Texas at Austin

April 19, 1985

T A B L E O F C O N T E N T S

Chapter	Page
I. INTRODUCTION	1
II. PARTICLE SIMULATION MODEL FOR LOW FREQUENCY MICROINSTABILITIES	9
2.1 Guiding Center Particle Simulation Method	12
2.2 Three Dimensional Guiding Center Model	43
2.3 Collision Operators for Particle Simulations	56
2.4 Diagnostic Methods	63
III. PARTICLE SIMULATION OF DRIFT WAVES IN A SHEARED MAGNETIC FIELD	77
3.1 Introduction	77
3.2 Linear Drift Wave Theory	81
3.3 Simulation Configuration and Parameters	90
3.4 Simulation Results (Strong Shear)	95
3.5 Simulation Results (Weak Shear)	120
3.6 Summary and Principal Results	129
IV. THREE DIMENSIONAL PARTICLE SIMULATION OF DRIFT WAVES IN A SHEARED MAGNETIC FIELD	131
4.1 Introduction	131
4.2 Nonlinear Drift Wave Theory	135
4.3 Simulation Configuration and Parameters	148
4.4 Simulation Results and Interpretation	151
4.5 Summary and Discussion	186
V. PARTICLE SIMULATION OF THE RESISTIVE G-MODE IN A SHEARED MAGNETIC FIELD	190
5.1 Introduction	190
5.2 Linear G-Mode Theory	194

Chapter	Page
V. (Continued)	
5.3 Simulation Configuration	205
5.4 Simulation Results (Fast Interchange) . . .	207
5.5 Simulation Results (Slow Interchange) . . .	211
5.6 Saturation of Resistive G-Modes	220
VI. THREE DIMENSIONAL PARTICLE SIMULATION OF THE RESISTIVE G-MODE IN A SHEARED MAGNETIC FIELD . .	230
6.1 Introduction	230
6.2 Simulation Configuration and Parameters . . .	232
6.3 Simulation Results and Interpretation . . .	236
6.4 Nonlinear Theory of the G-Mode	241
VII. CONCLUSIONS AND REMARKS	259
REFERENCES	262

L I S T O F F I G U R E S

Figure		Page
2.1	Particle orbits for predictor-corrector integration test	24
2.2	Time-averaged fluctuation spectrum as a function of wavenumber	34
2.3	Dispersion curves for thermally excited ion Bernstein modes	36
2.4	Autocorrelation for test mode (3,0) as a function of the lag time	37
2.5	Power spectrum for various test modes	40
2.6	Theoretical and simulation values for the thermal ion Bernstein mode dispersion	41
2.7	Autocorrelation function for various test modes (a) (1,1) mode and (b) the (2,1) mode	42
2.8	Spectrum of ion acoustic modes	44
2.9	Three dimensional normal mode expansion particle simulation model	46
2.10	Thermal fluctuation level versus mode number averaged over time	54
2.11	Ion Bernstein mode dispersion curves from simulation and theory using the $(k_x, k_y, 0)$ modes	55
2.12	Plasma Oscillation dispersion curves using the $(0, 0, k_z)$ modes	57
3.1	Linear theory results illustrating real (full curve) and imaginary (dotted curve) parts of wavefunction $\phi(x)$ as a function of x/ρ_s for (a) even parity modes and (b) odd parity modes	88

Figure	Page
3.2	Real and imaginary parts of eigenmode frequency ω/ω^* and γ/ω^* as a function of $k_y \rho_s$ for even and odd parity modes with same parameters as Fig. 3.1 89
3.3	Schematic of the particle simulation configuration and model 91
3.4	Time evolution of the total electrostatic energy normalized to the total kinetic energy for Case 1 97
3.5	Time evolution of the spatially averaged mode amplitude for (a) $k_y \rho_s = 0$ and (b) $k_y \rho_s = 0.49$ in Case 1 98
3.6	Power spectra of potential $\phi_k(x)$ as a function of real frequency ω/ω^* for (a) $k_y \rho_s = 0.49$ at $x/\rho_s = 9.6$ and (b) $k_y \rho_s = 0.49$ at $x/\rho_s = 12.8$ for Case 1 100
3.7	Real frequency, ω/ω^* , as a function of x/ρ_s for mode $k_y \rho_s = 0.49$ 101
3.8	Time evolution of total electrostatic energy normalized to total kinetic energy for Case 2 parameters 103
3.9	Time evolution of the spatially averaged mode amplitude for (a) $k_y \rho_s = 0$ and (b) $k_y \rho_s = 0.49$ in Case 2 104
3.10	Power spectra of the potential $\phi_{k_y}(x)$ as a function of real frequency ω/ω^* for mode $k_y \rho_s = 0.49$ for Case 2 105
3.11	The real and imaginary parts of the wave function obtained from theory and simulation (interferogram method) with $\omega/\omega^* = 0.32$ for mode $k_y \rho_s = 0.49$ 106
3.12	Electrostatic potential and mode amplitude at selected time $\omega^* t = 24.5$ 110

Figure	Page
3.13 Power spectra of mode $k_y \rho_s = 0.49$ versus real frequency ω/ω^* taken at local position $(x - x_0)/\rho_s = 3.2$ for Case 3	111
3.14 The real and imaginary parts of the wave function obtained from theory and simulation for Case 3	112
3.15 Power spectra of mode $k_y \rho_s = 0.49$ versus real frequency ω/ω^* taken as average over spatial positions $(x - x_0)/\rho_s = 2.0 - 5.0$	114
3.16 The real and imaginary parts of the wave function obtained from (a) theory and (b) simulation	115
3.17 Real and imaginary parts of the wave function for mode $k_y \rho_s = 0.49$ with parameters the same as Case 3, but with mixture of odd and even parity with respect to rational surface	117
3.18 Time evolution of total electrostatic energy normalized to total kinetic energy for parameters of Case 3 and (a) $L_s/L_n = 14$ which keeps ion resonance within system and (b) $L_s/L_n = 28$ which moves resonance outside simulation domain	119
3.19 Wave function obtained from shooting code for weak shear case, $L_s/L_n = 70$, and even parity	122
3.20 Time evolution of the spatially averaged mode amplitudes for (a) $k_y \rho_s = 0$ and (b) $k_y \rho_s = 0.98$ in weak shear case, $L_s/L_n = 70$, with ion resonance outside system	123
3.21 Space-time diagram and power spectra of mode $k_y \rho_s = 0.98$	124

Figure	Page	
3.22	Time evolution of the spatially averaged mode amplitude for (a) $k_y \rho_s = 0$ and (b) $k_y \rho_s = 0.78$ in weak shear case with ion resonance within simulation domain	127
3.23	Space-time diagram and power spectra of mode $k_y \rho_s = 0.78$	128
4.1	Comparison between solutions of nonlinear eigenmode equation using a shooting method and initial value solution of original drift-kinetic equation	149
4.2	Rational surface location for each mode number (m,n) with density profile superimposed	152
4.3	Growth rate curves for various mode numbers as a function of decorrelation frequency	154
4.4	Guiding center displacement of electrons as a function of time for Case 1	157
4.5	Local orbit divergence for pairs of test particles as a function of time in (a) the x-direction and (b) the y-direction	159
4.6	Mode analysis for (m,n) = (-1,1)	165
4.7	Mode analysis for (m,n) = (3,4)	167
4.8	Contours of electrostatic potential, $\phi_n(x,y)$, for (a) $n = 0$, (b) $n = 2$ taken at $\omega_{ci} t = 120$	168
4.9	Profiles of (a) electron density and (b) parallel electron temperature shown initially and at the end of the simulation	169
4.10	Growth rate curves for Case 2	171
4.11	Guiding center displacement of electrons as a function of time for Case 2	173

Figure	Page
4.12 Local orbit divergence in x-direction as a function of time for pairs of test particles	175
4.13 Diffusion coefficient as a function of x in resonance overlap region	176
4.14 Test particle orbits in $(x-v_{11})$ space	177
4.15 Mode analysis for $(m,n) = (1,0)$ in Case 2	179
4.16 Mode analysis for $(m,n) = (-2,0)$ in Case 2	180
4.17 Mode analysis for $(m,n) = (-3,0)$ in Case 2	181
4.18 Mode analysis for $(m,n) = (5,2)$ in Case 2	182
4.19 Electron density profile initially and at $\omega_{cit} = 200$ for Case 2	184
4.20 Real frequency and growth rate curves as a function of mode number	185
4.21 Various scale lengths measured from the simulation	187
5.1 Initial simulation configuration for single rational surface, g-mode evolution	196
5.2 Various parameter regimes describing kinetic and MHD behavior	204
5.3 Growth rate versus wavenumber for fast interchange mode case	209
5.4 Electrostatic potential contours, $\phi(x,y)$, taken at $\omega_{pe}t = 1600$, for fast interchange mode case	210
5.5 Saturation level versus mode number for fast interchange mode case	212

Figure	Page
5.6 (a) Spatially-averaged mode amplitude versus time for $k_{y\rho_s} = 0.12$, (b) Spatial amplitude of mode $k_{y\rho_s} = 0.12$ versus time	214
5.7 Contours of constant ion pressure taken at time steps (a) $\omega_{pet} = 3000$, (b) $\omega_{pet} = 3200$ and (c) $\omega_{pet} = 3600$	215
5.8 Growth rate versus resistivity for different mode numbers in the slow interchange case . . .	217
5.9 Electrostatic potential contours taken at (a) $\omega_{pet} = 1000$, (b) $\omega_{pet} = 1500$ and (c) $\omega_{pet} = 2000$ for the $\omega^* > \gamma$ regime	218
5.10 (a) Spatially-averaged mode amplitude versus time for two different modes	219
5.11 Contours of constant ion pressure taken at (a) $\omega_{pet} = 600$, (b) $\omega_{pet} = 1000$ and (c) $\omega_{pet} = 2600$	221
5.12 Localized wavefunction obtained from solution to eigenmode equation	226
5.13 Electron and ion density profiles shown at different times	227
5.14 Saturation amplitude versus resistivity for different mode numbers in the slow interchange case	228
6.1 Initial particle simulation configuration . . .	233
6.2 Rational surface positions for each mode number (m,n) with density profile superimposed	235
6.3 Time evolution of modes (a) (2,n) and (b) (8,n), spatially-averaged	237
6.4 Comparison between ion density profile evolution in (a) multiple rational surface and (b) single rational surface configurations . . .	239

Figure		Page
6.5	Spatially-averaged density evolution for (a) $m = 3$ mode and (b) $m = 9$ mode	240
6.6	Comparison between spatial mode evolution in (a) multiple rational surface and (b) single rational surface configurations	242
6.7	Particle positions in y-z plane taken at (a) $\omega_{cit} = 0$, (b) $\omega_{cit} = 18$ and (c) $\omega_{cit} = 20$	243
6.8	Saturation levels for spatial and n-averaged electrostatic potential fluctuations versus mode number	250
6.9	Saturation levels for spatially-averaged density fluctuations versus mode number	257

C H A P T E R I

INTRODUCTION

Low frequency fluctuations in magnetically confined toroidal plasmas have been intensively studied for many years and have recently been used to explain the absolute magnitude and scaling with various plasma parameters, of the energy and particle confinement time observed in several experimental devices. It is well known that tokamak plasmas exhibit high levels of anomalous particle and energy transport, in other words the fluxes of energy and particles across the magnetic field are large compared to the predictions from classical Coulomb collisions of the charged plasma particles.¹ It is believed that the observed low frequency microscopic fluctuations are the cause of anomalous transport;² however, the direct connection between the processes has not been firmly established. Moreover, it is not clear whether the electrostatic or the magnetic field fluctuations cause the anomalous losses. Understanding and controlling this transport is very important to the goal of achieving controlled nuclear fusion. An extensive review of the subject

has been written by Tang³ covering the period from 1970 to 1977. More recently, the review article by Liewer⁴ discusses the experimental and theoretical progress on anomalous transport from 1977 to present.

In the process of containment of a hot, dense plasma one introduces gradients in both temperature and density. Therefore, there is a free energy of expansion available to drive fluctuations and instabilities. This dissertation will be an investigation into two specific types of low frequency fluctuations, the drift wave and drift-resistive interchange (resistive g) mode which are driven by the expansion free energy in the plasma.

In toroidal confinement devices, such as the tokamak and reversed field pinch (RFP), the magnetic field lines are twisted or sheared by currents induced in the plasma and this complicates the analysis of these fluctuations. Drift wave instabilities, driven by non-uniformity in both the spatial distribution and temperature of the particles, are considered to be one of the most likely causes of observed microturbulence and anomalous processes.⁵ The observed frequencies and wavenumbers of the microscopic fluctuations in tokamaks are in the proper range for drift waves, however, anomalous

transport coefficients determined from drift wave theories have not given satisfactory agreement with tokamak experiments over a wide range of operating regimes.^{4,6} Because the plasma generally appears turbulent, a broad frequency range for fixed wavenumber is observed; it is impossible to identify linear waves or instabilities. The microscopic fluctuations may result from a linear instability or may be caused by nonlinear processes. Therefore, when a model of the turbulence is advanced to explain the observations one of the important questions to be asked is what drives the fluctuations.

There have been many different approaches towards modelling the nonlinear plasma processes and explaining the resultant anomalous transport. The approaches can be broadly classified as either stochastic magnetic field transport models or nonlinear drift wave models. The stochastic magnetic field models link small scale magnetic fluctuations to anomalous electron thermal conduction losses.⁷⁻⁹ The nonlinear drift wave models generally involve fluctuations in the electrostatic field as the dominant transport mechanism and this will be the approach taken in this dissertation.

Three different configurations are used in nonlinear drift wave models: (1) slab geometry with uniform

magnetic field, (2) slab geometry with magnetic shear and (3) toroidal geometry where curvature and radial toroidal field variation is retained. The latter two are of relevance to tokamaks since they possess strong magnetic shear. Drift waves in model (1) are absolutely unstable.¹⁰ The influence of radially nonlocal effects, such as magnetic shear, on the presence of absolutely unstable drift modes in a confined plasma is a fundamental problem. The existence of physically meaningful eigenfunctions for drift waves in plasmas with magnetic shear was demonstrated by Pearlstein and Berk in 1968.¹¹ A correct stability analysis of the eigenfunctions^{12,13} has conclusively established that the modes are absolutely stable for all values of magnetic shear and within the framework of linear theory cannot drive the fluctuations. Nonlinearly, however, it has been shown that under conditions relevant to experiment, the drift wave can be absolutely unstable and therefore constitutes a source of unstable fluctuations.¹⁴

Due to the nature of this nonlinear drift wave theory and recent interest, it is important to establish its validity. Because of the many simplifying assumptions which go into complex nonlinear kinetic theory

models of plasma turbulence it is important to use particle simulation methods as an aid to the physical intuition and formal analytic procedures one must use. This is the approach taken in this dissertation for understanding the physics of drift waves in model (2). Drift wave models in (3) have been shown to be absolutely unstable by the inclusion of toroidal coupling¹⁵ and trapped particle effects,¹⁶ however, these will not be considered in this study.

We now turn to the second problem addressed in this dissertation; the nonlinear evolution and spectrum of drift-resistive interchange modes in a sheared magnetic field. Low frequency fluctuations and transport have been studied in nontokamak toroidal devices such as the RFP and spheromak.¹⁷ The adverse curvature in the RFP causes it to be unstable to the localized resistive interchange mode¹⁸ or resistive g-mode so named because an effective gravity can be used to simulate the effect of unfavorable magnetic field curvature.¹⁹ In addition, compact toroidal devices such as the spheromak,²⁰ which have $q < 1$ and therefore unfavorable curvature, should be subject to such instabilities. Despite the achievement of long-lived quiescent plasmas, on the order of several

classical flux diffusion times, reversed field pinches are far from classical and seem to exhibit many anomalous effects.¹⁸ The energy confinement time for most experiments is around 100-200 μ sec whereas the classical energy confinement time prediction is closer to 100 msec. Therefore, there is anomalous energy loss which could be the result of the drift-resistive interchange mode. The density and field fluctuations from experiment are typically 1 percent which suggests a resistive or microinstability as opposed to a gross or ideal MHD instability is causing the transport. Also, the observed fluctuations have a nonzero frequency and are unlikely to be ideal or purely resistive fluctuations. In the ZT-40M²¹ RFP the frequency of the fluctuations is approximately equal to the electron drift frequency.

The resistive g-mode is driven by the interaction between pressure gradients and magnetic field curvature. When the plasma is collisional and the plasma beta low ($\beta < 1\%$) the basic instability is electrostatic in character, however, at larger beta values the magnetic fluctuation components become important. When the instability occurs magnetic islands can develop so that conduction losses may dominate the resistive diffusion losses.

In this dissertation the nonlinear effects of the resistive g-mode on stability and transport are investigated. Simpler models of the instability are considered with less emphasis on complicated geometry effects and more on important nonlinear dynamical processes. We concentrate on the electrostatic component of the resistive g-mode and examine the differences in nonlinear evolution between single and multiple rational surface models. The results of this work are relevant to the edge regions of the RFP or spheromak where plasma compressibility is not a dominant effect, the plasma beta is low and gradients in pressure are steep. While we cannot make quantitative comparison between RFP or spheromak experiments and the simulation results presented here, we can at least indicate the numerous anomalous effects present in experiments and illustrate the importance of various nonlinearities which are essential in constructing a theoretical model of the dynamical processes.

The remainder of this dissertation is organized as follows. In Chapter II the particle simulation methods used to investigate the drift wave and resistive g-mode are outlined in detail. Diagnostic methods used to compare the simulation results with theory are also

presented. The properties of the drift wave, localized about a single mode rational surface, are studied analytically and numerically in Chapter III. The results of Chapter III are extended to three dimensions in Chapter IV where multiple rational surfaces are present and comparisons between simulation and theory are made. Chapters V and VI comprise the second part of the dissertation, a particle simulation of the nonlinear evolution and spectrum of resistive interchange modes in a sheared magnetic field. Chapter V deals with the single rational surface case and Chapter VI the three dimensional extension. Conclusions and a summary appear in Chapter VII.

C H A P T E R . I I

PARTICLE SIMULATION MODEL FOR LOW FREQUENCY MICROINSTABILITIES

The most versatile and reliable tools for the study of the many-body properties associated with plasma dynamics and kinetic plasma behavior are particle simulation techniques. Particle simulation of plasmas began in the early 1960s^{22,23} and has now become a well-established branch of plasma physics. In a conventional particle simulation the Newton-Lorentz equations of motion are advanced to obtain velocity and position data from which charge and current densities are collected on a spatial mesh. These densities are then used as sources in Maxwell's equations which determine the self-consistent electric and magnetic fields. The conventional method requires resolution of the fundamental plasma time scale, an electron plasma oscillation, and length scale, the Debye length.

In real plasmas the electrons and ions can stream along field lines, gyrate around field lines, drift across field lines and collide with each other.

All of these motions possess their own characteristic frequency. A realistic simulation of the dynamical plasma phenomena over all of the above time scales is extremely difficult. One possibility is to modify the MHD fluid equations by introducing kinetic effects through finite Larmor radius terms and parallel resonant response. The other possibility is to modify the particle simulation methods to allow for time steps much longer than the period of high frequency plasma oscillations.²⁴

Choosing the latter possibility, the first issue which must be addressed is the choice of finite difference equations of motion for the particles. These must have the necessary stability at large time step and should be accurate enough to resolve the low frequency phenomena of interest. From the viewpoint of numerical analysis this is known as a 'stiff' problem since the phenomena we are interested in develops on a relatively slow time scale even though the system can support high frequency normal modes. The goal of using the largest possible time step to resolve interesting physics and minimizing computational expense while preserving numerical stability and accuracy makes stringent demands on the numerical methods. Because of the intense theoretical

interest in low frequency kinetic plasma phenomena and because of computer limitations the development of numerical techniques for improving particle simulation algorithms is an active area of plasma research.²⁵⁻³⁰

Particle pushing accounts for the major fraction of the computational burden in a particle simulation. In the simulation of low frequency phenomena in a magnetized plasma the mode frequency is far below the electron cyclotron frequency. Therefore an efficient low frequency particle simulation model should eliminate the detailed particle gyration and associated fast time scale. The appropriate model is the guiding center plasma simulation model in which individual particles represent guiding center positions. The differential equations describing guiding center motion have been considered by a number of authors^{31,32} and there have been several applications of such equations to plasma simulations.³³⁻³⁵

In this chapter a detailed description of the guiding center particle simulation model used for the study of low frequency microinstabilities is presented. This model forms the basis for the new results obtained in this dissertation. We focus on the thermal properties of the simulation model such as the fluctuation spectrum

and mode dispersion. Other standard checks on the model such as satisfactory energy conservation and single particle orbit behavior are discussed. The addition of collisions into the model and diagnostic methods which are used to extract information on the interesting physical effects are presented in detail.

2.1 Guiding Center Particle Simulation Method

What are the ingredients needed in a particle simulation model to describe the physics of low frequency microinstabilities in a nonuniform magnetic field? These can be listed as follows:

(1) In order to retain parallel electron inertial effects and resonant response the full Newton-Lorentz equation of motion for the electrons along the magnetic field must be solved.

(2) Finite electron gyroradius effects can be neglected since the wavenumber regime $k_{\perp}\rho_e < 1$, where k_{\perp} is the perpendicular wavenumber and ρ_e is the electron gyroradius, is relevant. Also, the frequency range $\omega \ll \omega_{ce}$, where ω_{ce} is the electron cyclotron frequency, is of interest. Therefore, the guiding center

approximation for the electron transverse motion can be used.

(3) Since the effects of particle inertia on the drift motion (finite mass introduces polarization plus higher order inertial drifts) are not included in the guiding center approximation, the ion dynamics is advanced with the Newton-Lorentz equation. Ion dissipation effects are therefore included correctly and accurately.

In this section we describe a 2-1/2 dimensional (three velocity components $V_x - V_y - V_z$ and two spatial coordinates $x-y$) particle simulation model which uses the guiding center approximation for the electron transverse motion.^{34,35} The electron drift approximation relaxes time step constraints and parameter regimes one can enter as compared with the full electron dynamics model.

2.1.a Particle Mover and Field Solver

Consider the equation of motion of a charged particle in the presence of an external magnetic field.

$$m_\alpha \frac{d\mathbf{v}_\alpha}{dt} = q_\alpha \left[\mathbf{E} + \frac{\mathbf{v}_\alpha \times \mathbf{B}}{c} \right] \quad (2.1)$$

where α denotes particle species. The guiding center approximation may be used when the total particle motion consists of a fast oscillatory motion (cyclotron) superimposed on another slower motion (ballistic). The slow time scale motion is approximated to lowest order when the left hand side of Eq. (2.1) is set to zero and the equation of motion for the guiding center becomes

$$\tilde{\mathbf{v}} = \frac{c}{B^2} (\tilde{\mathbf{E}} \times \tilde{\mathbf{B}}) \quad (2.2a)$$

$$\frac{d\mathbf{x}}{dt} = \tilde{\mathbf{v}} \quad (2.2b)$$

For the two-and-one-half dimensional (five dimensional phase space) slab model we are considering the magnetic field is oriented along the z-axis with a small y-component. Since the low frequency oscillations propagate nearly perpendicular to the magnetic field ($k_{\perp} \gg k_{\parallel}$) the particle motion can be decoupled into components parallel and perpendicular to the magnetic field

$$\frac{dx_{\perp}}{dt} = \tilde{v}_{\perp} = c \frac{\tilde{\mathbf{E}}_{\perp} \times \tilde{\mathbf{B}}}{B^2} \quad (2.3a)$$

$$\frac{dv_{\parallel}}{dt} = \frac{q\alpha}{m_{\alpha}} E_{\parallel} \quad (2.3b)$$

First, let us consider the equation for the parallel electron motion, Eq. (2.3b). The standard leapfrog finite difference scheme³⁶ can be used to solve for the positions and velocities

$$\frac{v_{\parallel}^{n+1} - v_{\parallel}^n}{\Delta t} = \frac{-|e|\hbar}{m_e} E_{\parallel}^{n+(1/2)}(x_{\parallel}^{n+(1/2)}) \quad (2.4a)$$

$$\frac{x_{\parallel}^{n+(3/2)} - x_{\parallel}^{n+(1/2)}}{\Delta t} = v_{\parallel}^{n+1} \quad (2.4b)$$

which is time-centered and accurate to $O(\Delta t^2)$. We note here that the time centering property is crucial to the time reversibility of the model.

If a leapfrog scheme is used for the perpendicular electron motion, Eq. (2.3a),

$$\frac{x_{\perp}^{n+(3/2)} - x_{\perp}^{n+(1/2)}}{\Delta t} = v_{\perp}^{n+1} = c \frac{E_{\perp}^{n+1}(x_{\perp}^{n+(1/2)}) \times B}{B^2} \quad (2.5)$$

this results in a nontime-centered (unstable) particle mover. Therefore, an alternate method must be used to solve for the electron transverse motion. A procedure used by Lee and Okuda³⁵ is adopted in which a predictor-corrector scheme is used to solve the differential equation describing the transverse motion. Eq. (2.3a) can be written in the form

$$\frac{dx_{\perp}}{dt} = f(x_{\perp}) \quad (2.6)$$

The predictor-corrector method³⁷ of solution for this first order ordinary differential equation is given by

$$x_{\perp \text{ pred}}^{n+1} = x_{\perp}^n + \Delta t f(x_{\perp}^n) \quad (2.7a)$$

$$x_{\perp \text{ corr}}^{n+1} = x_{\perp}^n + \frac{\Delta t}{2} [f(x_{\perp \text{ pred}}^{n+1}) + f(x_{\perp}^n)] \quad (2.7b)$$

Eq. (2.7a) is the predictor formula accurate to $O(\Delta t^2)$ and Eq. (2.7b) is the corrector step accurate to $O(\Delta t^3)$. To implement this algorithm into the particle simulation we use the following difference form

$$\frac{x_{\perp \text{ pred}}^{n+(3/2)} - x_{\perp}^{n-(1/2)}}{2\Delta t} = c \frac{E_{\perp}^{n+(1/2)}(x_{\perp}^{n+(1/2)}) \times B}{B^2} \quad (2.8a)$$

$$\begin{aligned} \frac{x_{\perp \text{ corr}}^{n+(3/2)} - x_{\perp}^{n+(1/2)}}{\Delta t} & \quad (2.8b) \\ & = c \frac{(E_{\perp}^{n+(1/2)}(x_{\perp}^{n+(1/2)}) + E_{\perp}^{n+(3/2)}(x_{\perp \text{ pred}}^{n+(3/2)})) \times B}{2B^2} \end{aligned}$$

For this scheme the Poisson equation must be solved twice per time step to obtain the longitudinal electric fields.

The ion dynamics can be treated in a similar manner; however, in order to preserve the finite ion Larmor radius effects the full Newton-Lorentz equation is solved using the time-centered leapfrog scheme

$$\frac{\mathbf{v}^{n+1} - \mathbf{v}^n}{\Delta t} = \frac{|e|}{m_i} [\mathbf{E}^{n+(1/2)} + \frac{(\mathbf{v}^{n+1} + \mathbf{v}^n) \times \mathbf{B}}{2c}] \quad (2.9a)$$

$$\frac{x^{n+(3/2)} - x^{n+(1/2)}}{\Delta t} = v^{n+1} \quad (2.9b)$$

Now that a stable, time-centered algorithm can be practically implemented let us look at the new set of constraints on the time step which are introduced. First, since the detailed cyclotron motion of the electrons is not present the condition $\omega_{ce}\Delta t < 1$ is no longer restrictive. The ions, however, must have the limitation $\omega_{ci}\Delta t < 1$ in order to resolve the cyclotron motion. Second, the electron ballistic motion along and across the magnetic field must satisfy the aliasing condition^{3a} $k_{\max}v_{\max}\Delta t < 1$ which states that the particle must not move more than a grid spacing, the shortest wavelength of the simulation, in one time step. For the transverse electron motion $k_{\max} = k_{\perp\max}$ and for parallel electron motion $k_{\max} = k_{\parallel\max}$ which is generally very small for the

low frequency microinstabilities of interest. Assuming the perpendicular electron motion is dominated by the $E \times B$ drift

$$\begin{aligned} k_{y\max} v_{\max} \Delta t &= k_{y\max} \frac{c}{B} \langle E_y^2 \rangle^{1/2} \Delta t \\ &= \frac{\omega_{pe}}{\omega_{ce}} k_y^2 \frac{e \langle \phi^2 \rangle^{1/2}}{T_e} \frac{v_e^2}{\omega_{pe}^2} \omega_{pe} \Delta t \end{aligned}$$

which gives

$$\frac{\omega_{pe}}{\omega_{ce}} (\tilde{k}_y^2)_{\max} \langle \frac{e\phi}{T_e} \rangle_{\text{rms}} \omega_{pe} \Delta t < 1 \quad (2.10)$$

where k_y is written in normalized units, $k_y = k_y \lambda_e$. For strong instabilities, $(e\phi/T_e)_{\text{rms}} \simeq 10^{-2} - 10^{-1}$, which implies $\omega_{ce}/\omega_{pe} > 1$ must be satisfied. With this condition present, usually $\omega_{pi} > \omega_{ci}$ and hence $\omega_{pi} \Delta t < 1$ becomes the fundamental limitation on the time step.

This section is concluded with a brief discussion on the method used to solve for the electrostatic fields. A spatial grid is introduced in the x-y plane and macroscopic quantities such as the electric field and charge density are computed at the grid points. This allows the use of the finite fast Fourier transform (FFT)

technique³⁹ to speed up the calculations. The finite Fourier transform in discrete form is

$$\begin{aligned} f(\underline{k}) &= \frac{1}{L_x L_y} \int_0^{L_x} dx \int_0^{L_y} dy f(\underline{x}) \exp[-i\underline{k} \cdot \underline{r}_g] \\ &= \frac{1}{M_x M_y} \sum_{i_x=0}^{M_x-1} \sum_{i_y=0}^{M_y-1} f(\underline{r}_g) \exp[-i\underline{k} \cdot \underline{r}_g] \end{aligned} \quad (2.11)$$

where $L_x = M_x \Delta$ and $L_y = M_y \Delta$. The inverse transform is

$$f(\underline{r}_g) = \sum_{i_x=0}^{M_x-1} \sum_{i_y=0}^{M_y-1} f(\underline{k}) \exp[i\underline{k} \cdot \underline{r}_g] \quad (2.12)$$

The charge density in the finite-size particle model is

$$\begin{aligned} \rho(\underline{r}) &= \sum_j q_j S(\underline{r} - \underline{r}_j) \\ &= \sum_j q_j [S(\underline{r} - \underline{r}_g) + \Delta \underline{r}_j \cdot \nabla_g S(\underline{r} - \underline{r}_g)] \end{aligned} \quad (2.13)$$

which is a Taylor expansion of the finite-size Gaussian-shaped particle

$$S(\underline{r} - \underline{r}_j) = \frac{1}{(2\pi) a_x a_y} \exp \left[\frac{-(x - x_j)^2}{2a_x^2} - \frac{(y - y_j)^2}{2a_y^2} \right] \quad (2.14)$$

about the nearest grid point \underline{r}_g . The charge density in the dipole approximation is given by

$$\rho(\underline{r}) \simeq S(\underline{r} - \underline{r}_g) Q(\underline{r}_g) + \underline{D}(\underline{r}_g) \cdot \nabla_g S(\underline{r} - \underline{r}_g) \quad (2.15)$$

where

$$Q(\underline{r}_g) = \sum_{j \in g} q_j \quad (\text{monopole moment}) \quad (2.15a)$$

$$\underline{D}(\underline{r}_g) = \sum_{j \in Y} q_j \Delta \underline{r}_g \quad (\text{dipole moment}) \quad (2.15b)$$

and $\Delta \underline{r}_g = \underline{r}_j - \underline{r}_g$. The notation $j \in g$ refers to the particle nearest to grid point \underline{r}_g . In order to reduce the number of Fourier transform operations we approximate derivatives appearing in the charge density calculations by finite differences. This is known as the subtracted dipole method (SUDS) due to Kruer and Dawson⁴⁰.

$$\begin{aligned} \rho(\underline{r}) &= S(\underline{r} - \underline{r}_g) Q(\underline{r}_g) + \frac{(\underline{D}(\underline{r}_{g+1}) - \underline{D}(\underline{r}_{g-1})) \cdot \hat{r}}{2\Delta} \\ &= S(\underline{r} - \underline{r}_g) G(\underline{r}_g) . \end{aligned} \quad (2.16)$$

The force on a particle whose center is at the grid point \tilde{r}_g is given by

$$\tilde{F}(\tilde{r}_g) = \int \tilde{E}(\tilde{r}) S(\tilde{r} - \tilde{r}_g) d^3r \quad (2.17)$$

which, when transformed leads to

$$\tilde{F}(\tilde{k}) = L_x L_y S(-\tilde{k}) \tilde{E}(\tilde{k}) \quad (2.18)$$

where

$$\begin{aligned} \tilde{E}(\tilde{k}) &= \frac{-4\pi i \tilde{k}}{|\tilde{k}|^2} \rho(\tilde{k}) \quad (2.19) \\ &= \frac{-4\pi i \tilde{k}}{|\tilde{k}|^2} q_0 M_x M_y S(\tilde{k}) G(\tilde{k}) \end{aligned}$$

and

$$S(\tilde{k}) = \frac{1}{L_x L_y} \exp\left[-a^2 |\tilde{k}|^2 / 2\right] \quad (2.20)$$

q_0 is the charge which is assigned to each particle and $q_0 = |e| n L_x L_y / N$ where the plasma has $n L_x L_y$ electrons and ions and N is the number of finite-sized particles which are followed. The force is now written as

$$\tilde{F}(\tilde{k}) = \tilde{C}(\tilde{k})G(\tilde{k}) \quad (2.21)$$

with

$$\tilde{C}(\tilde{k}) = \frac{-4\pi i k}{|k|^2} q_0 (M_x M_y) (L_x L_y) |s(\tilde{k})|^2 \quad (2.22)$$

and taking the inverse transform

$$\tilde{F}(\tilde{r}_g) = \sum_{i_x=0}^{M_x-1} \sum_{i_y=0}^{M_y-1} \tilde{F}(\tilde{k}) \exp[i\tilde{k} \cdot \tilde{r}_g] \quad (2.23)$$

After obtaining the force at the grid points the force on each particle can be computed using the same subtracted dipole scheme

$$\tilde{F}(\tilde{r}_j) \simeq \tilde{F}(\tilde{r}_g) + \Delta \tilde{r}_j \cdot \nabla_g \tilde{F}(\tilde{r}_g) \quad (2.24)$$

This force is then used in the time advancement scheme, shown earlier, to update the particle positions and velocities.

2.1.b Single Particle Orbit Analysis

To investigate the stability of the predictor-corrector algorithm used in the guiding center model we

consider the motion of the guiding centers of two charged particles of the same sign in a plane perpendicular to the magnetic field. Fig. 2.1 illustrates the particle locations initially and the resultant circular motion about the mean distance between the particles. The outward repulsive force between the particles produces $\vec{F} \times \vec{B}$ drifts equal in magnitude and opposite in direction, resulting in the circular motion.

The location of particle 1 is $(8\Delta, 16\Delta)$ and particle 2 is at $(24\Delta, 16\Delta)$. The magnetic field is directed out of the page and has magnitude $\omega_{ce}/\omega_{pe} = 5$. The time step used in Fig. 2.1a is $\omega_{pe}\Delta t = 0.5$ and produces a stable, almost circular orbit. Each solid circle represents a particle position as the particles rotate about each other. The open circle is the initial particle location. In Fig. 2.1b the time step used is $\omega_{pe}\Delta t = 2$ and the orbit becomes noncircular. The particles begin to move in toward each other as they are winding around. This occurs because the aliasing condition

$$k_{\perp} v_{\max} \Delta t < 1 \quad (2.25)$$

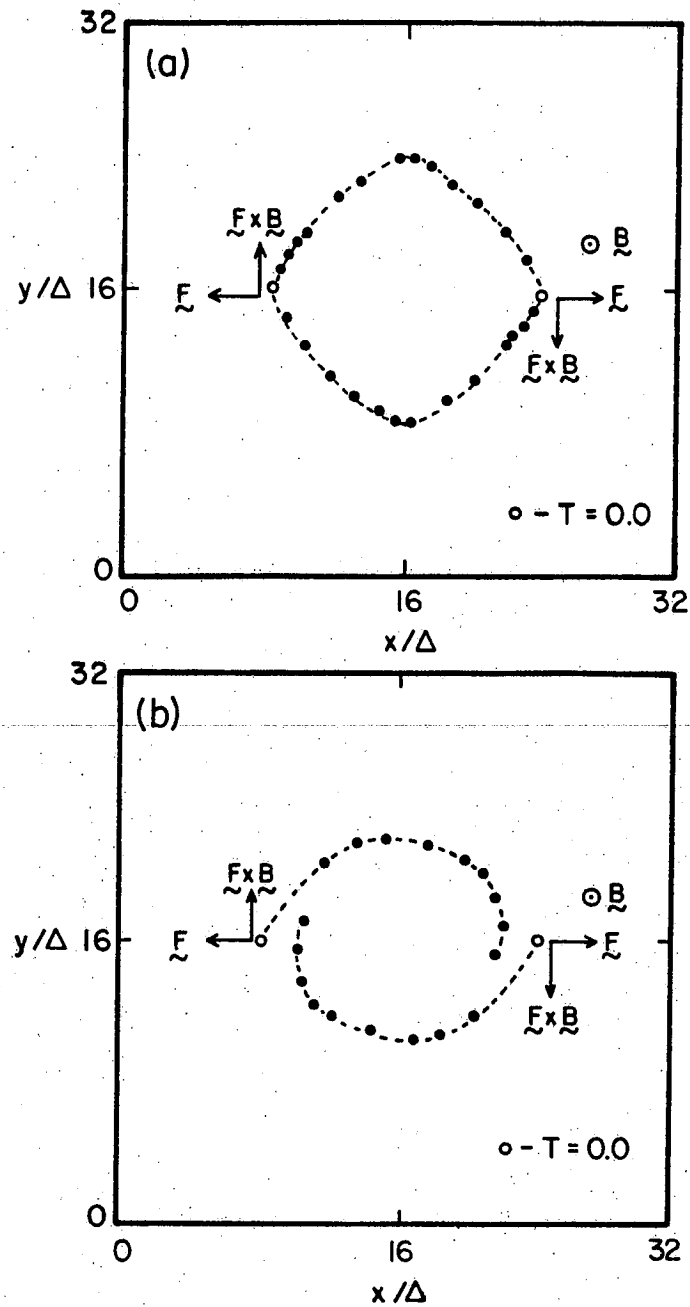


Fig. 2.1 Particle orbits for predictor-corrector integration test. Open circle (o) initial particle location and solid circles (●) give time evolution of orbit.

where $\lambda_{\max} = cE \times B/B^2$, is violated. The perpendicular wavelength, k_{\perp} , is given by the inverse of the distance between the particles.

2.1.c Boundary Conditions

All laboratory and natural plasmas are bounded with some appropriate conditions such as plasma-vacuum, plasma-wall or plasma-plasma. To model these conditions an efficient way to compute the fields is required. Since it is desirable to use the fast Fourier transform (FFT) algorithm to solve Poisson's equation, the FFT method can be adapted to model the bounded system.

To begin with we consider the two dimensional slab model, periodic in the y-direction and bounded in the x-direction. Outside the plasma slab there can exist a vacuum, conducting wall or a plasma. The vacuum conditions on the fields, utilizing FFT methods, have been discussed in detail by Decyk and Dawson,⁴¹ Buneman,⁴² and Hockney.⁴³ The Decyk-Dawson method solves for the Poisson equation inside the plasma slab and Laplace's equation outside the slab where there are no charges. The total potential is written as the sum of the potential obtained from the periodic solution, which is obtained from the

FFT method, and a correction due to the boundaries. This correction is determined by matching at the boundaries and is available in analytic form. The analytic form of the potential correction can be added to the periodic solution in k-space to give the correct solution to Poisson's equation in the plasma slab. A similar method can be used for the conducting wall conditions or whenever the potential must be specified on the boundaries.

For the physics problems addressed in this dissertation we require that either the potential, ϕ , vanish at the boundary of the plasma slab or the normal derivative vanish. Rather than use the Decyk-Dawson method, an alternate scheme was used which exploits symmetry operations in conjunction with the FFT-method to solve the Poisson equation. The key fact to note is that symmetries can restrict the perturbations which are accessible in the simulation. In the case where ϕ vanishes at the boundaries, located at $\bar{x} = 0$ and $\bar{x} = L_x$ in the plasma slab, an image charge density is determined between $x = L_x$ and $x = 2L_x$ using

$$\rho(x,y) = -\rho(2L_x - x,y) \quad (2.26)$$

and then the FFT is performed over the double system

$$\rho(k_x, k_y) = \frac{1}{2L_x L_y} \sum_{i_x=0}^{2M_x-1} \sum_{i_y=0}^{M_y-1} \rho(x, y) \exp [ik_x x_g] \quad (2.27)$$

where $L_x = M_x \Delta$ and $L_y = M_y \Delta$. Then, the Poisson equation is solved in k-space as in the previous section and the potential is transformed back to real space. In this way the potential is guaranteed to vanish at $x = 0$ and $x = L_x$. If it is required that the first derivative of the potential vanish at the boundaries then the image charge condition is

$$\rho(x, y) = \rho(2L_x - x, y) \quad (2.28)$$

The advantage of this method lies in its simplicity and implementation into FFT algorithms which solve the Poisson equation. A disadvantage is that twice as many array elements for the spatial mesh are needed in the bounded direction. However, this is not a significant problem in the electrostatic case.

Once a satisfactory algorithm has been devised to solve for the fields in a bounded plasma, special care must be taken to treat the plasma-boundary interactions

in order to minimize unphysical effects. For the particles, reflecting boundary conditions are used at $x = 0$ and $x = L_x$. The out-of-bounds particles are reflected back to the original system at every time step with new positions and velocities

$$v_x \rightarrow -v_x \quad (2.29a)$$

$$v_y \rightarrow -v_y \cos(2\theta) + v_z \sin(2\theta) \quad (2.29b)$$

$$v_z \rightarrow v_y \sin(2\theta) + v_z \cos(2\theta) \quad (2.29c)$$

$$x \rightarrow 2L_x - x \quad (2.29d)$$

For particle codes following exact dynamics of both species, electrons and ions, large sheath currents can be set up near the boundaries which is caused by differences in gyroradii between the species. Naitouret al.⁴⁴ have studied this problem in detail and several possible ways to circumvent the sheath effects are outlined. In the case where exact ion dynamics and guiding center electrons are followed, the problem is less severe and the conditions specified previously can be used.

Reflecting the ions and reflecting the guiding center electron velocity (equivalent to a sign change in the electric field of the particle) does not produce large relative shifts between electron and ion guiding centers. Over the time scales of the simulation the boundary effects are absent. The reflecting boundary condition on the particles conserves energy at each time step and prevents mixing of particles of different density in the inhomogeneous case. In the periodic, homogeneous y-direction, or the direction of translational symmetry, particles are reintroduced at the opposite ends, consistent with the condition on the periodicity of the potential and charge density in this direction.

2.1.d Fluctuation Spectrum and Mode Dispersion

In this section the time-averaged fluctuation spectrum versus mode number as well as the frequency versus wavenumber spectrum of the thermal fluctuations in the electron guiding center, full ion dynamic electrostatic particle code is presented. This analysis has been done for the full dynamic electron model by Kamimura et al.⁴⁵ In their study many properties of the

electron cyclotron modes were investigated such as the effects of diffusion and noise on the linear Bernstein mode dispersion relation. Spectral peaks at the electron cyclotron frequency and its harmonics, the upper hybrid frequency, $\omega_{UH} = (\omega_{pe}^2 + \omega_{ce}^2)^{1/2}$, and a zero frequency peak attributed to eddies associated with the charged flux tubes appeared to prevail in the simulation results.

In the guiding center electron model, analogous frequencies appear due to the ion motion. Harmonics appear at the ion cyclotron frequency and the upper hybrid peak is replaced by the lower hybrid frequency $\omega_{LH}^2 = \omega_{pi}^2 + \omega_{ci}^2$. The highest frequency of the system is on the order of the lower hybrid frequency $\omega_{LH} \simeq \omega_{pi}$. The electrostatic dispersion relation for small amplitude ion oscillations in a uniform magnetic field is given by:⁴⁶

$$1 + \frac{1}{k^2 \lambda_e^2} + \frac{1}{k^2 \lambda_i^2} \sum_{n=-\infty}^{\infty} \exp[-nb] I_n(b) \left[1 + \frac{\omega}{\sqrt{2} k_{\parallel} v_i} Z \left(\frac{\omega - n\omega_{ci}}{\sqrt{2} k_{\parallel} v_i} \right) \right] = 0 \quad (2.30)$$

where $b = k_{\perp}^2 \rho_i^2$, $\rho_i = v_i / \omega_{ci}$, $v_i = (T_i / m_i)^{1/2}$, $\omega_{ci} = eB / m_i c$ and $\lambda_i = (T_i / 4\pi n_0 e^2)^{1/2}$.

This dielectric contains Landau damping of the cyclotron harmonics. For Landau-damped Bernstein modes nothing appears at the lower hybrid frequency and whatever the density there is a cutoff band over each ion cyclotron harmonic. Low frequency ion acoustic modes are solutions to the dielectric and have the dispersion relation

$$\omega = k_{\parallel} c_s \quad (2.31)$$

where $c_s = ((T_e + 3T_i)/m_i)^{1/2}$ is the ion acoustic speed. Lower hybrid oscillations, $\omega \simeq \omega_{pi}$, and oblique plasma oscillations, $\omega = \omega_{pe} k_{\parallel}/k$, are shielded by the electrons. The ion Bernstein modes are approximated by

$$\omega = n\omega_{ci}(1 + I_n(b)\exp[-b]), n = 1, 2, \dots \quad (2.32)$$

In the limit $k_{\parallel} \rightarrow 0$ or, more precisely, in the wavenumber regime

$$k_{\perp} \rho_i \ll \sqrt{\frac{m_e}{m_i}} \frac{\omega}{\omega_{ci}} \quad (2.33)$$

the ion Bernstein modes become 'pure.' The linear dispersion relation in this limit becomes

$$1 - \frac{1}{k^2 \lambda_i^2} \sum_{n=-\infty}^{\infty} \exp(-nb) I_n(b) \frac{n\omega_{ci}}{\omega - n\omega_{ci}} = 0 \quad (2.34)$$

No complex terms appear in Eq. (2.34) which implies there should be undamped modes. Baldwin and Rowlands,⁴⁷ however, predicted that pure Bernstein modes should have a finite damping rate at approximately that given by Landau damping in the weak magnetic field limit. Since $\omega_{ci} < \omega_{pi}$ this result is valid in the ion Bernstein mode case.

In a dynamical system with a continuous frequency spectrum dissipation can arise due to phase mixing of the normal modes.⁴⁸ The key observation to note is that a finite or infinite discrete sum, $\sum_n \exp[i\omega_n t]$ oscillates whereas an integral, $\int a(\omega) e^{i\omega t} d\omega$, can decay. Therefore, for many frequencies associated with each wave-number there can be a collisionless damping due to phase mixing. The Bernstein modes collectively act to form a single quasi-mode which damps just like a Landau damped mode and which can be explained in terms of a synchrotron-type absorption of electrostatic waves. In order to maintain a thermal equilibrium there is a contribution to wave emission coming from acceleration of particles as well as Cerenkov types of emission.

Before beginning a study of the properties of thermally excited Bernstein modes it is necessary to

check whether the simulation plasma is truly in thermal equilibrium. This is done by measuring the time-averaged fluctuation spectrum in k-space, $\langle E_k(t)E_k^*(t) \rangle$, and comparing it with the results from a fluctuation-dissipation theorem⁴⁹ for a uniform plasma consisting of finite-sized Gaussian particles

$$\frac{E_k^2}{8\pi} = \frac{T_e}{2} \frac{1}{(1 + k^2 \lambda_D^2 \exp[a^2 k^2])} \quad (2.35)$$

For the first test of the model we consider a two-dimensional plasma with uniform magnetic field and periodic boundary conditions. The parameters used are: $L_x \times L_y = 32\Delta \times 32\Delta$, $n_0 = 16/\Delta^2$, $a_x = a_y = 1.5\Delta$, $\omega_{pe}\Delta t = 1$, $M_i/M_e = 100$, $T_e/T_i = 1$, $v_{th} = 1.0\omega_{pe}\Delta$ and $\omega_{ce}/\omega_{pe} = 2$. The simulation is run from $\omega_{ci}t = 0$ to $\omega_{ci}t = 40$. The time-averaged fluctuation spectrum is shown in Fig. 2.2 as a function of wavenumber. Near perfect agreement with theory was obtained except for a few long wavelength modes, for which the observed spectrum showed slight over-excitation due in part to initial conditions and low rate of thermal relaxation for these modes.

The time-averaged partition of field energy among the different modes does not give complete information about a thermal equilibrium plasma since, for a

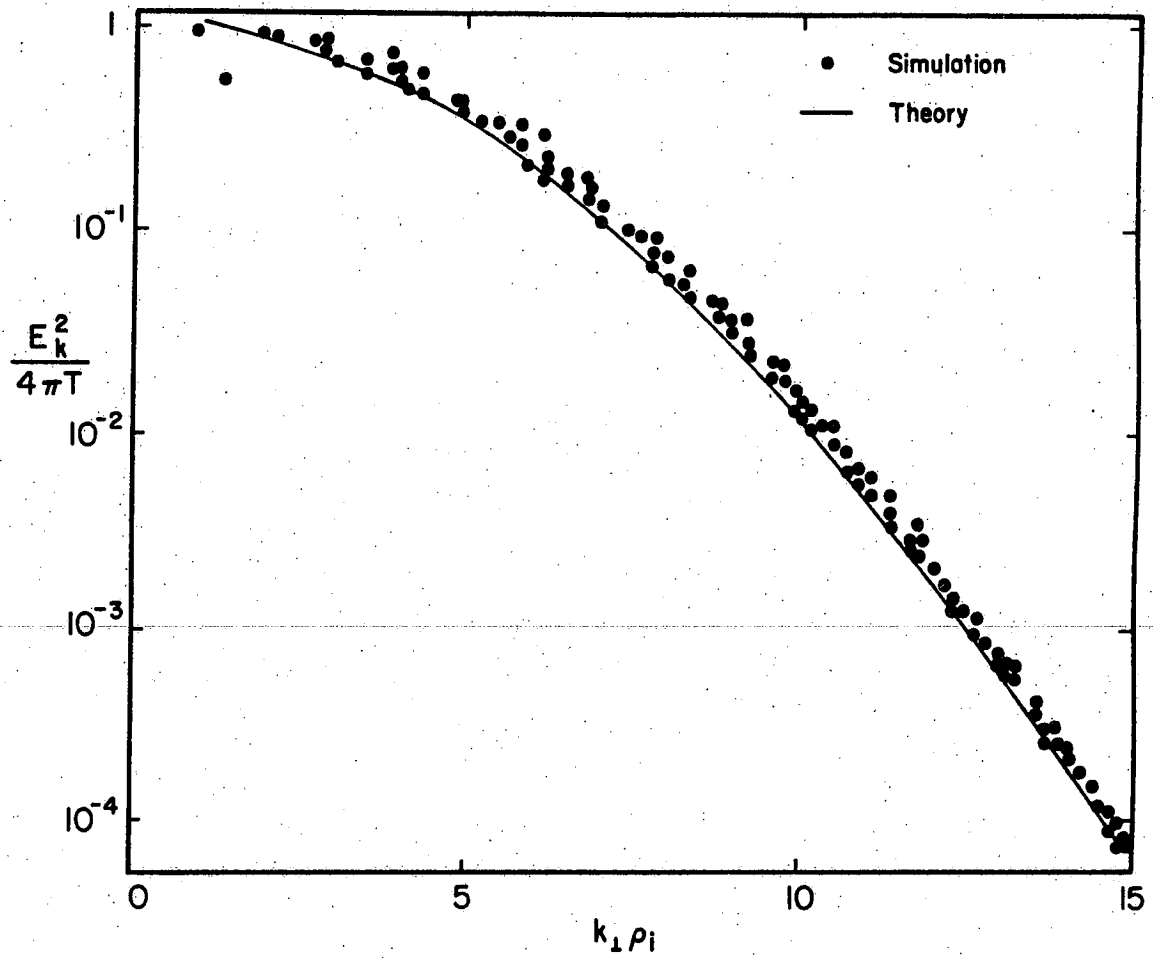


Fig. 2.2. Time-averaged fluctuation spectrum as a function of wavenumber.

fixed k , there are a number of modes with discrete frequencies. For each Fourier component, k , the time autocorrelation function of the electric field fluctuation

$$C_k(\tau) = \lim_{T \rightarrow \infty} \frac{1}{T} \int_{-T/2}^{T/2} dt E_k(t) E_k(t + \tau), \quad (2.36)$$

where τ is a variable lag time, and then a power spectral density

$$I_k(\omega) = \int_{-\infty}^{\infty} d\tau C_k(\tau) \exp[i\omega\tau] \quad (2.37)$$

was computed. Details of these diagnostic methods are given in the last section of this chapter. A number of well-separated peaks in the power spectrum were observed, each peak corresponding to a harmonic of the cyclotron frequency. The frequencies of the spectral peaks for different wavenumbers are plotted in Fig. 2.3, together with the ion Bernstein mode linear dispersion curves obtained from a solution to Eq. (2.34). Good agreement was obtained between the test run results and the theoretical curves.

Fig. 2.4 is a plot of the autocorrelation function for test mode (3,0), which has $k_x = 3(2\pi/L_x)$ and

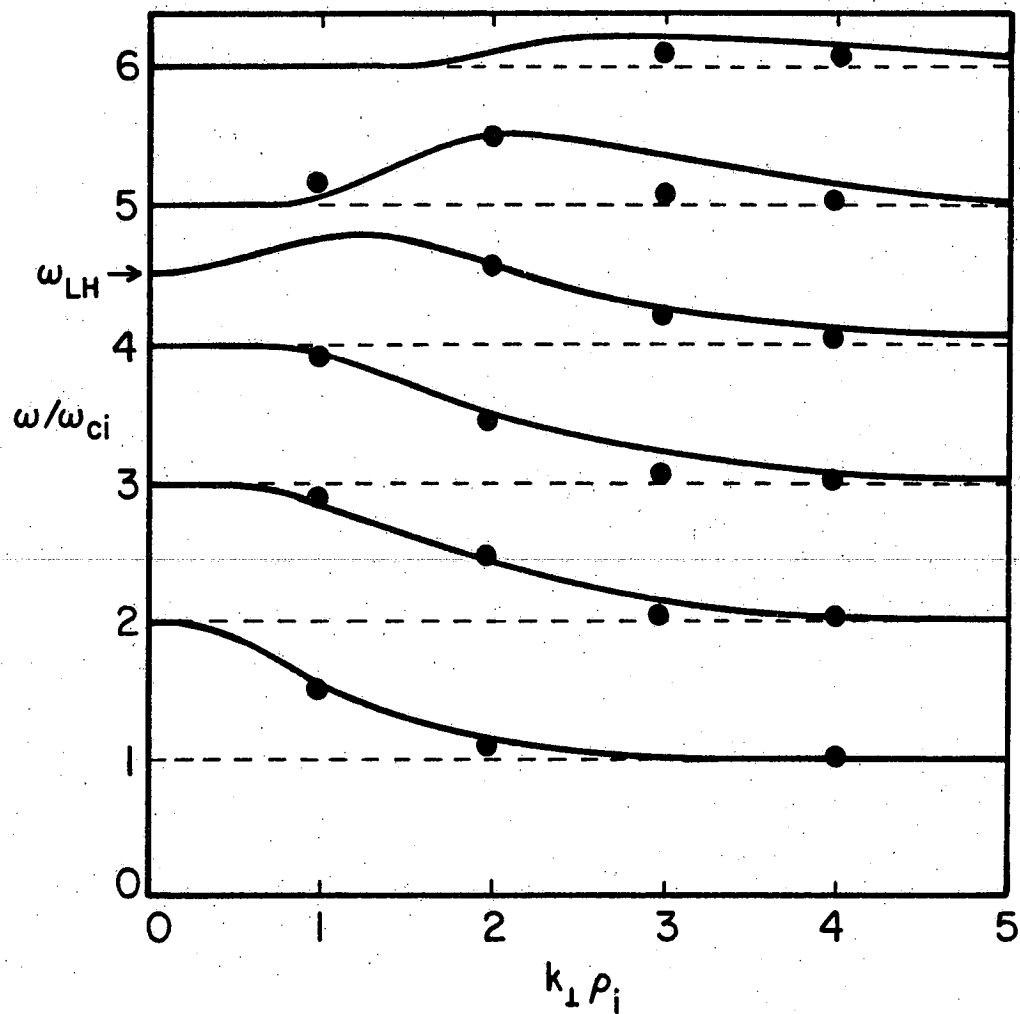


Fig. 2.3. Dispersion curves for thermally excited ion Bernstein modes. Solid lines represent the theoretical values.

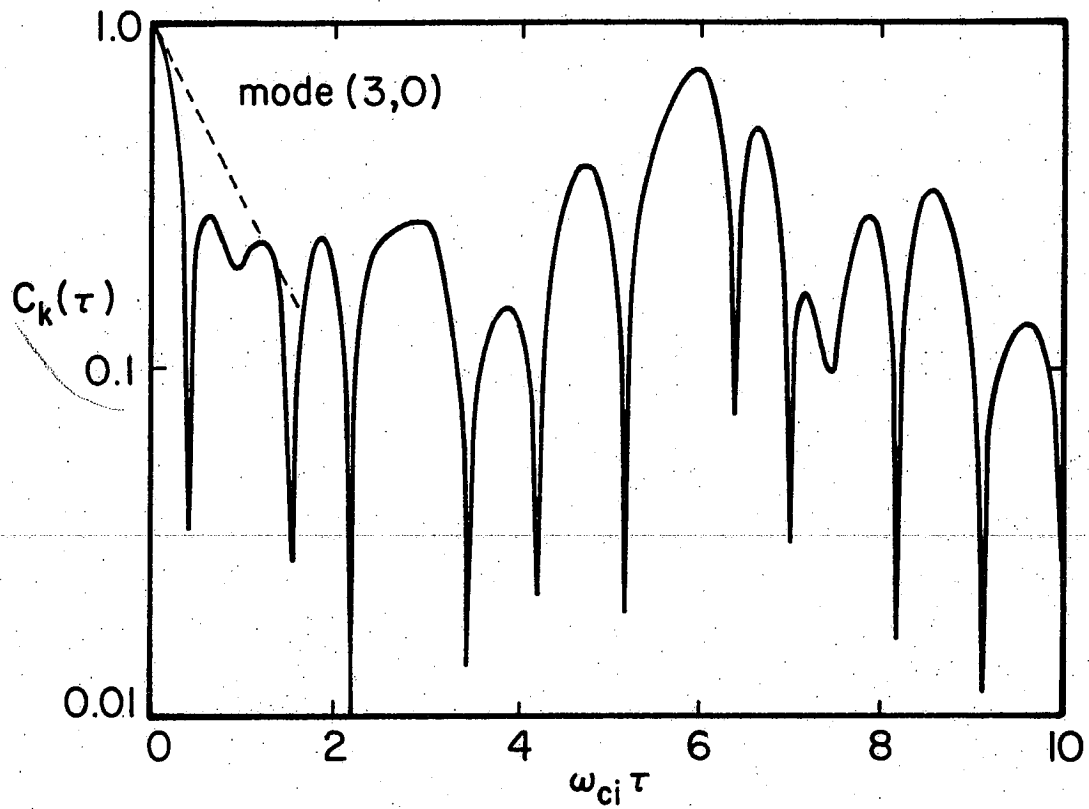


Fig. 2.4. Autocorrelation for test mode (3,0) as a function of the lag time.

$k_y = 0$. This is a short wavelength mode, $k_{\perp} \rho_S \simeq 3$, and the wavelength is comparable to the ion Larmor radius. It is clear from Fig. 2.4 that the amplitude of the autocorrelation function is exponentially damped in a much shorter time than an ion cyclotron period. This initial damping is due to the phase mixing of many cyclotron harmonics. After a time $\omega_{ci} \tau \simeq 6.2$, or one ion cyclotron period, phase coherence is reestablished and for the duration of the simulation the plasma exhibits quasi-periodic behavior with period $2\pi/\omega_{ci}$. The recurrence peaks in the autocorrelation function show diminishing amplitude presumably due to diffusion caused by collisions or convective plasma motion.

We now examine the effect of finite k_{\parallel} by using the two-and-one-half-dimensional plasma model. The magnetic field lines are parallel to the y-z plane. The modes which propagate only in the x-direction have no k_{\parallel} -component and therefore should behave just like the two-dimensional modes previously discussed. All other modes have a finite k_{\parallel} -component and therefore depend on the magnetic field angle in the y-z plane. The angle θ between the magnetic field and the z-axis was chosen to be 5° for the test run and other parameters used were:

$L_x \times L_y = 32\Delta \times 32\Delta$, $v_{th} = 1.5\omega_{pe}\Delta$, $m_i/m_e = 1600$, $T_e/T_i = 1$, $\omega_{ce}/\omega_{pe} = 13$, $\omega_{pe}\Delta t = 10$ and $n_0 = 8/\Delta^2$. Fig. 2.5 shows the power spectral intensity for the pure ion Bernstein modes ($k_y = 0$), Fig. 2.5a, and the Landau-damped ion Bernstein modes, Fig. 2.5b. The spectral peaks are well defined with more distortion in the oblique case due to the presence of Landau damping. The simulation and linear dispersion curves are shown in Fig. 2.6 with excellent agreement between the observed and predicted values. The autocorrelation function for test modes (1,1) and (2,1), corresponding to $k_{\perp}\rho_s \simeq 1$ and $k_{\perp}\rho_s \simeq 2$, respectively, is illustrated in Fig. 2.7. Test mode (1,1) shows very distinct Landau damping and only small amplitude fluctuations (noise) remain for long times. The quasi-periodic behavior is not clearly observed. For shorter wavelengths, such as the (2,1) mode, the autocorrelation function shows the same initial damping but has a more distinctive quasi-periodic time behavior. By examining shorter wavelength test modes it is found that recurrence peaks in the autocorrelation function begin to appear when $k_{\parallel}v_{th} < \omega_{ci}/2\pi$.

As a final test of the model the ion acoustic thermal spectrum was investigated. The simulation

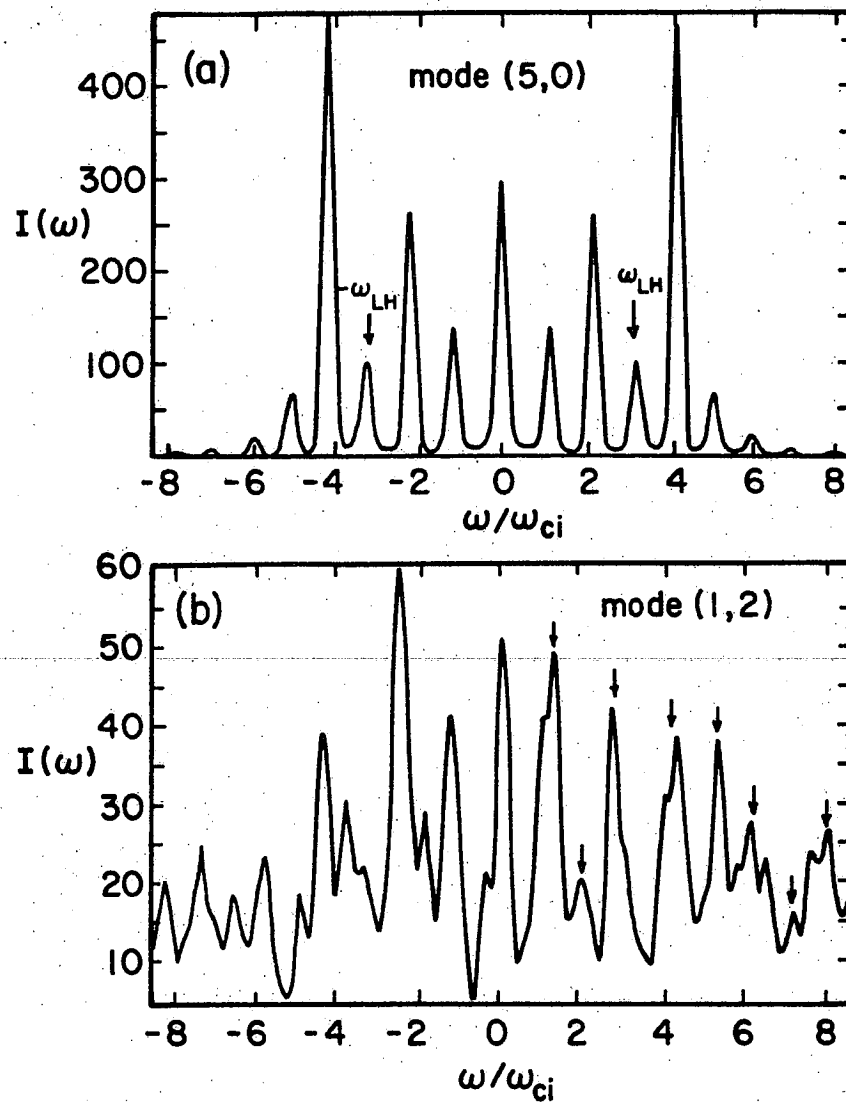


Fig. 2.5. Power spectrum for various test modes. (a) purely perpendicular mode (5,0) and (b) oblique mode (1,2). Arrows refer to the cyclotron harmonics.

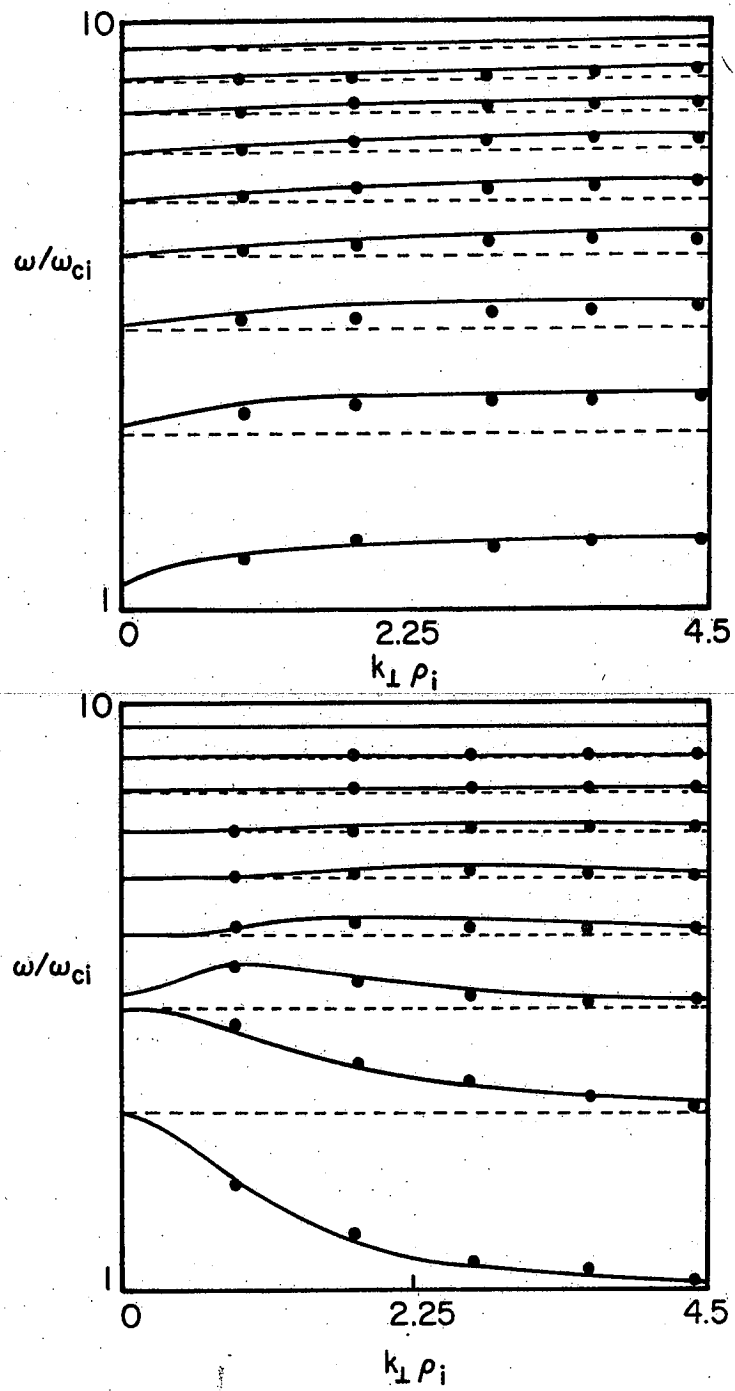


Fig. 2.6. Theoretical and simulation values for the thermal ion Bernstein mode dispersion.

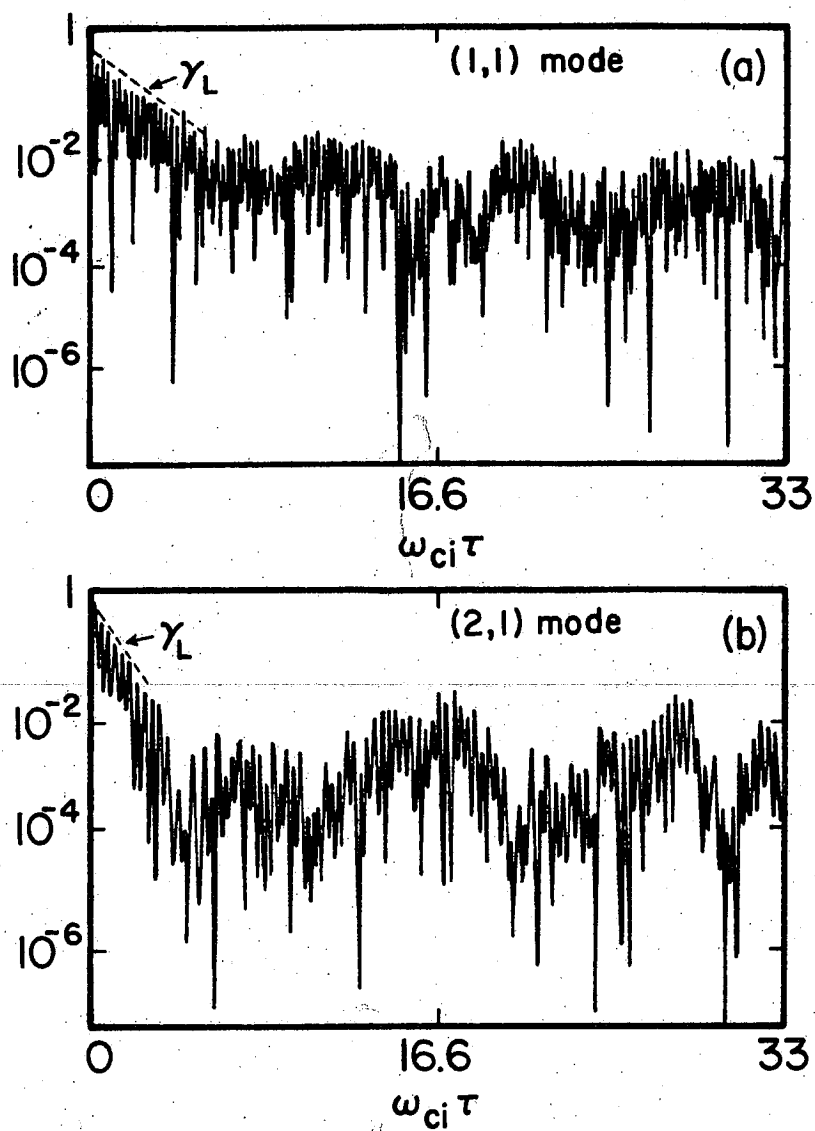
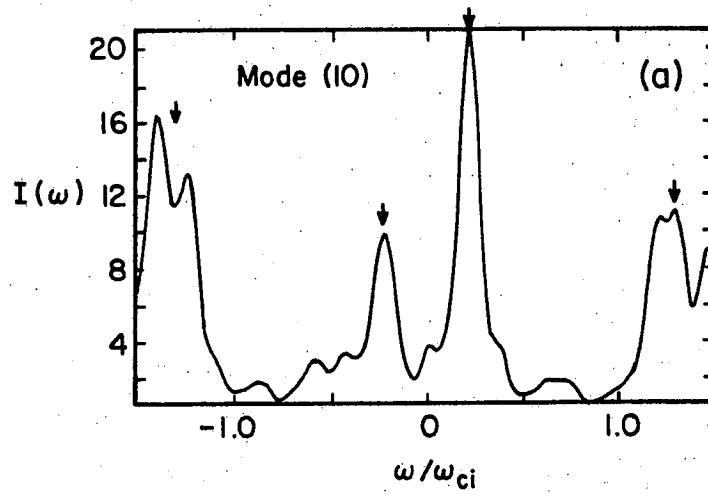


Fig. 2.7. Autocorrelation function for various test modes (a) (1,1) mode and (b) the (2,1) mode. γ_L refers to the Landau damping rate.

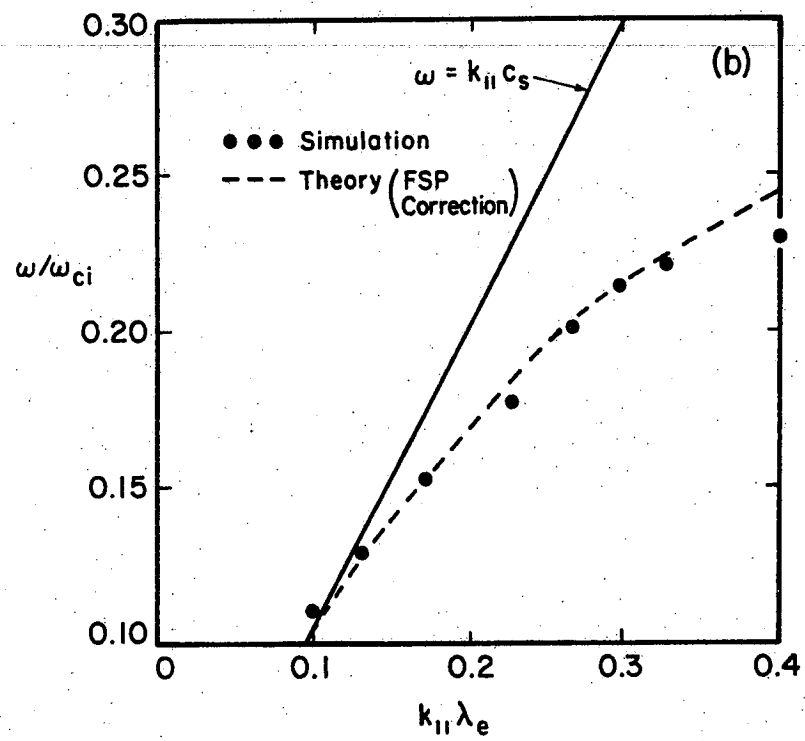
parameters are listed as follows: $\theta = 20^\circ$, $L_x \times L_y = 16\Delta \times 128\Delta$,
 $v_{th} = 1.5 \omega_{pe}\Delta$, $m_i/m_e = 100$, $T_e/T_i = 20$, $\omega_{ce}/\omega_{pe} = 5$,
 $\omega_{pe}\Delta t = 2$, $a = 1.5\Delta$, $n_0 = 8/\Delta^2$. Fig. 2.8a shows the
 power spectrum obtained for the $(k_x, k_y) = (0, 2\pi(10)/L_y)$
 mode. The low frequency ion acoustic peaks are clearly
 visible as well as the first ion cyclotron harmonic.
 Fig. 2.8b is the mode dispersion curves obtained from
 theory, with and without finite particle size correc-
 tions, along with the simulation results.

2.2 Three Dimensional Guiding Center Model

In a three dimensional plasma model the third
 dimension along the magnetic field must be included in
 the equations of motion and in Maxwell's equations. In
 experimental devices for controlled fusion research such
 as the tokamak, stellarator or reversed field pinch, the
 axial length is much longer than the transverse dimension
 (≥ 10 times). If the same resolution along the magnetic
 field is required as across no computer, presently, could
 model the plasma. Fortunately, the important collective
 oscillations associated with plasma confinement have very
 long wavelength along the field line compared to the



(a) Test mode (0,10) is chosen and two inner peaks are acoustic mode. The outer peaks are cyclotron modes.



(b) Linear dispersion of the acoustic modes.

Fig. 2.8. Spectrum of ion acoustic modes.

short wavelengths ($\sim 1-10\rho_i$) across. Therefore, if we perform Fourier expansions in both directions, only a few modes (10-20) need to be kept in the parallel direction in order to retain the necessary physics. By employing a hybrid approach of eigenfunction expansion along the magnetic field and multiple expansion on a spatial grid across the magnetic field, we eliminate the problems of aliasing which would arise due to the finite length grid parallel to the magnetic field. This method was first used by Cheng and Okuda³⁴ in 1977 for modelling drift instabilities in cylindrical and toroidal models.

In this section the basic algorithm is outlined and some of the tests made for a uniform thermal plasma to ensure the validity of the algorithm. If the simulation is able to reproduce linear plasma theory with sufficient resolution then the model can be used to study the nonlinear behavior of plasma microinstabilities.

2.2.a Normal Mode Expansion Method

Consider the three dimensional slab model shown in Fig. 2.9. We assume the three dimensional box to be filled with particles of finite-size, having a Gaussian shape factor

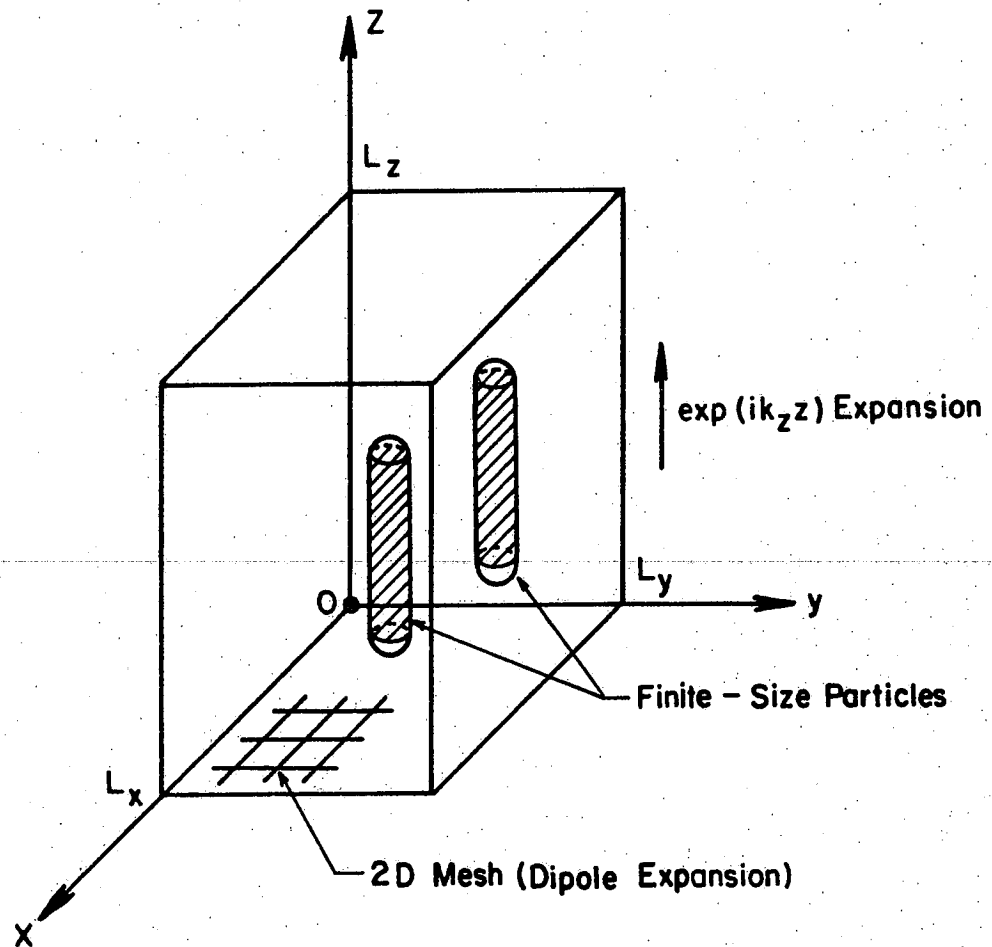


Fig. 2.9. Three dimensional normal mode expansion particle simulation model.

$$S(\underline{x} - \underline{x}_j) = \frac{1}{(2\pi)^{3/2} a_x a_y a_z} \exp - \left[\frac{(x - x_j)^2}{2a_x^2} + \frac{(y - y_j)^2}{2a_y^2} + \frac{(z - z_j)^2}{2a_z^2} \right] \quad (2.38)$$

where (x_j, y_j, z_j) is the charge center location and $a_{x,y,z}$ is the particle size in each direction. The charge density is given by

$$\rho(x,y,z) = \sum_i q_i S(\underline{x} - \underline{x}_i) \quad (2.39)$$

and Poisson's equation is

$$\nabla^2 \phi = -4\pi \rho \quad (2.40)$$

To apply the normal mode expansion method we Fourier analyze the potential with respect to z and this gives

$$\phi(x,y,z) = \sum_{n=-N}^N \phi_n(x,y) \exp^{-[ik_z z]} \quad (2.41)$$

where L_z is the length in the z -direction, $k_z = 2\pi n/L_z$, $n = 0, 1, \dots, N$. Typically, $N = 5 - 20$ is satisfactory. Similarly, the charge density can be expanded

$$\rho(x,y,z) = \sum_{n=-N}^N \rho_n(x,y) \exp[ik_z z] \quad (2.42)$$

where

$$\begin{aligned} \rho_n(x,y) &= \frac{1}{L_z} \int_0^{L_z} \rho(x,y,z) \exp[-ik_z z] dz \\ &= \frac{1}{2\pi a_x a_y L_z} \exp\left[-\frac{a_z^2 k_z^2}{2}\right] \sum_i q_i \\ &\quad \exp\left[-\frac{(x-x_i)^2}{2a_x^2} - \frac{(y-y_i)^2}{2a_y^2}\right] \exp[-ik_z z_i] \end{aligned} \quad (2.43)$$

The equation for $\phi_n(x,y)$ is found to be

$$[\nabla_{xy}^2 - (2\pi n/L_z)^2] \phi_n(x,y) = -4\pi \rho_n(x,y) \quad (2.44)$$

which is a two dimensional Poisson equation to be solved for each mode number, n . This can be done readily using standard FFT methods and then the three dimensional potential is obtained from Eq. (2.41).

The charge density is computed on the two dimensional spatial grid by Taylor expansion about the nearest grid point and in the dipole approximation is

$$\begin{aligned}
\sum_i q_i S(\underline{x} - \underline{x}_i) \exp[-ik_z z_i] &= \sum_i q_i [S(\underline{x} - \underline{x}_g) \\
&+ \Delta \underline{x}_g \cdot \nabla_g S(\underline{x} - \underline{x}_g)] \exp[-ik_z z_i] \\
&= S(\underline{x} - \underline{x}_g) Q(\underline{x}_g) + D(\underline{x}_g) \cdot \nabla_g S(\underline{x} - \underline{x}_g) \quad (2.45)
\end{aligned}$$

where

$$Q(\underline{x}_g) = \sum_{i \in g} q_i \exp[-ik_z z_i] \text{ (monopole moment)} \quad (2.45a)$$

$$D(\underline{x}_g) = \sum_{i \in g} q_i \Delta \underline{x}_g \exp[-ik_z z_i] \text{ (dipole moment)} \quad (2.45b)$$

The finite-size particle model makes the multipole expansion method converge rapidly. In order to reduce the number of Fourier transform operations we approximate derivatives appearing in the charge density calculation by finite differences and this gives

$$\begin{aligned}
\rho_n(x, y) &= \frac{\exp\left[\frac{-a_z^2 k_z^2}{2}\right]}{2\pi a_x a_y l_z} S(\underline{x} - \underline{x}_g) \left[Q(\underline{x}_g) \right. \\
&\quad \left. + \frac{(D(\underline{x}_{g+1}) - D(\underline{x}_{g-1})) \cdot \hat{r}}{2} \right] \quad (2.46)
\end{aligned}$$

The factor $\exp[-ik_z z_1]$ is left unexpanded because there is no grid in the z-direction and is a weighting factor for the charge as well as the force.

The transform of the charge density can now be obtained for each n to give

$$\rho_n(k_x, k_y) = \frac{S(k_x, k_y) \exp\left[-\frac{a_z^2 k_z^2}{2}\right]}{2\pi a_x a_y L_x L_y L_z} M_{x\Sigma}^{-1} M_{y\Sigma}^{-1} \Big|_{i_x=0} \Big|_{i_y=0} \times [Q(\underline{x}_g) + \dots] \exp[i\mathbf{k} \cdot \mathbf{k}_g] \quad (2.47)$$

and the electric field is calculated from

$$\underline{E}_n(k_x, k_y) = \frac{-4\pi i \mathbf{k}}{|\mathbf{k}|^2} \rho_n(k_x, k_y) \quad (2.48)$$

Rather than working with \underline{E} in the Lorentz-Newton equation of motion we use the force \underline{F} on a particle and compute it on the grid points. In order to obtain the force on a particle from the electric field we must account for two effects. First, the particle is not necessarily located at a grid point and appropriate interpolation must be performed; the same way the charge density is interpolated. Secondly, the finite size of the particle must be accounted for. In the finite-size

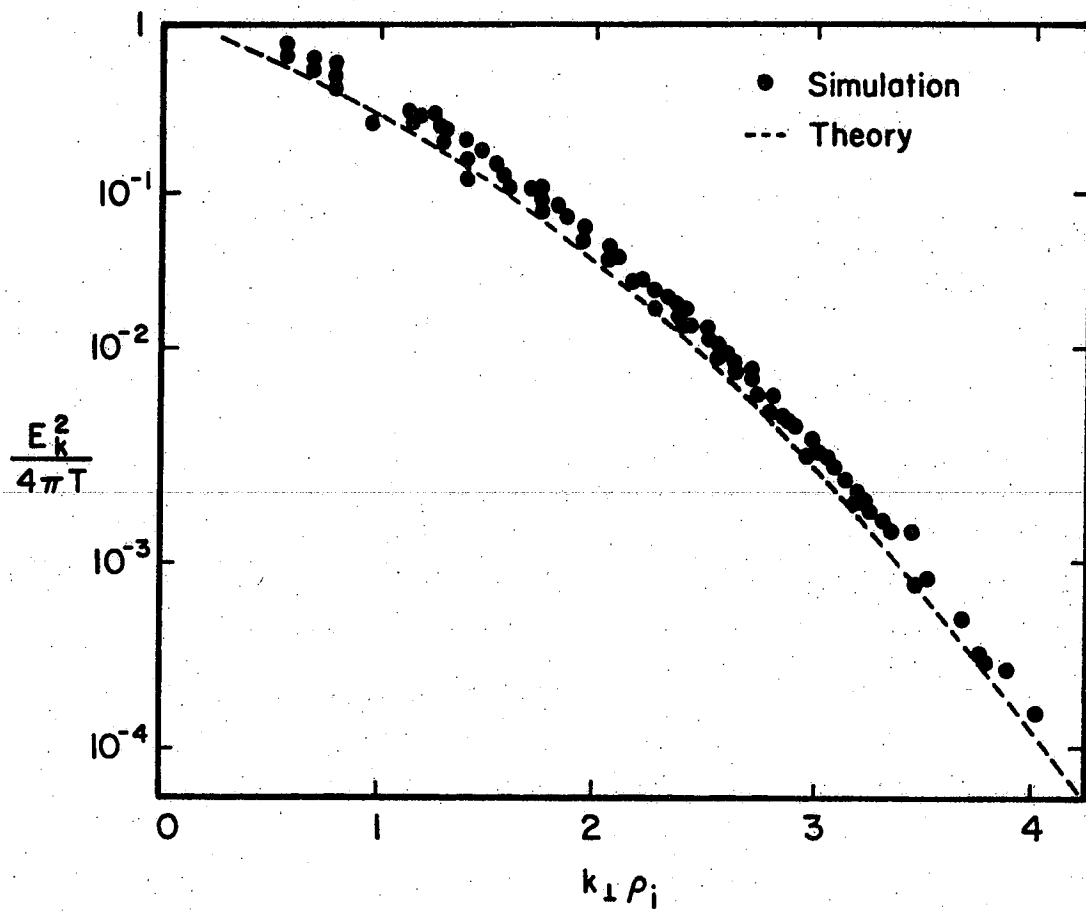


Fig. 2.10. Thermal fluctuation level versus mode number averaged over time.

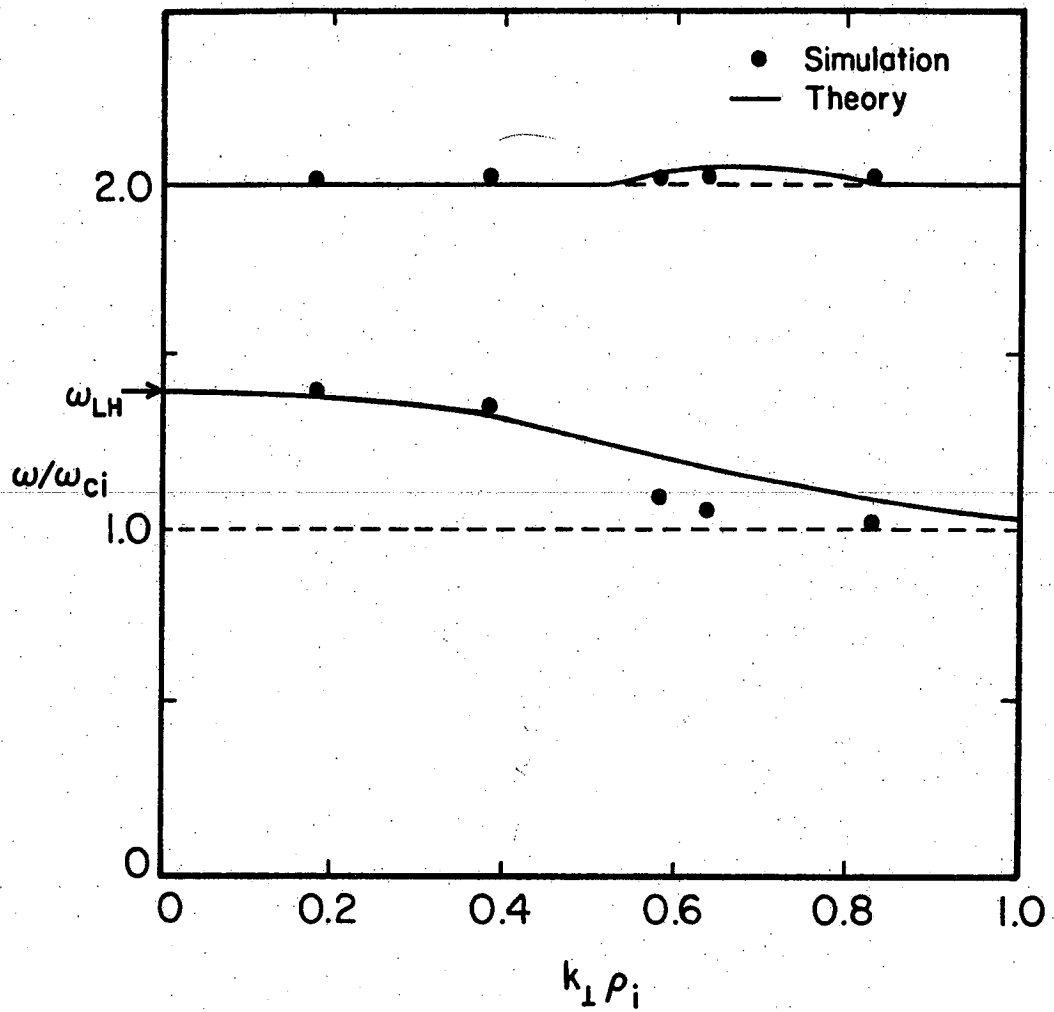


Fig. 2.11. Ion Bernstein mode dispersion curves from simulation and theory using the $(k_x, k_y, 0)$ modes.

were present. In Fig. 2.12 the $(0,0,k_z)$ modes agree well with the linear dispersion relation. The width of the spectral peaks at half maximum gives the approximate error in the measured value. These are indicated on the figure. The large error bars are in part due to the short time length of the simulation run. The $(0,0,k_z)$ modes can be eliminated from the spectrum in order to avoid the high frequency plasma oscillations.

2.3 Collision Operators for Particle Simulations

2.3.a Monte-Carlo Methods

In many problems collisionality among different particle species must be included. The finite-size particle methods were designed to eliminate the collisional effects and in order to enhance the classical collisionality it may be necessary to add scattering. The collision operator presented here is described in detail by Shanny et al.⁵⁰ and gives accurate small angle Coulomb collisions for electrons scattered by the fixed ion background (Lorentz gas collision model). This model conserves energy but not momentum for each collisional event. The main problem in adapting a collision operator to a

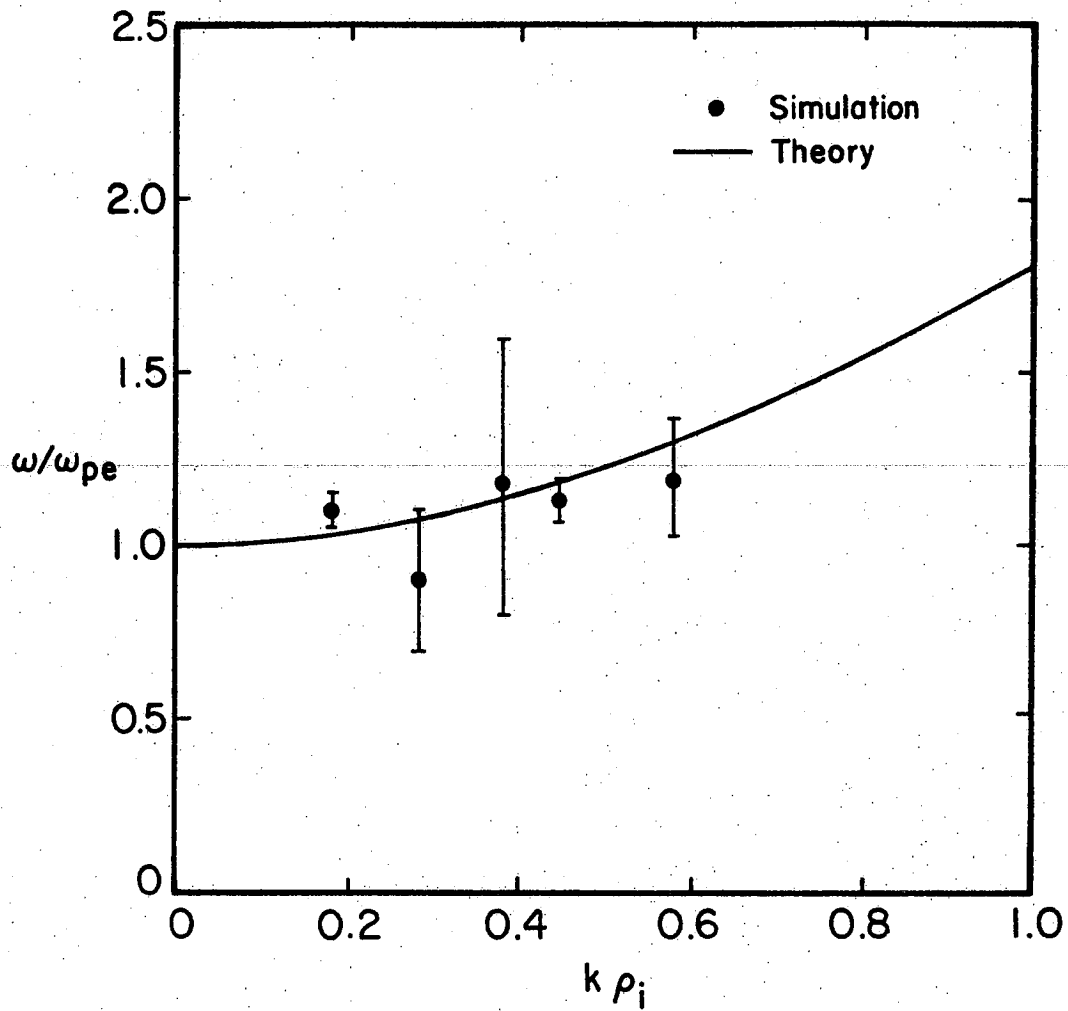


Fig. 2.12. Plasma Oscillation dispersion curves using the $(0,0,k_z)$ modes.

particle code is maintaining the velocity dependence of the scattering rate close to that of a laboratory plasma.

In the Monte-Carlo method the electrons are scattered in the three dimensional velocity space through small angle collisions with the stationary ions. Since the method is energy conserving there is only energy exchange between parallel, V_z , and perpendicular, $V_x - V_y$, motion, with no exchange between electrons and ions. In other words, there is only change of direction in velocity but not in magnitude during time step, Δt .

We assume the velocity vector lies on a spherical surface in velocity space with deflection angles (ϕ, ψ) where ϕ is the angle of deflection in $V_x - V_z$ space and ψ is the orientation of the scattering around the deflection cone. The angle ψ is chosen randomly between 0 and 2π , while ϕ is designed to agree with the Spitzer formula⁵¹ for small angle scattering.

The probability for a scattering to be in the range ϕ to $\phi + d\phi$ at time t , is

$$P(\phi)d\phi = \frac{\phi d\phi}{\langle \phi^2 \rangle \Delta t} \exp[-\phi^2/2 \langle \phi^2 \rangle \Delta t] \quad (2.55)$$

where

$$\langle \phi^2 \rangle = \frac{3}{2} \omega_{pe} \frac{\ln(\Lambda)}{\Lambda}, \quad \Lambda = C \left[\frac{v_1^2 + v_z^2}{\omega_{pe}^2} \right]^{3/2},$$

$C = 6\pi n_o/z$, a numerical constant and $\omega_{pe}^2 = 4\pi n_o e^2/m_e$.

The distribution function

$$C(\phi) = \int_0^\phi P(\phi) d\phi = 1 - \exp \left[-\phi^2/2 \langle \phi^2 \rangle \Delta t \right] \quad (2.56)$$

can be inverted by letting $C(\phi) = R_2$ where R_2 is a uniform set of random numbers between 0 and 1. The desired scattering angle is

$$\phi = C^{-1}(R_2) = \left[-2 \langle \phi^2 \rangle \Delta t \ln(1 - R_2) \right]^{1/2} \quad (2.57)$$

The collision frequency is

$$\nu_{ei} = \frac{1}{2} \langle \phi^2 \rangle \quad (2.58)$$

and is velocity dependent, behaving like $1/v^3$ if we ignore the velocity dependence of $\ln(\Lambda)$. Thus the operator agrees with the Spitzer resistivity velocity dependence.

In practice the operator is straightforward to implement.³⁸ First, we find the angles of the initial velocity vector with components v_x, v_y, v_z . Defining

$v_{\perp}^2 = v_x^2 + v_y^2$, $\sin(P) = v_y/v_{\perp}$, $\cos(P) = v_x/v_{\perp}$, $v^2 = v_{\perp}^2 + v_z^2$,
 $\sin(T) = v_{\perp}/v$ and $\cos(T) = v_z/v$. Then the scattering
 angles are calculated

$$\psi = 2\pi R_1, \quad 0 < R_1 < 1 \quad (2.59a)$$

$$\phi = \left[-4\Delta t v_{ei} \left[\frac{v_{th}}{v} \right]^3 \ln(1 - R_2) \right]^{1/2}, \quad 0 < R_2 < 1 \quad (2.59b)$$

and taking sines and cosines of the angles, the velocity
 increments by components can now be obtained

$$\begin{aligned} \Delta v_x = v & [\sin(\phi) \sin(\psi) \cos(T) \cos(P) \\ & - \sin(\phi) \cos(\psi) \sin(P) \\ & - 2 \sin^2(\phi/2) \sin(T) \cos(P)] \end{aligned} \quad (2.60a)$$

$$\begin{aligned} \Delta v_y = v & [\sin(\phi) \sin(\psi) \cos(T) \sin(P) \\ & + \sin(\phi) \cos(\psi) \cos(P) \\ & - 2 \sin^2(\phi/2) \sin(T) \sin(P)] \end{aligned} \quad (2.60b)$$

$$\Delta v_z = v[-\sin(\phi)\sin(\psi)\sin(T) - 2\sin^2(\phi/2)\cos(T)] \quad (2.60c)$$

These increments are then added to the previous velocities

$$v_x^{\text{new}} = v_x + \Delta v_x \quad (2.61a)$$

$$v_y^{\text{new}} = v_y + \Delta v_y \quad (2.61b)$$

$$v_z^{\text{new}} = v_z + \Delta v_z \quad (2.61c)$$

2.3.b Other Operators

An alternate method of adding collisions to particle simulation models in a manner consistent with Fokker-Planck theory has been proposed by Oliphant and Nielsen.⁵² This method conserves both energy and momentum to a satisfactory degree and closely resembles a Krook collision operator. The simulation collision process is taken to be a binary collision between two particles in close proximity and conceptually one could randomly select two particles from a given space-grid cell and let them undergo momentum and energy changes. With such large particle numbers this could not be done efficiently, therefore a

computationally simpler model must be set up, which on the average gives the same effect.

First, for each cell of the simulation, a vector sum of the particle velocities and a scalar sum of the squares of the particle velocity magnitudes are accumulated. From this information the root mean square deviation from the average velocity is computed

$$v_{\text{rms}} = (\langle v^2 \rangle - \bar{v}^2)^{1/2} \quad (2.62)$$

Since the particle density in each cell is known, an equivalent Maxwellian distribution is defined,

$$f_0 = \frac{n_c}{(2\pi)^{3/2} v_{\text{rms}}^3} \exp \left[-\frac{3v^2}{2v_{\text{rms}}^2} \right] \quad (2.63)$$

where v refers to the velocity with respect to the center of mass velocity of the cell, taken to be the local laboratory frame. In the computational routine for performing the collision, the cell of the test particle is located and an integral number of collisions is performed based on $N(\chi)$. The number $N(\chi)$ is the number of relaxation times a particle experiences in time step Δt and is

$$N(\chi) = \Delta t / \tau(\chi) \quad (2.64)$$

where $\tau(\chi)$ is the relaxation time for an accumulated deviation of angle χ ,

$$\tau(\chi) = \tau_s \sin^2(\chi) \quad (2.65)$$

with $\tau_s = av_{rms}^3/n_c$ which is the Spitzer relaxation time⁵¹ for an accumulated 90° deviation. The number, a , is a cell independent constant which depends on the units. Typically $\chi \simeq 5^\circ$ and $a = 200$. The constant, a , can be adjusted to alter the relative importance of collisions.

In each collision process a collision pair is manufactured statistically according to the distribution function given by Eq. (2.63) with the given cell parameters. The recoil momentum of the collision companion can be added into a cell sum and is distributed uniformly among the simulation particles in each cell. This method has been used and tested against numerical solutions to the Fokker-Planck equation with satisfactory agreement between the two.

2.4 Diagnostic Methods

Computer simulations often allow measurements of quantities which can be compared directly with theory

and experiments. One finds great use in applying laboratory diagnostic methods to computer simulation experiments with the advantage that the act of measurement does not disturb the system. Since the simulation provides very detailed dynamical information of the system, particularly in three dimensions, one must be very clever at discerning the meaningful quantities of interest.

A more comprehensive review of diagnostic methods applied to particle simulations has yet to be compiled but the review article by Dawson⁵³ describes in detail some of the commonly used methods. Interacting and noninteracting test particle motion, temporal evolution of Fourier modes, spatial and temporal correlations are just a few of the quantities which can be determined from the simulation and will be described in this section.

2.4.a Particle Measurements

From the positions and velocities (x, v) the various slices through phase space and real space can be made $(x - v_x, x - v_y, x - y, y - v_y, y - v_x, \text{etc.})$ giving us a composite picture of the detailed particle

motion. This allows one to observe the eddies, flows and depressions in the phase and real space.^{54,55}

An important measurement from the particle data is the distribution function. This is obtained by dividing a velocity axis into uniform cells and counting the number of particles present in each cell. The accuracy of the distribution function can be determined by statistics on the sample and the error in $f(v)$ is given by the square root of the number of particles found in the particular cell. This error can be reduced by using more particles or time averaging procedures. The method used above can be done at various spatial positions giving a combined spatial-velocity distribution function. This allows one to construct two point correlation functions $\langle \delta f(x_1, v_1, t) \delta f(x_2, v_2, t) \rangle$ which provides information about fluctuations δf of the distribution function, $\delta f = f - \langle f \rangle$. For a spatially periodic and homogeneous system the ensemble average is approximated by a finite spatial average over the system length L ,

$$\begin{aligned} & \langle \delta f(x_1, v_1, t) \delta f(x_2, v_2, t) \rangle \\ &= \frac{1}{L} \int_0^L dx \delta f(x_1+x, v_1, t) \delta f(x_2+x, v_2, t) \end{aligned} \quad (2.66)$$

Particle data can be stored or displayed at selected time intervals depending on the amount of resolution one needs. A wealth of information can be obtained from test particle analysis, in particular, we are interested in how particles diffuse in velocity and real space. To compute velocity space diffusion the mean square velocity change of a group of test particles which started out in a small region of velocity space is determined

$$\begin{aligned} \langle \Delta v^2 \rangle &= \langle (v - \langle v \rangle)^2 \rangle \\ &= \frac{1}{N_p} \sum_{i=1}^{N_p} [v_i(t) - v_i(t=0)]^2 \end{aligned} \quad (2.67)$$

where N_p is the number of test particles and $v_i(t)$ is the velocity of the i th particle at time t . From the theory of irreversible statistical mechanics⁵⁶ $\langle \Delta v^2 \rangle$ increases like t^2 for early times and after a certain time, τ_c , known as the decorrelation time, different members of the group feel different forces which changes the quadratic dependence to a linear time dependence

$$\langle \Delta v \Delta v \rangle = 2D\tau_c \quad (2.68)$$

Another test particle quantity of interest is the mean square relative velocity change among pairs of test particles. To compute this we first select particles initially separated in velocity and position, $v_1(t=0) - v_2(t=0) = v_- \pm \alpha v_{th}$ and $x_1(t=0) - x_2(t=0) = x_- \pm \beta \lambda_D$. Then the mean square velocity change is computed as

$$\langle \Delta v_-^2(x_-, v_-) \rangle = \frac{1}{N_-} \sum [(v_2(t) - v_2(t=0)) - (v_1(t) - v_1(t=0))]^2 \quad (2.69)$$

where the sum is over N_- pairs.

In an analogous way the spatial diffusion can be measured. For this measurement it is more convenient to use the guiding center displacement since it does not contain the rapid cyclotron motion. The position of the guiding center of a charged particle in a magnetic field is given by

$$\tilde{x}_{gc} = \tilde{x} - \frac{\tilde{\omega}_c \times \tilde{v}}{|\tilde{\omega}_c|^2} \quad (2.70)$$

where $\tilde{\omega}_c = qB/mc$. The diffusion rate is measured from

the mean-square displacement of the guiding centers of a set of test particles

$$\begin{aligned} \langle \Delta x_{gc}^2 \rangle &= \langle [x_{gc}(t) - x_{gc}(t=0)]^2 \rangle \\ &= \frac{1}{N_p} \sum_{i=1}^{N_p} [x_{gc}(t) - x_{gc}(t=0)]_i^2 \end{aligned} \quad (2.71)$$

Similarly, the mean square relative position change

$$\begin{aligned} \langle \Delta x_-^2 \rangle &= \frac{1}{N_-} \sum [(x_2(t) - x_2(t=0)) \\ &\quad - (x_1(t) - x_1(t=0))]^2 \end{aligned} \quad (2.72)$$

can be useful for determining the spatial decorrelation rates from pairs of particles initially close to each other.

2.4.b Wave Measurements

The plasma exhibits a wide variety of wave-like fluctuations. Associated with the waves are electric and magnetic fields. From the simulations we can measure the fields at various spatial points and at various times. If the plasma is spatially uniform the waves are

sinusoidal and Fourier analysis can be performed to separate the k-components of the fields. For the following discussion on wave measurements we will use the electrostatic potential as the field variable.

First, if we consider a uniform plasma in thermal equilibrium, the time-averaged potential, $\langle \phi_k(t) \phi_k^*(t) \rangle$, for a given wavenumber can be compared to predictions from an equilibrium fluctuation theory.⁴⁹

A quantity related to the spectral density of the potential is the time correlation function

$$C_k(\tau) = \lim_{T \rightarrow \infty} \frac{1}{T} \int_0^T \phi_k(t) \phi_k^*(t + \tau) dt \quad (2.74)$$

where $C_k(\tau) = C_k^*(-\tau)$ for a uniform and stationary ensemble. If the correlation function is nonzero then there exists some periodicity in the function and it is not completely random. From the simulation we measure the correlation function in time by first measuring the desired potential $\phi(t)$ at time t and then at time $t + \tau$ over a longer period of time (T), where τ is fixed and is known as the lag time. The product is taken and the result is integrated over the time interval T . The integrated product, divided by T , is then placed on a graph as

the value of $C(\tau)$ for each τ . Since the data extends only over a finite length of time we cannot estimate the correlation function for arbitrarily long lags, τ . Therefore, a discrete form of the correlation given by⁴⁵

$$C_k(r\Delta t) = \frac{1}{N-r} \sum_{m=1}^{N-r} \phi_k(n\Delta t) \phi_k^*((n+r)\Delta t) \quad (2.73)$$

is used where $r = 0, 1, \dots, m$ is the lag number, m is the maximum lag number and N is the number of data points. The discrete correlation function is calculated using FFT methods so N is chosen to be $N = 2^k$, where k is an integer. It is desirable to keep $m \lesssim N/4$ to reduce statistical errors. If the potential fluctuation are stationary $C_k(\tau)$ should be real. Therefore, it is important to check that $I_m(C_k(\tau))$ be much less than $Re(C_k(\tau))$ for the simulation modes. The finite value of $I_m(C_k(\tau))$ arises from the mild nonstationarity associated with the finite sample length but is generally very small.

Since the correlation function and power spectrum are Fourier transform pairs, related by the Wiener-Khintchine relation,⁵⁷

$$I_k(\omega) = \int_{-\infty}^{\infty} d\tau C_k(\tau) \exp[i\omega\tau] \quad (2.75)$$

the power spectral intensity $I_k(\omega)$ can be calculated by applying a discrete Fourier transform to the sequence $C_k(r\Delta t)$. In order to smooth the estimate of the power spectral density function, a lag window $L(\tau)$ is introduced which controls the resolution and reliability of the spectrum⁵⁸

$$\begin{aligned} I_k(\omega) &= \int_{-\infty}^{\infty} d\tau C_k(\tau) L_k(\tau) \exp[i\omega\tau] \\ &= \frac{1}{2\pi} \int_{-\infty}^{\infty} d\omega' C_k(\omega') L_k(\omega - \omega') \end{aligned} \quad (2.76)$$

and $L(\tau)$ is normalized so that

$$L(\tau = 0) = \frac{1}{2\pi} \int_{-\infty}^{\infty} L(\omega) d\omega = 1 \quad (2.77)$$

A lag window generally used for our purposes is the Parzen window⁵⁹ defined by

$$L(r\Delta t) = \begin{cases} 1 - 6(r/m)^2 + 6(r/m)^3, & r = 0, 1, \dots, m/2 \\ 2(1 - r/m)^3, & r = m/2 + 1, \dots, m \\ 0, & r > m \end{cases} \quad (2.78)$$

and

$$L(\omega) = \frac{3}{4} T_m \left[\frac{\sin(\omega T_m/4)}{\omega T_m/4} \right]^4 \quad (2.79)$$

with $T_m = 2\pi/\Delta\omega$. The frequency bandwidth resolution is $\Delta\omega \simeq 2\pi/m\Delta t$. Statistical errors in the spectrum are reduced by choosing $m \ll N$ and high resolution is obtained if m is large. Finally, we should note that in this method of spectral determination linear trends in the oscillatory sampled data should be removed to prevent large frequency distortions.

An alternate way of estimating the power spectrum is the maximum entropy method.⁶⁰ Using the statistical definition of entropy, η , written in terms of the spectral density

$$\eta_k = \int \ln(I_k(p)) dp \quad (2.80)$$

The correlation function, which is known, gives a constraint on $I(p)$ and is given by

$$C_k(n\Delta t) = \sum_{j=1}^L g_{n-j} C(n - j\Delta t) \quad (2.81)$$

where

$$I_k(p) = \int_{-\infty}^{\infty} d\tau C_k(\tau) \exp[ip\tau] \quad (2.82)$$

The quantity g is a set of coefficients of a predictive filter and L is the filter length. Eq. (2.81) is a set of linear finite difference equations of the form

$$x(k) = \sum_{j=1}^L g_{k-j} x(k-j) + \epsilon_k \quad (2.83)$$

where ϵ_k is the error and these equations are solved in matrix form in order to find the best filter. This is equivalent to the process of maximizing the entropy η . A set of recursion relations, known as the Burg relations,⁶⁰ are used to provide efficient solutions for the linear coefficients g_{k-j} and error ϵ_k . From the solution of the correlation function the power spectral density can be obtained, consistent with a minimization of the entropy η . The advantage of this method over the FFT method is that better spectral resolution is obtained for shorter time samples. A disadvantage is that more low amplitude uncorrelated signals may appear over long time samples.

For nonuniform plasmas, which will be of main concern in this dissertation, the normal modes are more complex than simple sine waves. In order to find the normal modes we must measure quantities associated with the wave at various positions in the plasma, in other words, two point spatial correlations as well as the two time correlations considered previously. The spatial correlation function

$$C_k(x, x', \tau) = \lim_{T \rightarrow \infty} \frac{1}{T} \int_0^T \phi_k(x, t) \phi_k^*(x', t + \tau) dt \quad (2.84)$$

and spectral intensity

$$I_k(x, x', \omega) = \int_{-\infty}^{\infty} d\tau C_k(x, x', \tau) \exp[i\omega\tau] \quad (2.85)$$

give the spatial form of the normal mode and normal mode frequency, respectively.

A modification of this procedure for computing the above correlation functions can be used to analyze the spatial and temporal evolution of the normal modes. Typically, a spectrum will consist of a continuous as well as a discrete part. The discrete spectral lines correspond to normal modes of the plasma. If we wish to

find the shape of the wave function associated with the normal mode of frequency ω_0 we can correlate the measured simulation potential with an external source $\sin(\omega_0 t)$. In other words, we form the correlation⁶¹

$$C_k(x, \tau) = \frac{1}{T} \int_0^T \phi_k(x, t+\tau) \sin(\omega_0 t) dt \quad (2.86)$$

which can be written in discrete form

$$C_k(x, r\Delta t) = \frac{1}{N-r} \sum_{m=1}^{N-r} \phi_k(x, (m+r)\Delta t) \sin(\omega_0 m\Delta t) \quad (2.87)$$

with $r = 0, 1, \dots, m$ and r is the lag number, m the maximum lag and N is the number of data points. This gives an accurate representation of the wave function at various lag times provided the integration length, T , is long enough to resolve the frequency ω_0 but not so long that slow changes in the zero-order plasma properties are included. When the integral or sum over time is computed, the time span T should be less than the damping time, γ^{-1} , of the normal mode, otherwise initial oscillations will die out during the integration time and oscillations at some random phase will be excited. If the wave function is stationary for all lag times it is characterized as a standing wave and if there is propagation

in a particular direction the phase velocity of the wave can be measured. This method of analysis of the wave function is known as the interferogram method and has been used with success in particle simulations of lower hybrid heating.⁶¹

C H A P T E R I I I

PARTICLE SIMULATION OF DRIFT WAVES IN A SHEARED MAGNETIC FIELD

3.1 Introduction

The presence of density, temperature and electric field fluctuations in a confined, inhomogeneous magnetized plasma causes a drift motion of the charged plasma particles. This diamagnetic drift⁶² allows for the existence of an additional collective mode of oscillation called the drift wave (or universal mode), which is not present in a homogeneous plasma. At the simplest level the electron and ion $E \times B$ drifts are the same and no effective momentum or energy exchange exists. When wave-particle resonances and finite ion Larmor radius effects are taken into account the electron and ion $E \times B$ drifts can be driven out of phase. The particles can give up energy to the waves and cause them to grow.

The theoretical study of the collisionless drift mode driven by a density gradient was initiated many years ago and has remained an active research subject. In the early work on these instabilities, Krall

and Rosenbluth⁶³ considered equilibrium variations in the density profile of a low beta, collisionless plasma slab immersed in a strong sheared magnetic field. They were able to find a restricted class of unstable, exponentially decaying (nonpropagating) radial normal modes.

Rutherford and Frieman⁶⁴ found that the collisionless drift wave in a sheared magnetic field (B has a small y -component varying with x , the radial coordinate) can take the form of convectively unstable wave packets which can be stabilized by sufficiently strong magnetic shear. In 1969 Pearlstein and Berk⁶⁵ introduced outgoing wave boundary conditions into the mode analysis of Krall and Rosenbluth and discovered a general class of propagating modes. By balancing the destabilizing (x -dependent) resonant electron contribution against the stabilizing ion Landau damping, Pearlstein and Berk⁶⁵ found the necessary amount of shear to stabilize the drift wave. The time domain wave packet analysis led to qualitatively equivalent results.⁶⁶

In 1978 Ross and Mahajan¹² as well as Tsang et al.,¹³ in independent numerical calculations, found that the drift wave eigenmodes of Pearlstein and Berk⁶⁵ are in fact always absolutely stable in sheared slab

geometry. The stability arises from the inclusion of the contribution from nonresonant electron effects in the immediate vicinity of the mode rational surface. These effects are not understood in simple physical terms. Antonsen⁶⁷ proved analytically that no bound, growing eigensolutions exist for drift waves in a sheared magnetic field. Using a complex transformation technique the drift wave eigenmode equation resembles Schrödinger's equation for the motion of a particle in a potential at zero energy. From the shape of the potential and the fact that it has finite depth Antonsen⁶⁷ has shown that no growing eigenmodes exist. Even though the drift wave is not absolutely unstable, the convectively unstable form of the collisionless drift wave^{64,67} may persist and the shear stabilization condition can be useful in assessing the importance of amplification of thermal fluctuations.⁶⁸⁻⁷¹

In order to investigate the subtle linear properties and nonlinear effects of the drift wave Lee and Okuda⁷² began particle simulations of the universal mode in 1976. Their pioneering effort was successful in verifying the linear drift wave theory for a shearless slab model. Also, they found quasi-linear flattening of

the density profile to be the primary saturation mechanism. For the cases with magnetic shear the stabilization thresholds were found to be approximately the same as that given by Pearlstein and Berk.⁶⁵ The simulations did not resolve whether the modes were absolute or convective in nature.⁷³ In 1979 Lee et al.⁷⁴ investigated the convective nature of the modes and argued that unstable local "transients" dominated the simulations. The eigenmode structure predicted by linear theory was not observed.

As far as applications to tokamak plasmas are concerned the sheared slab model with a single mode rational surface is not considered to be of interest but serves as a starting point. In these plasmas toroidal geometry^{15, 16} and multiple mode rational surfaces may allow for many qualitatively new effects including a possible absolute or nonlinear instability.¹⁴ Nevertheless, particle simulations of drift waves in a sheared slab with single mode rational surface have yet to be reconciled with linear theory. Also, the convective amplification of drift wave packets is still an open question.⁶⁸⁻⁷¹ For example, the amplification may occur at such high levels that nonlinear effects could occur prior to attainment of the predicted fluctuation levels. Conventional

linear theory deals with steady state while the wave packet approach considers transient phenomena.⁶⁴ The particle simulation can describe the transient effects and over long enough times can characterize the steady state. Therefore this is a useful approach to the drift wave problem.

The organization of this chapter is as follows: The linear drift wave theory is reviewed and the linear eigenmode equation is solved for the parameters relevant to the simulation. The simulation configuration is outlined and the parameter regime under investigation. The simulation results and interpretation for strong as well as weakly sheared magnetic fields is presented. Finally, a summary of the main results is given.

3.2 Linear Drift Wave Theory

Most studies of the drift wave have been carried out in the simplest possible geometry ignoring toroidal effects and details of the confinement configuration. Accordingly, we consider a plane slab of plasma which is nonuniform in the x -direction with a main magnetic field in the z -direction. A smaller field component in the y -direction which is a function of x

provides shear and causes rotation of the direction of the field vector, \vec{B} , as one traverses the slab. To relate this to tokamaks we identify x with the minor radius r , y with the poloidal distance $r\theta$ and z with the toroidal distance $R\theta$. The magnetic field in the z -direction corresponds to the toroidal field, B_T , generated by external coils and $B_y(x)$ relates to the poloidal field, B_p , produced by the plasma current in the toroidal direction. The B_y field is assumed to vary linearly along the density gradient and is given by

$$\vec{B} = B(\hat{z} + \frac{x}{L_s} \hat{y}) \quad (3.1)$$

where $L_s^{-1} = B'_y(x)/B$ is the shear length. In this magnetic field the parallel wavenumber varies with x and is given by

$$k_{\parallel}(x) = k_z + k_y \frac{x}{L_s} \quad (3.2)$$

For appropriate values of k_y and k_z there exists a surface, which is called the singular or mode-rational surface, where $k_{\parallel} = 0$. In a tokamak this corresponds to the region where the field lines close on themselves. In the neighborhood of the singular surface we can write:

$$k_{\parallel}(x) \simeq \frac{k_y(x - x_0)}{L_s} \quad (3.3)$$

In this geometry low frequency ($\omega \ll \omega_{ci}$) perturbations have a space-time variation of the form

$$f(x) \exp[-i\omega t + ik_y y + ik_{\parallel} z] \quad (3.4)$$

The physical properties of the drift wave in the presence of magnetic shear is now outlined. In the local approximation we would solve the dispersion relation for drift waves at each magnetic surface x . This approach is not valid when there is significant magnetic shear and we must construct an eigenfunction in x . Physically, finite ion Larmor radius effects cause a phase shift between the ion and electron $E \times B$ drifts which lowers the effective frequency of the diamagnetic drift oscillation, ω_* , such that $\omega < \omega_*$. This frequency shift causes an inverse Landau damping of electrons resonating with the wave. The electrons give energy to the wave around the point x_e , where $\omega = k_{\parallel}(x_e)v_e$, and therefore the electron Landau resonance is located at $x_e = |L_s \omega / k_y v_e|$. This energy supplied to the wave is convected, in the presence of shear, to large x until it reaches the resonance point

of the ions $x_i = |L_s \omega / k_y v_i|$, where it is absorbed directly by Landau damping. For $\omega \simeq \omega_*$ we have $x_i \simeq \rho_i (L_s / L_n)$ which is the characteristic scale length of the eigenfunction.

Very close to the mode rational surface where $x < x_e$ and $v_e < |\omega / k_{\parallel}|$, most electrons are nonresonant. These electrons maintain the quasi-neutrality of the low frequency fluctuations by $E \times B$ drifting with the ions. It is these electrons which play an important role in the stabilization of the mode. If neglected or improperly treated in the theory an erroneous prediction of stability follows.⁶⁵ The electrons located in the region $x > x_e$ maintain charge neutrality by electron bunching along the magnetic field since k_{\parallel} is larger.

In order to quantify the physical picture we begin by writing the Vlasov equation for the ion species

$$\frac{\partial f_i}{\partial t} + \tilde{v} \cdot \frac{\partial f_i}{\partial \tilde{x}} + \frac{|e|}{m_i} \left(\tilde{E} + \frac{\tilde{v} \times \tilde{B}}{c} \right) \cdot \frac{\partial f_i}{\partial \tilde{v}} = 0 \quad (3.5)$$

The ion distribution is written as the sum of an average part, $\langle f_i \rangle$, and a fluctuating part, \hat{f}_i . The perturbed ion density is given by

$$Q(\tilde{x}, \omega) = \frac{T_e}{T_i} - k_y^2 \rho_s^2 + \frac{[(1 + \frac{T_e}{T_i}) \frac{\omega}{\omega_*} + (\frac{\omega}{\omega_*} - 1) \zeta_e Z(\zeta_e)]}{(\frac{\omega}{\omega_*} + \frac{T_i}{T_e}) \zeta_i Z(\zeta_i)}$$

and $\tilde{x} = x/\rho_s$. The prime denotes differentiation with respect to \tilde{x} .

The electron and ion resonance locations are determined from the condition $\zeta_\alpha = 1$. The complex frequency, ω , with $\text{Im}(\omega) > 0$ corresponds to absolute instability while $\text{Im}(\omega) = 0$ gives marginal stability. The modes $\hat{\phi}(\tilde{x})$ are centered around the rational surface, $\tilde{x} = 0$, and exhibit a parity since the effective potential is symmetric about $\tilde{x} = 0$. The eigenfunction for even ($\hat{\phi}(\tilde{x}) = \hat{\phi}(-\tilde{x})$) and odd ($\hat{\phi}(\tilde{x}) = -\hat{\phi}(-\tilde{x})$) parity modes, with respect to the rational surface are displayed in Figs. 3.1a and 3.1b, respectively. The shear strength $L_s/L_n = 28$ and mode $k_y \rho_s = 0.49$ are used. The wavefunctions and eigenfrequencies are obtained from a numerical solution of Eq. (3.11) using a standard shooting code method. Outgoing wave boundary conditions are used at large x .

The real frequency and damping rates for various wavenumbers, $k_y \rho_s$, are shown in Fig. 3.2 using $L_s/L_n = 28$, $m_e/m_i = 0.01$ and $T_e/T_i = 1$. The real frequencies for odd and even parity were nearly the same numerically and therefore only the values for the even parity are shown.

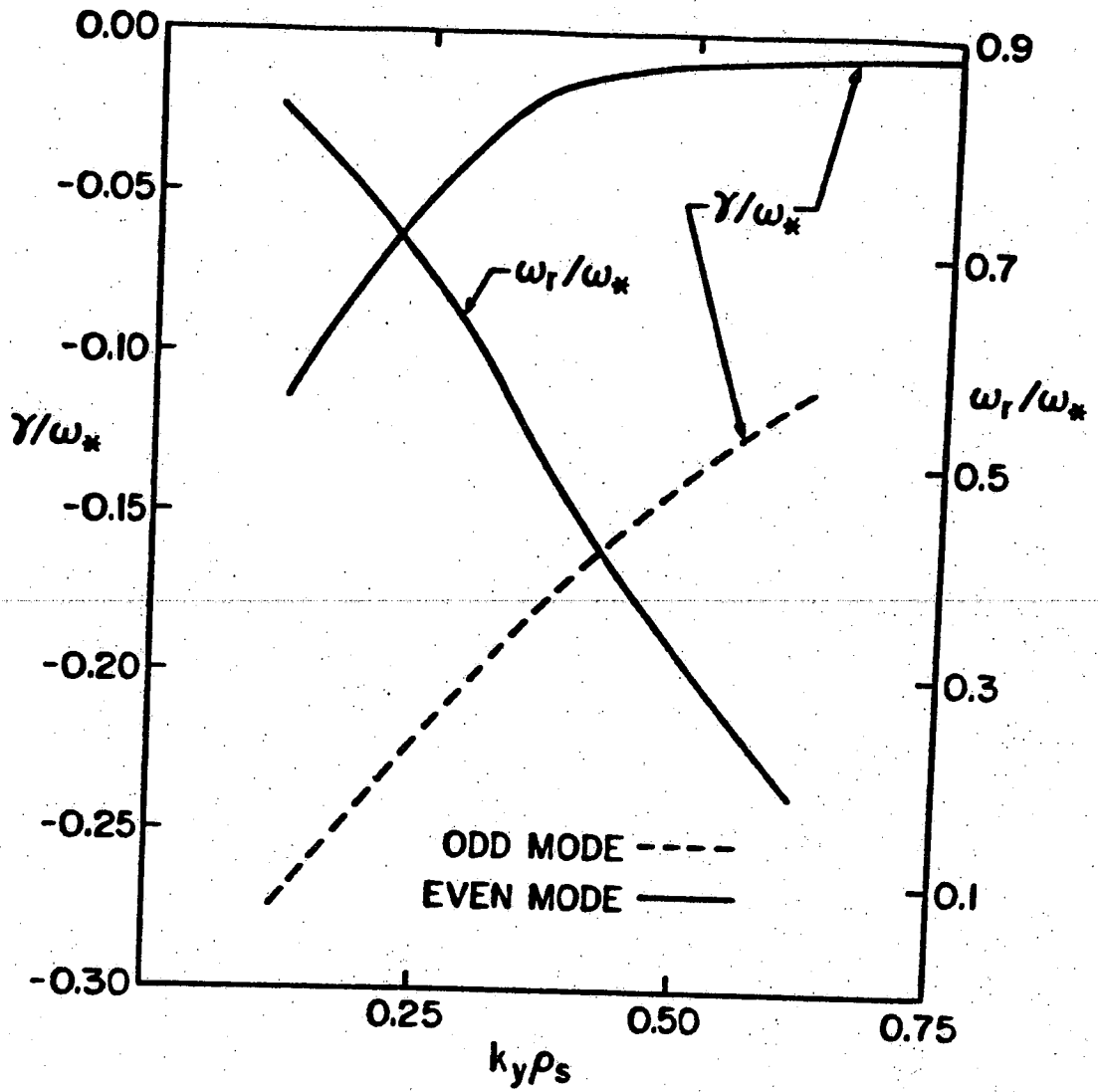


Fig. 3.2. Real and imaginary parts of eigenmode frequency ω/ω_* and γ/ω_* as a function of $k_y \rho_s$ for even and odd parity modes with same parameters as Fig. 3.1.

In all cases linear theory predicts stable, linearly damped modes for both even and odd parity. Since the even parity mode is less heavily damped it is the usual physical parity of the universal mode.

3.3 Simulation Configuration and Parameters

In order to address questions about the existence of drift eigenmodes and convective effects we have carried out particle simulations of drift waves in a sheared magnetic field with single rational surface.⁷⁷ The results extend the work of Lee et al.⁷⁴ because a wider parameter regime, as well as different boundary conditions are investigated.

For the results in this chapter we use the 2-1/2D (x - y positions, v_x - v_y - v_z velocities) electrostatic guiding center electron, full ion dynamics particle code described in the previous chapter. The system is periodic and uniform in particle density in the y -direction and bounded with an inhomogeneous particle distribution in the x -direction.

The initial configuration is shown in Fig. 3.3. The plasma is confined between two boundaries located at

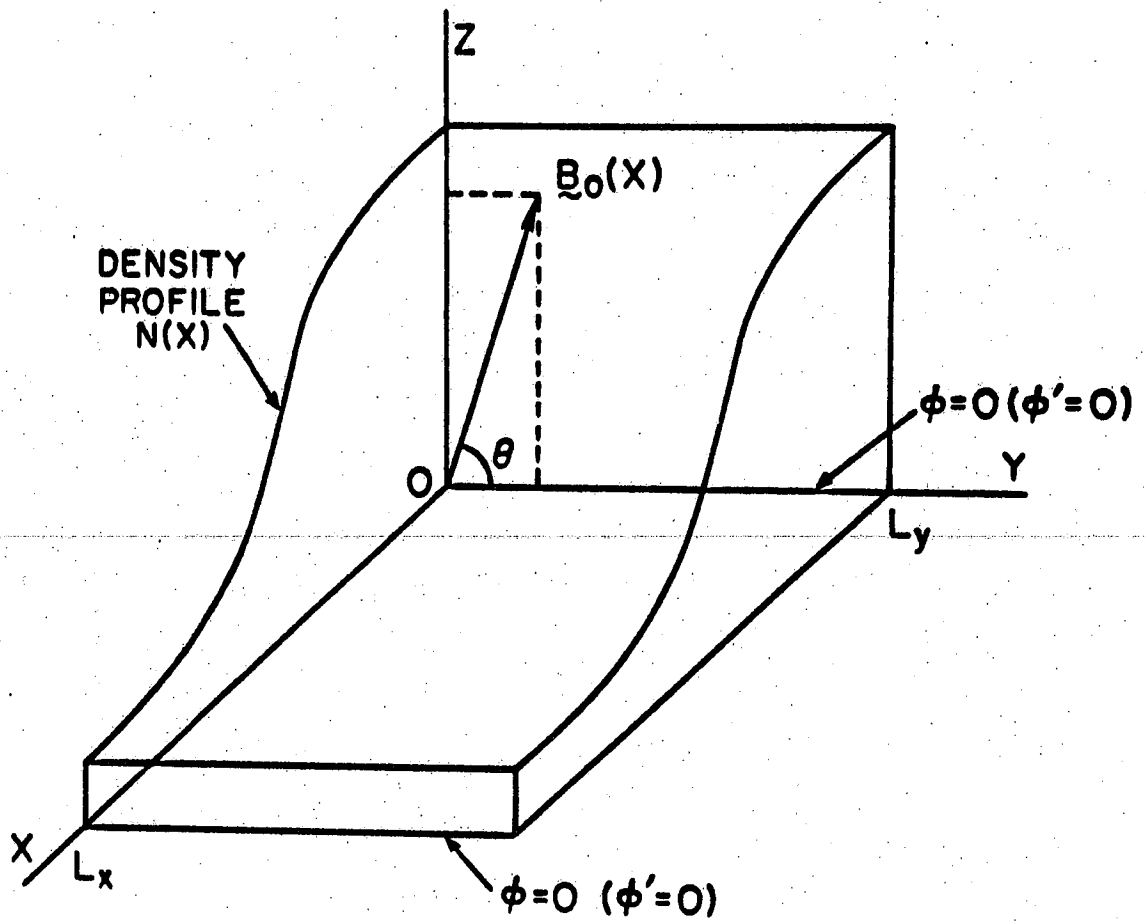


Fig. 3.3. Schematic of the particle simulation configuration and model.

$x = 0$ and $x = L_x$. A strong confining sheared magnetic field is externally imposed with

$$\vec{B} = B \left[\hat{z} + \left(\frac{x - x_0}{L_s} \right) \hat{y} \right] \quad (3.12)$$

where x_0 defines the location of the rational surface. The wavenumbers in the model are $\vec{k} = k_x \hat{x} + k_y \hat{y}$, $k_x = 2\pi m/L_x$, $m = 0, \pm 1, \dots, \pm L_x/2$, $k_y = 2\pi n/L_y$, $n = 0, \pm 1, \dots, \pm L_y/2$ and therefore

$$k_{\parallel} = \frac{\vec{k} \cdot \vec{B}}{B} \approx k_y \frac{(x - x_0)}{L_s} \quad (3.13)$$

The plasma is assumed to have, initially an exponential density profile of the form

$$n(x) = n_0 \kappa L_x \exp[-\kappa x] / (1 - \exp[-\kappa L_x]) \quad (3.14)$$

This profile gives a constant density gradient scale length $L_n (\equiv 1/\kappa, \text{ with } \kappa = -n'(x)/n)$. There is no temperature gradient imposed initially.

The boundary conditions on the electrostatic potential at the endpoints $x = 0$ and $x = L_x$ are of two types. The first requires $\phi(0) = 0 = \phi(L_x)$ which allows

for odd parity modes with respect to the endpoints of the simulation. The second type used is $\partial\phi/\partial x (x = 0) = 0 = \partial\phi/\partial x (x = L_x)$ which corresponds to even parity modes. Therefore, the eigenmode parity, about the rational surface, is determined by its position relative to the simulation boundary. For example, if the rational surface is placed at $x = 0$ and odd parity simulation modes are imposed with respect to the boundary points, then the eigenmodes are odd with respect to the rational surface. If the rational surface is placed at $x = L_x/2$, the middle of the simulation domain, the eigenmodes are even with respect to the rational surface. These various conditions allow us to test the effects of simulation boundary conditions on the drift wave eigenmodes.

We consider the two regimes of strong ($L_s/L_n \lesssim 28$) and weak ($L_s/L_n > 28$) magnetic shear. The shear scale length as well as rational surface position is chosen so that the ion resonance point, x_i , is always within the system ($x_i < L_x$), unless specified otherwise. This will ensure that in our model the wave energy supplied at the electron resonance, x_e , is absorbed near the ion resonance, x_i . In this way we realize the outgoing wave boundary condition present in the linear theory which

reflects the damping of wave energy at the ion resonance layer (the ion shear damping).

In the strong shear limit we would like to find out if the simulation supports the predicted, linearly stable eigenmodes in the steady state, i.e., over long simulation time scales. In the weak shear regime the electron and ion resonances are well separated and it is of interest to examine the effects of 'transients' as well as the eigenmode formation at early time, i.e., the time dependent evolution of drift wave packets.

The system size used for the strong shear results is $L_x \times L_y = 65\Delta \times 32\Delta = 25.6\rho_s \times 12.8\rho_s$ where Δ is a unit grid spacing. The average number density is $n_0 = 16/\Delta^2$, ion to electron mass ratio $m_i/m_e = 100$, temperature ratio, $T_e/T_i = 1$ and electron thermal velocity $v_e = 2.5\omega_{pe}\Delta$. The ion Larmor radius is $\rho_i = 2.5\Delta$ where $\rho_i = v_i/\omega_{ci}$, $\omega_{ce}/\omega_{pe} = 10$ and time step $\omega_{pe}\Delta t = 2-4$. The density gradient scale length is $L_n = 1/\kappa = 14.3\Delta$ and the shear scale length is varied from $L_s = 400\Delta$ ($\omega_{pe}\Delta t = 4$) to $L_s = 200\Delta$ ($\omega_{pe}\Delta t = 2$). The rational surface position has been placed either at $x_0 = 0$ or at $x_0 = L_x/12 = 12.8\rho_s$. The system described above supports discrete wavenumbers $k_y\rho_s = 0.49m$, $m = 0, \pm 1, \dots, \pm L_y/2$

and the electron diamagnetic drift frequency is $\omega_*/\omega_{ci} = 0.086m$. The simulations are run from $\omega_*t = 0$ to $\omega_*t = 70$.

The diagnostics involve the determination of the frequencies of the potential fluctuations at different wavenumbers, $k_y\rho_s$, and at various positions in the x-direction. These are obtained from power spectra of the potential by FFT and maximum entropy correlation methods described in Chapter II. The wave functions obtained from theory are compared with two-time correlation functions of the electrostatic potential analyzed using the interferogram method. Since the modes we consider are near marginal stability and have long lifetimes ($1/\gamma$) this is a valid analysis method for this problem.

3.4 Simulation Results (Strong Shear)

Various cases corresponding to different boundary conditions and different positions of the mode rational surface, as well as different shear strengths ($L_s/L_n = 14, 28$) are presented in this section. We consider both even and odd mode parities.

Case 1: Odd Parity Modes with Rational Surface $x_0 = 0$

This simulation is carried out with $\phi(0) = 0 = \phi(L_x)$ boundary conditions. With rational surface at $x_0 = 0$, we are simulating a half-space which supports odd parity modes only, i.e., $\tilde{\phi}(x) = \sum_n \phi_n \sin(n\pi x/L_x)$, $n = 0, \pm 1, \dots, \pm L_x/2$. A value of $L_s/L_n = 28$ is used and with $\omega_*/\omega_{pe} = 0.0086$ the ion resonance location is at $x_i(\omega_*) = 49.5\Delta$ which gives $x_i(\omega) < x_i(\omega_*) < L_x$, where ω is the eigenfrequency. Therefore the ion resonance layer is well within the system since $L_x = 64\Delta$. Note that $x_i(\omega_*)$ evaluated at v_i is the most stringent condition to ensure the ion shear damping layer is within the simulation domain. Since ion Landau damping is maximum at v_i , the ion resonance location is well approximated by $x_i(\omega)$. The time evolution of the total electrostatic energy is shown in Fig. 3.4 and a weak instability is found to occur. An increase by a factor of two is observed from $\omega_*t = 0 - 70$. This increase is due to the enhancement of mode $k_y \rho_s = 0$, the ambipolar mode. Other modes with finite $k_y \rho_s$ show no increase from their initial fluctuation levels and this is illustrated in Fig. 3.5. In this figure we have given the spatially averaged fluctuation level per mode since the eigenmode

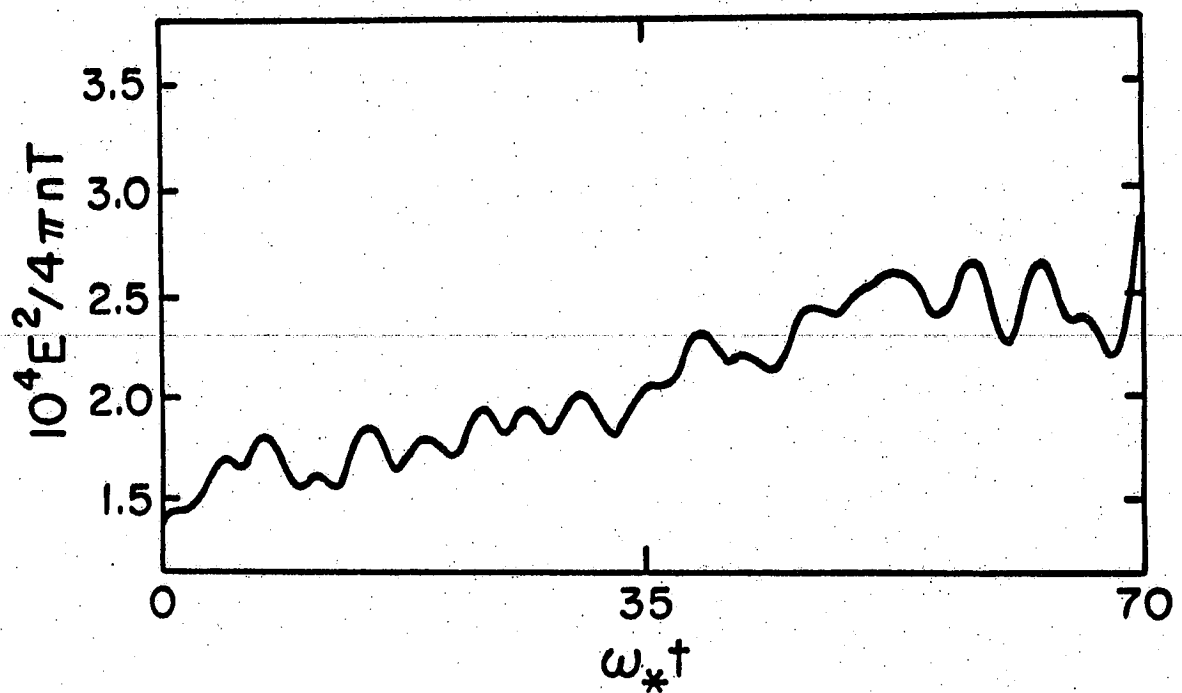


Fig. 3.4. Time evolution of the total electrostatic energy normalized to the total kinetic energy for Case 1.

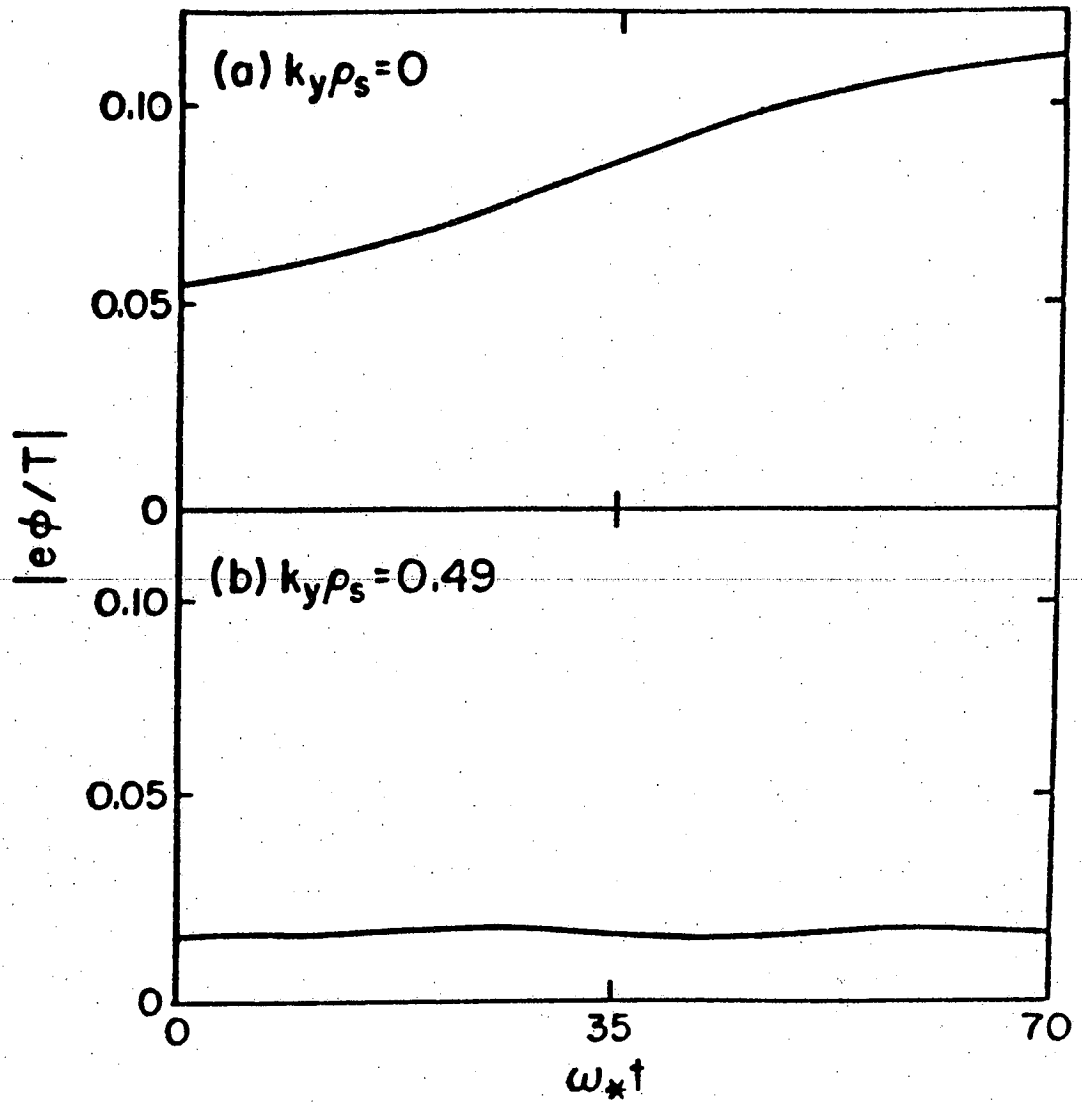


Fig. 3.5. Time evolution of the spatially averaged mode amplitude for (a) $k_y \rho_s = 0$ and (b) $k_y \rho_s = 0.49$ in Case 1.

structure is nonlocal and we are attempting to observe net sustained growth of the fluctuations.

The local power spectrum of the fluctuations at positions $x/\rho_s = 9.6$ and $x/\rho_s = 12.8$, corresponding to regions of maximum mode amplitude for $k_y \rho_s = 0.49$, are given in Fig. 3.6. The measured frequency, $\omega/\omega_* \approx 0.9 \pm 0.03$ is a factor of two larger than the eigenfrequency $\omega/\omega_* = 0.44$. Fig. 3.7 shows the agreement between measured frequencies at various x-positions and values obtained by solving the local dispersion relation [$k_x^2 = 0$ in Eq. (3.10)]. This suggests that local fluctuations are prevalent and the theoretically predicted eigenmodes are not observed. A similar result was obtained by previous authors.⁷⁴

Case 2: Even Parity Modes with Rational Surface $x_0 = 0$

The simulation parameters are identical to the previous case and the only difference is that $\partial\phi/\partial x = 0$ boundary conditions are used at $x = 0$ and $x = L_x$. With rational surface at $x = 0$ only even modes given by $\tilde{\phi} = \sum_n \phi_n \cos(n\pi x/L_x)$ are allowed in the simulation. According to linear theory these modes are stable and are less heavily damped than the odd parity.

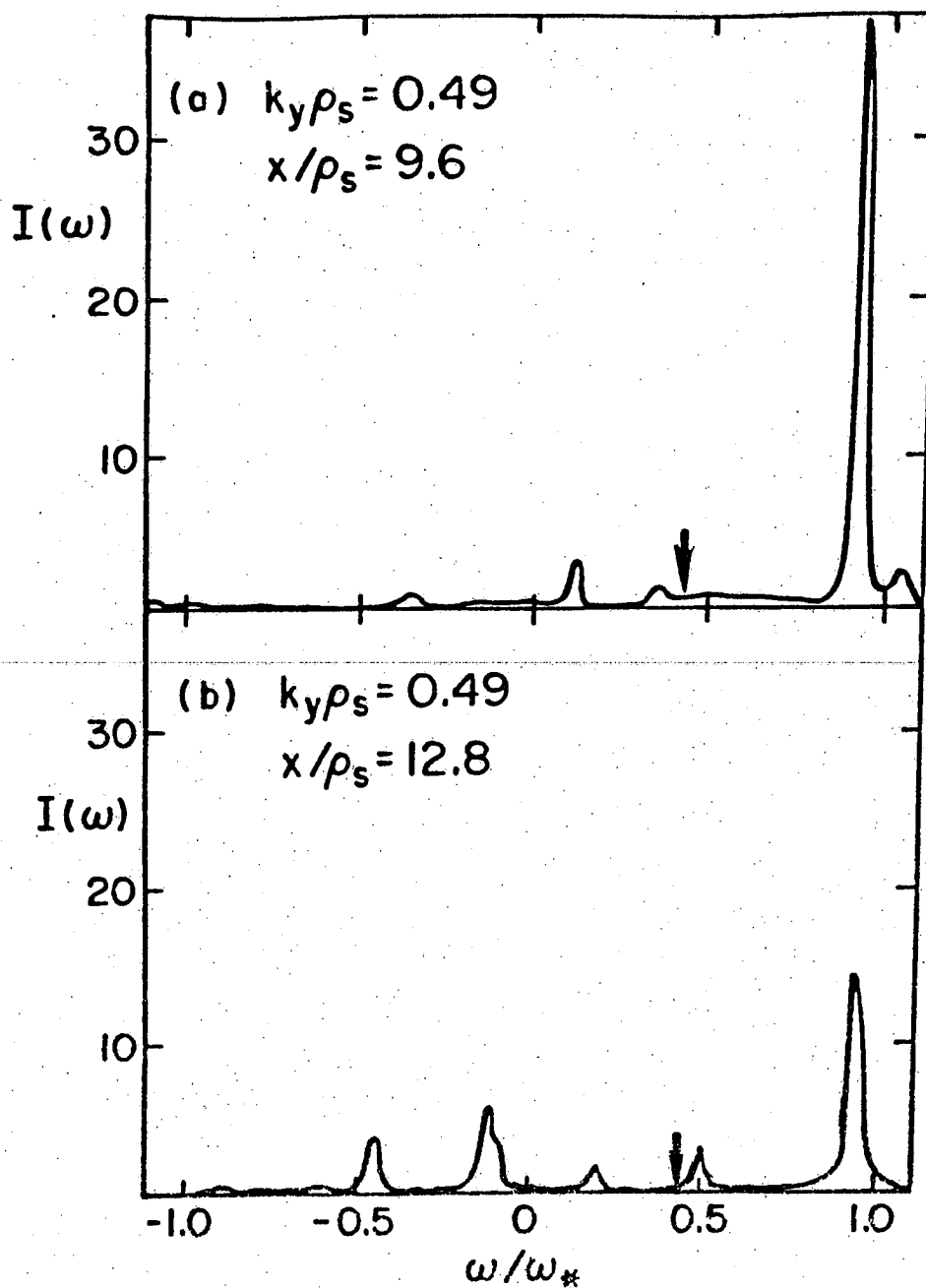


Fig. 3.6. Power spectra of potential $\phi_{ky}(x)$ as a function of real frequency ω/ω_* for (a) $k_y \rho_s = 0.49$ at $x/\rho_s = 9.6$ and (b) $k_y \rho_s = 0.49$ at $x/\rho_s = 12.8$ for Case 1. The eigenmode frequency from linear theory ($\omega/\omega_* = 0.44$) is indicated by an arrow on the frequency axis.

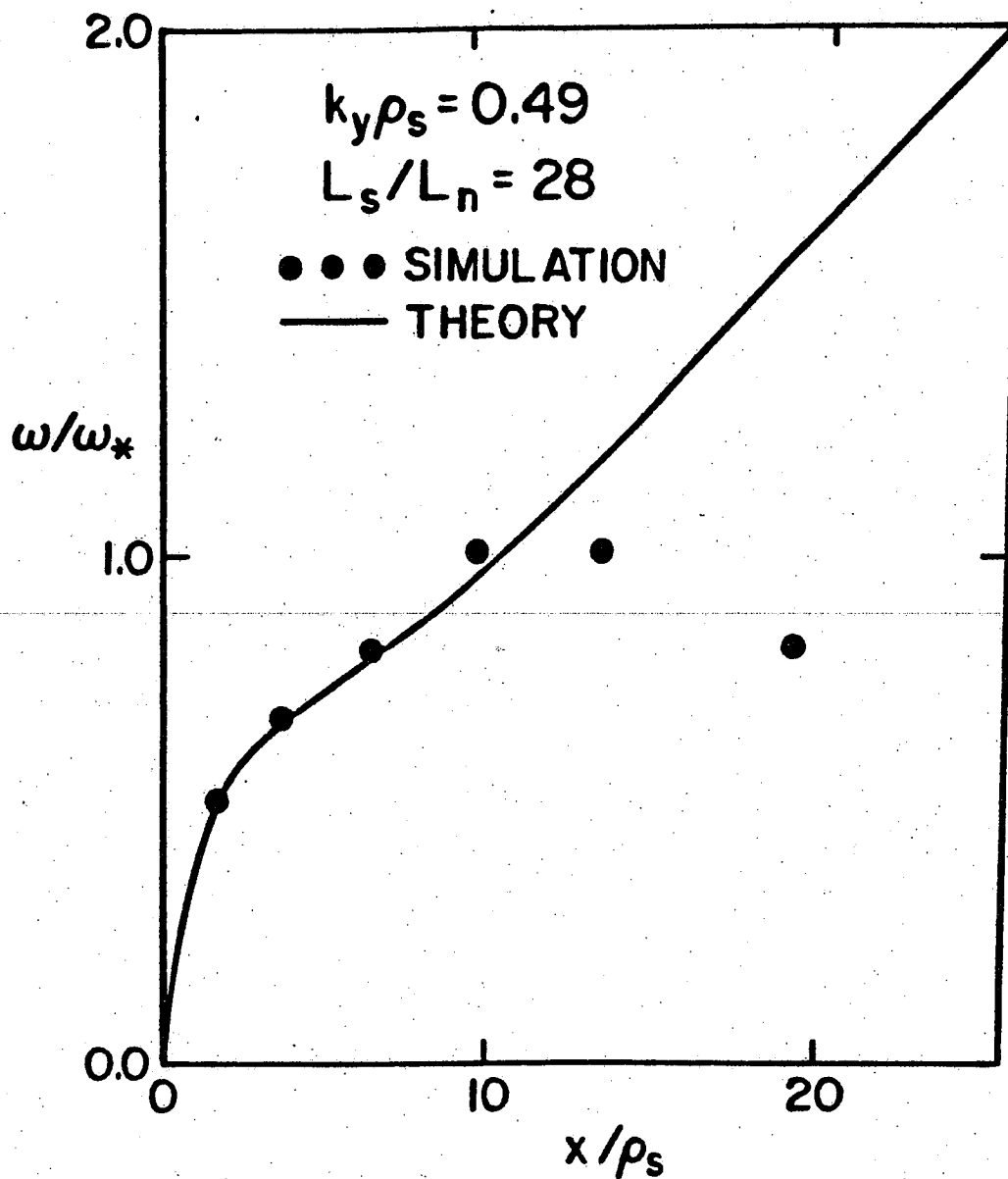


Fig. 3.7. Real frequency, ω/ω_* , as a function of x/ρ_s for mode $k_y\rho_s = 0.49$. Theoretical result is indicated by full curve and dots represent simulation values for Case 1 parameters.

The time evolution of the total electrostatic energy is depicted in Fig. 3.8. There is no observable increase in the total electrostatic energy or in the energy of the individual discrete modes, as shown in Fig. 3.9. The electrostatic energy is dominantly in the $m = 0$ and $m = 1$ modes because finite particle size as well as shielding effects enter for $m > 1$.

The power spectrum of the potential fluctuations for $k_y \rho_s = 0.49$ is illustrated in Fig. 3.10. Fig. 3.10a represents the power spectrum for all x -positions and Fig. 3.10b is the spectral intensity at $x/\rho_s = 4$ where the spectral maximum occurs. The measured frequency is $\omega/\omega_* = 0.43 \pm 0.02$ and this is in reasonable agreement with the shooting code result, $\omega/\omega_* = 0.33$, from Fig. 3.2a. We note that the local theory gives a value of $\omega/\omega_* = 0.7$ at $x/\rho_s = 4$ as obtained from Fig. 3.7. The interferogram of the potential fluctuations at the measured frequency for mode $k_y \rho_s = 0.49$, is displayed in Fig. 3.11 along with the shooting code results. Good agreement is found for both the real and imaginary parts of the potential structure.

The results from this case indicate that an eigenmode structure is established and is stable, which

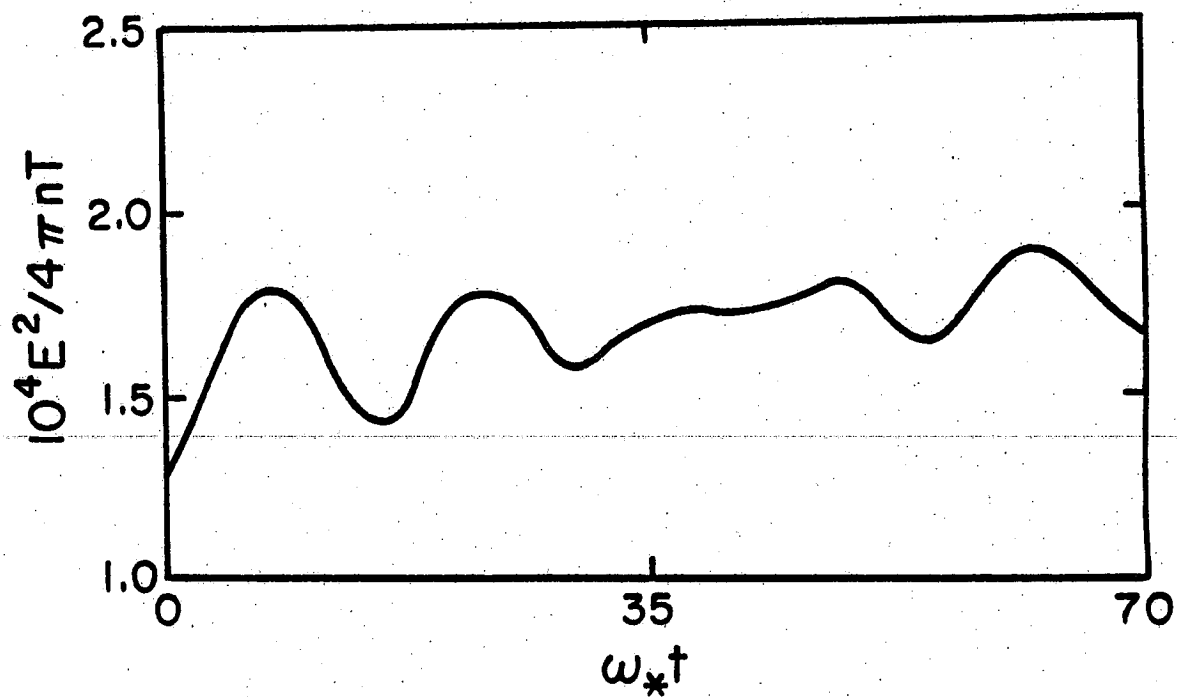


Fig. 3.8. Time evolution of total electrostatic energy normalized to total kinetic energy for Case 2 parameters.

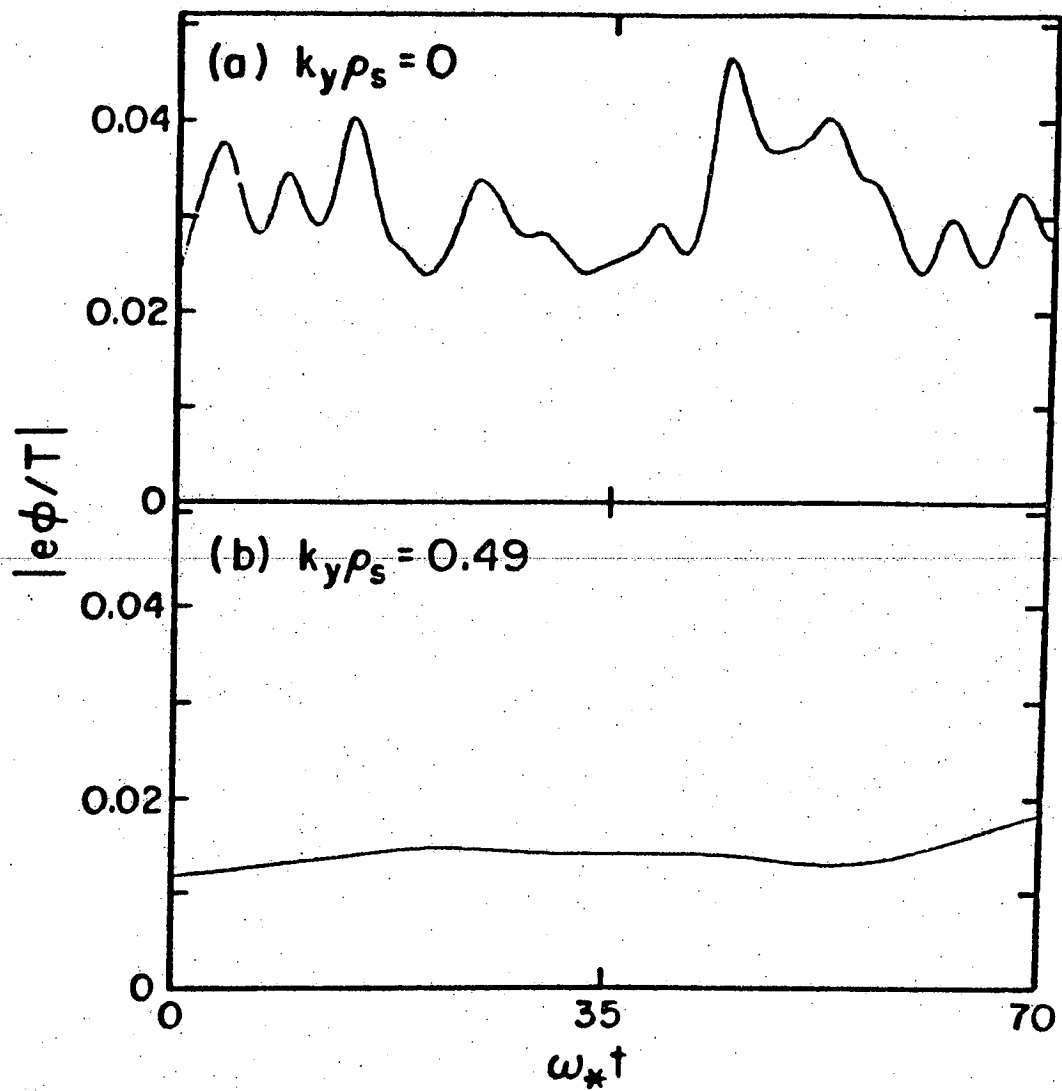


Fig. 3.9. Time evolution of the spatially averaged mode amplitude for (a) $k_y \rho_s = 0$ and (b) $k_y \rho_s = 0.49$ in Case 2.

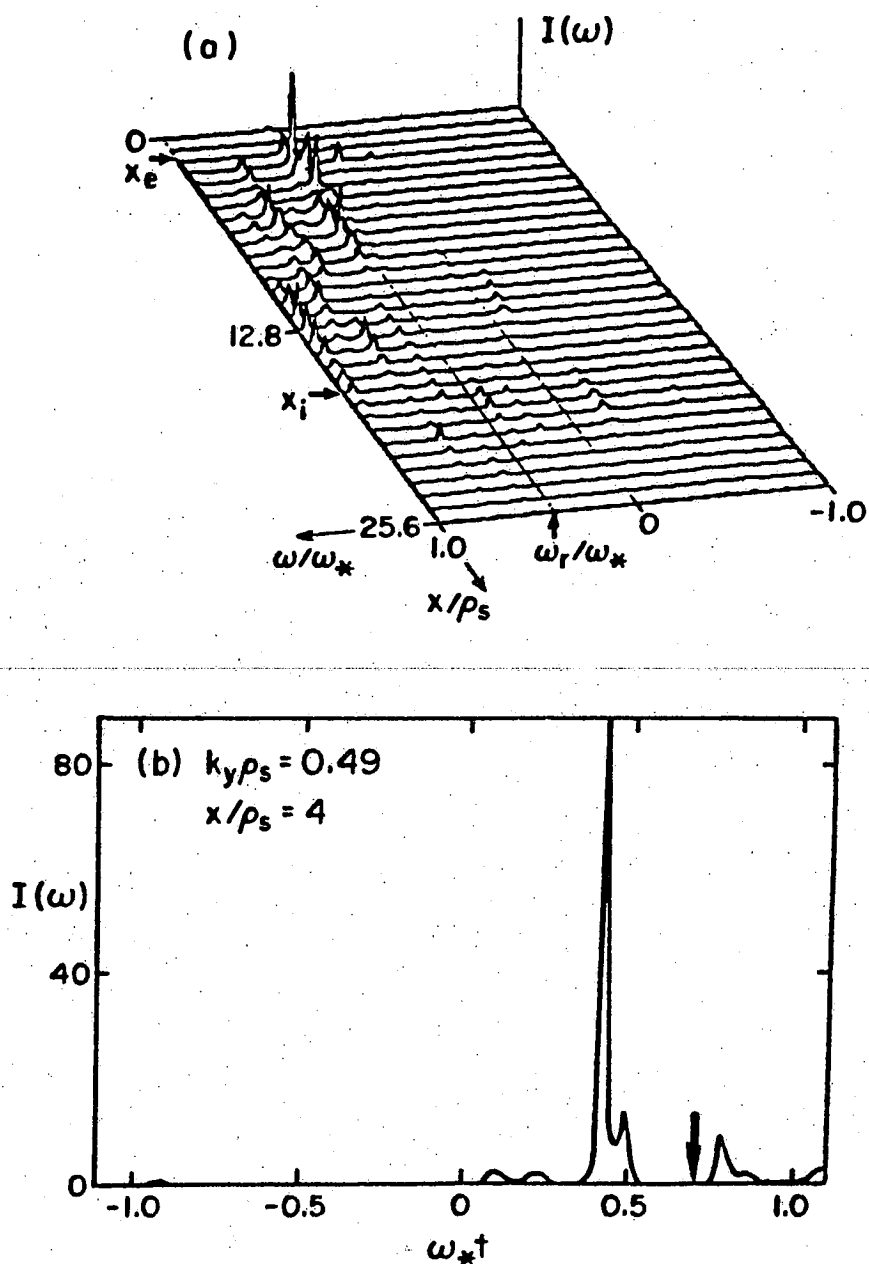


Fig. 3.10. Power spectra of the potential $\phi_{k_y}(x)$ as a function of real frequency ω/ω_* for mode $k_y \rho_s = 0.49$ for Case 2. (a) Power spectrum, $I(\omega)$ over all points in space (x/ρ_s). The eigenmode frequency $\omega/\omega_* = 0.324$ is indicated by an arrow on the frequency axis. (b) The arrow on the frequency axis indicates the local frequency $\omega/\omega_* = 0.7$.

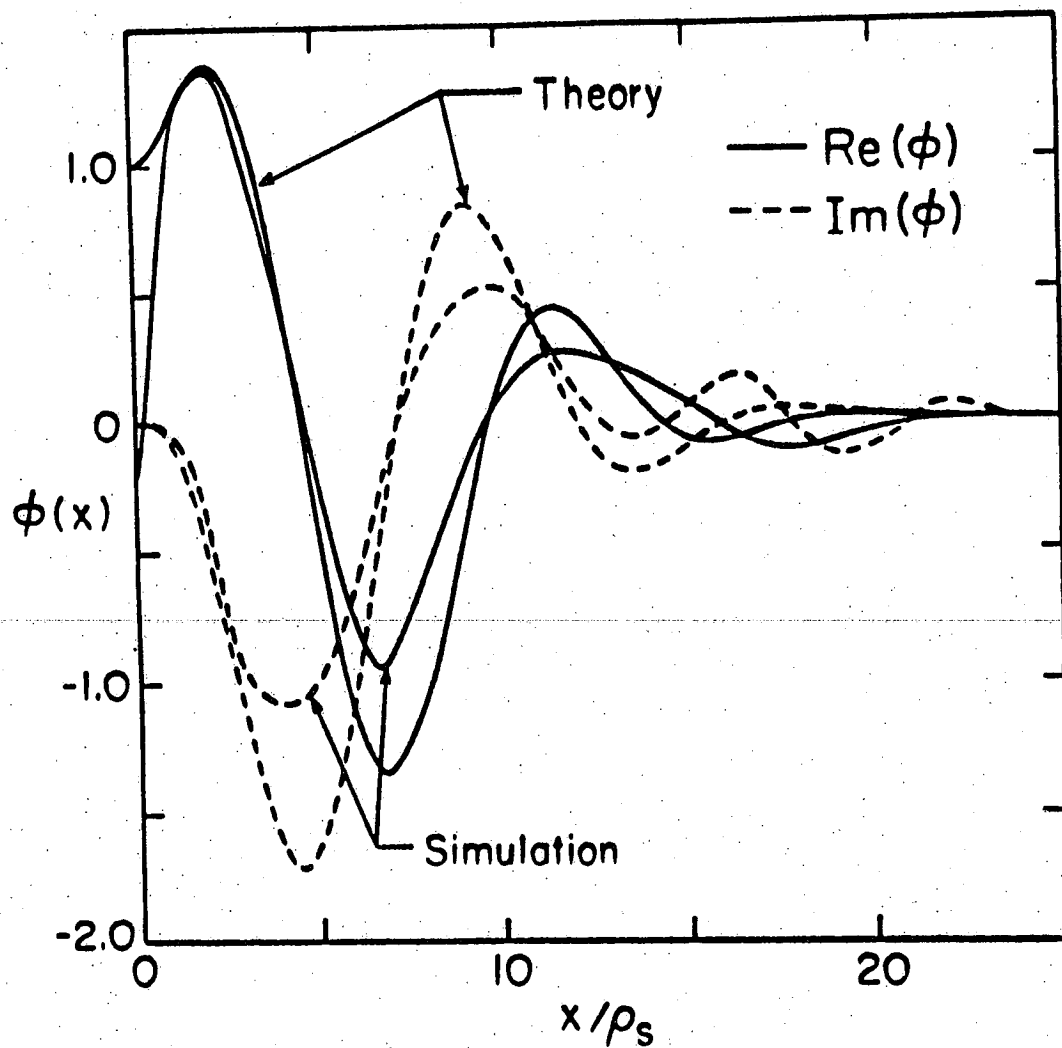


Fig. 3.11. The real and imaginary parts of the wave function obtained from theory and simulation (interferogram method) with ω/ω_* = 0.32 for mode $k_y \rho_s = 0.49$. The results are for Case 2 parameters.

is in agreement with the linear theory of the universal mode. The long time evolution represents the steady state sustained by energy balance between "Cerenkov emission" of electron kinetic energy into the wave at the electron resonance and shear damping of the wave into parallel ion kinetic energy at the ion Landau resonance. Because of this energy exchange from electrons to waves to ions, there is a net energy flow even though the eigenmodes are stable. In fact, we observe that the electron momentum in the y-direction, near $x = x_e$, gives up a finite value in the electron diamagnetic drift direction. To quantitatively estimate the momentum transfer we use the quasi-linear value and, assuming resonant diffusion is dominant, the diffusion coefficient is given by

$$D_x = \left[\frac{c}{B} \right]^2 \sum_k k_y^2 |\phi_k|^2 \pi \delta(k_{\parallel} v_{\parallel} - \omega_k), \quad (3.15)$$

using the fact that $\gamma \ll \omega$ and $\omega < \omega_*$. The evolution of the average distribution is governed by

$$\frac{\partial f_0}{\partial t} = \frac{\partial}{\partial x} \left[D_x \frac{\partial f_0}{\partial x} \right], \quad (3.16)$$

and the rate of change of momentum is

$$\frac{d}{dt} \int f_0 v_{\parallel} dv_{\parallel} \approx \pi \sum_k \left| \frac{e\phi_k}{T_e} \right|^2 \frac{\omega_k}{k_{\parallel}^2} \omega_*^2 f_0 \left[\frac{\omega_k}{k_{\parallel}} \right]. \quad (3.17)$$

For fluctuation levels of $|e\phi_k/T_e| \sim 10^{-3} - 10^{-2}$ we obtain

$$\frac{d \langle v_{\parallel} \rangle / v_e}{d(\omega_{pe} t)} \sim 2 \times 10^{-6},$$

which is compared with the observed value of 10^{-6} . The ion momentum in the y-direction, near $x = x_i$, acquires a finite value in the direction of the electron diamagnetic drift as a result of the wave-particle interaction. Eq. (3.17) also gives agreement within a factor of two for the rate of change of momentum in the ions. The energy transport and momentum transport in the x-direction is, therefore, nonzero even in the absence of instability (i.e., beyond the collisional contributions).

Case 3: Even Parity Modes with Respect to $x_0 = L_x/2$

The simulation parameters are identical to the previous cases except that $L_s/L_n = 14$ is used in order to keep $x_i < L_x$. In this case $x_i(\omega_*) = 57\Delta < L_x = 64\Delta$ and $\phi = 0$ boundary conditions are used at $x = 0$ and L_x . This

allows modes of the form $\tilde{\phi}(x) = \sum_{n'} \phi_{n'} \sin(n'\pi x/L_x)$, however, we keep only the modes with $n' = 2n - 1$, $n = \pm 1, \pm 2, \dots, \pm L_x/2$ in the simulation. This insures that only modes with even parity with respect to the rational surface are present. The purpose of this case and the next is to make sure the results of Case 2 were not influenced by any deleterious boundary effects.

As was found in Case 2, no increase in the total electrostatic energy or the individual mode energies is observed. Contours of the electrostatic potential taken at $\omega_* t = 30$ are shown in Fig. 3.12. Note the symmetry of the potential with respect to the rational surface. The power spectrum of the potential fluctuations at $(x - x_0)/\rho_s = 3.2$ is displayed in Fig. 3.13 and the measured frequency is $\omega/\omega_* = 0.35 \pm 0.03$ which is to be compared with the shooting code result $\omega/\omega_* = 0.36$. The stable drift wave eigenfunction for $k_y \rho_s = 0.4^2$ is given in Fig. 3.14 and the agreement between simulation and theory is excellent. Note the evanescent character of the mode away from the rational surface and that the ion resonance, located at $x_i/\rho_s = 8.65$, is the cause of this spatial decay.

Our simulation results in Cases 2 and 3 establish the existence of drift wave eigenmodes of linear

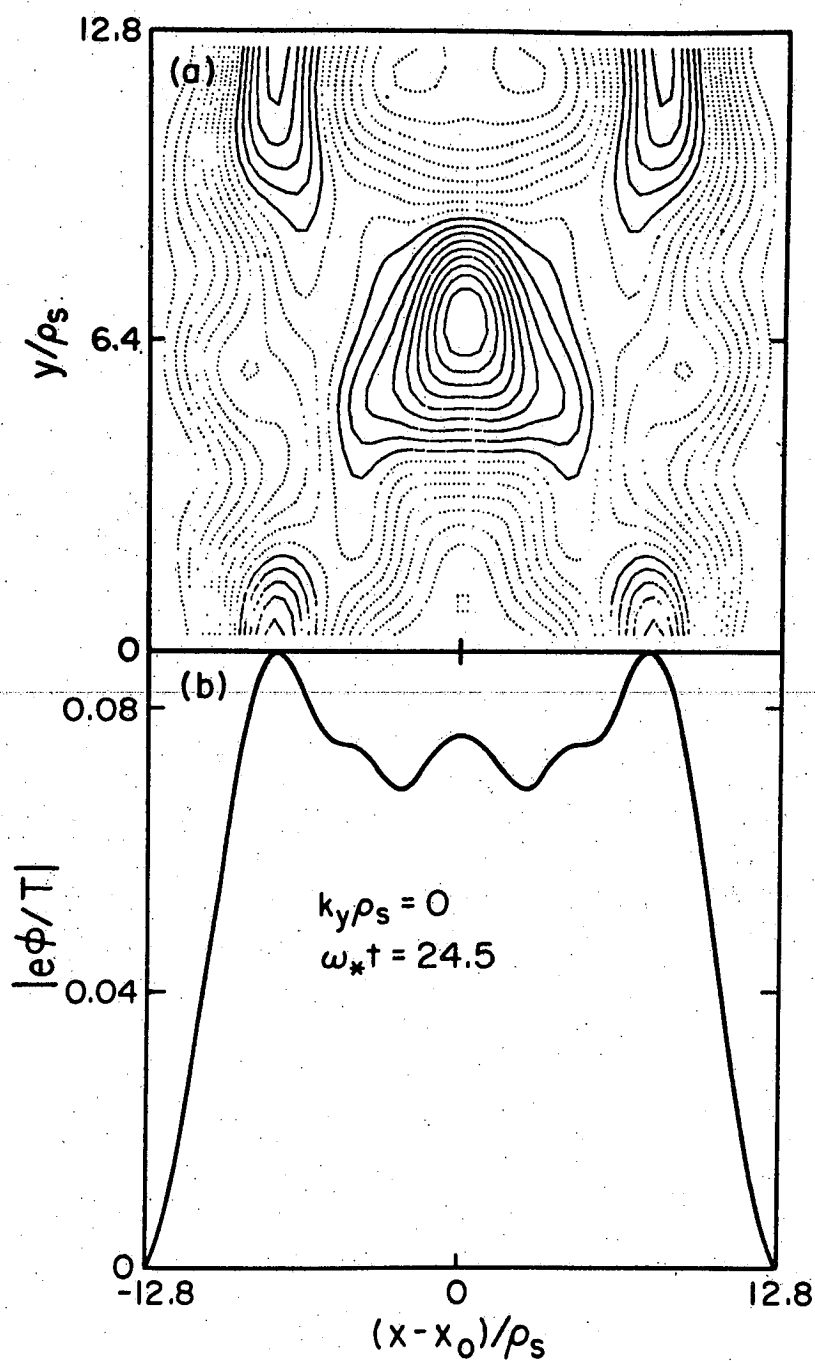


Fig. 3.12. Electrostatic potential and mode amplitude at selected time $\omega_* t = 24.5$. (a) Electrostatic potential contours in x - y plane and (b) mode amplitude of $k_y \rho_s = 0$ as a function of $(x-x_0)/\rho_s$ for Case 3.

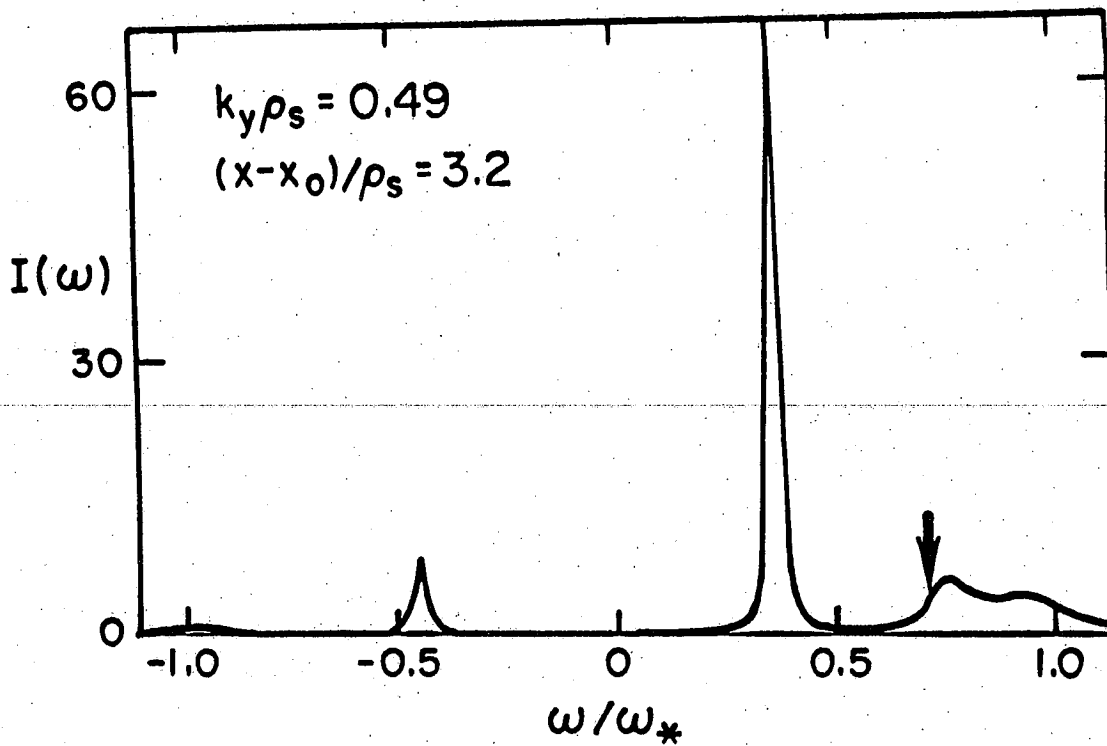


Fig. 3.13. Power spectra of mode $k_y \rho_s = 0.49$ versus real frequency ω/ω_* taken at local position $(x - x_0)/\rho_s = 3.2$ for Case 3. The arrow indicates the value of the local frequency $\omega/\omega_* = 0.7$.

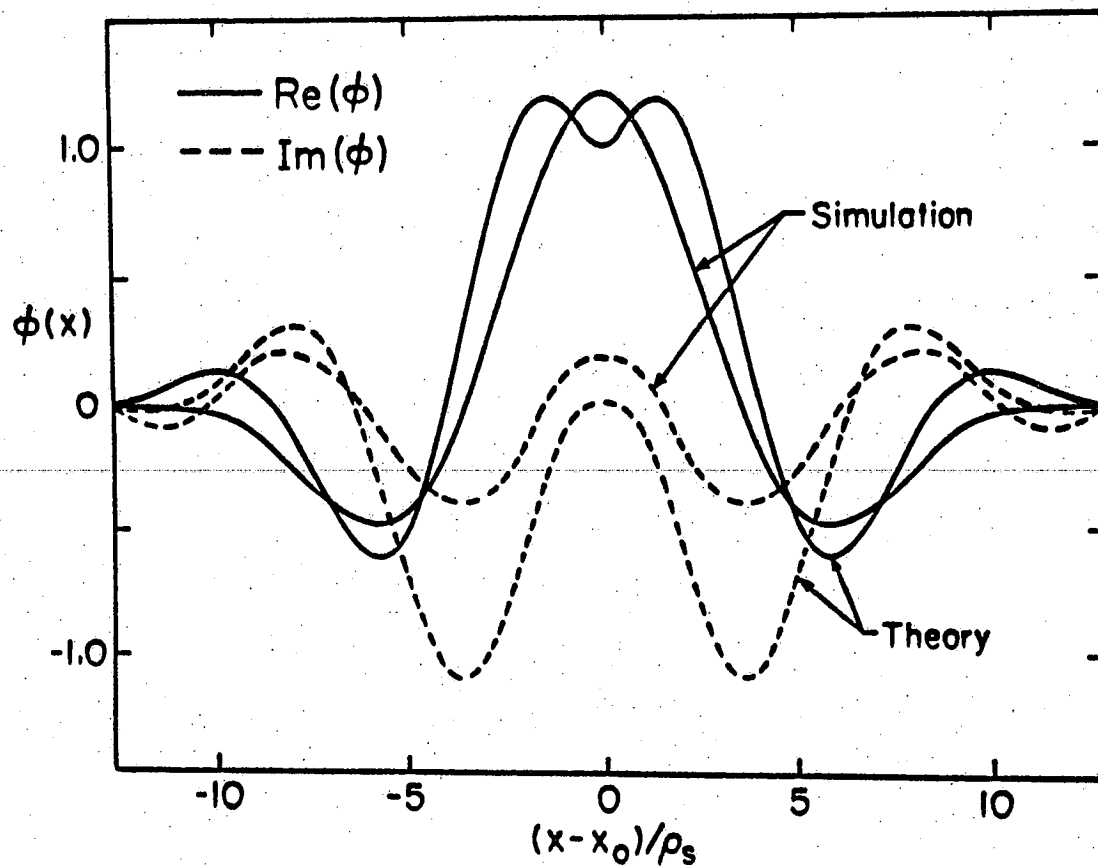


Fig. 3.14. The real and imaginary parts of the wave function obtained from theory and simulation for Case 3. This is for mode $k_y \rho_s = 0.49$.

theory for even parity, irrespective of the position of the rational surface with respect to the simulation boundaries.

Case 4: Odd Parity Modes with Respect to $x_0 = L_x/2$

The simulation parameters used are identical to the previous case. The shear scale length is $L_s/L_n = 14$ and $\phi(0) = 0 = \phi(L_x)$. The potential fluctuations are described by $\tilde{\phi} = \sum_{n'} \phi_{n'} \sin(n'\pi x/L_x)$ and only modes with $n' = 2n$, $n = \pm 1, \dots, \pm L_x/2$ are allowed in the simulation. Therefore, only modes with odd parity with respect to the rational surface are described by the code.

As was found in the previous case, the potential fluctuations are stable and the time history of the total electrostatic energy shows no enhancement above the initial noise level. An energy per mode analysis, gives a similar result. The power spectrum of the potential fluctuations for mode $k_y \rho_s = 0.49$, averaged over several x-positions near the rational surface, is displayed in Fig. 3.15 and a mode frequency of $\omega/\omega_* = 33 \pm 0.1$ is observed which agrees well with the shooting code result of $\omega/\omega_* = 0.36$. An interferogram of the potential fluctuations for $k_y \rho_s = 0.49$ is illustrated in Fig. 3.16a

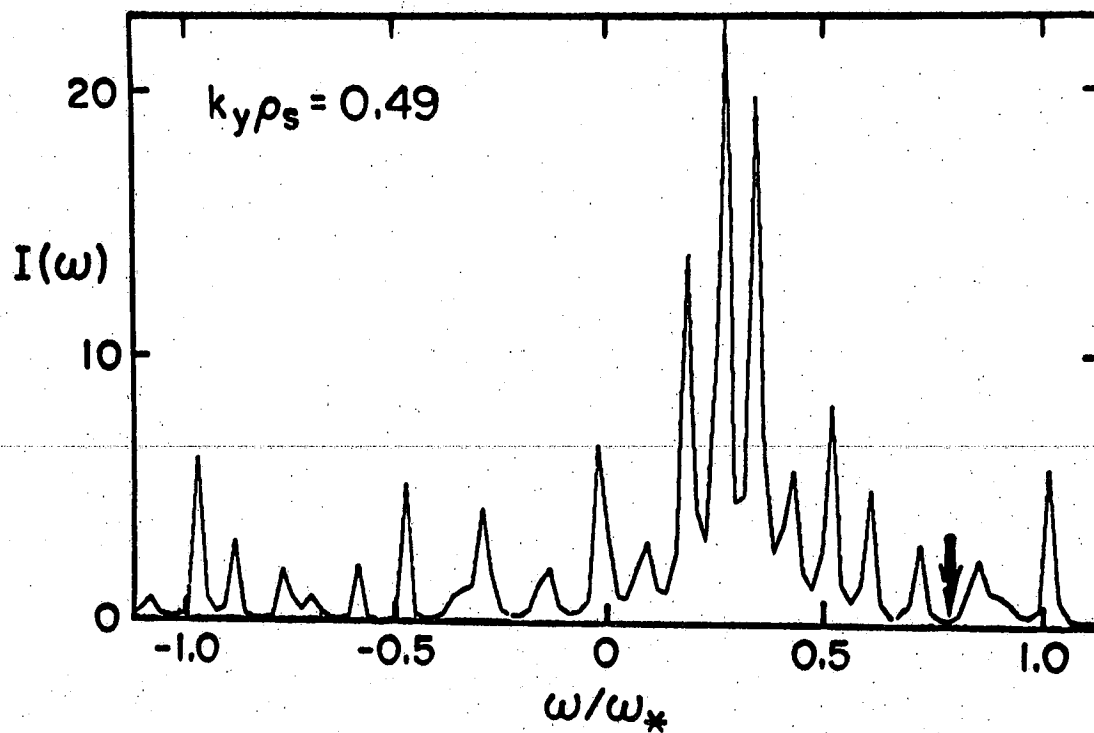


Fig. 3.15. Power spectra of mode $k_y \rho_s = 0.49$ versus real frequency ω/ω_* taken as average over spatial positions $(x - x_0)/\rho_s = 2.0 - 5.0$. The local frequency from linear theory, $\omega/\omega_* = 0.7$, is indicated by the arrow. This is for Case 4 parameters.

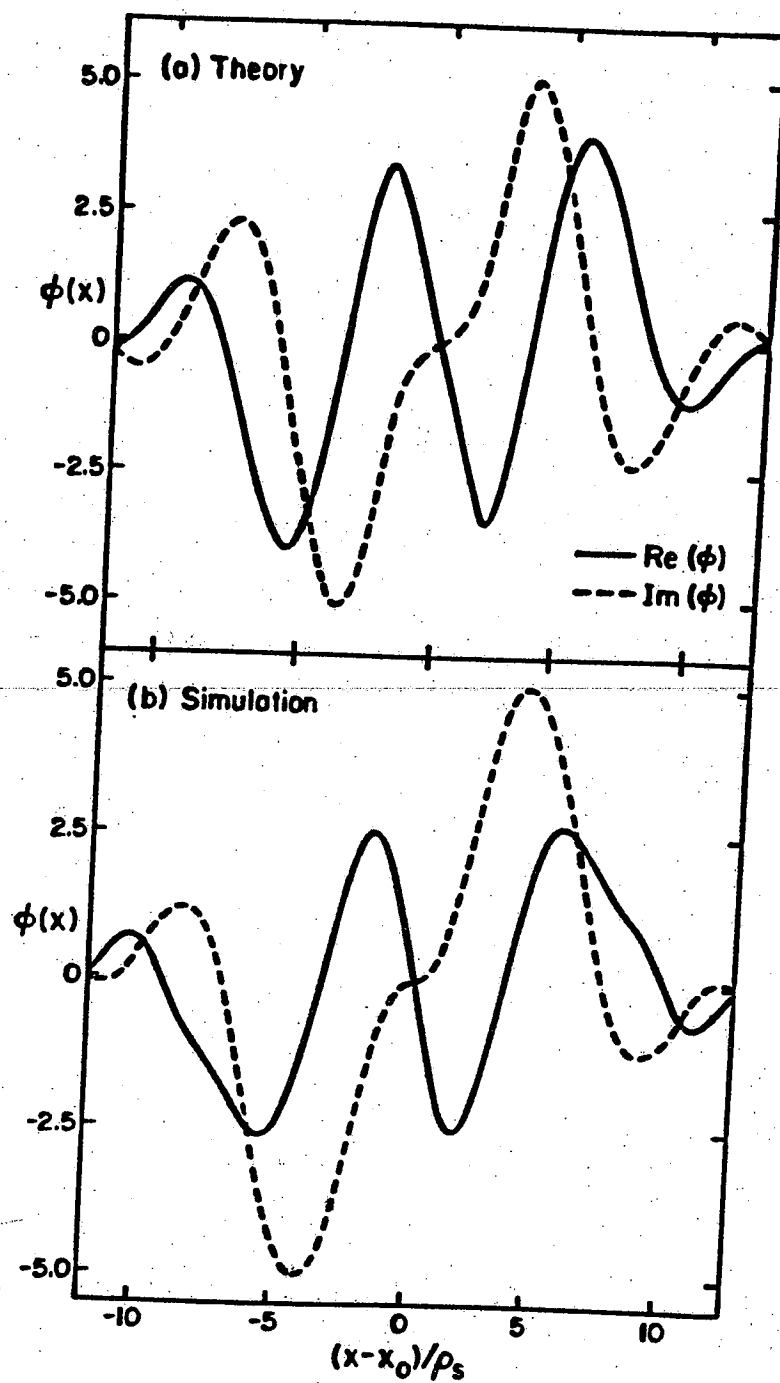


Fig. 3.16. The real and imaginary parts of the wave function obtained from (a) theory and (b) simulation. The results are for mode $k_y \rho_s = 0.49$ in Case 4.

along with the wave function of the shooting code in Fig. 3.16b. Again, excellent agreement is obtained between the theory and simulation.

From the results of Cases 1 and 4, for odd drift wave parity, we conclude that the particle simulation model gives the expected linear eigenmode structure only when the rational surface does not coincide with the simulation boundaries.

To conclude this section we illustrate two situations which do not produce the eigenmodes predicted by linear theory. In the first situation, let us consider the parameters and boundary conditions of Case 3. As has been discussed, if only even modes with respect to the rational surface are kept, the simulation and theoretical wave functions agree very well. However, if both even and odd parity modes are kept, the wave functions obtained from the simulation does not match the linear theoretical result. This is shown in Fig. 3.17. The nonsymmetry of the wave function arises from the mixture of parities retained in the simulation. The measured frequency agrees very well with the eigenmode frequency, which suggests that the odd parity mode gives only a small contribution to the dominant even modes.

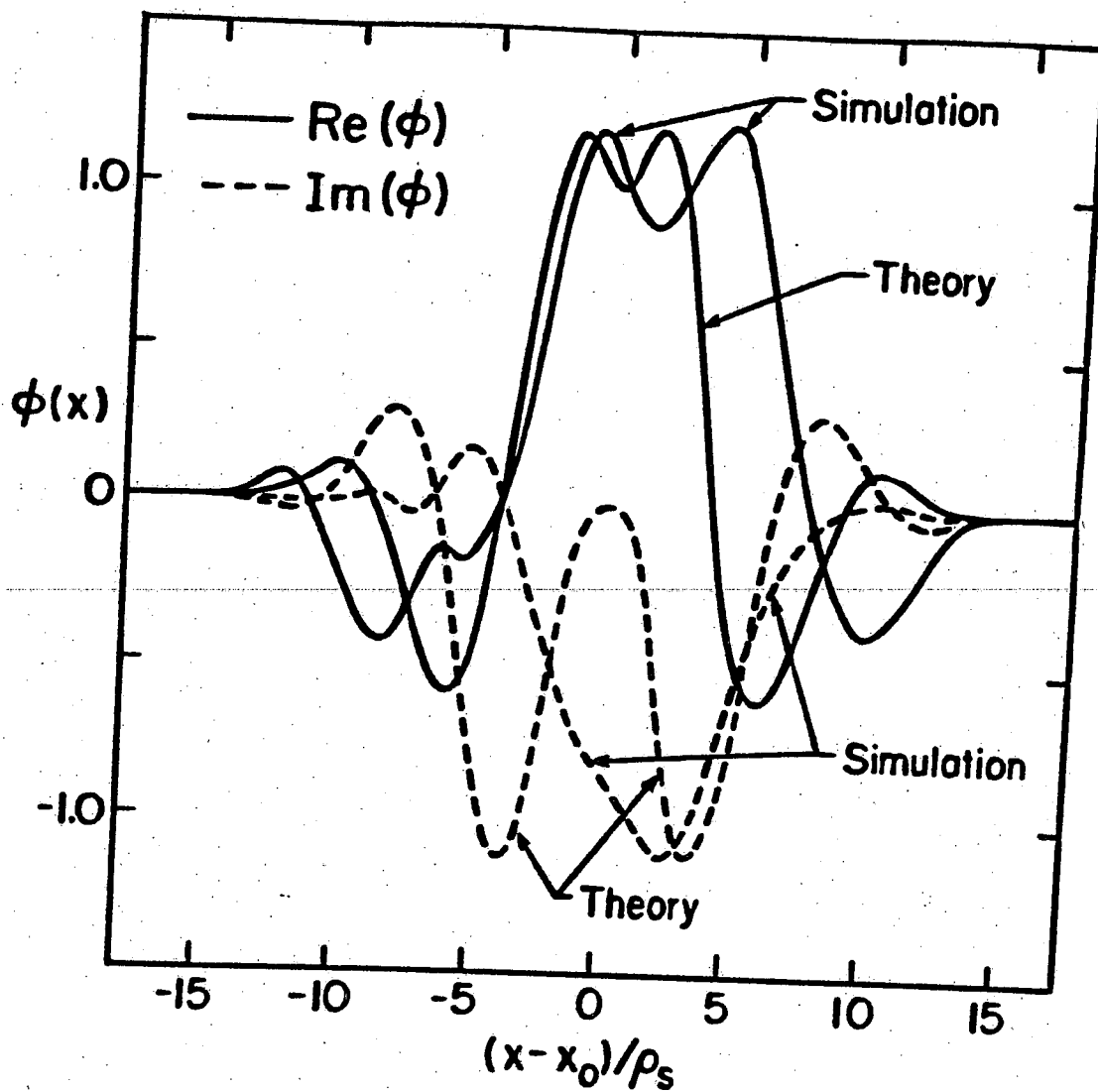


Fig. 3.17. Real and imaginary parts of the wave function for mode $k_{yp_s} = 0.49$ with parameters the same as Case 3, but with mixture of odd and even parity with respect to rational surface.

A second situation which can produce undesirable results is the parameter regime where the ion resonance layer lies outside the simulation domain or is very near the boundaries. Once again, Case 3 is chosen but the shear is allowed to vary in order to demonstrate what can occur when $x_i(\omega_*) > L_x$. For shear strength of $L_s/L_n = 14$, Fig. 3.18a illustrates that the fluctuation level remains at thermal noise over the entire length of the run and $x_i(\omega_*) = 41\Delta < L_x$. As is evident from Fig. 3.18b the fluctuation level is enhanced above thermal noise when $L_s/L_n = 28$ and $x_i(\omega_*) = 81\Delta > L_x$. This enhancement occurs because the boundary at L_x affects the outward propagation of energy and does not allow for the spatial decay of the wave function. It is important to note that the fluctuations do not grow because the electron and ion resonances are more separated. This can be seen by comparing the results of this case with Case 2. In Case 2 the fluctuations remain at the thermal noise level even though the electron and ion resonances are the same distance apart as in the above situation.

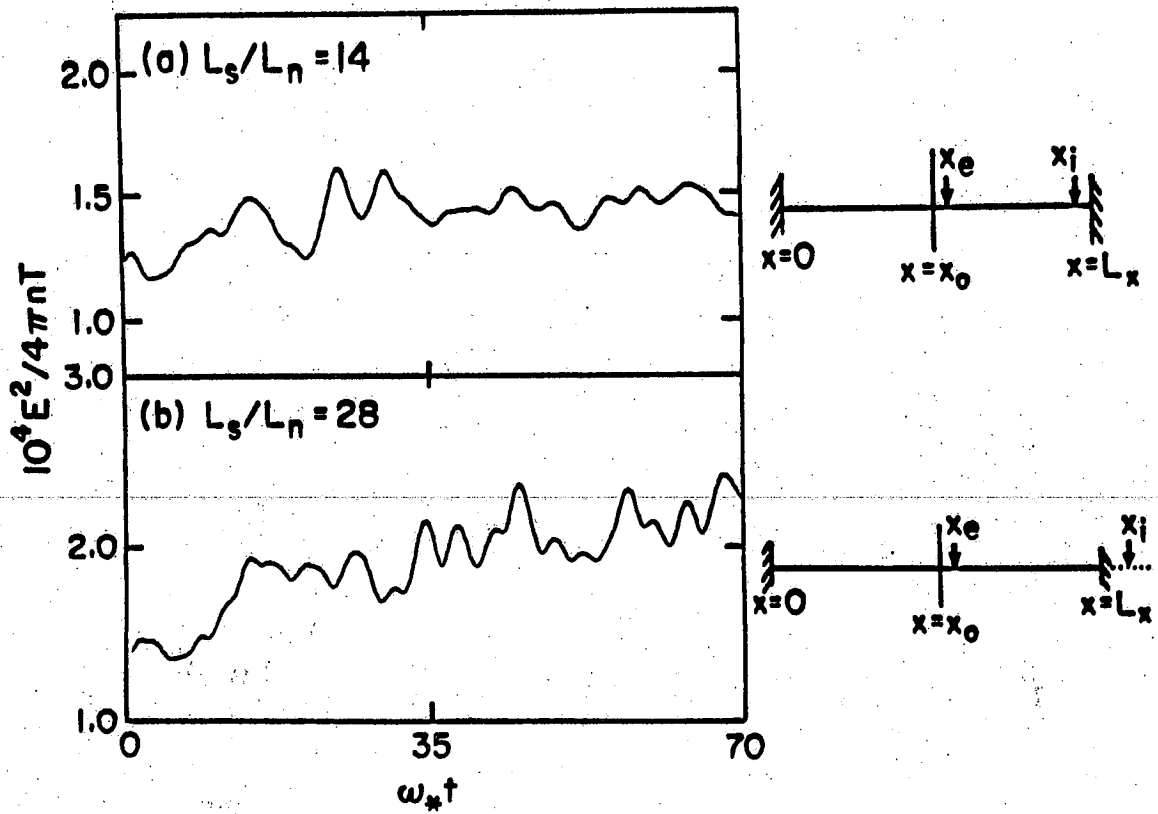


Fig. 3.18. Time evolution of total electrostatic energy normalized to total kinetic energy for parameters of Case 3 and (a) $L_s/L_n = 14$ which keeps ion resonance within system and (b) $L_s/L_n = 28$ which moves resonance outside simulation domain.

3.5 Simulation Results (Weak Shear)

In this section we consider systems with weakly sheared magnetic fields ($L_s/L_n > 30$). When the magnetic shear becomes very weak, the electron and ion resonance regions become well separated spatially and the eigenfunction is highly oscillatory. If the resonances are well separated one expects that there will be a finite time before shear damping by the ions occurs. During this finite lag time the local growth of the drift wave eigenmode could be large enough to cause modification of the equilibrium density profile. Therefore, the purpose of this section is to determine whether or not this indeed does occur and to establish the resultant fluctuation levels of the eigenmodes in weakly sheared systems.

Two separate cases have been considered. In the first case the simulation parameters used were, $L_x \times L_y = 128\Delta \times 32\Delta$, $n_0 = 16/\Delta^2$, $m_i/m_e = 400$, $T_e/T_i = 4$, $\omega_{ce}/\omega_{pe} = 10$, $\lambda_e = 2.5\Delta$, $a_x = a_y = 1.5$, $\omega_{pe}\Delta t = 4$, $\kappa = 1/L_n = .035$, $k_y\rho_i = 0.5m$ and $\omega_*/\omega_{pe} = .00437m$ where $m = 0, \pm 1, \dots, \pm L_y/2$. The shear strength was chosen to be $L_s/L_n = 70$ and the rational surface location at $x = 0$. The boundary condition $\phi'(0) = 0 = \phi'(L_x)$ is chosen, which corresponds to even parity modes with respect to the rational surface.

A shooting code is used to determine the eigenvalue and eigenfunction with the above parameters. The wave function is displayed in Fig. 3.19 and the oscillatory character of the mode is clearly seen. The eigenvalue is given by ($\omega/\omega_* = 0.167$, $\gamma/\omega_* = -.46 \times 10^{-4}$) for $k_y \rho_s = 0.98$, which indicates the mode is near marginal stability.

From the simulation, the potential fluctuation levels of modes $k_y \rho_s = 0$ and $k_y \rho_s = 0.98$ versus time are shown in Figs. 3.20a and 3.20b, respectively. The fluctuation level of $k_y \rho_s = 0.98$ increases by a factor of two above the initial noise level and saturates at $\omega_* t \approx 7$. At this time the energy in mode $k_y \rho_s = 0$ begins to increase and saturates near the end of the run. This increase corresponds to a modification of the density profile locally near the electron resonance. In order to establish the spatial characteristics of the mode $k_y \rho_s = 0.98$, a space-time diagram is constructed and illustrated in Fig. 3.21a. The x-axis represents the spatial coordinate, the y-direction is the time axis and mode amplitude, $e\phi/T$, is in the z-direction. The electron resonance, denoted by x_e , is represented by the dashed line and the ion resonance is outside the simulation domain,

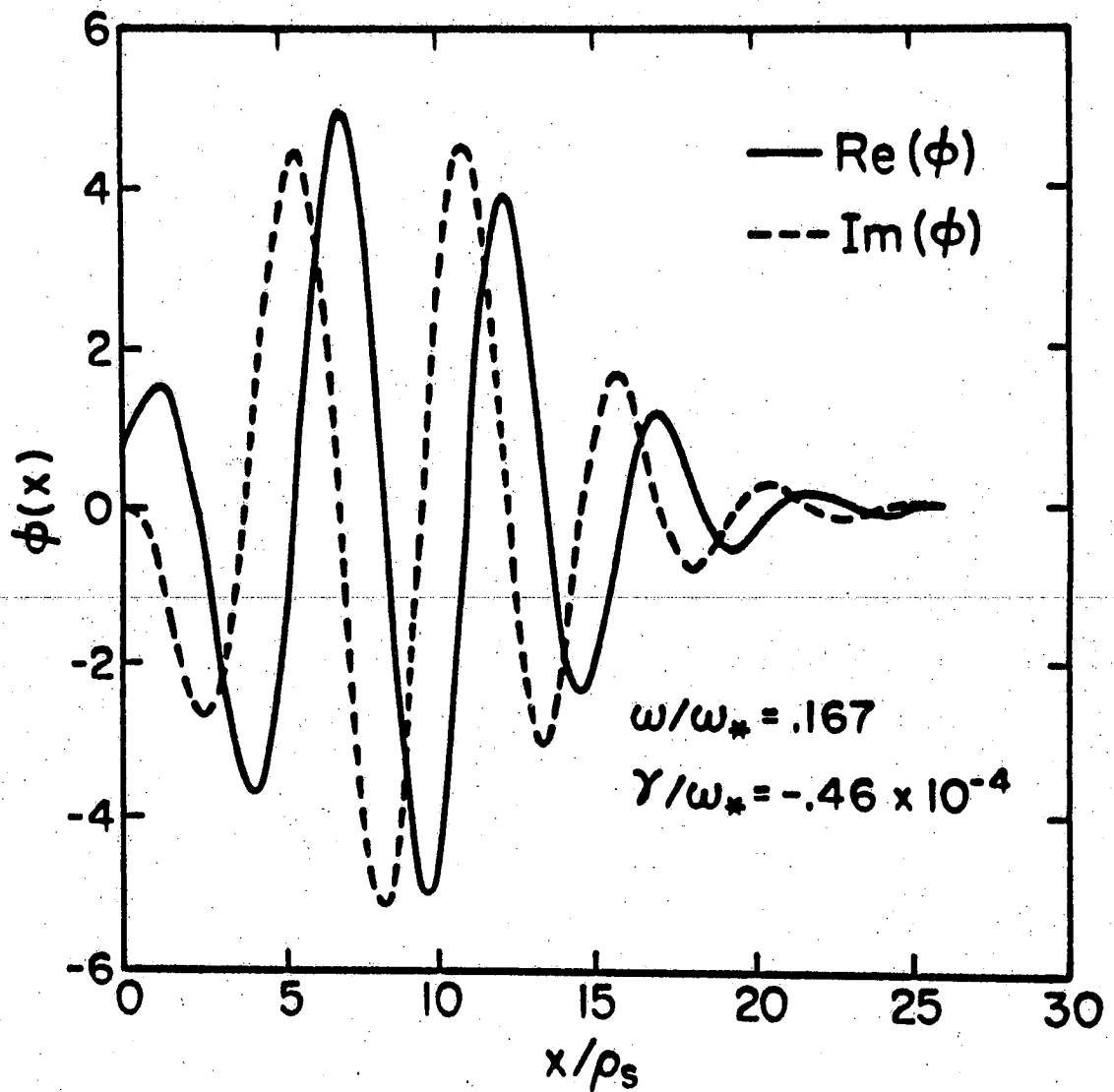


Fig. 3.19. Wave function obtained from shooting code for weak shear case, $L_S/L_n = 70$, and even parity. Solid curve is the real part and dotted line is the imaginary part of the wave function.

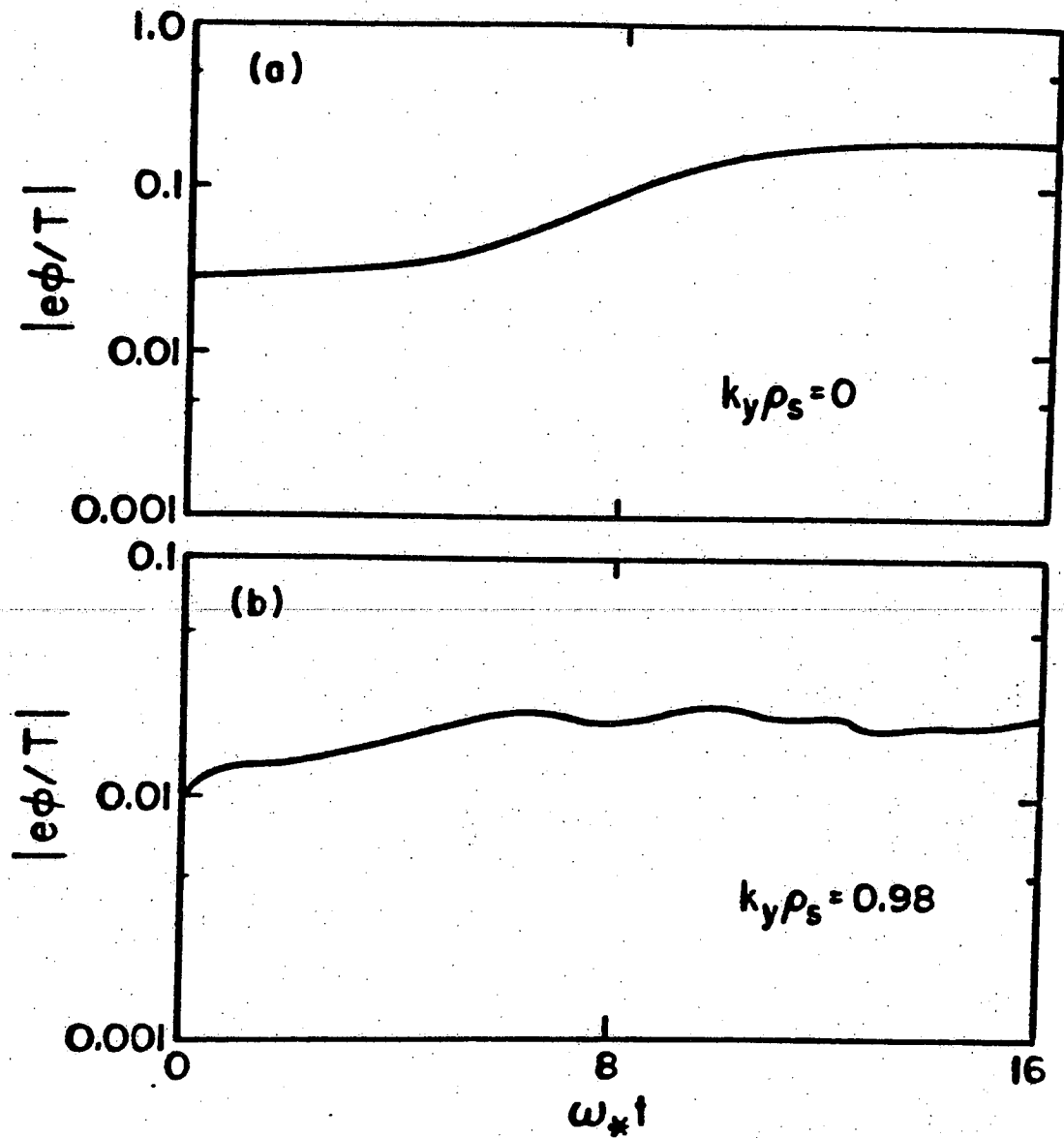


Fig. 3.20. Time evolution of the spatially averaged mode amplitudes for (a) $k_y\rho_s = 0$ and (b) $k_y\rho_s = 0.98$ in weak shear case, $L_S/L_\eta = 70$, with ion resonance outside system.

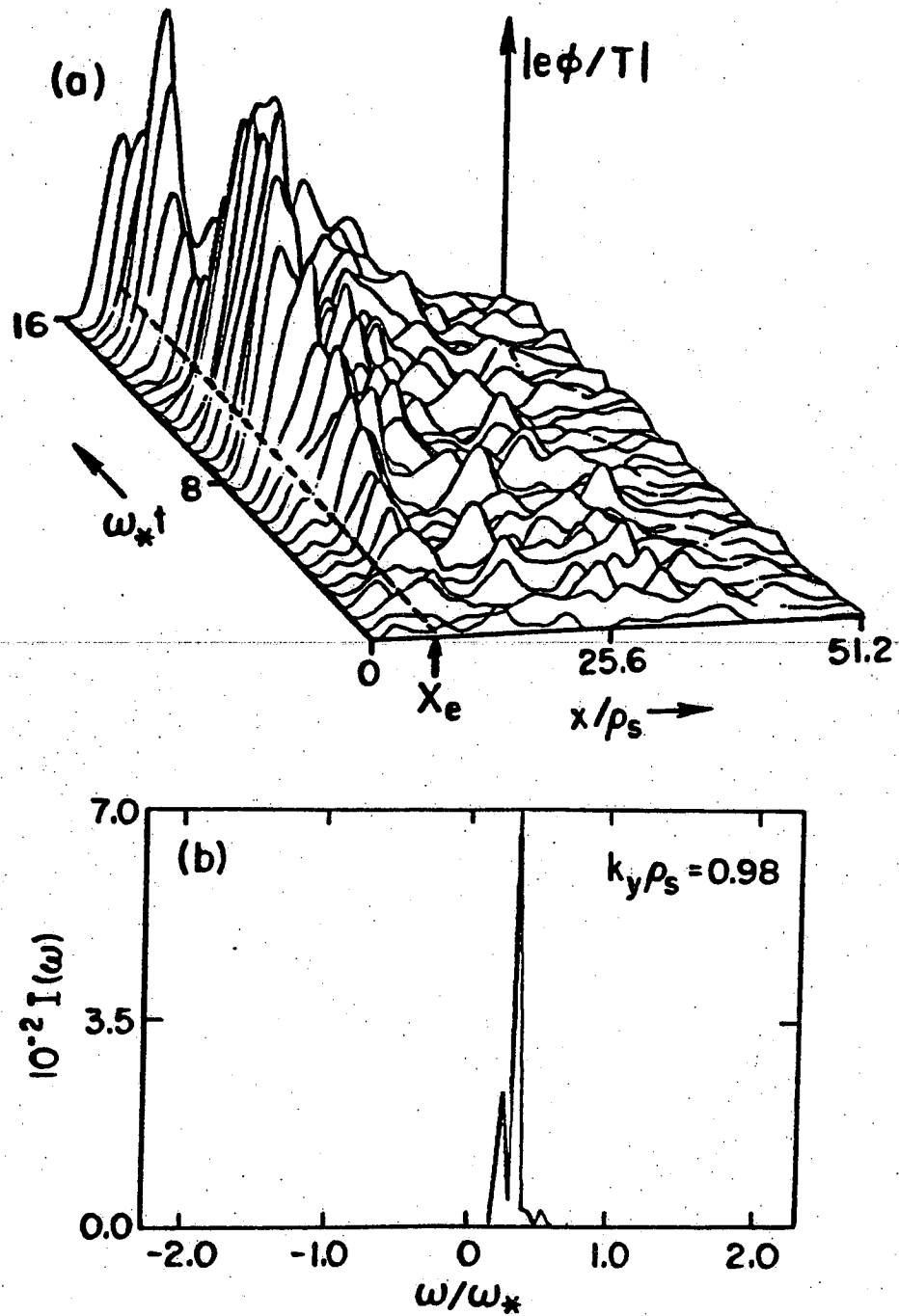


Fig. 3.21. Space-time diagram and power spectra of mode $k_y \rho_s = 0.98$. (a) Mode amplitude, $|e\phi/T|$, versus (x/ρ_s) and time $(\omega_* t)$. Electron resonance is labeled by x_e . (b) Power spectrum taken at $x = x_e$.

in the sense that the evaluated x_i is given by $x_i(\omega_*) > L_x > x_i(\omega_0)$, where ω_0 is the eigenfrequency. The mode begins to grow locally at the electron resonance and saturates at $\omega_* t \simeq 7$. After saturation the electron density profile begins to flatten about x_e and the mode amplitude of $k_y \rho_s = 0.98$ decreases at x_e and increases in amplitude at $x > x_e$. The mode amplitude rises slightly at the electron resonance and continues to oscillate with diminished amplitude. In order to determine the frequency of oscillation near the electron resonance, a power spectrum is computed locally at $x = x_e$ and from Fig. 3.21b a frequency of $\omega/\omega_* = 0.32 \pm .03$ is measured which is larger than the eigenmode frequency $\omega/\omega_* = 0.167$. The local frequency, determined by setting $k_x^2 = 0$ in Eq. (3.10), is found to be $\omega/\omega_* = 0.39$. Therefore the local frequency appears to agree more closely with the measured simulation value.

To understand the weak shear results it is necessary to use a time-dependent approach. The fluctuation spectrum can be expressed as a superposition of local wave packets of the form $\exp[i/k_x dx]$. If the potential, $\hat{\phi}$, has a time dependence it is possible to follow the time evolution of a locally unstable wave packet before

the eigenmode is fully developed.^{78,79} The wave packet initially grows in amplitude while it lies within a region whose local properties lead to instability. The packets eventually move and disperse and when no longer confined to the locally unstable region they decay, in order to conform with the overall stability. From the simulation results, the initial amplification resulted in a modification of the zeroth order plasma profiles in the region of local growth.

For the second case, the parameters chosen previously were used except for $m_i/m_e = 100$, $\lambda_e = 1.0\Delta$, $k_y\rho_i = 0.098$, and $\omega^*/\omega_{pe} = 0.00068m$ where $m = 0, 1, \dots, L_y/2$ so that $x_i(\omega) < x_i(\omega^*) < L_x$. The mode corresponding to $k_y\rho_s = 0.78$ showed a factor of two increases above its initial noise level over the length of the run while all other modes remained at their initial fluctuation levels. This is illustrated in Fig. 3.22b. The equilibrium level which the modes reach is related to convective losses or redistribution of equilibrium thermal energy due to the eigenmode. From Fig. 3.22a it appears the growth in $k_y\rho_s = 0.78$ was not sufficient to modify the equilibrium electron density profile. A space-time diagram of $k_y\rho_s = 0.78$ is given in Fig. 3.23a and the maximum amplitude is

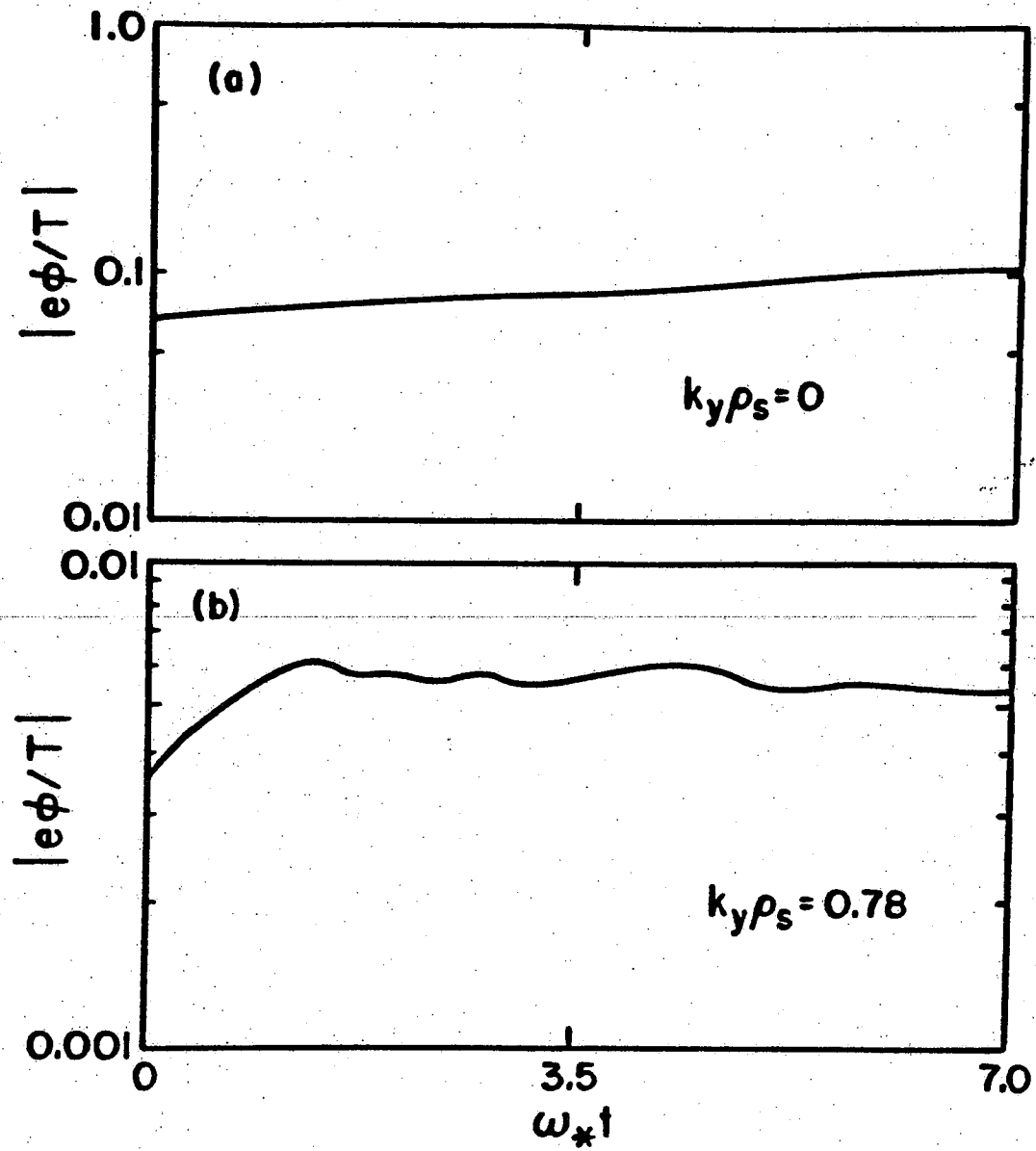


Fig. 3.22. Time evolution of the spatially averaged mode amplitude for (a) $k_y \rho_s = 0$ and (b) $k_y \rho_s = 0.78$ in weak shear case with ion resonance within simulation domain.

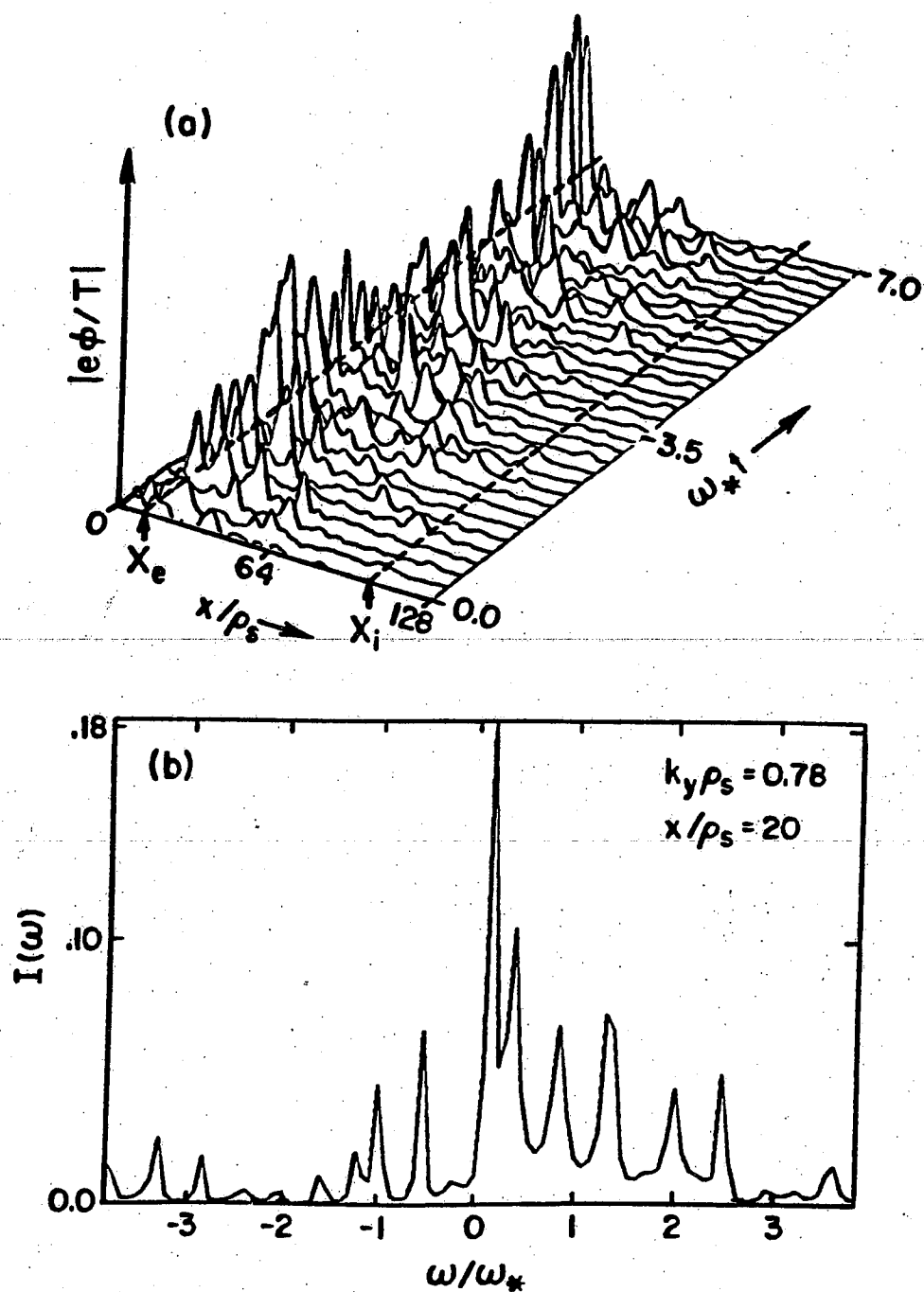


Fig. 3.23. Space-time diagram and power spectra of mode $k_\rho = 0.78$. (a) Mode amplitude, $|e\phi/T|$, versus space (x/ρ_S) and time (ω^*t). Electron and ion resonances are indicated by x_e and x_i , respectively. (b) Local power spectrum versus real frequency, ω/ω_* , taken at position $x/\rho_S = 20$.

$e\phi/T \simeq 0.006$. Note the oscillatory structure of the mode near the electron resonance, x_e , and the spatial decay of the mode amplitude at the ion resonance, x_i . The local power spectrum, shown in Fig. 3.23b and taken at $x/\rho_s = 20$, indicates the frequency peaks near the eigenmode frequency, $\omega/\omega_* = 0.3$, obtained from the shooting code. The local frequency is $\omega/\omega_* = 0.65$. The simulation frequency is measured by using data over the entire length of the run. Therefore the main contribution to the measured frequency comes from the flat portion of the mode energy versus time curve of Fig. 3.22b. After $t = 1.5\omega_*^{-1}$ the eigenmode structure appears to have been set up.

3.6 Summary and Principal Results

In this chapter we have investigated the stability of drift waves in the sheared slab model using the methods of particle simulation. We have considered a variety of boundary conditions at the endpoints of the simulation domain, rational surface positions with respect to the boundaries, i.e., different drift wave parities, different ion resonance layer locations and shear strengths. The principal results can be summarized as follows.

For strongly sheared magnetic fields ($L_s/L_n < 28$), the stable eigenmodes predicted by linear theory are found to be present as long as the ion resonance layer is well within the simulation domain. The eigenmodes are observed for the even parities irrespective of the rational surface position. They are also observed for the odd parity whenever the rational surface position does not coincide with the simulation boundary. The stable eigenmodes of linear theory are not found when these two positions coincide and this is probably a result of boundary effects on the drift wave eigenmode parity which is present only in this situation. These effects may arise because the mode parity is imposed on the background as well as the perturbed potential and density.

A number of runs were carried out in systems with weak magnetic shear. It was found that when the electron and ion resonances are well enough separated, local growth near the electron resonance is sufficient to modify the equilibrium density profile which in turn limits the growth of the mode. With weak shear and ion resonance layer within the simulation domain a slight increase in the fluctuation level of the mode with $k_y \rho_s \approx 1$ occurred; however, the eigenmode frequency predicted by linear theory resulted over the entire length of the run.

C H A P T E R I V

THREE DIMENSIONAL PARTICLE SIMULATION OF DRIFT WAVES IN A SHEARED MAGNETIC FIELD

4.1 Introduction

The sheared slab model with a single mode rational surface is a very idealized description of non-local universal mode behavior in a toroidal plasma. From the results of the previous chapter, it cannot provide an adequate explanation of the observed suprathermal density fluctuations.⁸⁰⁻⁸⁴ Recently, much effort has been directed towards finding additional effects which could destabilize the universal mode in simple and realistic geometries. This is partly motivated by the desire to keep the universal mode a viable candidate for explaining anomalous transport in magnetically confined plasmas.

Two approaches have been taken. The first focuses on effects which are absent in the simplified sheared slab model such as toroidal geometry,^{15,16} trapped particles⁸⁵ and strong density gradients.⁸⁶ The second is to consider the influence of a given micro-turbulence background, originating from thermal noise, on

the linear eigenmodes described in the previous chapter. In this dissertation the latter approach is taken.

Using a strong turbulence theory, based on the resonance-broadening procedure developed by Dupree,⁸⁷ Hirshman and Molvig¹⁴ reported that drift waves could be made unstable by the presence of a finite amount of turbulence. The pioneering work of Hirshman and Molvig showed that the turbulent diffusion of electrons across the rational surface, caused by the combination of shear and random $E \times B$ fluctuations, could result in a non-linear destabilization of the universal mode. Physically, the presence of low frequency drift modes centered on closely packed rational surfaces can induce stochastic motions of the particles across the magnetic field and hence change the stability properties of the linear problem. The radial diffusion from the stochastic motion occurs when the islands for the electrostatic potential, around the different resonant surfaces, strongly overlap. Potential fluctuation level measurements indicate that island overlap is well satisfied for many experimental devices exhibiting anomalous transport. The turbulent electron scattering leads to a spatial broadening of the modes which enhance the shear damping. The saturation

of the nonlinearly destabilized modes occurs when, at higher turbulence levels, the damping due to turbulent diffusion is sufficient to stabilize the mode.

Several defects appear in the original analysis given by Hirshman and Molvig.¹⁴ First, it has been shown that the renormalization procedure they used failed to conserve energy.⁸⁸ Diamond and Rosenbluth⁸⁹ used a proper energy-conserving renormalization method and found qualitatively similar behavior in the original theory at high enough turbulence levels. Second, at these turbulence levels nonlinear ion scattering effects contribute additional nonlinear damping which can lead to stabilization of the modes.^{88,90}

The scenario proposed by Hirshman and Molvig in which drift waves would self-destabilize and consistently saturate leads to a spectrum, at saturation, which is sharply peaked in wavenumber and frequency (a signature not observed experimentally). Some progress has been made theoretically to remedy this defect. Mode coupling due to ion nonlinearities has been invoked in the theory and is shown to distribute energy between different modes.⁸⁸

An alternate approach, to explain the broad frequency spectrum, has been to consider the two point

correlation function for the phase space density correlation function.⁹¹ A turbulent, steady state spectrum results from the detailed balance of energy emission and absorption which cannot be obtained from the single-mode nonlinear marginal stability analysis (one-point theory). The state computed from the one-point theory is not a true steady state since most modes would damp in the absence of sources. In the turbulent plasma, energy emission is due in part to phase space structures called clumps. These are produced by mode coupling and incoherent wave emission. It has been shown, however, that the clump ballistic emission is suppressed by orbit decorrelation.⁹¹ Recently, it has been found that clumps can significantly enhance the rate at which electrons can extract free energy from the density gradient and this leads to significant nonlinear growth rates.⁹²

The effects of microturbulence on the linear drift wave eigenmodes has awaited detailed investigation by means of self-consistent particle simulation methods. This dissertation is one of the first attempts at studying the complex structure of drift wave fluctuations in the three dimensional sheared slab.

The remainder of this chapter is organized as follows. The nonlinear drift wave theory is outlined

and quantitative results are obtained in order to enter the appropriate parameter regime for the simulations. Then, the simulation configuration and parameters are given followed by the results and interpretation.

4.2 Nonlinear Drift Wave Theory

The turbulent electron model,¹⁴ in a three dimensional sheared slab geometry, is a novel nonlinear instability mechanism for drift waves. Therefore, it is important to assess the validity of the theory using self-consistent particle simulation methods. The theory serves as a useful guide to the configuration and relevant parameter regime necessary to perform the simulations. In this section the nonlinear drift wave theory with turbulent electron response and linear ion response is outlined.¹⁴ Although the presentation of the theory by Hirshman and Molvig¹⁴ is inaccurate, other approaches give qualitatively similar results.^{88,89}

It has been mentioned previously that the basic physical mechanism responsible for the destabilization of the universal mode is turbulent radial diffusion of electron orbits combined with the free streaming along the magnetic field. The significant timescale in this

process is the correlation time, τ_c , which is the time for particles to be randomly decorrelated by the combination of radial diffusion and free streaming over a radial mode width. To estimate τ_c , we note that an electron situated on the mode rational surface ($k_{\parallel} = 0$, $x = 0$) will diffuse radially a distance, x_c , the correlation length, in time τ_c

$$x_c = (2D\tau_c)^{1/2} \quad (4.1)$$

where D is the radial diffusion coefficient. This creates a change in k_{\parallel} , so that the effective inclination of the field line is $\Delta k_{\parallel} = k'_{\parallel} x_c$ where $k'_{\parallel} = k_y/L_s$. In the same time, τ_c , particles free stream between wave crests, with parallel thermal velocity v_e , a distance

$$v_e \tau_c = 1/\Delta k_{\parallel} = 1/k'_{\parallel} x_c \quad (4.2)$$

Solving for τ_c and using Eq. (4.1) we obtain

$$\tau_c = [2D(k'_{\parallel} v_e)^2]^{-1/3} \quad (4.3)$$

When $1/\tau_c = \omega_c > \omega$, where ω is the drift mode frequency, the nonlinear electron resonance broadening can dominate the ballistic wave-particle resonance. This affects the eigenmode stability by modifying the behavior of the stabilizing electrons near the mode rational surface. In comparison, the ions are nonlinearly decorrelated at a rate approximately given as $k_{\perp}^2 D$. For the parameter regime of interest the electron decorrelation rate is much large.

The radial diffusion necessary for destabilization arises physically from either collisional spatial diffusion or intrinsic orbital stochasticity, by neighboring drift waves, of the Chirikov type.³⁴ The latter diffusion process occurs because of the three dimensional nature of the problem. Electrons move along the sheared magnetic field

$$\vec{B} = B \left[\hat{z} + \frac{x}{L_s} \hat{y} \right] \quad (4.4)$$

in the presence of electrostatic waves

$$\phi(\vec{x}, t) = \sum_{m, n} \phi_{mn}(x) \exp[i(k_y y + k_z z - \omega_{mn} t)] \quad (4.5)$$

In the sheared magnetic field, the equations of motion for the electrons, in the guiding center approximation, are

$$\dot{\tilde{x}}_{\perp} = \frac{c}{B^2} (\tilde{\mathbf{E}} \times \tilde{\mathbf{B}}) \quad (4.6a)$$

$$\dot{v}_{\parallel} = \frac{-|e|\hbar}{m_e} E_{\parallel} \quad (4.6b)$$

For small x , $|x|/L_s \ll 1$, and the equations of motion in component form are

$$\dot{x} = cE_y/B \quad (4.7a)$$

$$\dot{y} = -cE_x/B + v_{\parallel}x/L_s \quad (4.7b)$$

$$\dot{z} = v_{\parallel} = \text{constant} \quad (4.7c)$$

Letting $x(0) = x_0$, $y(0) = y_0 + v_{\parallel}x_0t/L_s$ be the unperturbed orbits for $\mathcal{E} = 0$, we can transform coordinates from (x, y) to $(\delta x = x - x(0), \delta y = y - y(0))$. The equations for the perturbed orbits become

$$\delta \dot{x} = \frac{-c}{B} \frac{\partial \phi}{\partial \delta y} \quad (4.8a)$$

$$\dot{\delta y} = \frac{c}{B} \frac{\partial \phi}{\partial \delta x} - v_{\parallel} \frac{\delta x}{L_s} \quad (4.8b)$$

and have been studied extensively by Molvig et al.⁹⁵ The first term on the right hand side of Eq. (4.8a) and Eq. (4.8b) represents the radial diffusion from the background of fine scale fluctuations (thermal noise) seen by the particles. The second term in Eq. (4.8b) gives the free streaming contribution along the magnetic field. From the form of the potential in Eq. (4.5) resonances occur when

$$k_{\parallel}(x_0)v_{\parallel} - \omega_{mn} = 0 \quad (4.9)$$

Around each resonant position, x_0 , located at

$$k_{\parallel} = k_z + \frac{k_y x_0}{L_s} = 0 \quad (4.10)$$

there is an island in $(\delta x, \delta y)$ space, in which the particles are trapped if the islands are well separated. The island width can be estimated by assuming

$$\dot{\delta x} = \frac{c}{B} k_y \bar{\phi} \sin(k_y \delta y) \simeq \frac{c}{B} \bar{\phi} k_y^2 \delta y \quad (4.11)$$

and substitution into Eq. (4.8b) gives

$$\delta\dot{y} + \frac{c}{B} \bar{\phi} k_y^2 \frac{v_{\parallel}}{L_s} \delta y = 0 \quad (4.12)$$

where $\bar{\phi}$ is a root mean square value of the local potential. The width of the resonant island is given by the trapping width

$$\delta x = 4 \left[\frac{c}{B} \frac{L_s}{v_{\parallel}} \bar{\phi} \right]^{1/2} \quad (4.13)$$

From Eq. (4.10) the rational surfaces are located at

$$x_{mn} = \frac{-L_y L_s}{L_z} \frac{n}{m} \quad (4.14)$$

with spacing

$$\Delta x_{mn} \approx \frac{L_y L_s}{L_z} \frac{n}{m(m+1)} \quad (4.15)$$

where n is held fixed and m varies. This gives an overestimate of the spacing.

When $\delta x > \Delta x_{mn}$, the Chirikov condition⁹⁴ is satisfied and resonance overlap occurs, resulting in stochastic particle orbit behavior. This means two particles moving along nearly identical trajectories will

separate exponentially according to the general formula

$$\frac{\Delta x(t)}{\Delta x(0)} \propto \exp[t/\tau_c] \quad (4.16)$$

The characteristic time scale of exponentiation, τ_c , is the approximate inverse Kolmogorov entropy and $\Delta x(0)$ is the initial separation. On a time scale large compared to τ_c , the net effect of stochastic behavior is diffusion of the electron orbits.

Using a modification of the resonance-broadening technique of Dupree, Hirshman and Molvig¹⁴ derived a re-normalized equation to describe the behavior of electrons in a strongly turbulent plasma embedded in a sheared magnetic field. The electron distribution function is taken to obey the drift-kinetic equation

$$\begin{aligned} \frac{\partial f_e}{\partial t} + \nabla_{\perp} \cdot (\hat{n} v f_e) + \nabla_{\perp} \cdot \left(\frac{c}{B} \hat{E} \times \hat{n} f_e \right) \\ - \frac{|e|}{m_e} E_{\parallel} \frac{\partial f_e}{\partial v} = 0 \end{aligned} \quad (4.17)$$

where $\underline{B} = B \hat{n}$ and $\hat{n} = \hat{z} + (x/L_S) \hat{y}$. If we separate the distribution function into its average (f_0) and fluctuating (\hat{f}_e) parts the equation for the fluctuating part of the electron distribution is

$$\left[\frac{\partial \hat{f}_e}{\partial t} + v \hat{n} \cdot \nabla + (\hat{n} \times \nabla \hat{\phi}) \cdot \nabla \right] \hat{f}_e$$

$$= -\frac{|e|}{T_e} f_0 [v_* (\hat{n} \times \hat{x}) \cdot \nabla - v \hat{n} \cdot \nabla] \hat{\phi} \quad (4.18)$$

In this equation only the $E \times B$ nonlinearity is kept and $\omega_* = k_y v_{*e}$, with $v_{*e} = v_e^2 / L_n \omega_{ce}$.

Several simplifying assumptions are made in order to proceed with the solution of this equation. First, since stochastic electron diffusion is perpendicular to the magnetic field, the electron $E \times B$ nonlinearity is approximated by an x -space diffusion operator, $D \partial^2 / \partial x^2$. The coefficient, D , replaces all nonlinearities in the problem and is itself a functional of the potential fluctuation spectrum,

$$D = \sum_{\omega, k} G_{k, \omega} k_y^2 \langle |\hat{\phi}_{k, \omega}|^2 \rangle \quad (4.1)$$

where $G_{k, \omega}$ is the Green's function of the particle motion. Second, the only nonlinear terms retained in the expression for $(\hat{f}_e)_k$ are ones explicitly proportional to $\hat{\phi}_k$. This implies that we keep only the part of \hat{f}_k which is phase-coherent with $\hat{\phi}_k$. This assumption is essential in the one-point renormalization method.

Formally, we integrate the equation for \hat{f}_e along the nonlinear orbits. The drift-kinetic equation for the perturbed electron distribution function is

$$\begin{aligned} & \left[-i(\omega - k_{\parallel} v_{\parallel}) - \frac{D \partial^2}{\partial x^2} \right] \hat{f}_e \\ & = \frac{-i|e|}{T_e} f_0 \left[\omega_* - k_{\parallel} v_{\parallel} - \frac{iD \partial^2}{\partial x^2} \right] \hat{\phi} \end{aligned} \quad (4.20)$$

The last term on the right hand side of Eq. (4.20) assures that diffusion does not affect the adiabatic response of \hat{f}_e . If we write Eq. (4.20) in terms of the nonadiabatic electron response

$$\hat{h}_e = \hat{f}_e - \frac{|e|}{T_e} \hat{\phi} f_0 \quad (4.21)$$

the drift-kinetic equation becomes

$$\begin{aligned} & \left[-i(\omega - k_{\parallel} v_{\parallel}) - \frac{D \partial^2}{\partial x^2} \right] \hat{h}_e(x) \\ & = i(\omega - \omega_*) \frac{|e|}{T_e} f_0 \hat{\phi}(x) \end{aligned} \quad (4.22)$$

The integral operation solution to the nonadiabatic diffusive electron response is

$$\begin{aligned}
\hat{h}_e(x, v_{\parallel}) = & \int_0^{\infty} d\tau \int_{-\infty}^{\infty} dx' \exp \left[\frac{i(\omega - k_{\parallel} v_{\parallel})\tau - \frac{1}{3}(k_{\parallel} v_{\parallel})^2 D \tau^3}{\sqrt{4\pi D \tau}} \right] \\
& \cdot \exp \left[\frac{-(x - x' - iDk_{\parallel} v_{\parallel} \tau^2)}{4D\tau} \right] \\
& \cdot \left[i(\omega - \omega_*) \frac{|e| f_0}{T_e} \hat{\phi}(x') \right]. \tag{4.23}
\end{aligned}$$

To solve the integral equation we note that

$$\hat{h}_e(x, v_{\parallel}) = \int dx' G(x, x', v_{\parallel}) \hat{\phi}(x') \tag{4.24}$$

where G is the kernel of Eq. (4.23). G is a peaked function of $(x - x')$ with a width, x_c . $x_c = \omega_c / k_{\parallel} v_e$ is the correlation length for the radial diffusion. The scale length of $\hat{\phi}(x)$ is x_T , the approximate width of the eigenfunction. For $x_c < x_T$, we can Taylor expand $\hat{\phi}(x')$ around $x = x'$, to give

$$\begin{aligned}
\hat{h}_e(x, v_{\parallel}) = & \int d(\delta x) G(x, x + \delta x, v_{\parallel}) \left[\hat{\phi}(x) \right. \\
& \left. + \delta x \frac{d\hat{\phi}}{dx} + \frac{(\delta x)^2}{2} \frac{d^2\hat{\phi}}{dx^2} + \dots \right] \tag{4.25}
\end{aligned}$$

where $\delta x = x - x'$.

The nonadiabatic perturbed electron density response is

$$n_e^{\text{NA}} = \int dv_{\parallel} \hat{h}_e(x, v_{\parallel}) \quad (4.26)$$

and the total perturbed density response becomes

$$\hat{n}_e = \frac{|e| n_0 \hat{\phi}}{T_e} + \hat{n}_e^{\text{NA}} \quad (4.27a)$$

$$= \frac{|e| n_0 \hat{\phi}}{T_e} + \left[c_e^{(0)} + c_e^{(1)} \frac{d}{dx} + c_e^{(2)} \frac{d^2}{dx^2} \right] \hat{\phi} \quad (4.27b)$$

The coefficients, c_e , are defined as

$$c_e^{(0)} = \frac{|e| n_0}{T_e} i \left[1 - \frac{\omega_*}{\omega} \right] \frac{\omega}{\omega_c} I^{(0)} \quad (4.27c)$$

$$c_e^{(1)} = \frac{|e| n_0}{T_e} \left[1 - \frac{\omega_*}{\omega} \frac{\omega}{\omega_c} \right] I^{(1)} \quad (4.27d)$$

$$c_e^{(2)} = \frac{|e| n_0}{T_e} 3i \left[1 - \frac{\omega_*}{\omega} \right] \frac{\omega}{\omega_c} x_c^2 I^{(2)} \quad (4.27e)$$

where

$$I^{(0)} = \int_0^{\infty} \frac{ds}{(1+s^3)^{1/2}} \exp \left[i \left[\frac{\omega}{\omega_c} \right] s - \frac{1}{4} \left[\frac{x}{x_c} \right]^2 \frac{s^2}{1+s^3} \right] \quad (4.27f)$$

$$I^{(1)} = \int_0^\infty \frac{s^3 ds}{(1+s^3)^{3/2}} \exp \left[i \left[\frac{\omega}{\omega_c} \right] s - \frac{1}{4} \left[\frac{x}{x_c} \right]^2 \frac{s^2}{1+s^3} \right] \quad (4.27g)$$

$$I^{(2)} = \int_0^\infty \frac{dss}{(1+s^3)^{1/2}} \left\{ 1 - \frac{3}{4} \frac{s^3}{(1+s^3)} \left[1 - \frac{1}{2} \left[\frac{x}{x_c} \right]^2 \frac{s^2}{(1+s^3)} \right] \right\} \exp \left[i \left[\frac{\omega}{\omega_c} \right] s - \frac{1}{4} \left[\frac{x}{x_c} \right]^2 \frac{s^2}{1+s^3} \right] \quad (4.27h)$$

The $c_e^{(0)}$ term is the turbulently modified electron source and $c_e^{(2)}$ is the enhanced shear damping which results from the turbulence-induced spatial broadening of the mode.

As a first step, the linear ion response is used. The perturbed ion density fluctuation becomes

$$\hat{n}_i = \frac{-|e|\hat{n}_0}{T_i} + \left[c_i^{(0)} + c_i^{(2)} \frac{d^2}{dx^2} \right] \hat{\phi} \quad (4.28)$$

using a finite gyroradius expansion and defining the coefficients

$$c_i^{(0)} = \frac{-|e|n_0}{T_i} \xi_i Z(\xi_i) \left[1 - \frac{\omega_{*i}}{\omega} \right] \Gamma_0(b) \quad (4.28a)$$

$$c_i^{(2)} = \frac{-|e|n_0}{T_i} \xi_i Z(\xi_i) \left[1 - \frac{\omega_{*i}}{\omega} \right] \frac{d\Gamma_0(b)}{db} \rho_i^2 \quad (4.28b)$$

where $\xi_i = \omega/\sqrt{2}k_{\parallel}v_i$, $b = k_{\perp}^2 \rho_i^2$ and $\Gamma_0(b) = I_0(b) \exp[-b]$.

The renormalized electron density response, now treated as a linear equation, is coupled to the linear

ion response through the quasi-neutrality condition. This gives the eigenmode equation for the perturbed potential

$$\frac{d^2 \hat{\phi}}{d\tilde{x}^2} + Q(\tilde{x})\hat{\phi} = 0 \quad (4.29)$$

where

$$Q(x) = \frac{\left[1 + \tau \frac{\omega}{\omega_*} + \xi_i Z(\xi_i) \left[1 + \tau \frac{\omega}{\omega_*} \right] \Gamma_0(b) + i \left[\frac{\omega}{\omega_*} - 1 \right] \frac{\omega}{\omega_c} I(0) \right]}{\left[\xi_i Z(\xi_i) \left[\frac{\omega}{\omega_*} + \frac{1}{\tau} \right] (\Gamma_0 - \Gamma_1) + 3i \left[\frac{\omega}{\omega_*} - 1 \right] \frac{\omega}{\omega_c} x_c^2 I(2) \right]}$$

and $\tilde{x} = x/\rho_s$, $\tau = T_e/T_i$. The boundary conditions are the same as in the linear eigenmode problem; outgoing waves.

The electron response integrals are numerically evaluated and the eigenmode equation can be solved using the standard shooting code method. The eigenfunctions, $\hat{\phi}(\tilde{x})$, and eigenvalues, $\omega = \omega_r + i\gamma$, are determined by varying the parameters, $k_y \rho_s$, τ , L_s/L_n , m_i/m_e and ω_c/ω_* . The last parameter is a measure of the strength of the background fluctuations causing the turbulent radial diffusion. In order to verify the eigenmode equation gives quantitatively accurate results we have made comparisons with numerical solutions to Eq. (4.20). This has been done by Beasley et al.^{96,97} using an initial value code which follows the time evolution of the perturbed

distribution function and electrostatic potential. Fig. 4.1 is a comparison of the results obtained from the eigenmode solution of Eq. (4.29) and the initial value code solution. The parameters used for this case are: $m_i/m_e = 1.837$, $L_s/L_n = 16$ and $\tau = 1$.

4.3 Simulation Configuration and Parameters

In order to determine the stability of drift wave eigenmodes in the three dimensional sheared slab configuration, particle simulations have been carried out using the model described in Chapter II. This extends the work of the previous chapter and allows us to investigate theoretical questions concerning the drift wave stability which have recently been introduced. Since many more self-consistent effects are included in the simulation, comparison with analytic work is difficult. However, theoretical models serve as a useful guide to the relevant parameter regime and measurement of physically interesting quantities.

For the results presented in this chapter we use the three dimensional electrostatic particle code which is periodic and uniform in particle density in the

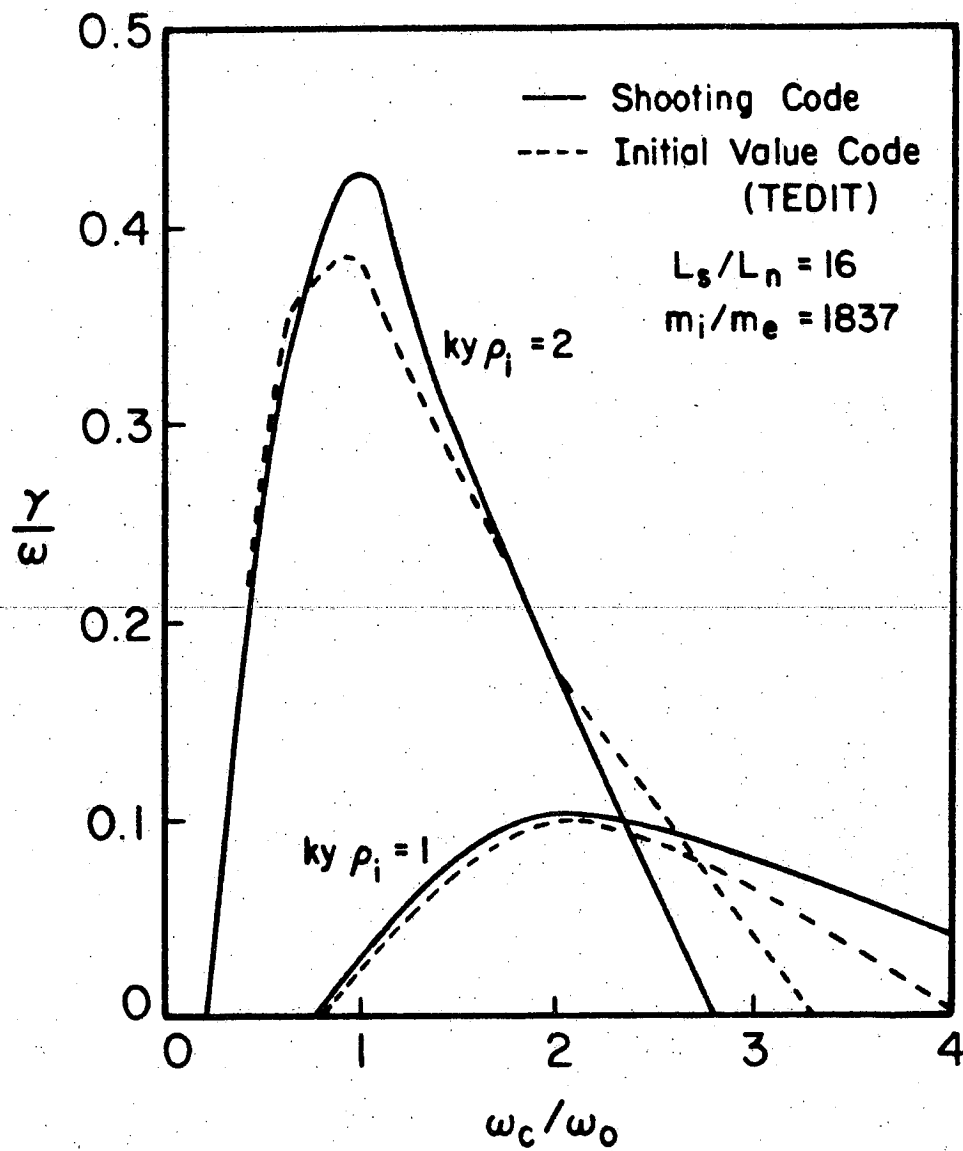


Fig. 4.1. Comparison between solutions of nonlinear eigenmode equation using a shooting method and initial value solution of original drift-kinetic equation.

y and z-directions. It is bounded and nonuniform in the x-direction and the plasma is confined between two boundaries located at $x = 0$ and $x = L_x$. A strong, confining sheared magnetic field is externally imposed and is given by

$$\underline{B} = B \left[\hat{z} + \frac{(x - x_0)}{L_s} \hat{y} \right]$$

where x_0 defines the position of the rational surfaces relative to $x = 0$. The value $x_0 = L_x/2$ is chosen and the rational surfaces are concentrated near the middle of the simulation domain. The boundary condition $\phi(0) = 0 = \phi(L_x)$ is imposed and therefore the eigenmode parities are dominantly even. The rational surface positions are determined from the condition

$$k_{\parallel} = k_z + k_y \frac{(x - x_0)}{L_s} = 0$$

or

$$x_{mn} = x_0 \pm \frac{n}{m} \frac{L_s L_y}{L_z} \quad (4.30)$$

where $k_y = 2\pi m/L_y$ and $k_z = 2\pi n/L_z$. The rational surface

distribution, or packing, depends upon the shear strength, system length and (m,n) mode numbers allowed in the simulation.

Typical parameters used are listed as follows:

$L_x \times L_y \times L_z = 12\rho_s \times 6\rho_s \times 1200\rho_s$, particle size $a_x = 1.5\Delta$, $a_y = \Delta$, $a_z = 275\Delta$, $T_e/T_i = 1$, $m_i/m_e = 500$, $L_s/L_n = 14$, $v_e/\omega_{pe}\Delta = 2.6$, $\omega_{ce}/\omega_{pe} = 11$, $\omega_{*e}/\omega_{ci} = 0.34m$, $\rho_s = 5.3\Delta$, $k_y\rho_s = 1.04m$, $n_0 = 15$ particles/cell, $\omega_{pe}\Delta t = 3$, and $m = 0, \pm 1, \dots, \pm 16$, $n = 0, \pm 1, \dots, \pm 5$. The rational surfaces are, therefore, located at

$$x_{mn}/\rho_s = 6 \pm 0.21 (n/m)$$

and are shown as solid circles in Fig. 4.2. The rational surfaces are plotted as a function of mode number, (m/n) , and the initial density profile is superimposed on the same figure. It is important to note that the rational surface pattern is arranged such that the ion Landau resonance point of the outermost mode rational surfaces, $x_{\pm 1,5}$, lies within the simulation domain.

4.4 Simulation Results and Interpretation

In this section a detailed analysis of the simulation results is presented. The analysis will

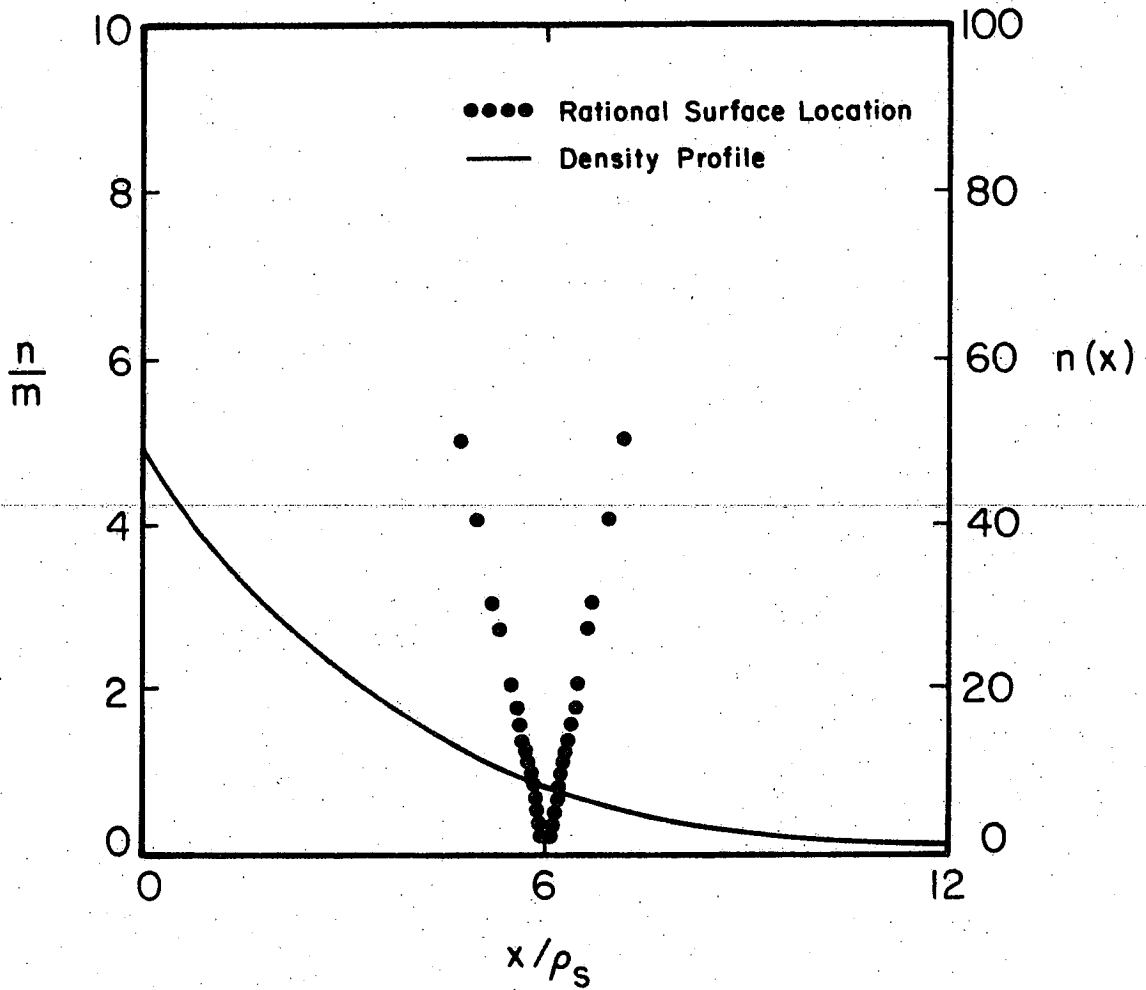


Fig. 4.2. Rational surface location for each mode number (m,n) with density profile superimposed.

consist of two parts. First, test particle orbits and diffusion are considered in order to obtain quantitative estimates of the diffusion coefficient. This allows a comparison between the eigenmode frequency and decorrelation rate. Second, the drift wave fluctuations are temporally and spatially analyzed in order to determine their stability.

Case 1

Using the parameters of the previous section. Eq. (4.29) is solved numerically and the resultant real frequency and growth rates are determined. In Fig. 4.3 the growth rate normalized to the real frequency is plotted as a function of the decorrelation frequency normalized to the drift frequency. The solid circles are the simulation values of the decorrelation frequency, and the determined value of ω_c/ω_* , obtained from the test particle data, will be given in following paragraphs. The growth rates of the first three, longest wavelength modes are predicted to be finite and positive, lying near the peaks of the growth rate curves.

Electron test particles are selected randomly in the vicinity of the mode rational surfaces. The

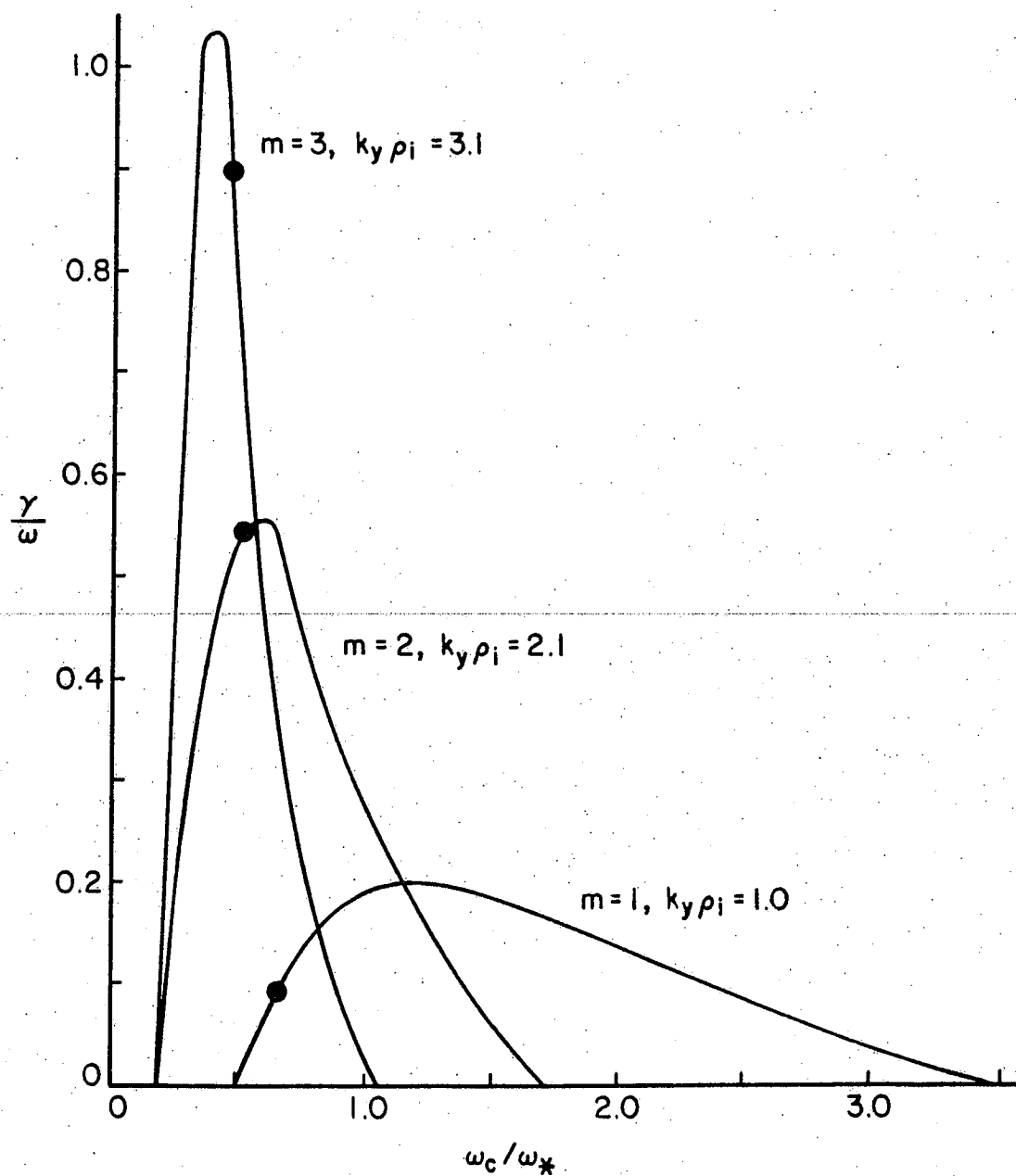


Fig. 4.3. Growth rate curves for various mode numbers as a function of decorrelation frequency. Solid circles refer to simulation values.

positions and velocities are stored at each time step in order to obtain the diffusivity of the particles. To determine whether or not the Chirikov condition is satisfied at the thermal fluctuation level of the simulation, the island width at the electron resonances is compared with the mode rational surface separation. In the neighborhood of the electron resonance, the island width is,

$$\frac{\Delta x_T}{\rho_s} \sim \frac{4}{\rho_s} \left[\frac{cL_s |\phi_{mn}|}{Bv_e} \right]^{1/2} \sim 9 \left[\frac{e\phi_{mn}}{T_e} \right]^{1/2} \quad (4.31)$$

for the simulation parameters. From Eq. (4.14) a crude, overestimate of the rational surface spacing can be made. Holding n fixed and varying m gives

$$\frac{\Delta x_{mn}}{\rho_s} = \frac{-LyL_s}{\rho_s L_z} \frac{\Delta n}{\Delta m} \sim \frac{0.21n}{m(m+1)} \quad (4.32)$$

For fluctuation levels, $10^{-3} \lesssim e\phi/T_e \lesssim 10^{-1}$, measured in the simulation, it is clear $\Delta x_T > \Delta x_{mn}$ is satisfied.

The diffusion coefficient for test particles is measured as

$$D = \lim_{t \rightarrow \infty} \frac{1}{2Nt} \sum_{i=1}^N (\Delta \bar{x}_i)^2 \quad (4.33)$$

where Δx_i is the change in position of the guiding center for the i th particle in time t and N is the number of test particles. The guiding center displacement of test electrons in the x -direction, initially lying in the range $5.6 \simeq x/\rho_s \simeq 7.5$, as a function of time is shown in Fig. 4.4. The value of the test particle diffusion coefficient is $D \simeq 0.006 \rho_s^2 \omega_{ci}^2$. With this value of D , the decorrelation rate is given by $\omega_c/\omega_* \simeq 0.6 m^{-1/3}$. From Fig. 4.4 it is also evident that the diffusion coefficient decreased beyond $\omega_{ci}t = 132$. This is an indication that the diffusion process is time-dependent and, as will be shown later, is related to the saturation of the potential fluctuations.

The test particles can provide information about the type of diffusive process which occurs. By measuring the divergence of pairs of electrons, initially located in the resonance overlap region and separated a small distance apart, it is possible to obtain quantitative estimates of particle diffusion and intrinsic orbital stochasticity (i.e., Liapounov exponents). Selecting pairs of test particles and averaging over a large number of pairs, the separations in x ,

$$\langle \Delta x_-^2 \rangle = \frac{1}{N} \sum_{i,j} [(x_i(t) - x_i(0)) - (x_j(t) - x_j(0))]^2 \quad (4.34)$$

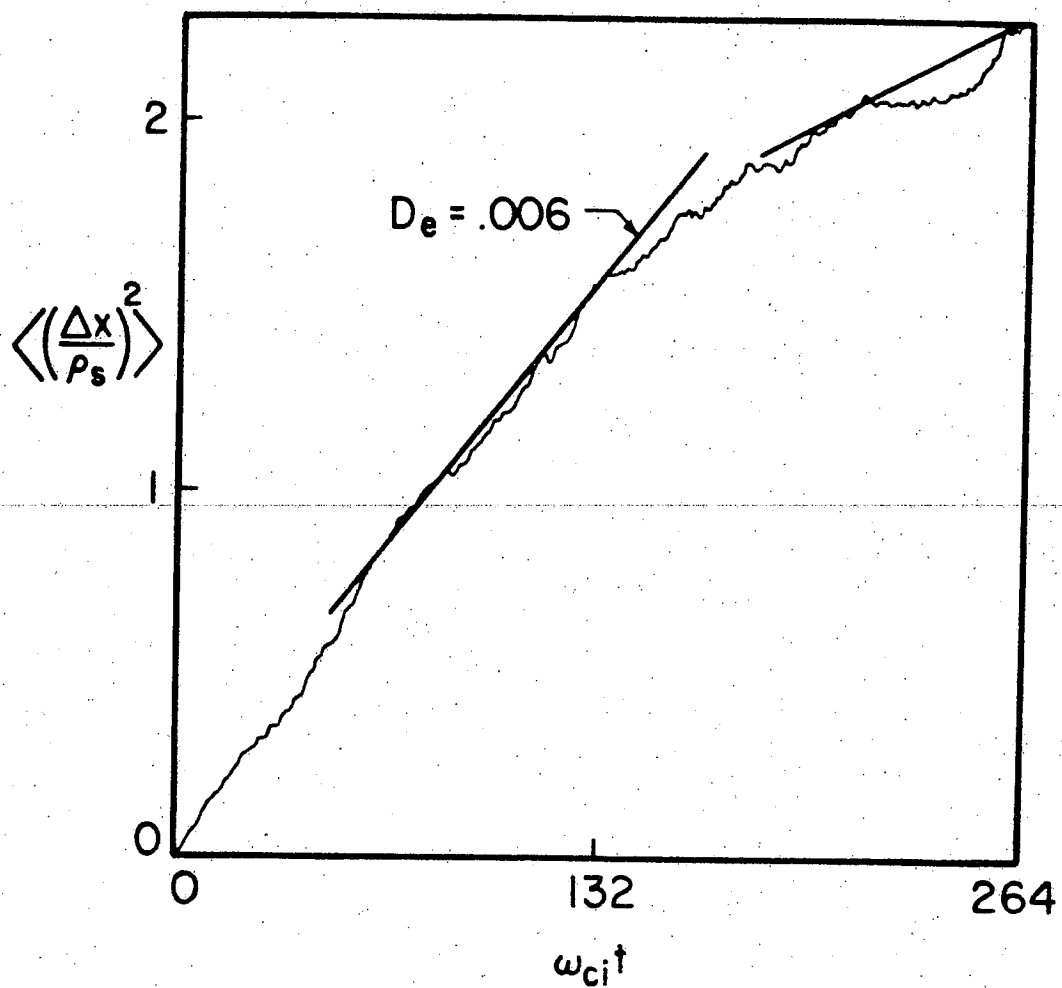


Fig. 4.4. Guiding center displacement of electrons as a function of time for Case 1.

and in the y-direction

$$\langle \Delta y^2 \rangle = \frac{1}{N} \sum_{i,j} [(y_i(t) - y_i(0)) - (y_j(t) - y_j(0))]^2 \quad (4.34a)$$

are shown in Fig. 4.5. The results indicate that the orbit divergences have strong time dependence and the exponents do not appear to be constant. The separation in x, from Fig. 4.5a, varies between a linear and exponential time behavior which makes a measurement of the slope difficult. The separation in y, illustrated in Fig. 4.5b, also has a time varying slope. This complex orbit behavior is related to the change in magnitude of the test particle diffusion in x mentioned earlier. Let us now consider the diffusion processes in the resonance overlap region in view of the simulation configuration.

From the perturbed orbit, Eqs. (4.8) and the potential, Eq. (4.5), the displacement in x is given as

$$\begin{aligned} \delta x(t) = & \frac{-c}{B} \sum_{mn} ik_y \phi_{mn} \int_0^t dt' \exp i[k_y(y_0 + \delta y(t')) \\ & + (k_{\parallel} v_{\parallel} - \omega_{mn})t] \end{aligned} \quad (4.35)$$

where $k_{\parallel} = k_z + k_y x_{mn}/L_s$. The diffusion coefficient can,

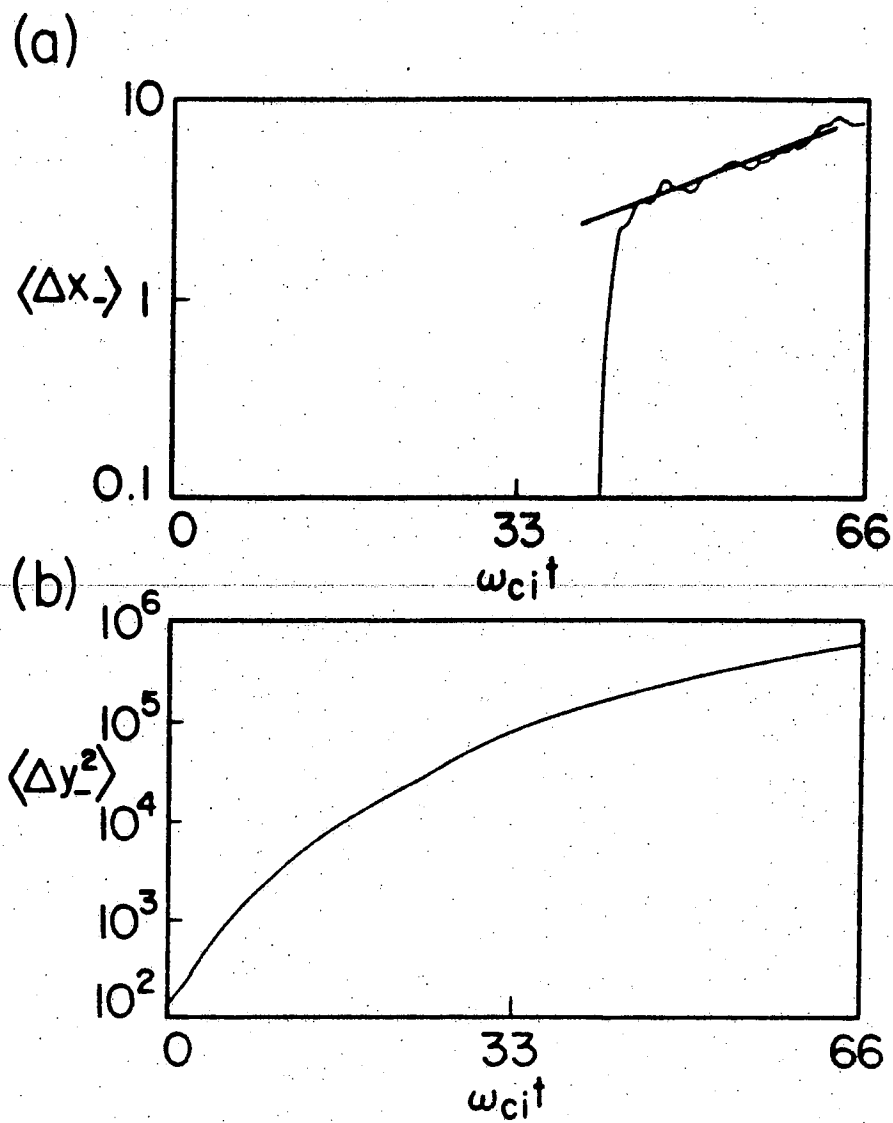


Fig. 4.5. Local orbit divergence for pairs of test particles as a function of time in (a) the x-direction and (b) the y-direction.

therefore be obtained from

$$D = \frac{1}{2t} \langle \delta x(t)^2 \rangle \quad (4.36)$$

and is written as

$$D = \frac{c^2}{B^2} \sum_{mn} |k_y \phi_{mn}|^2 \frac{1}{2t} \int_0^t dt' \int_0^{t'} d\tau \exp \left[i(k_{\parallel} v_{\parallel} - \omega_{mn})\tau - \frac{1}{2} k_y^2 \langle (\delta y(t') - \delta y(t' - \tau))^2 \rangle \right] \quad (4.37)$$

where the relation

$$\langle \exp [i(ax + bx')] \rangle = \exp \left[-\frac{1}{2} (ax + bx')^2 \right] \quad (4.38)$$

has been used. From Eq. (4.8b) the perturbed orbit in y is expressed as

$$\delta y(t) \simeq -\int_0^t dt' \frac{v_{\parallel}}{L_s} \delta x(t') \quad (4.39)$$

and using Gaussian statistics

$$\langle (\delta y(t') - \delta y(t' - \tau))^2 \rangle = \frac{2}{3} \frac{v_{\parallel}^2}{L_s^2} D\tau^2 [3t' - 2\tau] \quad (4.40)$$

For the special case where $t' = \tau$ the diffusion coefficient becomes

$$D = \frac{c^2}{B^2} \sum_{mn} |k_y \phi_{mn}|^2 \int_0^\infty d\tau \exp \left[i(k_{\parallel} v_{\parallel} - \omega_{mn})\tau - \frac{k_y^2 v_{\parallel}^2}{3L_s^2} D \tau^3 \right] \quad (4.41)$$

In the limit where the resonance region width $\Delta k_{\parallel} v_{\parallel} > \omega_c$, $\omega_c = (k_y^2 v_{\parallel}^2 D / (3L_s^2))^{1/3}$, the diffusion becomes time-independent and is

$$D = \frac{c^2}{B^2} \sum_{mn} k_y^2 |\phi_{mn}|^2 \pi \delta(k_{\parallel} v_{\parallel} - \omega_{mn}) \quad (4.42)$$

In the opposite limit $\omega_c > \Delta k_{\parallel} v_{\parallel}$, the diffusion coefficient is,

$$D = \frac{c^2}{B^2} \sum_{mn} |k_y \phi_{mn}|^2 \frac{1}{2t} \int_0^t dt' \int_0^{t'} d\tau \exp \left[i(k_{\parallel} v_{\parallel} - \omega_{mn})\tau - \frac{k_y^2}{3} \frac{v_{\parallel}^2}{L_s^2} D \tau^2 [3t' - 2\tau] \right] \quad (4.43)$$

which is a function of time.

In the realistic case where the electron resonance regions of different mode rational surfaces extend

beyond the ion resonance region of a given test mode we have $\Delta k \simeq k_{\parallel}^i x_i$, where $k_{\parallel}^i = k_y/L_s$ and $x_i \simeq \omega L_s/k_y v_i$. Therefore, $\Delta k_{\parallel} v_{\parallel} \simeq \sqrt{\frac{m_i}{m_e} \frac{T_e}{T_i}} \omega > \omega_c$ and the diffusion coefficient given by Eq. (4.42) can be used. In the simulation case, however, only a finite number of modes (m,n) are available and the rational surfaces are located in a narrow region as shown in Fig. 4.2. The electron and ion resonance regions remain separated. The effective parallel wavenumber range is

$$\Delta k_{\parallel} \simeq k_{\parallel}^i \Delta x_{mn} = k_{\parallel}^i \frac{L_s L_y}{L_z} \Delta \left[\frac{n}{m} \right] \quad (4.44)$$

and fixing m gives $\Delta k_{\parallel} v_{\parallel} \simeq (2\pi/L_z) (\Delta n/m) v_{\parallel} \gtrsim \omega_c$ using the simulation parameters. For long times, Eq. (4.43) is a more correct form for the diffusion coefficient since the autocorrelation time of the modes becomes comparable to the particle decorrelation time. This is a possible explanation for the temporal dependence of the diffusion coefficient in Fig. 4.4.

The estimate for D in Eq. (4.42) is considered an upper bound and it is interesting to compare its magnitude with the test particle value. Since $k_{\parallel} = k_{\parallel}(x)$ and $\phi_{mn} = \phi_{mn}(x)$, the mode structure must be accounted for

in the estimate. ⁹⁷ Choosing m and n as continuous variables

$$\sum_{mn} \rightarrow \int dm \int dn$$

and assuming $dm = (L_y/2\pi)dk_y$, $dn = (mL_z/L_sL_y)dx_{mn}$ gives

$$D = \int dk_y \int dx \frac{L_z n}{2\pi L_s} \frac{c^2}{B^2} k^2 |\phi_{mn}|^2 \frac{2\pi x_e}{\omega} \delta(x - x_e) \quad (4.45)$$

We assume the spectrum of modes has the Pearlstein-Berk variation in x , ⁹⁷

$$|\phi_{mn}|^2 \simeq \frac{2\pi L_s}{nL_z} S(k_y) \frac{1}{x_i} \theta(\alpha x_i - |x|) \bar{\phi}^2 \quad (4.46)$$

where $x_{e,i} = \omega L_s / \sqrt{2} k_y v_{e,i}$, $\bar{\phi}$ = local average of the potential and α = constant $\simeq 0.5 - 1.0$. $S(k_y)$ is the spectrum form factor and

$$\theta(\alpha x_i - |x|) = \begin{cases} 1, & \alpha x_i \geq |x| \\ 0, & \alpha x_i < |x| \end{cases} \quad (4.47)$$

Therefore, the diffusion coefficient is

$$D \simeq \frac{c^2}{B^2} \bar{\phi}^2 \frac{x_e}{\omega x_i} \int k_y dk_y S(k_y) k_y^2 \quad (4.48)$$

which can be expressed in the following way,

$$D = \sqrt{\frac{T_i}{T_e} \frac{m_e}{m_i}} \left[\frac{\omega_{ci}}{\omega} \right] \rho_s^2 \omega_{ci} \left[\frac{e\bar{\phi}}{T_e} \right] \left\langle k_y^2 \rho_s^2 \right\rangle \quad (4.42)$$

For the simulation parameters, $m_i/m_e = 500$, $T_e/T_i = 1$, $\omega_{ci}/\omega \simeq 18-20$, $e\bar{\phi}/T_e \simeq 10^{-1} - 10^{-2}$, $k_y \rho_s \simeq 1 - 2$, the diffusion coefficient is approximately $D \simeq 0.008 \rho_s^2 \omega_{ci}$. This compares with $D \simeq 0.006 \rho_s^2 \omega_{ci}$ obtained from the test particle measurement.

We turn now to an analysis of the eigenmode structure and stability measurements from the simulation. The test mode analysis is carried out for the $m = 1$ ($k_y \rho_s = 1$) and $m = 3$ ($k_y \rho_s = 3.1$) modes. Fig. 4.6 is a composite of the time history for $(m,n) = (-1,1)$. There is a 20-30 percent enhancement of the mode amplitude above the thermal fluctuation level which occurs over several drift periods. The growth rate of the fluctuations corresponds closely to the predictions from the nonlinear eigenmode equation, given in Fig. 4.3. From the power spectrum of the test mode, the real frequency is ω/ω_* 0.2, which gives $\omega_c/\omega \simeq 3$. The variation of the mode in the x-direction is also shown on the same figure. It agrees with the wave function obtained from the solution to the nonlinear eigenmode equation. A similar analysis

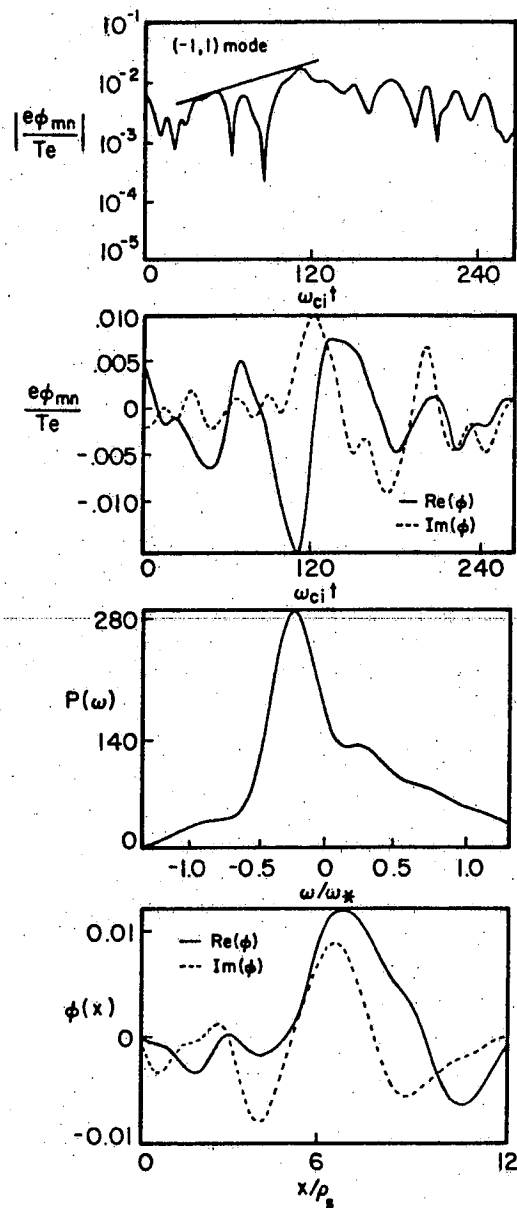


Fig. 4.6. Mode analysis for $(m,n) = (-1,1)$. Spatially-averaged electrostatic potential, power spectrum and spatial mode structure are shown.

is performed on the $(m,n) = (3,4)$ mode shown in Fig. 4.7. The real frequency is $\omega/\omega_* = 0.03$ and $\omega_c/\omega \simeq 12$, which is in agreement with the theoretical value. The measured growth rate of the fluctuation is $\gamma/\omega_{ci} \simeq 0.06$ and, hence, $\gamma/\omega \simeq 2$. This is a factor of two larger than the value predicted by the nonlinear theory.

The largest amplitude of the fluctuations, at saturation, is in the lowest m mode numbers. Fig. 4.8 illustrates the electrostatic potential contours in the x - y plane, for given n modes, taken at $\omega_{ci}t = 120$. A clear localization occurs around the mode rational surfaces for the $(1,0)$ and $(1,2)$ modes.

The enhanced fluctuation level is large enough to cause modifications to the equilibrium density profile. This is shown in Fig. 4.9a where the electron density profile is shown initially, and at the end of the simulation. The largest profile relaxation occurs in the vicinity of the resonance overlap region. From Fig. 4.9b minor changes are observed in the parallel electron temperature profiles.

The connection between the saturation of the fluctuations and the local test particle diffusion analysis is now made. The decrease in the diffusion coefficient

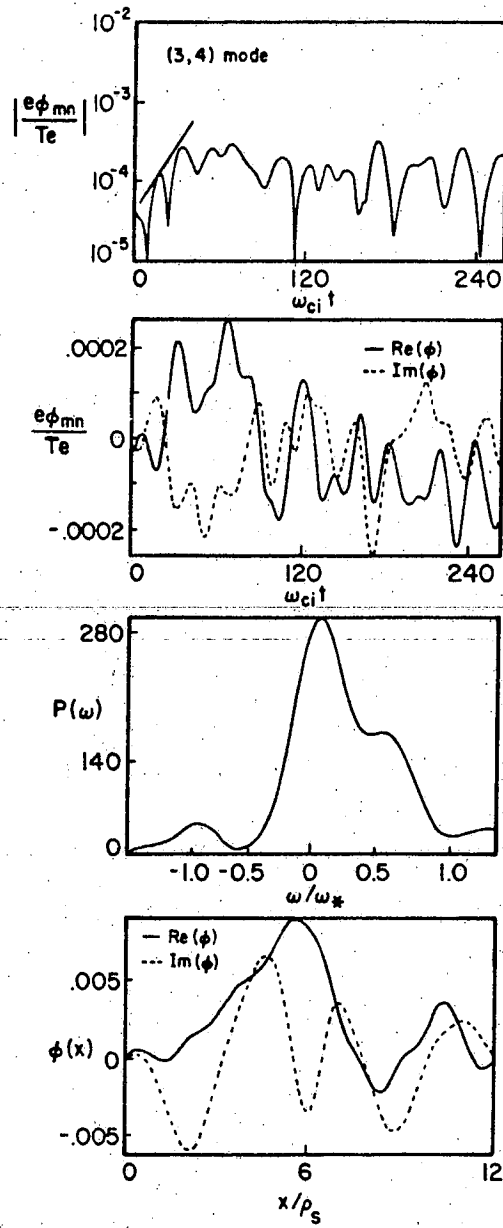


Fig. 4.7. Mode analysis for $(m,n) = (3,4)$

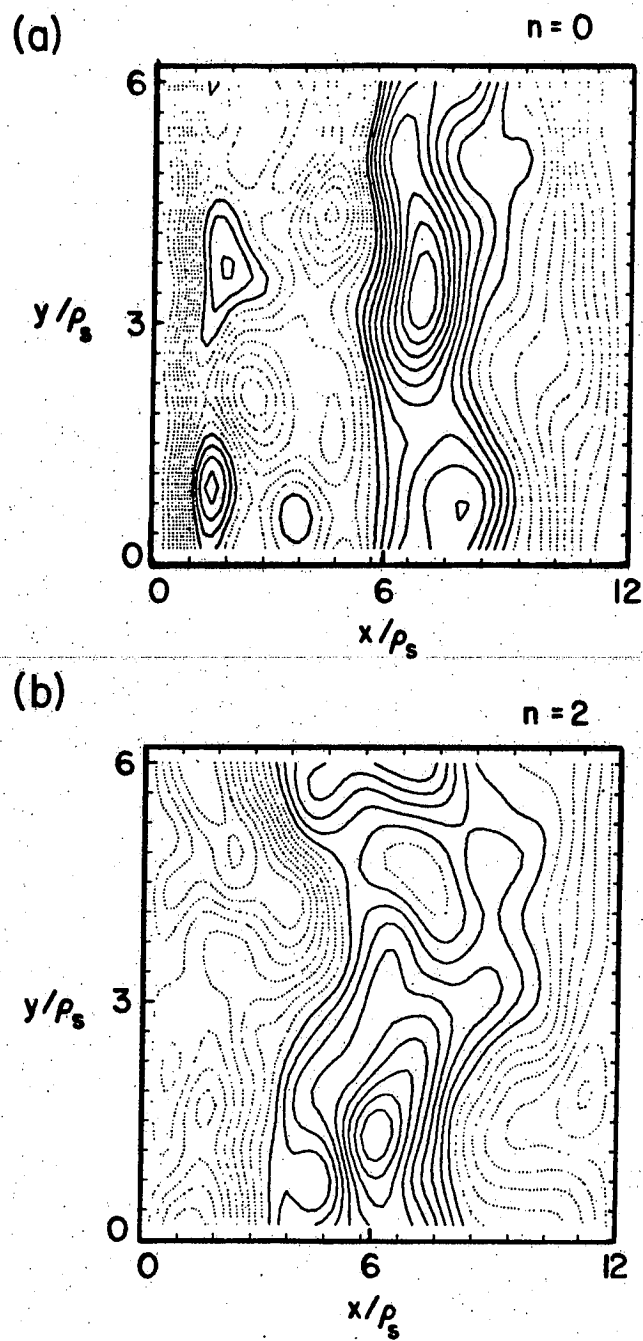
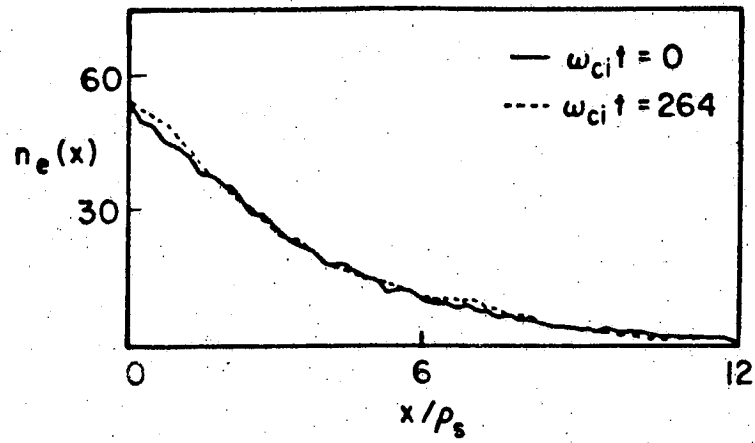


Fig. 4.8. Contours of electrostatic potential, $\phi_n(x, y)$, for (a) $n = 0$, (b) $n = 2$ taken at $\omega_{ci}t = 120$.

(a)



(b)

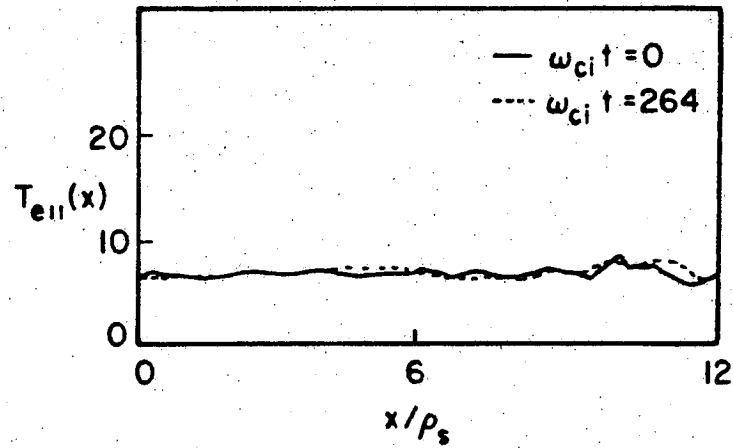


Fig. 4.9. Profiles of (a) electron density and (b) parallel electron temperature shown initially and at the end of the simulation.

of the electrons, illustrated in Fig. 4.4, coincides with the saturation time of the longest wavelength, $(m,n) = (-1,1)$ mode. It appears that the increased amplitude of the fluctuations is sufficient to push the particles out of the resonance overlap region. This changes the diffusivity of the particles which in turn affects the stability of the fluctuations. The particle diffusion out of the resonance overlap region manifests itself as a local equilibrium density profile relaxation.

Case 2

In the previous case, the simulation parameters were chosen such that the entire range of $k_y \rho_s$ gave positive growth rates. We consider the situation where stable, long wavelength modes are present in the spectrum ($k_y \rho_s \simeq 1$), along with unstable, short wavelength modes ($k_y \rho_s > 1$). The parameters used are the same as in the previous case except for $v_e / \omega_{pe} \Delta = 2.5$, $\omega_{ce} / \omega_{pe} = 35$, $\omega_* / \omega_{ci} = 0.06$, $k_y \rho_s = 0.31m$ and $\omega_{pe} \Delta t = 2$. A solution of the nonlinear eigenmode equation with the new parameters gives the growth rate curves shown in Fig. 4.10. The solid circles are the growth rates predicted from the initial simulation turbulence level determined by test particle diffusion measurement. From

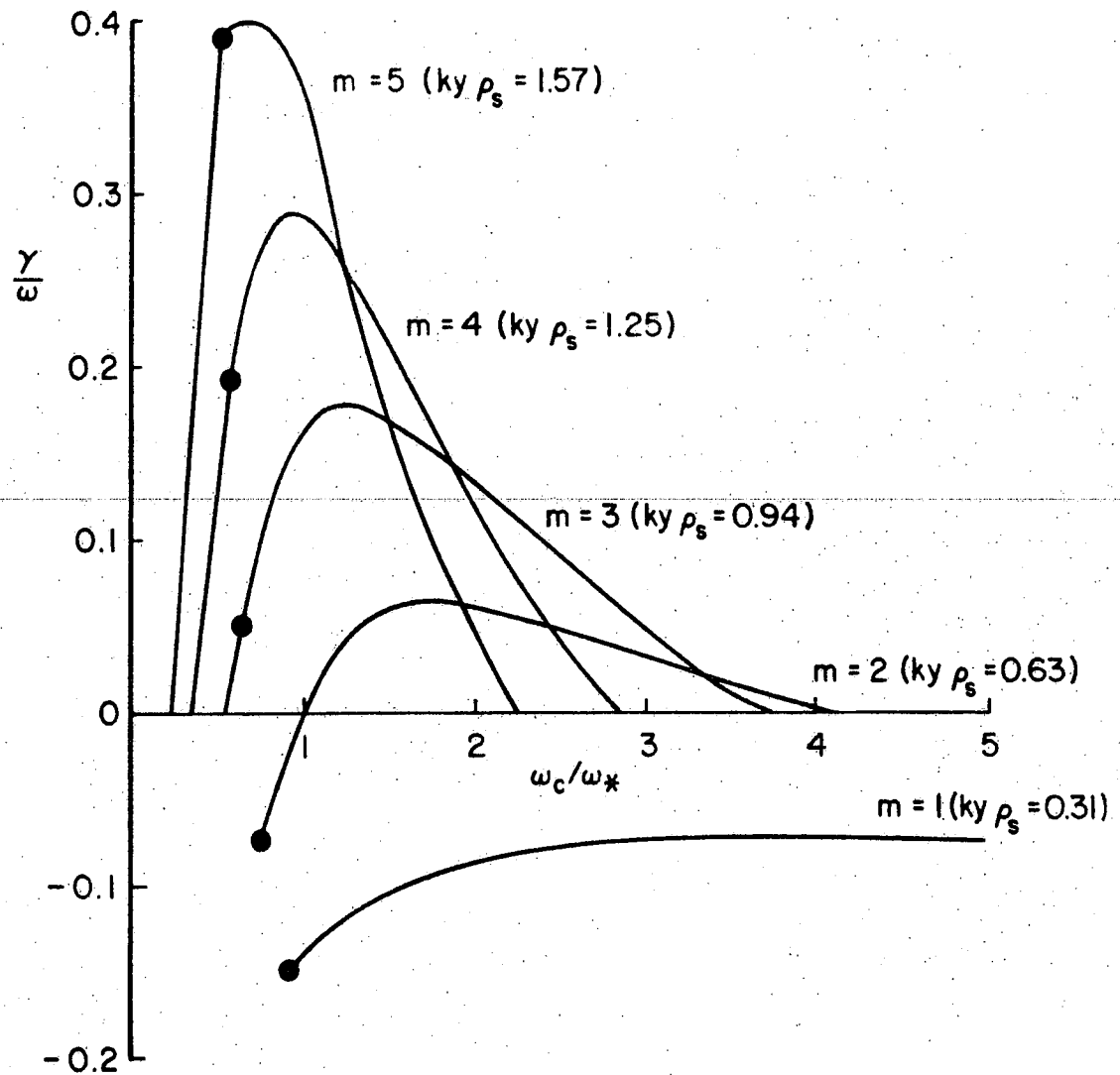


Fig. 4.10. Growth rate curves for Case 2. Solid circles refer to simulation values of the decorrelation frequency.

this figure we note that the first two longest wavelength modes, $k_y \rho_s = 0.314$ and $k_y \rho_s = 0.62$, are predicted to be stable whereas the modes with $k_y \rho_s \simeq 0.94$ have positive growth rates.

Before discussing the mode stability we present the test particle analysis and determination of the decorrelation frequency. The resonance island width in the vicinity of the mode rational surface, for the above parameters, is

$$\frac{\Delta x_T}{\rho_s} = \frac{4}{\rho_s} \left[\frac{c L_s \phi}{v_e B} \right]^{1/2} \simeq 5.95 \left[\frac{e \phi}{T_e} \right]^{1/2}$$

The approximate rational surface separation becomes

$$\frac{\Delta x_{mn}}{\rho_s} = \frac{L_s}{\rho_s} \frac{L_y}{L_z} \frac{n}{m(m+1)} = \frac{0.35n}{m(m+1)}$$

Using the time-averaged fluctuation amplitudes for each mode it is straightforward to show that the island overlap criterion is well satisfied.

The guiding center displacement of test electrons, selected from the overlap region, is shown in Fig. 4.11. The measured test particle diffusion coefficient is $D \simeq 0.01 \rho_s^2 \omega_{ci}^2$. This gives a value of $\omega_c / \omega_* \simeq 0.9$ for the decorrelation frequency. Beyond $\omega_{ci} t = 280$

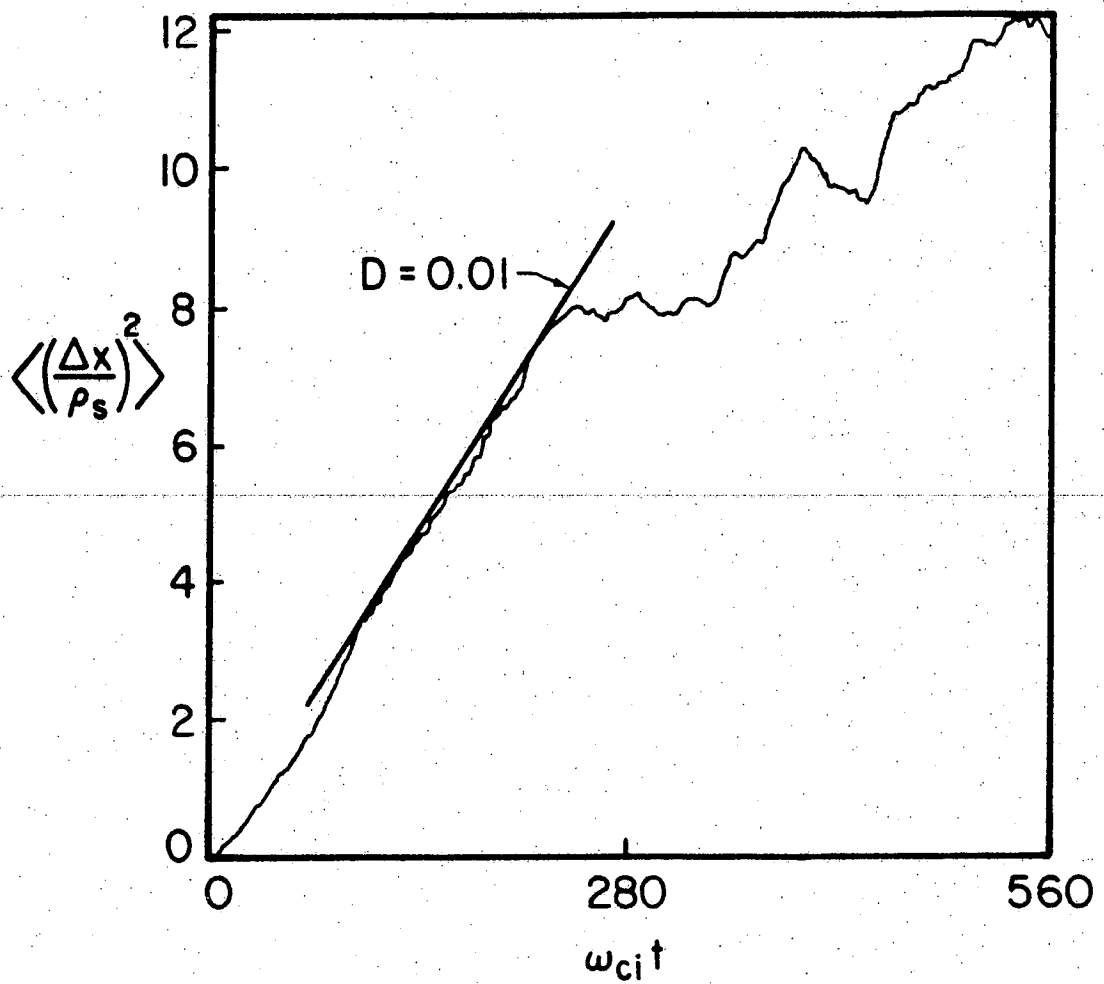


Fig. 4.11. Guiding center displacement of electrons as a function of time for Case 2.

the diffusion coefficient decreases and the guiding center displacements exhibit complex motions. This occurs because the condition $\omega_c \simeq \Delta k_{\parallel} v_{\parallel} \simeq k'_{\parallel} \Delta x_{mn} v_{\parallel}$ is satisfied and Eq. (4.43) must be used to describe the diffusive behavior. In Fig. 4.12 the relative separation of nearest neighbor test particle pairs is shown. There is a tendency for the pairs to diverge exponentially, however, the time dependence is variable.

Two additional pieces of information are presented from the test particle data. First, the diffusion coefficient is shown to have a very weak spatial dependence in the region of the rational surface locations. This is illustrated in Fig. 4.13 where three separate bins of test particles were chosen. Outside the rational surface region the diffusion coefficient drops to its classical value, which is a factor of ten lower.

Second, electron orbits in (x, v_{\parallel}) space, shown in Fig. 4.14, indicate that particles encountering the overlapping resonance region can excuse large distances in the x-direction. This is graphically illustrated in Figs. 4.14 a, b, c and e, where the open circles refer to the initial location of the particle. The dotted curve represents its subsequent motion in time. Particles

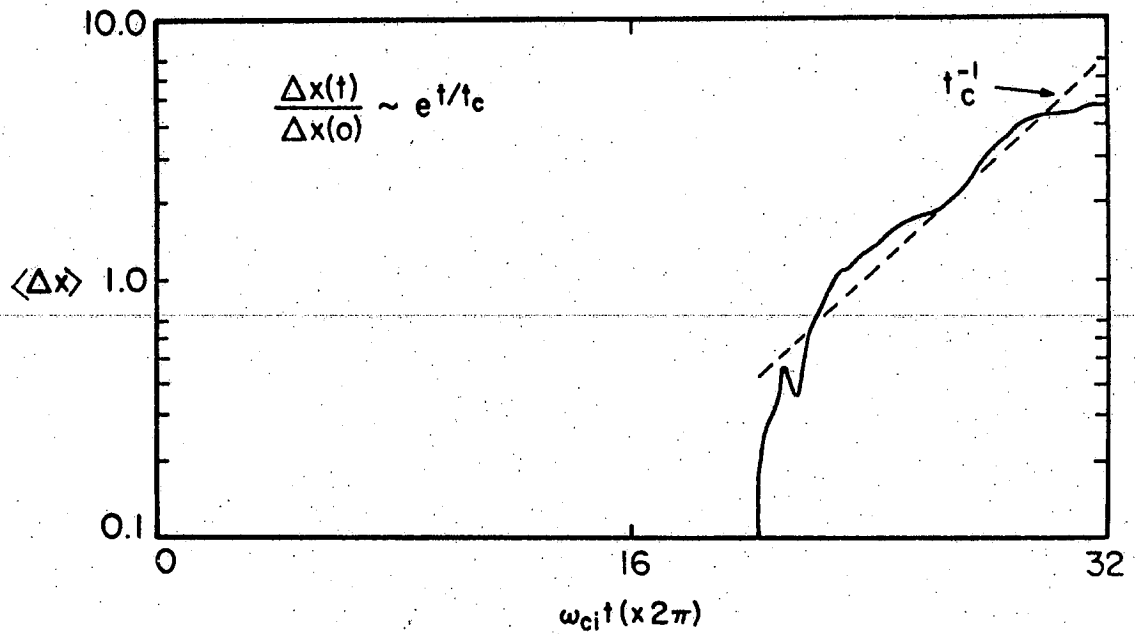


Fig. 4.12. Local orbit divergence in x-direction as a function of time for pairs of test particles.

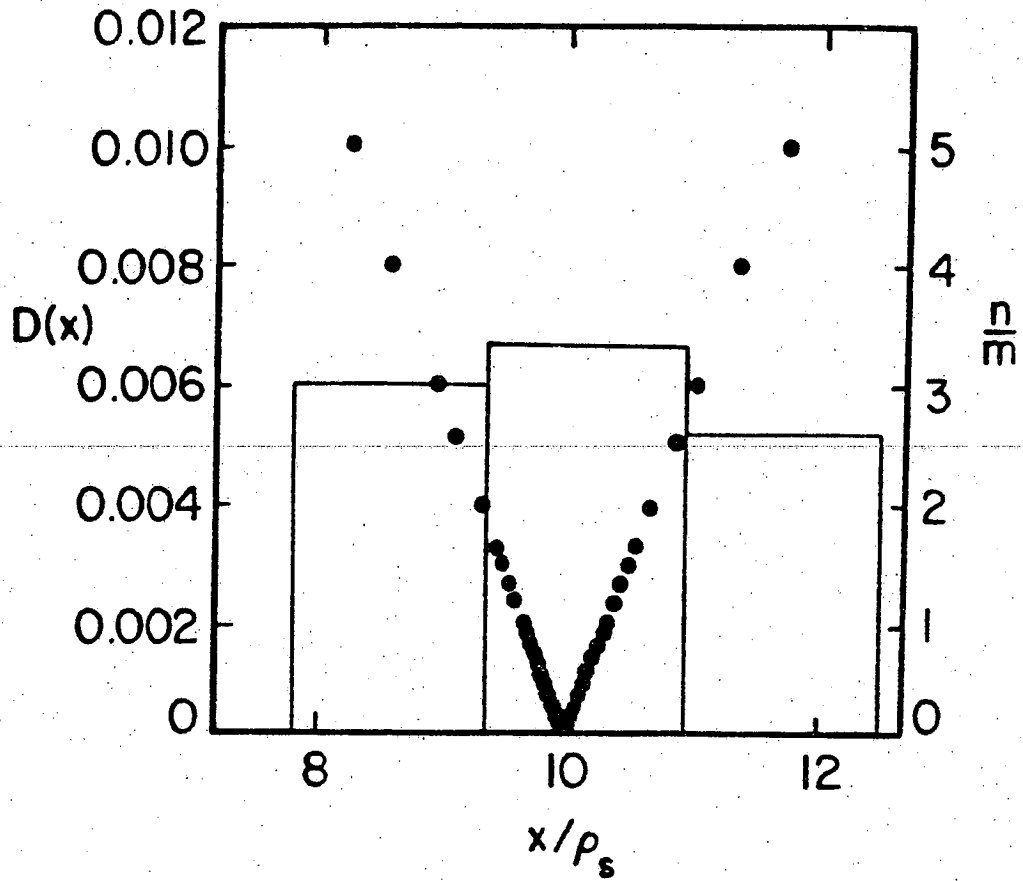


Fig. 4.13. Diffusion coefficient as a function of x in resonance overlap region. Rational surfaces are overlaid on the same figure.

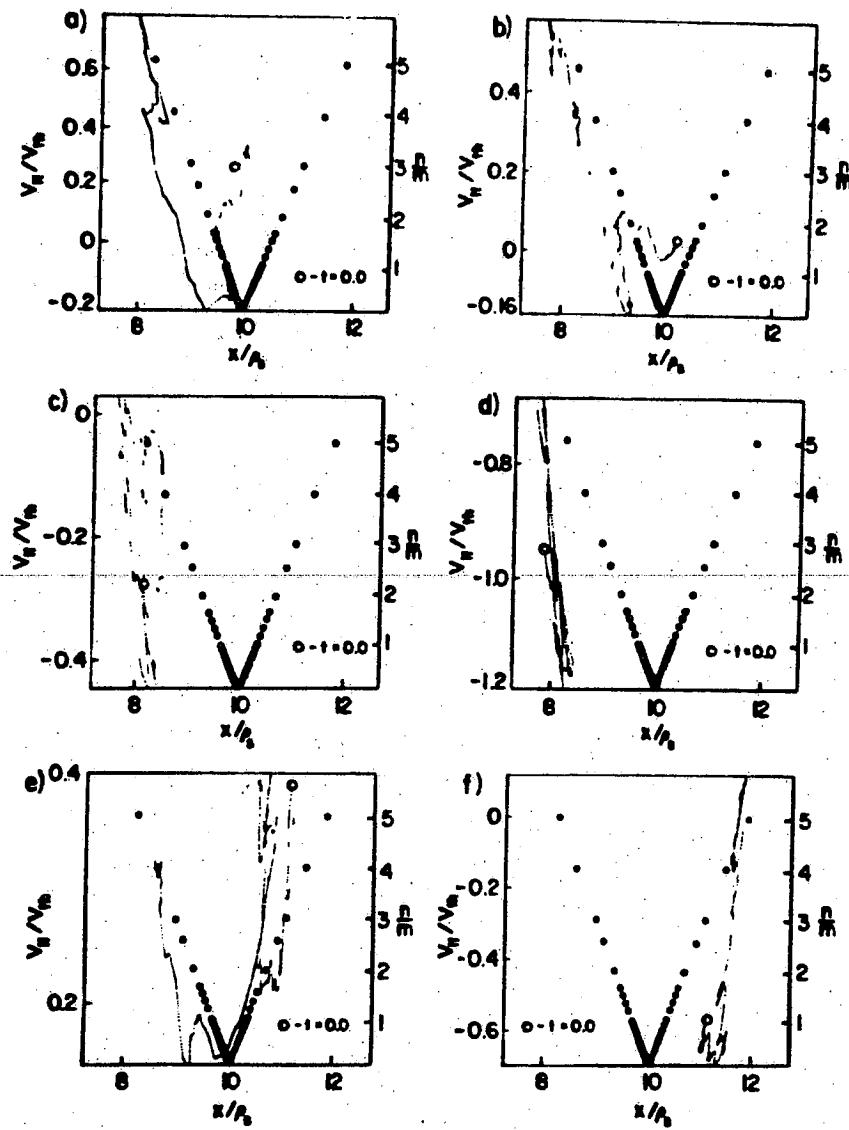


Fig. 4.14. Test particle orbits in $(x-v_{11})$ space. Open circle refers to initial particle location and dotted curve is its motion in time.

selected initially outside the resonance region, Figs. 4.1 d and f, show very little diffusion in the x-direction.

The test mode analysis is carried out for the low m mode numbers and the large m modes. Fig. 4.15 gives the time history, power spectrum and variation in x, of the electrostatic potential fluctuations for $(m,n) = (1,0)$, corresponding to $k_y \rho_s = 0.32$. The fluctuation level rises a very slight amount above the thermal level but the amplitude remains nearly constant over the length of the run. The measured frequency is $\omega/\omega_* \simeq 0.7$ which gives $\omega_c/\omega \simeq 1$. The real frequency and mode structure in x agree with the nonlinear eigenmode equation solution.

Fig. 4.16 and 4.17 illustrate the time evolution of modes $(-2,0)$ and $(-3,0)$. These modes remain at their initial thermal level over the entire length of the run. The real frequencies and mode structure also agree with the solutions to the nonlinear eigenmode equation. For shorter wavelength fluctuations, such as the $(5,2)$ mode, corresponding to $k_y \rho_s = 1.6$, shown in Fig. 4.18, there is a decay in amplitude following an initial enhancement.

The fluctuation levels of the electrostatic potential are at thermal level for the entire run and no

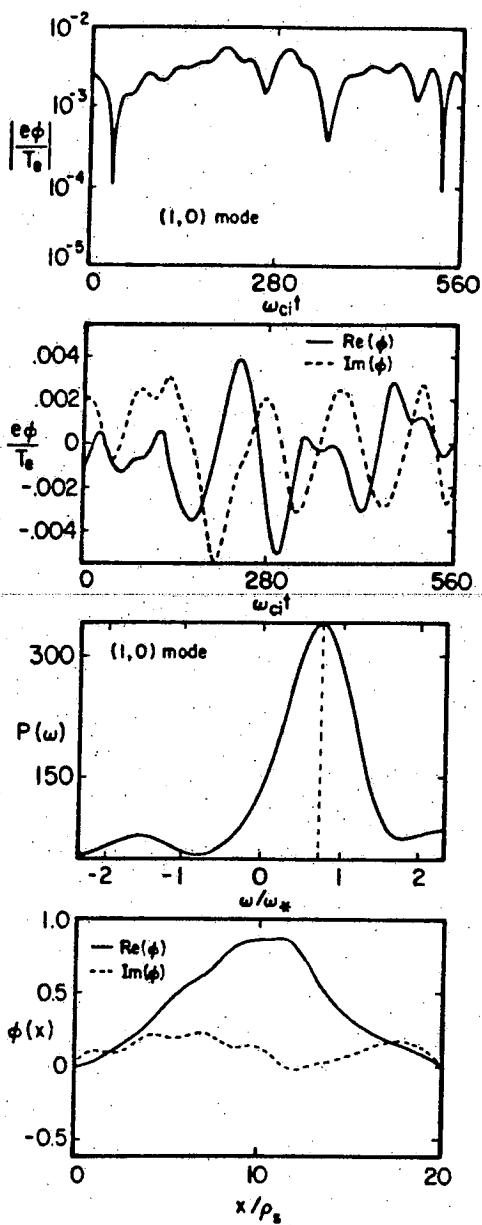


Fig. 4.15. Mode analysis for $(m,n) = (1,0)$ in Case 2.

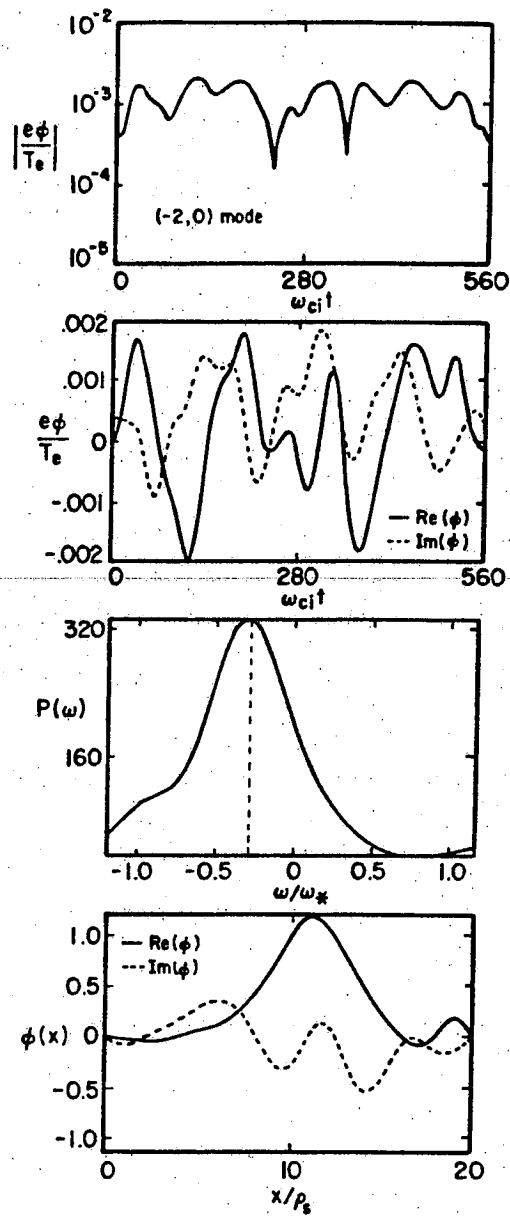


Fig. 4.16. Mode analysis for $(m,n) = (-2,0)$ in Case 2.

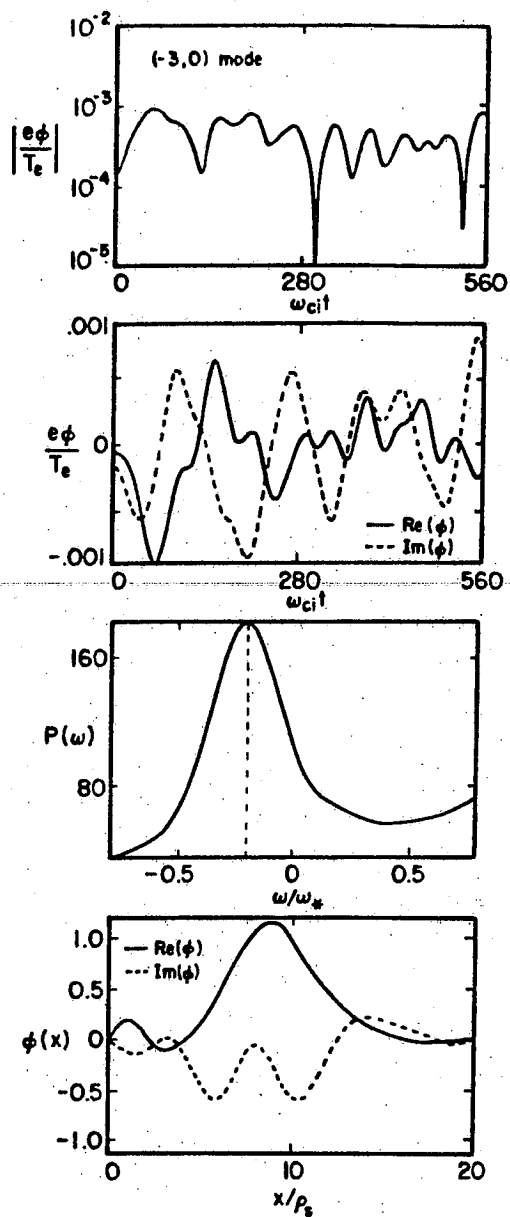


Fig. 4.17. Mode analysis for $(m,n) = (-3,0)$ in Case 2.

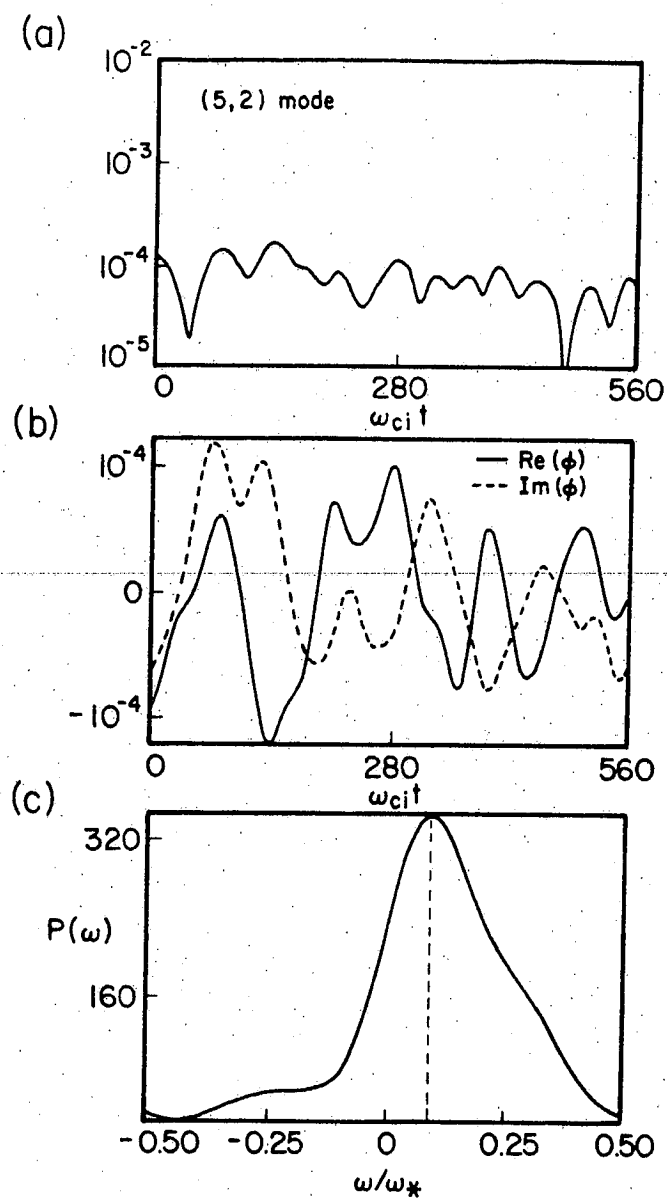


Fig. 4.18. Mode analysis for $(m,n) = (5,2)$ in Case 2.

changes in the equilibrium density profile occur. This is illustrated in Fig. 4.19. Fig. 4.20 is an illustration of the measured real frequencies as a function of the mode number. These are compared with the values obtained from the solutions to the linear and nonlinear eigenmode equations. The solutions of the nonlinear eigenmode equation, which contains the turbulent electron response, differ from the linear electron response model in the wavenumber range $k_y \rho_s \geq 0.9$. In this range the imaginary part of the frequency becomes positive. The predicted growth rates were not observed in this wavenumber range. This suggests the nonlinear eigenmode equation is incomplete in its description of the stability of the simulation eigenmodes.

The apparent discrepancy between the simulation and theory arises from the addition of the longer wavelength fluctuations. These wavelengths are less affected by the nonlinear electron dynamics and provide a sink of energy for the more unstable, shorter wavelengths. Indirect evidence for this coupling exists in the time history of the potential fluctuations for each mode number.

Another possible effect on the eigenmode stability is the nonlinear ion wave-particle interactions.

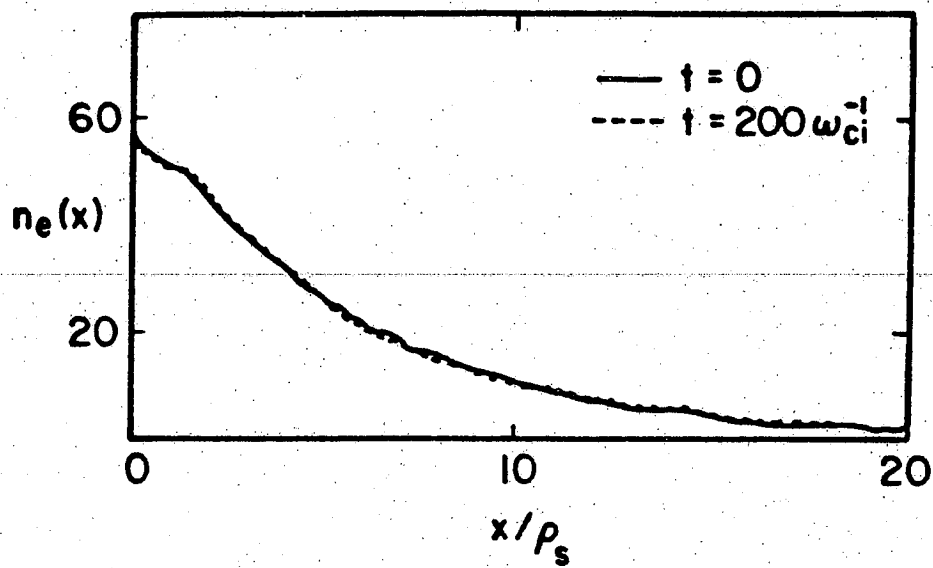


Fig. 4.19. Electron density profile initially and at $\omega_{ci}t = 200$ for Case 2.

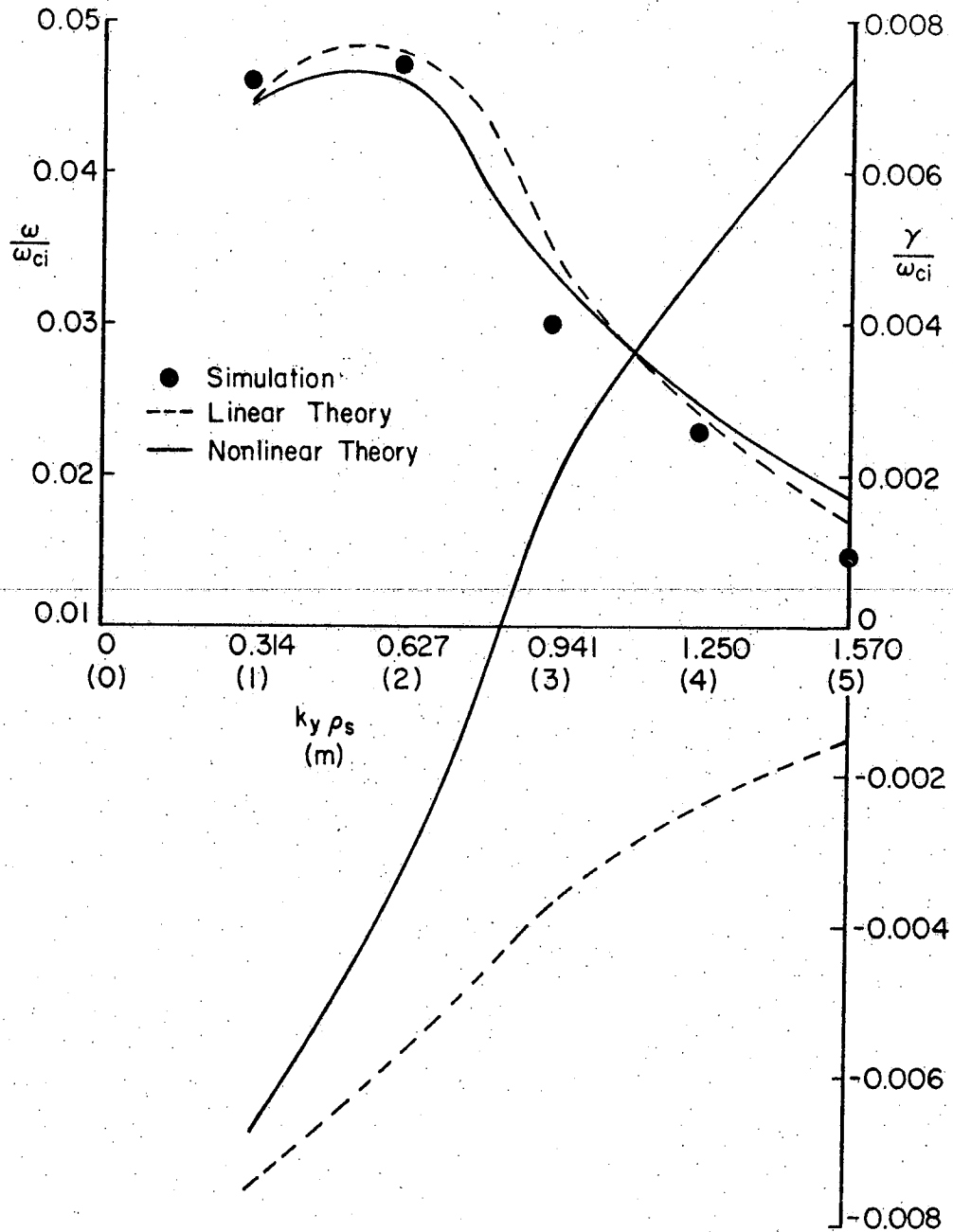


Fig. 4.20. Real frequency and growth rate curves as a function of mode number. Solid circles refer to simulation values.

Fig. 4.21 is a composite of the measured scale lengths for different mode numbers. The resonance points (x_e , x_c and x_i) are determined from the observed real frequency whereas the trapping width, x_{Tr} , is obtained from the electrostatic potential fluctuation levels. It is evident from this figure that modes with $m \geq 3$ have their ion resonance locations situated within the resonance region of the electrons. Therefore, nonlinear Landau damping effects (i.e., Compton scattering) may be a factor in determining the eigenmode stability.

4.5 Summary and Discussion

From the three dimensional simulation results, it has been found that the thermal potential fluctuations of the drift waves, centered about closely packed mode rational surfaces, can induce orbital stochasticity in the electron dynamics. The thermal noise produces decorrelation frequencies in excess of the linear eigenmode frequency. This has an affect on the ballistic wave-particle resonance and is shown to have an influence on the linear eigenmode stability.

When wavenumbers in the range $k_y \rho_s \geq 1$, the favorable regime for nonlinear instability, are allowed

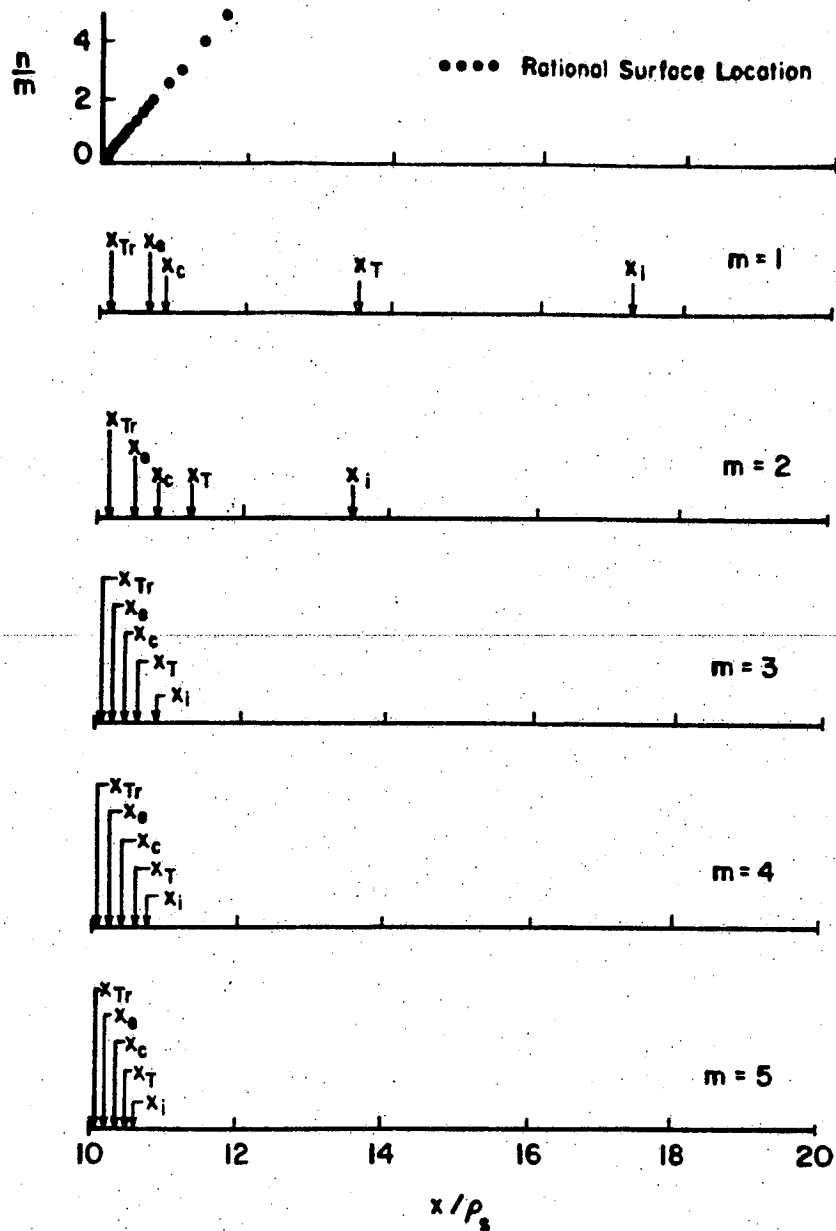


Fig. 4.21. Various scale lengths measured from the simulation. Trapping width, x_{Tr} , electron and ion resonance points, $x_{e,i}$, turning point x_T and correlation length, x_c for modes $(m,0)$.

in the simulation, a growth in the electrostatic potential fluctuations above the thermal level is observed. The growth rates observed are slightly larger than predictions from the nonlinear, turbulent electron theory. The enhancement of the fluctuations produces a loss of particles from the resonance overlap region. This manifests itself as a local quasi-linear relaxation process which saturates the growth of the fluctuations.

When the range of wavenumber is enlarged, $0.3 \lesssim k_y \rho_s \lesssim 2$, large amplitude enhancements in the modes do not appear. Small changes in the fluctuation levels occur in the lowest and highest mode numbers, however, overall stability results. It has been speculated that higher order nonlinear effects, such as mode coupling as well as nonlinear ion Landau damping, could play a role in determining the resultant eigenmode stability. Due to the complexity of these interactions and the fact that the nonlinear processes, mentioned above, may be occurring simultaneously, further detailed diagnostics and extensive parameter variation is required. Furthermore, it may be necessary to design the simulation experiments with an external drive in order to magnify the nonlinear effects.

The application of these results to experiment is difficult because of the configuration. In a tokamak rational surfaces are located everywhere and the ion Landau resonance regions can couple with the electron resonance regions. Due to the limited number of mode rational surfaces in the simulation this interaction is minimal.

C H A P T E R V

PARTICLE SIMULATION OF THE RESISTIVE G-MODE IN A SHEARED MAGNETIC FIELD

5.1 Introduction

Because of the unfavorable curvature of the magnetic field, the Reversed Field Pinch (RFP) is susceptible to resistive interchange modes (g-modes). A study of resistive g-mode stability and associated transport is important for the RFP since it is a relatively high beta device relying on strong magnetic shear rather than average minimum-B for the control (stabilization) of localized modes. Resistive g-modes cannot be stabilized by either shear or conducting walls above. When they appear, the associated magnetic perturbation can cause formation of magnetic islands. This may result in enhanced thermal conduction losses. The turbulence generated by overlapping islands and associated thermal losses is especially important at, and beyond the field reversal point in the RFP. The reason is that the enhanced thermal conduction causes leakage from the core plasma to the wall.

The earliest investigation of the resistive g-mode was by Furth, Killeen and Rosenbluth¹⁹ using slab geometry and a fictitious gravity term to model curvature effects. Coppi⁹⁸ considered the effects of Hall terms and finite Larmor radius in the original analysis. Later Coppi, Greene and Johnson⁹⁹ did a systematic study of g-modes in a cylindrical plasma and found differences from the slab results in the high pressure limit. Hender and Robinson¹⁰⁰ used an initial value code to study the effects of Hall terms and parallel ion viscosity. Using a model with zero equilibrium pressure gradient and infinite parallel electron thermal conductivity Finn et al.²¹ found that both compressibility and large Hall terms were necessary for total stabilization of the resistive g-mode. This study used analytic and numerical methods in a cylindrical RFP model. A more detailed analysis by Mirin et al.,¹⁰¹ using an initial value code, has been done including the thermal force vector in Ohm's law as well as finite electron and ion temperature.

The simulation work by Schnack et al.¹⁰² and Hender and Robinson^{103,104} has centered on determining the gross plasma motion and saturation levels for interchange modes in diffuse pinches. The implications of

resistive g-mode stability for mechanisms of sustainment (several resistive diffusion times) of field reversal, as well as anomalous energy transport have also been considered.¹⁰⁵ In particular, the dynamo theory which relies on the nonlinear beating of magnetic field and kinetic disturbances.

The resistive g-mode has been observed in Levitron experiments at Culham¹⁰⁶ and is thought to be a cause of the magnetic field fluctuations measured in the HBTX-I RFP.¹⁰⁷ The plasma in devices such as the RFP can be divided into a hotter core plasma and a colder edge. The field reversal point, which is nearer to the edge, approximately divides the two regions. The dominant MHD activity in the RFP appears to be the $m = 1$ tearing mode and is observed inside the field reversal point or core plasma. Near the field reversal point, and outside the core region local MHD fluctuations are prevalent¹⁰⁸ which could be a result of the resistive g-mode.

Two observations suggest that the electrostatic resistive g-mode plays an important role in anomalous losses in the RFP.¹⁰⁹ First, the $m = 1$ tearing mode is found to suppress the tearing parity interchange. Second, the magnetic field fluctuations appear to have the same

saturation levels with or without the pressure drive. Since the electrostatic resistive g-mode is localized to the singular surface and is disconnected from the outer region MHD activity, its consequences on anomalous transport are important to assess.

In the following two chapters we investigate the linear and nonlinear evolution of the resistive g-mode using electrostatic particle simulation methods. This electrostatic model, in the appropriate regime, still allows us to consider kinetic modifications, which can alter the scaling of the growth rate with resistivity.

The reasons particle simulation methods are uniquely suited to investigate the evolution of the resistive g-mode are listed as follows. First, the stability of short wavelength modes ($k_{\perp} \rho_s \gtrsim 1$) can be investigated. Second, when multirational surfaces are introduced and overlapping islands are present, the regime $L < v_e/v_{ei}$, where L is the parallel stochastic magnetic field decorrelation length, can be studied. This allows one to examine the stochastic magnetic field line calculation of heat transport as well as investigate anomalous electron viscosity. These difficult problems will not be addressed in this dissertation since the electrostatic model contains

many interesting and complex nonlinear processes.

In this chapter the simulation model and initial configuration are presented. The linear theory of the resistive g-mode is reviewed and simulation results presented for the fast and slow interchange growth regimes. The saturation mechanism of the unstable g-mode is discussed along with a comparison of the predicted values with the simulation results.

5.2 Linear G-mode Theory

In a sheared magnetic field, the resistive g-mode is a localized mode around the resonant surface, $\mathbf{k} \cdot \mathbf{B} = 0$, which is the position where the fluid motion and field can most easily decouple. This can be seen from Ohm's law

$$\mathbf{E} + \frac{\mathbf{v} \times \mathbf{B}}{c} = \eta \mathbf{J} \quad (5.1)$$

and the z-component of the current in sheared slab geometry is

$$J_z = \frac{x}{L_s} \frac{B}{c} \frac{v_x}{\eta} \quad (5.2)$$

Therefore, the restraining force exerted on the plasma is given by

$$\mathbf{F} = -\frac{\mathbf{J} \times \mathbf{B}}{c} = -\left[\frac{Bx}{cL_s} \right]^2 \frac{v_x}{\eta} \hat{x} \quad (5.3)$$

and for $x > 0$ and η small the force is very large. This means the plasma cannot slip across the field lines. However, for $x \approx 0$, corresponding to $\tilde{\mathbf{k}} \cdot \tilde{\mathbf{B}} = 0$, the restraining force is small and the plasma can slip through the field to localize the mode.

On a more microscopic scale, a simple physical picture of the resistive g-mode instability can be made. From Fig. 5.1 the sheared magnetic field $B_0(x/L_s)\hat{\mathbf{y}}$ imposed upon the uniform field $B_0\hat{\mathbf{z}}$ together with the unfavorable curvature $\tilde{\mathbf{g}} = g\hat{\mathbf{x}}$ pointing opposite to the gradient in density are illustrated. The curvature-induced drift of electrons and ions leads to a charge separation which is enhanced by the plasma $\tilde{\mathbf{E}} \times \tilde{\mathbf{B}}$ motion. The presence of shear in the magnetic field allows electrons to move along the field lines to neutralize the destabilizing charge separation. However, due to the presence of collisions this process cannot occur fast enough in a region around $x = 0$ where the electron diffusion time is slow compared to a wave period,

$$k_{\parallel}^2 D = k_y^2 x^2 v_e^2 / L_s^2 v_{ei} < \omega .$$

Therefore an instability, localized near the rational

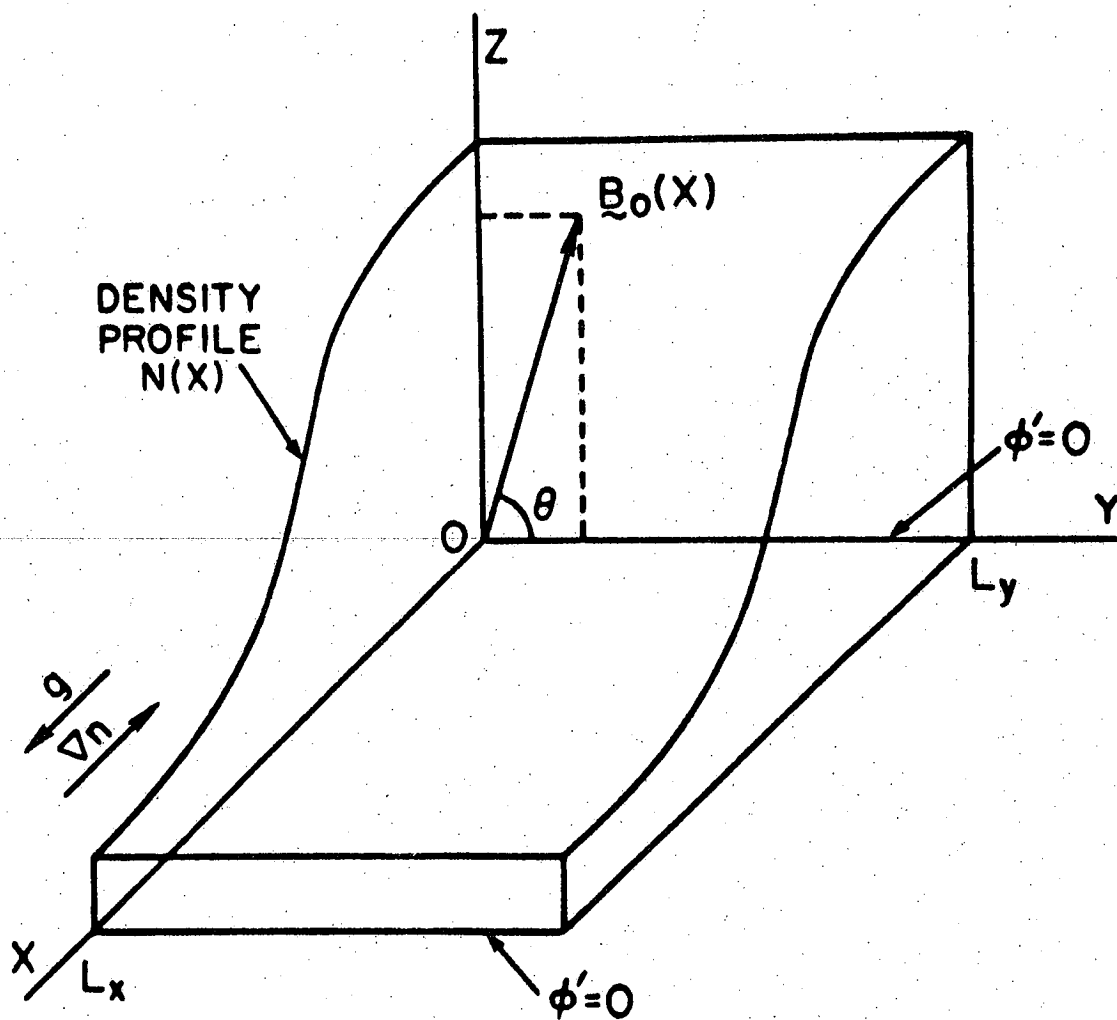


Fig. 5.1. Initial simulation configuration for single rational surface, g-mode evolution.

surface ($k_{\parallel} = 0$) remains. This unstable region is broadened by either reducing the shear or increasing the collisionality.

In order to quantify this picture and determine how the growth rate and mode widths scale with shear and collisionality we consider a kinetic model of the g-mode. The moment equations describing the mode are derived from the ion and electron gyrokinetic equations.

The low frequency ($\omega < \omega_{ci}$) gyrokinetic equation for species $s (= e, i)$ is given by

$$\begin{aligned}
 & -i(\omega - \omega_{Ds})\hat{g}_s + ik_{\parallel}v_{\parallel s}\hat{g}_s + C(s, s')\hat{g}_s \\
 & = -\frac{iq_s}{T_s} (\omega - \omega_{*s}) \langle f_s \rangle J_0(k_{\perp}\rho_s)\hat{\phi}
 \end{aligned} \tag{5.4}$$

where \hat{g}_s is the nonadiabatic perturbed distribution function, $\langle f_s \rangle$ is the average distribution function taken to be a Maxwellian, $\rho_s = m_s v_s / q_s B$, $v_s = (T_s / m_s)^{1/2}$, $\omega_{*s} = k_y \rho_s v_s / L_n$, $\omega_{Ds} = k_y \rho_s v_s / L_c$, $C(s, s')$ is a number conserving collision operator for interspecies collisions and $J_0(k_{\perp}\rho_s)$ is the Bessel function which results from the average over gyro-orbits. The density fluctuation for species s is

$$\hat{n}_s = \frac{-q_s}{T_s} \hat{\phi} + \int d^3v \hat{g}_s J_0(k_\perp \rho_s) \quad (5.5)$$

Two macroscopic equations are necessary to describe the g-mode and they are obtained by taking moments of the gyrokinetic equations. The first of these equations is the continuity equation for both species.

For the electrons, we assume a short mean free path, $k_\parallel v_\parallel < \nu_{ei}$ and also $k_\perp \rho_e \simeq 0$. Taking the zeroth moment of Eq. (5.4) for the electrons gives

$$\frac{k_\parallel \hat{J}_{\parallel e}}{\omega(-|e|n_0)} = \frac{|e|\hat{\phi}}{T_e} + |e| \frac{(\omega - \omega_{*e})}{\omega} \hat{\phi} - \int \frac{\omega_{De}}{\omega} \hat{g}_e d^3v \quad (5.6)$$

where the first term of the right hand side is the adiabatic electron response. The ion response is obtained similarly

$$\frac{k_\parallel \hat{J}_{\parallel i}}{\omega(-|e|n_0)} = \frac{|e|\hat{\phi}}{T_i} + \frac{|e|}{T_i} \frac{(\omega - \omega_{*i})}{\omega} \Gamma_0(k_\perp^2 \rho_i^2) \hat{\phi} + \int \frac{\omega_{Di}}{\omega} \hat{g}_i J_0(k_\perp \rho_i) d^3v \quad (5.7)$$

where $\omega_{*i} = -T_i \omega_{*e} / T_e$, $\omega_{Di} = -T_i \omega_{De} / T_e$ and $\Gamma_0(x) = \exp[-x] I_0(x)$. Adding the electron and ion contributions

gives

$$\frac{-T_e k_{\parallel} (\hat{J}_{\parallel i} + \hat{J}_{\parallel e})}{\omega |e|^2 n_0} = \frac{T_e}{T_i} \left[1 - \frac{\omega_{*i}}{\omega} \right] (\Gamma_0(k_{\perp}^2 \rho_i^2) - 1) \hat{\phi} + \frac{T_e}{|e|} \left(\int \frac{\omega_{Di}}{\omega} \hat{g}_i J_0(k_{\perp} \rho_i) d^3 v - \int \frac{\omega_{De}}{\omega} \hat{g}_e d^3 v \right) \quad (5.8)$$

which is the continuity equation and is equivalent to

$$\nabla_{\parallel} \cdot \hat{J} = 0 \quad (5.9)$$

or

$$-\nabla_{\parallel} \hat{J}_{\parallel} = \nabla_{\perp} \cdot \hat{J}_{\perp} \quad (5.9a)$$

The terms on the left hand side of Eq. (5.8) represent field line bending while the terms on the right hand side represent ion inertia (polarization drift) and curvature drift. The destabilizing curvature and pressure terms, which are contained in the last expression in brackets on the right hand side of Eq. (5.8), are evaluated by computing $\hat{g}_{e,i}$ from the gyrokinetic equations. To first order they are given by

$$\hat{g}_s = \frac{q_s}{T_s} \frac{(\omega - \omega_{*s})}{(\omega - \bar{\omega}_{Ds})} \langle f_s \rangle J_0(k_\perp \rho_s) \hat{\phi} \quad (5.10)$$

where $\bar{\omega}_{Ds} = \int d^3v \langle f_s \rangle \omega_{Ds}$.

Since $\omega > \bar{\omega}_{Ds}$ the expansion

$$\frac{1}{1 - \frac{\bar{\omega}_{Ds}}{\omega}} \simeq 1 + \frac{\bar{\omega}_{Ds}}{\omega} \quad (5.11)$$

is used and this incorporates the stabilizing effect of perpendicular compression to first order. By assuming $k_\perp \rho_i < 1$, which gives $\Gamma_0(k^2 \rho_i^2) \simeq 1 - k_\perp^2 \rho_i^2$, and making the substitution $k_\perp^2 = (\partial^2 / \partial x^2) - k_y^2$ we obtain the eigenmode equation

$$\begin{aligned} \rho_s^2 \left[\frac{\partial^2}{\partial x^2} - k_y^2 \right] \hat{\phi} - \frac{\bar{\omega}_{De} \omega_{*e} (1 + T_i/T_e)}{\omega(\omega - \omega_{*i})} \hat{\phi} \\ = \frac{-T_e k_\parallel (\hat{J}_{\parallel e} + \hat{J}_{\parallel i})}{|e|^2 n_0 (\omega - \omega_{*i})} \end{aligned} \quad (5.12)$$

The second macroscopic equation needed is the equation for the parallel current or Ohm's law. Taking the v_\parallel -moment of the electron gyrokinetic equation and using

$$\int v_\parallel^2 \hat{g}_e d^3v = \frac{-|e|}{m_e} \left[1 - \frac{\omega_{*e}}{\omega} \right] \hat{\phi} \quad (5.13a)$$

$$\int v_{\parallel} \hat{g}_e d^3v = \frac{-\hat{J}_{\parallel e}}{|e| n_0} \quad (5.13b)$$

$$\int v_{\parallel} C d^3v = \frac{-v_{ei} \hat{J}_{\parallel e}}{|e| n_0} \quad (5.13c)$$

the Ohm's law with finite diamagnetic frequency modifications is

$$(-i\omega + v_{ei}) \hat{J}_{\parallel e} = \frac{-ik_{\parallel} |e|^2 n_0}{m_e} \left[1 - \frac{\omega_{*e}}{\omega} \right] \hat{\phi} \quad (5.14)$$

We have used Eq. (5.10) in (5.8) to compute the parallel pressure and close the moment hierarchy.

By assuming $\omega \ll v_{ei}$ and that the major contribution to the current density comes from the electrons we obtain the final eigenmode equation

$$\rho_s^2 \left[\frac{\partial^2}{\partial x^2} - k_y^2 \right] \hat{\phi} - \frac{\bar{\omega}_i \omega_{*e} (1 + T_i/T_e)}{\omega(\omega - \omega_{*i})} \hat{\phi} - \frac{ik_{\parallel}^2 v_e^2 (\omega - \omega_{*e})}{v_{ei} \omega (\omega - \omega_{*i})} \hat{\phi} = 0 \quad (5.15)$$

where $\rho_s = \sqrt{T_e/T_i} \rho_i$ and $k_{\parallel} = k_y x/L_s$. The fast and slow interchange mode growth rates can be derived from this differential equation.

For the first interchange mode we let $k_y > k_x$, $\omega \simeq i\gamma > \omega_*$ and the growth rate is found to be¹¹⁰

$$\gamma = \left[\frac{T_e + T_i}{m_i L_n L_c} \right]^{1/2} \quad (5.16)$$

which is independent of magnetic field strength and resistivity.

To obtain the slow interchange mode we let $k_x > k_y$ and assume an eigenfunction of the form

$$\hat{\phi} = \exp[-\alpha x^2/2], \quad \text{Re}(\alpha) > 0 \quad (5.17)$$

in Eq. (5.15). We obtain the dispersion relation

$$\omega(\omega - \omega_{*e})(\omega - \omega_{*i}) = -i\gamma_0^3 \quad (5.18)$$

where

$$\gamma_0 = \left[1 + \frac{T_i}{T_e} \right]^{2/3} \left[\frac{L_s}{L_n} \right]^{2/3} \left[\frac{L_n}{L_c} \right]^{2/3} \left[\frac{m_e}{m_i} \right]^{1/3} \left[\frac{v_{ei}}{\omega_{*e}} \right]^{1/3} \quad (5.19)$$

Three limiting cases are considered. For $\omega < \omega_{*i} = -\omega_{*e}$,

$$-i\omega = \gamma_0^3 / \omega_{*e}^2 \propto v_{ei} \quad (5.20a)$$

in the limit $\omega_{*i} < \omega < \omega_{*e}$ it is found that

$$-i\omega = (\gamma_0^3 / 2\omega_{*e})^{1/2} \propto v_{ei}^{1/2} \quad (5.20b)$$

and finally for $\omega \gg \omega_{*i} = -\omega_{*e}$

$$-i\omega = \gamma_0 \propto v_{ei}^{1/3} \quad (5.20c)$$

Therefore, diamagnetic effects can substantially alter the growth rate scaling with resistivity.

We note that in the limit $\gamma < \omega_*$ even though $\gamma \propto v_{ei}$ the growth rate is still faster than resistive diffusion since the perpendicular step size is ρ_i . In contrast to $\gamma_0 \propto m^{2/3}$ for the limit $\gamma > \omega_*$, we find γ is independent of the mode number which implies that for large m a finite diamagnetic frequency has a strong stabilizing influence relative to the MHD limit.

The eigenvalues of the differential equation (5.15) depend on four parameters: L_n/L_c , $m_i/m_e(L_n/L_s)^2$, v_{ei} and k_{ypS} . In Fig. 5.2 the various regimes are shown using numerical and analytic solutions of the eigenmode equation. For $T_e = T_i$ and letting

$$A = \frac{m_i}{m_e} \left[\frac{L_n}{L_s} \right]^2, \quad B = \frac{L_n}{L_c} \quad \text{and} \quad C = \frac{v_{ei}}{\omega_{*e}},$$

the kinetic regime ($\omega_{*e} > \gamma$) lies to the left of the dashed line while the MHD regime ($\gamma > \omega_{*e}$) lies below.

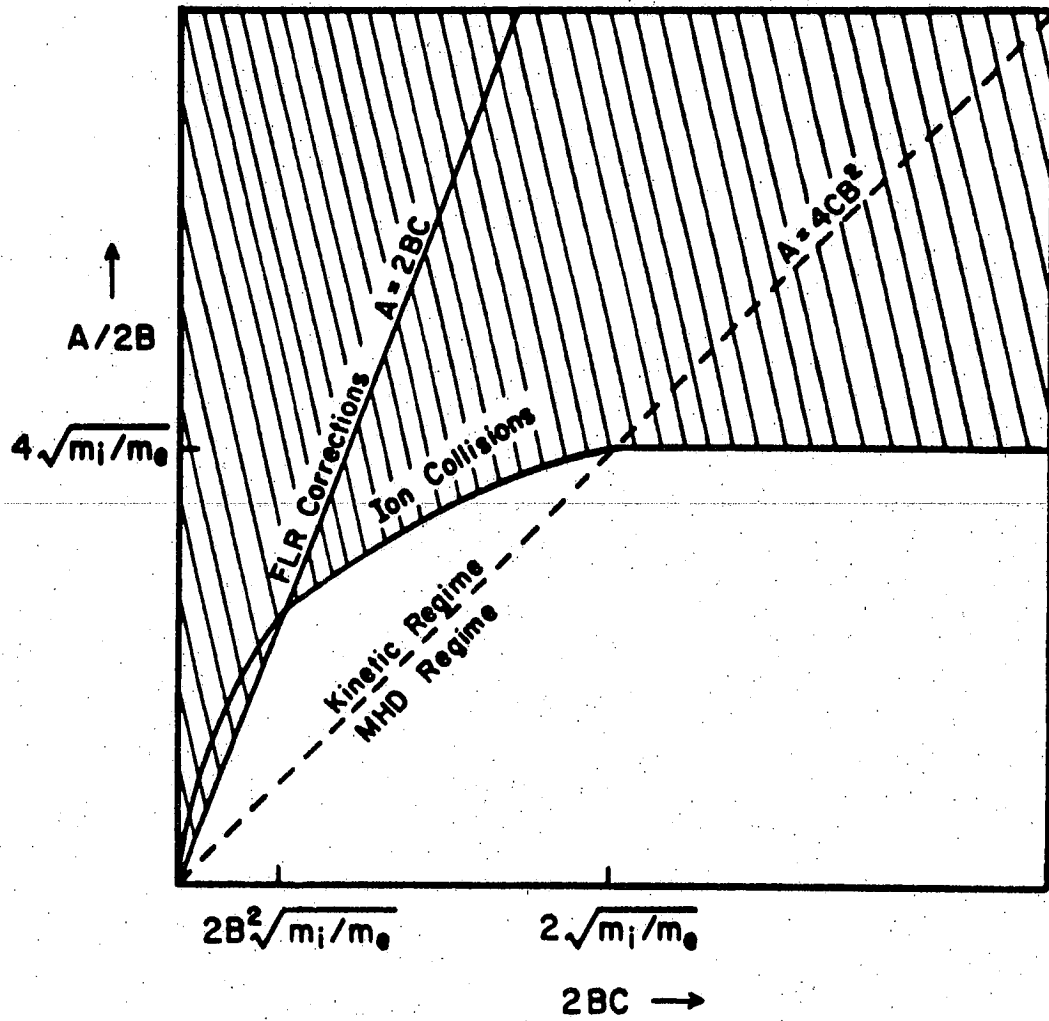


Fig. 5.2. Various parameter regimes describing kinetic and MHD behavior.

$$A = (m_i/m_e)(L_n/L_c)^2, \quad B = L_n/L_c \quad \text{and} \quad C = v_{ei}/\omega_*$$

In the kinetic regime finite Larmor radius corrections are necessary when $k_{\perp} \rho_i \gtrsim 1$ which falls to the left of the solid line $A = 2BC$, i.e., $A/2BC < 1$.

Finally, ion viscosity becomes important when $\nu_{ii} k_{\perp}^2 \rho_i^2 / 4\omega \gtrsim 1$ where ν_{ii} is the ion-ion collision frequency. Approximating $k_{\perp}^2 \simeq 1/\Delta^2$, where Δ is the linear mode width, and ω as the linear growth rate, we obtain the condition

$$\frac{A}{4BC} > \left[\frac{2B}{C} \right]^{1/2} \left[\frac{m_i}{m_e} \right]^{1/4}$$

in the kinetic regime and

$$\frac{A}{B} > 8 \left[\frac{m_i}{m_e} \right]^{1/2}$$

in the MHD regime. The influence of ion viscosity is denoted by the hatched region of Fig. 5.2. A more detailed discussion of the various regimes can be found in the articles by Stringer^{111, 112} and Chang.¹¹³

5.3 Simulation Configuration

To circumvent the enormous difficulty of incorporating many physical effects in realistic geometry

we adopt the simpler magnetized plane slab model of Furth, Killeen and Rosenbluth.¹⁹ The destabilizing effect of magnetic field curvature is represented by an effective gravitational field. In this model the equilibrium magnetic field lies in the (y,z) plane and is given by $\vec{B} = (0, B_0 x/L_s, B_0)$ as shown in Fig. 5.1. To relate this to a cylindrical plasma column, the x -axis may be regarded as the radial coordinate with $x = r - r_0$, where r_0 is the position of the mode rational surface. Therefore, the wavenumber along the magnetic field, k_{\parallel} , is given by $k_{\parallel} = \vec{k}_{\parallel} \cdot \vec{B}/|\vec{B}| \simeq k_y (r - r_0)/L_s$ where $k_y = 2\pi m/L_y$, $m = 0, \pm 1, \dots, \pm L_y/2$ and L_s is the shear scale length of the magnetic field. The density is assumed to vary radially and the profile used initially is

$$n(x) = n_0 \kappa L_x [\exp[-x]/(1 - \exp[-\kappa L_x])] \quad (5.21)$$

which gives a constant density gradient scale length, L_n ($\equiv -1/\kappa$ where $\kappa = -n'(x)/n(x)$) and L_x is the system length in the x -direction. No gradients in temperature are included.

In order to incorporate magnetic field curvature, we introduce a gravitational field in a direction

opposite to the density gradient. The gravitational acceleration is defined as

$$\vec{g} = \frac{m(v_{\parallel}^2 + v^2/2)}{L_C} \hat{e}_x \quad (5.22)$$

where L_C is the curvature scale length and this models the curvature drift of charged particles. We consider the case of a constant centrifugal force only.

The model used for the results in this chapter is the two-and-one-half dimensional (x-y spatial dimension with $v_x - v_y - v_z$ velocity dimension) guiding center electrostatic particle code described in Chapter II. The parity of the eigenmodes we will be considering is the even parity (drift-parity) which is the least heavily damped of the resistive g-modes. In order to include a finite electron-ion collision frequency a Monte-Carlo collision operator, which correctly simulates small-angle collisions and models the Lorentz collision operator, is used. This particular operator gives a Spitzer value for the resistivity ($\nu_{ei} \propto T_e^{-3/2}$).

5.4 Simulation Results (Fast Interchange)

In this section, the simulation results for the fast interchange mode in a sheared magnetic field are

presented. In order to obtain the fast interchange mode growth rate we require $k_y > k_x$ and the interchange term in Eq. (5.15) to be larger than the resistive term. Therefore the parameters used are listed as follows; $L_x \times L_y = 64\delta \times 64\delta$, $T_e/T_i = 1$, $m_e/m_i = .01$, $\omega_{ce}/\omega_{pe} = 10$, $L_s/L_n = 14$, $L_n/L_c = 0.1$, $v_e = 1.4\omega_{pe}\delta$, $a_x = a_y = 1.5\delta$, $\omega_{pe}\Delta t = 2$, $n_0 = 16/\delta^2$ and $k_y\rho_s = 0.13m$, $m = 0, \pm 1, \dots, \pm L_y/2$. The collision frequency is $\nu_{ei}/\omega_* = 20$ and the rational surface is located at $x = 0$. Hence, only modes of even parity with respect to the rational surface are allowed in the system.

Several long wavelength modes were observed to grow exponentially at the fast interchange growth rate, given by Eq. (5.16), and then saturated at a later time. Fig. 5.3 illustrates the measured growth rates as a function of wavenumber. The theoretical values obtained from Eq. (5.16) are also given on the same figure. The electron and ion density profiles are observed to flatten near the mode rational surface and this reduces the gradient in density which drives the instability. The strong shear has a localizing effect on the unstable modes.

In Fig. 5.4 contours of the electrostatic potential at $\omega_{pe}t = 1,600$ are shown. The mode localization

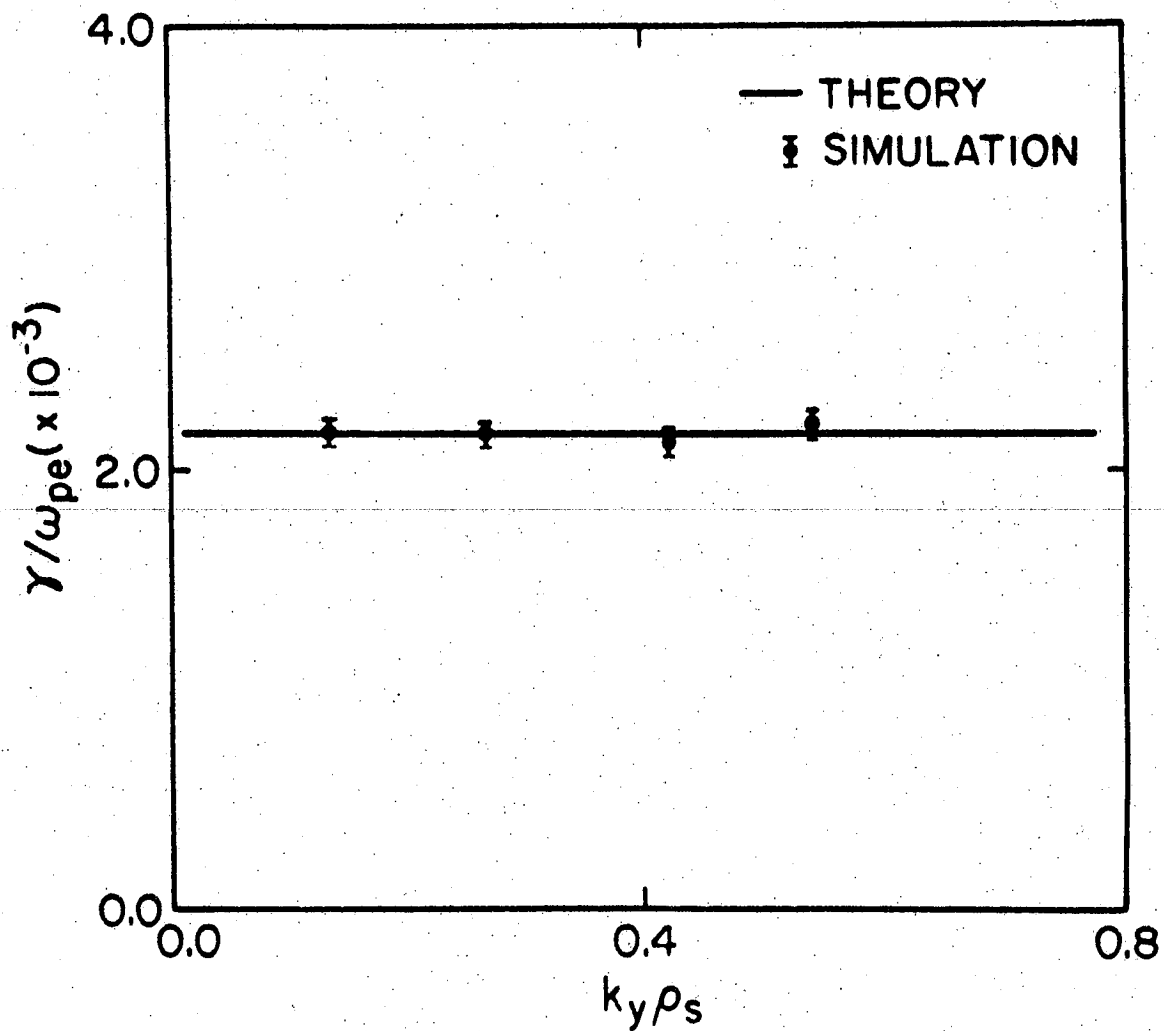


Fig. 5.3. Growth rate versus wavenumber for fast interchange mode case.

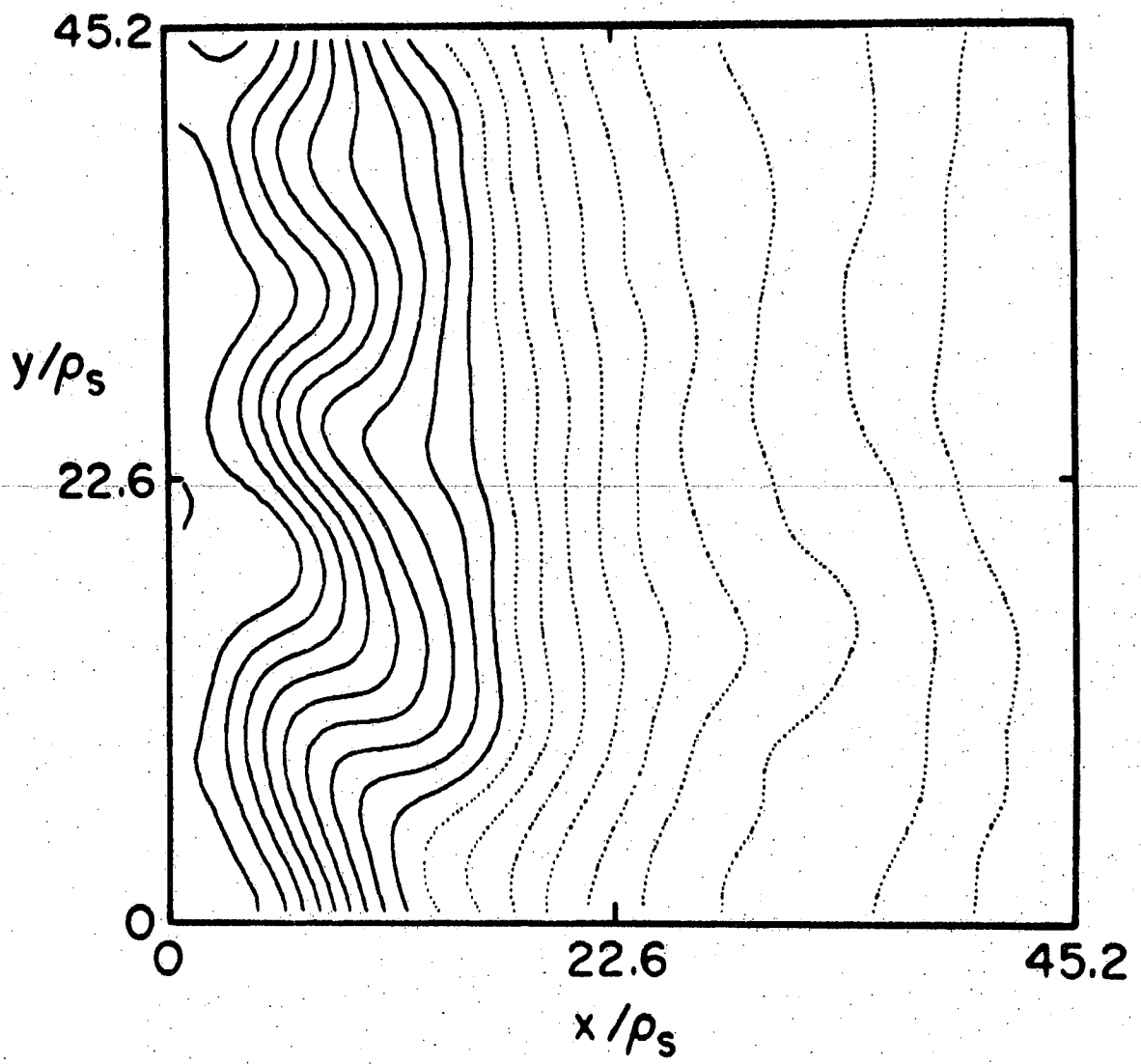


Fig. 5.4. Electrostatic potential contours, $\Phi(x,y)$, taken at $\omega_{pe}t = 1600$, for fast interchange mode case.

is clearly visible, as well as the unstable wavelength, $k_y \rho_s = 0.39$ ($m = 3$). The fluctuation levels of various modes at saturation is illustrated in Fig. 5.5 and $|e\phi/T_e|_{\max} \simeq 0.15$, decreasing slightly for the shorter wavelengths. In this parameter regime the magnetic shear has a negligible effect on the saturation amplitude and growth of the g-mode.

5.5 Simulation Results (Slow Interchange)

The simulation results using the slow interchange mode ordering are presented in this section. The two regimes, $\omega \simeq i\gamma > \omega_*$ and $\gamma < \omega_*$, are examined in detail with regard to the linear growth and saturation levels of the unstable modes.

First, we consider the time evolution of a single mode in a sheared magnetic field and localized about one rational surface. The regime $\gamma \geq \omega_*$ is chosen. In order to satisfy $k_x > k_y$ with $k_x^{-1} \simeq \Delta$, the linear mode width, a system size of $L_x \times L_y = 25.6\rho_s \times 48\rho_s$ was selected with parameters: $T_e/T_i = 1$, $m_e/m_i = 0.01$, $\omega_{ce}/\omega_{pe} = 2$, $L_s/L_n = 28$, $L_n/L_c = 0.01$, $v_e = 0.5\omega_{pe}\delta$, $a_x \times a_y = 1.5\delta \times 1.5\delta$, $\omega_{pe}\Delta t = 2$, $L_n = 7.14\delta$, $k_y\rho_s = 0.12m$

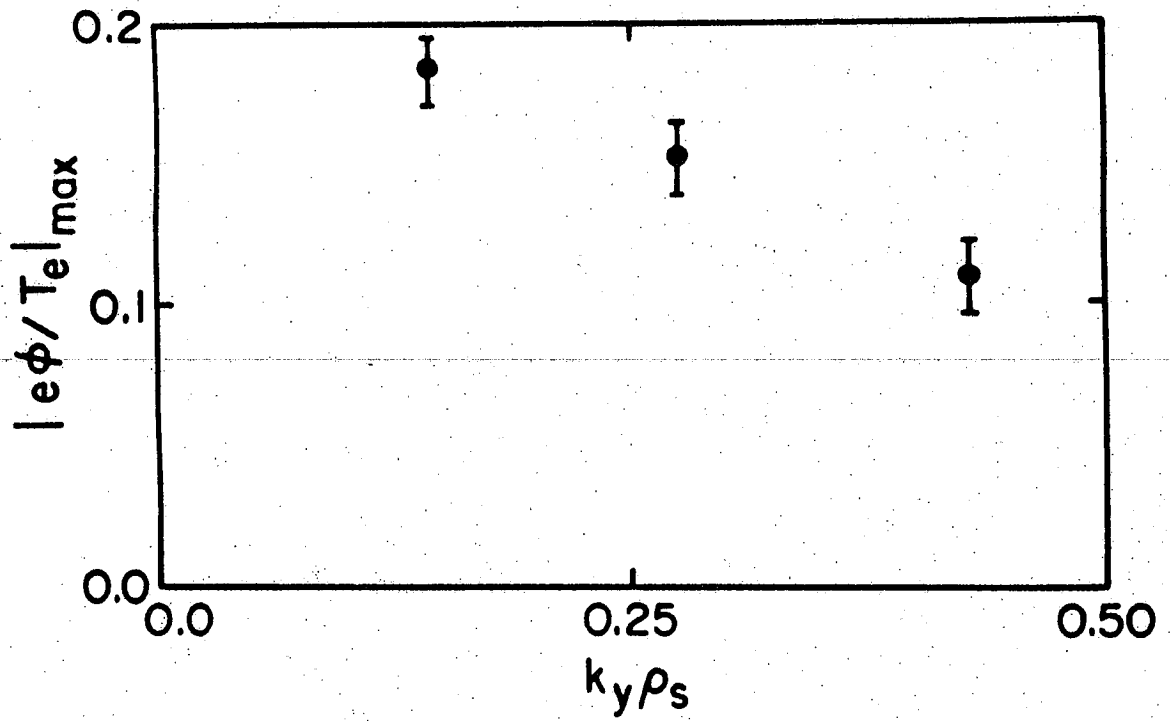


Fig. 5.5. Saturation level versus mode number for fast interchange mode case.

and $\omega_*/\omega_{pe} = 0.00086m$, $m = 0, 1$. The collision frequency is taken to be $v_{ei}/\omega_* = 465$ and the rational surface is located at $x/\rho_s = 12.8$. Using the analytic expression for the linear growth rate and mode width, as well as a numerical evaluation of the eigenmode equation, we find $\gamma/\omega_* = 1.9$ and $\Delta/\rho_s = 7.7$ for the above parameters.

The time evolution of the electrostatic potential for mode $k_y\rho_s = 0.12$ ($m = 1$), averaged over the x-direction, is shown in Fig. 5.6a. The measured growth rate is approximately $\gamma/\omega_* \simeq 2$. Fig. 5.6b illustrates the spatial mode amplitude at various times $\omega_{pe}t = 3,000$, 3,200 and 3,600. The measured mode width at $\omega_{pe}t = 3,000$ is $\Delta/\rho_s \simeq 7.0$ and spreads outward in x at a linear rate with time beyond $\omega_{pe}t = 3,000$. The maximum mode amplitude at saturation is $\langle e\phi/T_e \rangle \simeq 0.6$.

In Fig. 5.7 the time evolution of the contours of constant ion pressure in the x-y plane are shown at $\omega_{pe}t = 3,000$, 3,200 and 3,600. From this figure it is evident that there is a convection of pressure centered around the rational surface. The scale size for convection, in the x-direction, is on the order of the linear eigenmode width. The details of the saturation process and quantitative comparisons between simulation and theory will be given in the next section.

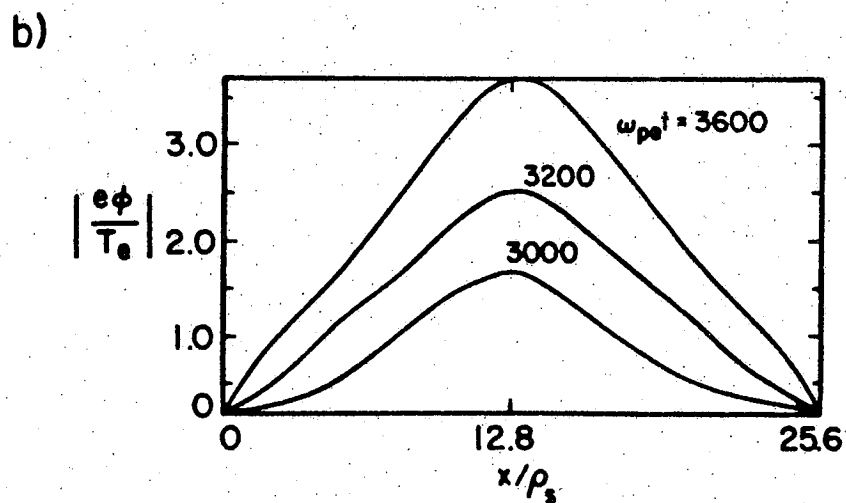
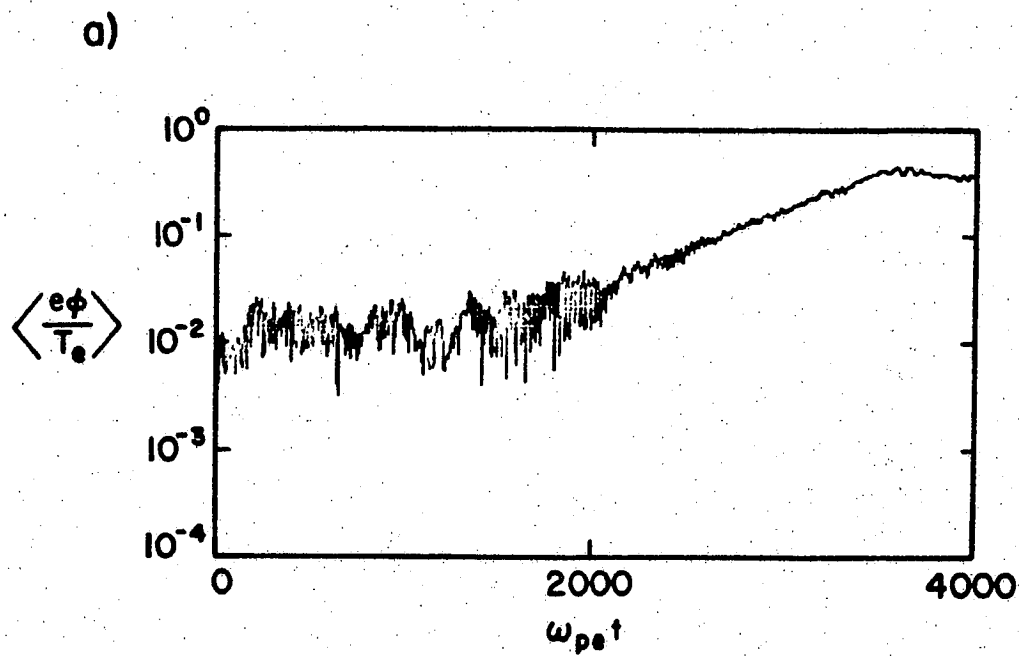


Fig. 5.6. (a) Spatially-averaged mode amplitude versus time for $k_{y\rho_s} = 0.12$, (b) Spatial amplitude of mode $k_{y\rho_s} = 0.12$ versus time.

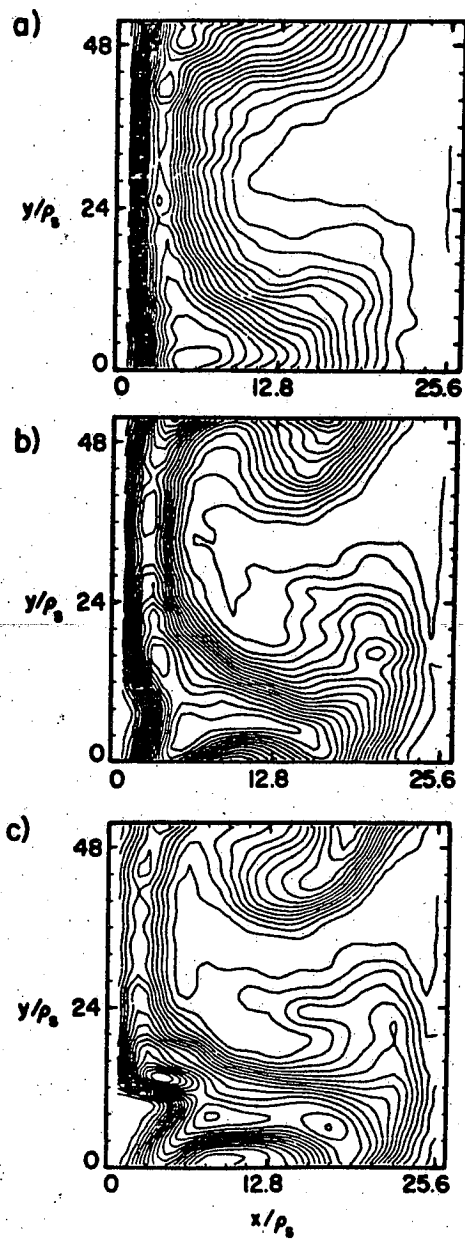


Fig. 5.7. Contours of constant ion pressure taken at time steps (a) $\omega_{pet} = 3000$, (b) $\omega_{pet} = 3200$ and (c) $\omega_{pet} = 3600$.

To verify the growth rate scaling with resistivity for the slow interchange mode several simulations were performed keeping the above parameters fixed and varying the resistivity. The results are given in Fig. 5.8 where the theoretical and measured growth rates are plotted versus resistivity to the one-third power. By lowering the resistivity to $v_{ei}/\omega_* = 50$ and changing $v_e/\omega_{pe} \delta$ from 0.5 to 1.75 the linear growth rate becomes $\gamma/\omega_* = 0.2$ and mode width $\Delta/\rho_s = 3.2$. Fig. 5.9 shows the time evolution of the potential contours with the $k_y \rho_s = 0.25$ ($m = 1$) mode clearly visible. The rational surface is at $x/\rho_s = 3.2$. The nonlinear evolution of the mode proceeds just as in the previous case.

The main difference lies in the finite diamagnetic drift of the mode in the y -direction as it spreads in the x -direction. The spreading in x is due to the equilibrium modification of the density profile as a result of instability.

Next, the spectrum of unstable modes is increased from $k_y \rho_s = 0.12$ to $0.12 \lesssim k_y \rho_s \lesssim 1.56$, keeping the parameters for the $\gamma \gtrsim \omega_*$ regime. Fig. 5.10a illustrates the spatially-averaged mode amplitude as a function of time. Each mode grows at the predicted linear

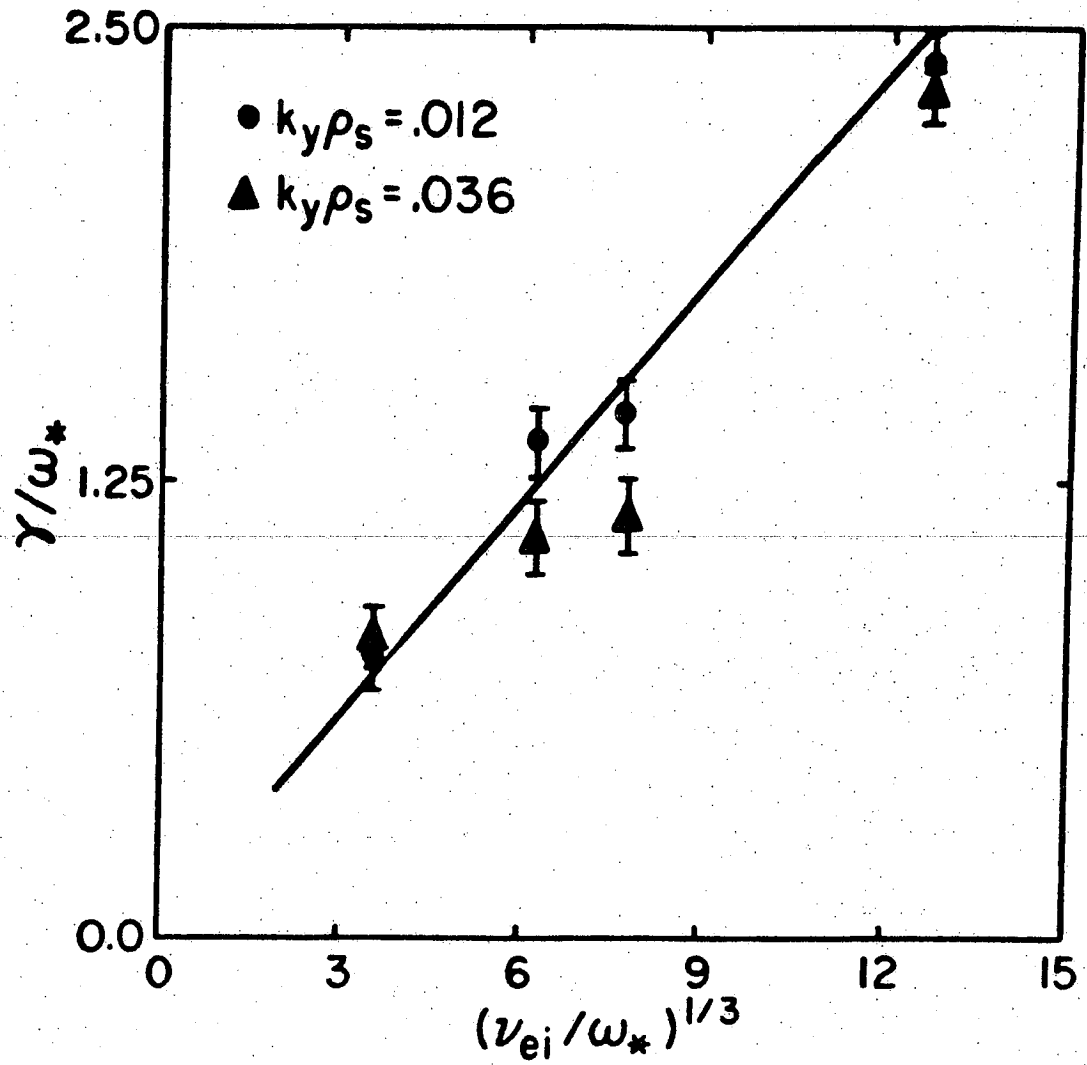


Fig. 5.8. Growth rate versus resistivity for different mode numbers in the slow interchange case.

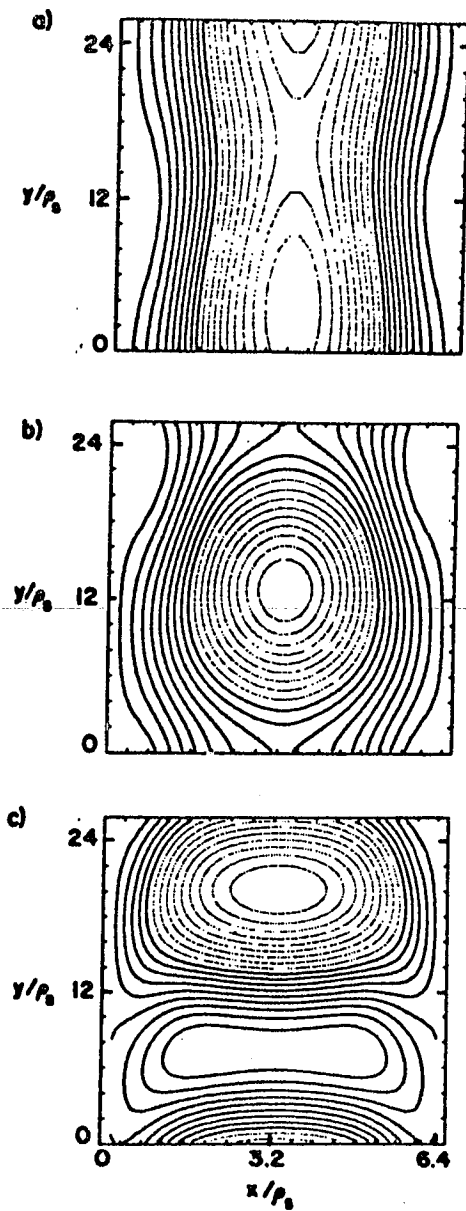


Fig. 5.9. Electrostatic potential contours taken at (a) $\omega_{pe}t = 1000$, (b) $\omega_{pe}t = 1500$ and (c) $\omega_{pe}t = 2000$ for the $\omega_* \geq \gamma$ regime.

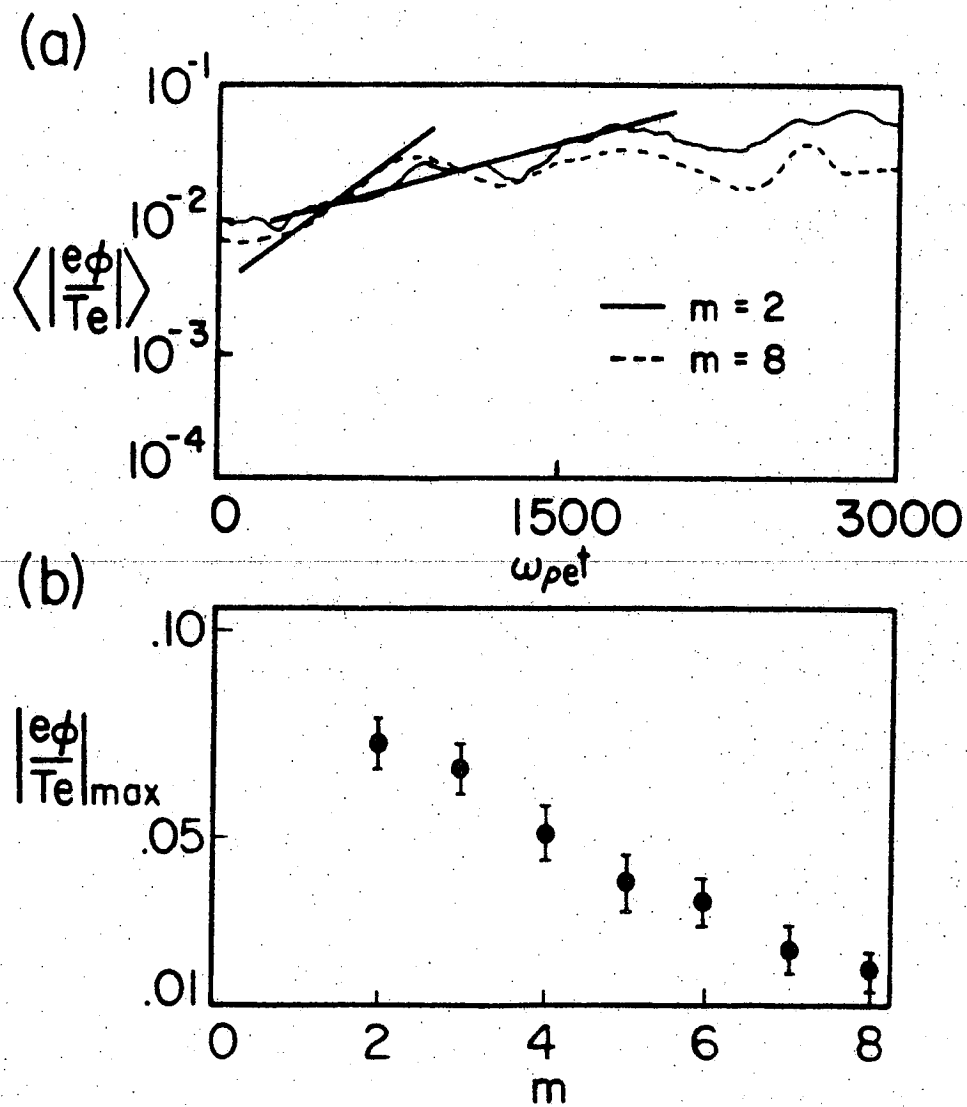


Fig. 5.10. (a) Spatially-averaged mode amplitude versus time for two different modes. (b) Saturation amplitude as function of mode number for the slow interchange case.

growth rate and in Fig. 5.10b the saturation level versus mode number is plotted. The saturation level of the potential fluctuations scale with mode number approximately as $|\phi| \sim m^{2/3}$.

The contours of constant ion pressure at time steps $\omega_{pe}t = 600, 1,000, \text{ and } 2,600$ are given in Fig. 5.11. The small scale fluctuations grow the fastest and at later times the longest wavelength, $k_y \rho_s = 0.12$ ($m = 1$), mode dominates. From the contours of ion pressure at time step $\omega_{pe}t = 2,600$ it can be seen that the long wavelengths convect the short wavelength perturbations a distance comparable to the width of the $m = 1$ eigenmode. A discussion of this mixing process and an estimation of the saturation levels will be given in the next section.

5.6 Saturation of Resistive G-Modes

In this section we discuss the saturation mechanism of the resistive g-modes and compare theoretically predicted values with the simulation results. Two mechanisms for saturation have been proposed. The first is compressional stabilization which has been discussed by Manheimer.¹¹⁴ The idea is that the energy released by the unstable plasma ceases to drive unstable modes and

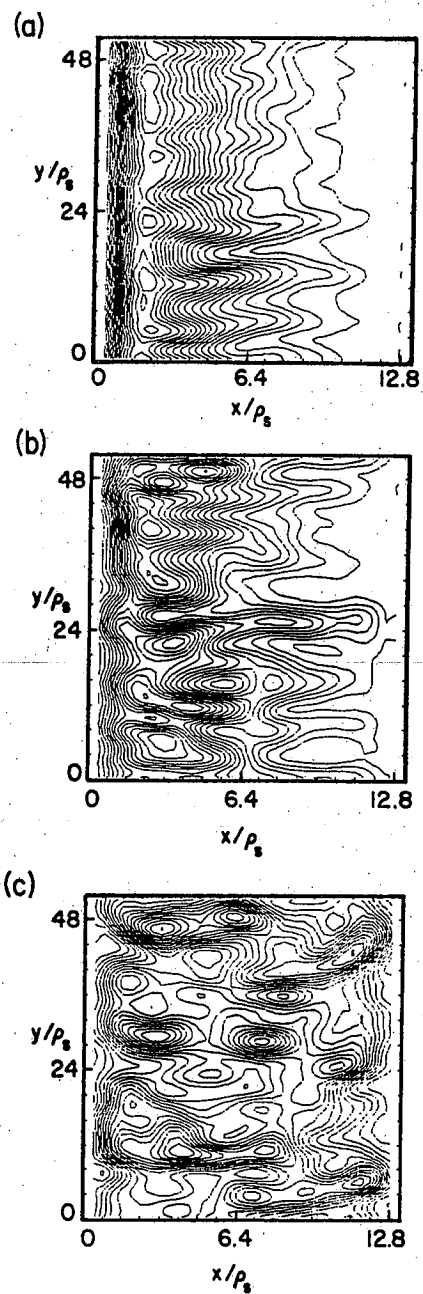


Fig. 5.11. Contours of constant ion pressure taken at (a) $\omega_{pe} t = 600$, (b) $\omega_{pe} t = 1000$ and (c) $\omega_{pe} t = 2600$.

begins to compress the plasma. The resulting saturation level is obtained by balancing the gravitational energy density and compressional energy of a displaced fluid element. This mechanism would predict higher saturation levels than is observed because it ignores the damping due to resistive line bending. Previous simulation work has shown compressional effects have a small stabilizing influence on the interchange mode.¹¹⁵

The second mechanism of saturation is by convective mixing of pressure or density. This saturation process has been proposed by Carreras et al.¹¹⁶ for resistive ballooning modes. A similar method has been applied to rippling modes where resistivity, rather than pressure, is convected.¹¹⁷ An estimate of the saturation level can be made by considering a simple model equation for the convection process,

$$\frac{\partial n}{\partial t} + \tilde{v} \cdot \tilde{\nabla} n = 0 \quad (5.23)$$

where $\tilde{v} = \tilde{E} \times \tilde{B} / B^2$. Letting $n = \langle n \rangle + \hat{n}$ and $\tilde{v} = \langle \tilde{v} \rangle + \hat{v}$ we obtain an equation for the perturbed density

$$\frac{\partial}{\partial t} (\langle n \rangle + \hat{n}) + \hat{v} \cdot \tilde{\nabla} (\langle n \rangle + \hat{n}) = 0 \quad (5.24)$$

under the assumption that no equilibrium flow is present,

$\langle \hat{v} \rangle = 0$. Using

$$\frac{\partial \langle n \rangle}{\partial t} = - \langle \hat{v} \cdot \nabla \hat{n} \rangle \quad (5.25)$$

we can subtract Eq. (5.25) from Eq. (5.24) to give

$$\frac{\partial \hat{n}}{\partial t} + \hat{v} \cdot \nabla \langle n \rangle = - \hat{v} \cdot \hat{n} + \langle \hat{v} \cdot \nabla \hat{n} \rangle \quad (5.26)$$

The first term on the right hand side of Eq. (5.26) represents the nonlinear convection term while the second term represents the background density modification effects on the perturbed density. If we substitute Eq. (5.26) into Eq. (5.24) and neglect the right hand side of Eq. (5.26) to lowest order we obtain

$$\frac{\partial \langle n \rangle}{\partial t} = \frac{\partial}{\partial x} \left[\gamma |\xi_x|^2 \frac{\partial \langle n \rangle}{\partial x} \right] \quad (5.27)$$

where $\partial/\partial t \rightarrow \gamma$, $|\hat{v}_x|^2 = |\xi_x|^2 \gamma^2$ and $k_x > k_y$. From this relation we note that the growth of fluctuations can give rise to a quasi-linear evolution of ensemble average quantities.

If we substitute this result into Eq. (5.26) and neglect the nonlinear term, the equation for the

perturbed density becomes

$$\frac{\partial \hat{n}}{\partial t} + \hat{v}_x \frac{\partial \langle n \rangle}{\partial x} = \frac{-\partial}{\partial x} \left[\gamma |\hat{\xi}_i|^2 \frac{\partial \langle n \rangle}{\partial x} \right] \quad (5.28)$$

or

$$\hat{n} = -|\hat{\xi}_x| \left[1 - \frac{\partial^2 |\hat{\xi}_x|^2}{\partial x^2} \right] \frac{\partial \langle n \rangle}{\partial x} \quad (5.29)$$

The perturbed density response vanishes when $\partial^2 |\hat{\xi}_x|^2 / x^2 \rightarrow 1$ or $k_x^2 |\hat{\xi}_x|^2 \simeq 1$. Using $k_x^{-1} \simeq \Delta_k$, where Δ_k is the eigenmode width, the saturation level is given by

$$|\hat{\xi}_x| \simeq \Delta_k \quad (5.30)$$

Physically, the saturation occurs when the density fluctuation is displaced or convected a distance comparable to the width of the eigenmode in one growth time.

The displacement or convection occurs mainly by $\underline{E} \times \underline{B}$ motion and approximating the velocity perturbation by $\hat{v}_x \simeq \gamma \hat{\xi}_x$, where γ is the linear growth rate, the fluctuation level of the unstable modes at saturation is

$$\frac{e \hat{\phi}_k}{T_e} \simeq \frac{\gamma \Delta_k e B}{k_y T_e} \quad (5.31)$$

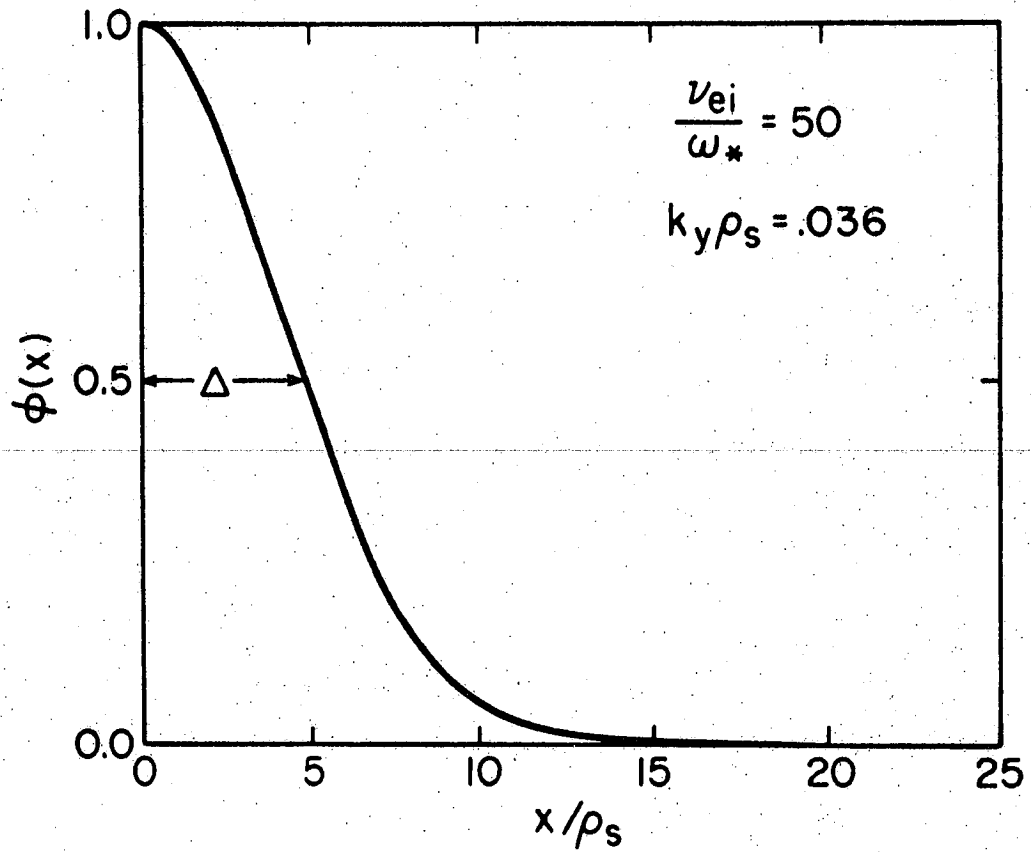


Fig. 5.12. Localized wavefunction obtained from solution to eigenmode equation. Δ refers to mode width.

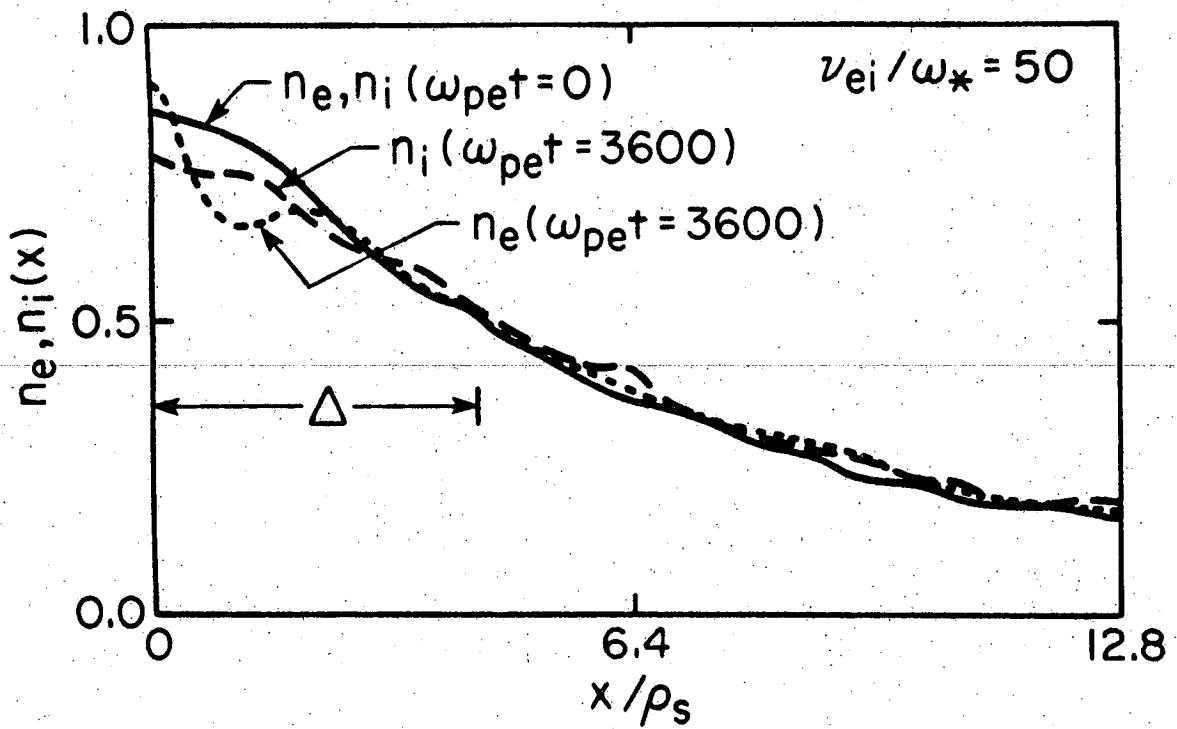


Fig. 5.13. Electron and ion density profiles shown at different times. Also, the mode width, Δ , is indicated on the same figure.

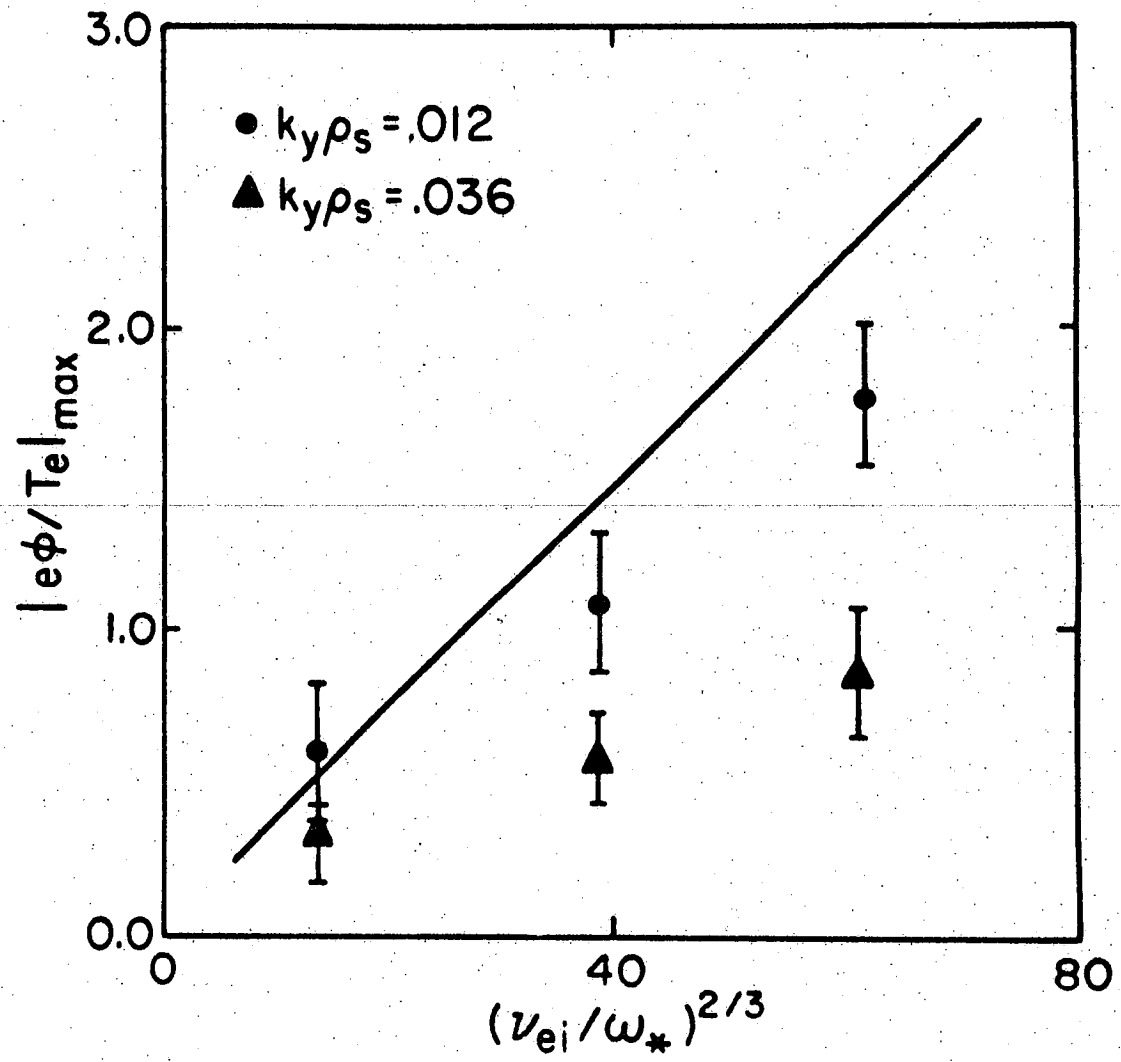


Fig. 5.14. Saturation amplitude versus resistivity for different mode numbers in the slow interchange case.

In conclusion, the physical picture of pressure mixing over the eigenmode widths provides an adequate picture of saturation in the single rational surface case. In the multiple rational surface model this picture changes because overlapping eigenmodes, closely spaced, can maintain the profile (source). The nonlinear convection terms of Eq. (5.26) can therefore play a role in determining the saturation levels.

C H A P T E R V I

THREE DIMENSIONAL PARTICLE SIMULATION OF THE RESISTIVE G-MODE IN A SHEARED MAGNETIC FIELD

6.1 Introduction

The results of the previous chapter concerning the linear and nonlinear evolution of the resistive g-mode localized about a single mode rational surface do not provide a viable basic model for anomalous transport in devices such as the RFP. The reason is that rational surfaces exist throughout the RFP and unstable modes overlap for very low fluctuation levels. Therefore, a more physically realistic model of the resistive g-mode is a configuration with many overlapping, interacting g-modes localized about different mode rational surfaces. In this chapter a nonlinear theory of the g-mode is constructed using computational and analytic methods. The following questions are addressed:

- (1) What is a reasonably accurate theory of turbulence driven by pressure gradients via mechanisms such as the resistive g-mode?

- (2) What are the principal nonlinear effects?
- (3) What is the spectrum of the resistive g-mode turbulence at saturation?

One can study the linear theory of the g-mode more accurately, modelling the geometry realistically with many kinetic effects included, hoping stable parameter regimes emerge. In this chapter an alternate approach is taken. We choose to examine the saturated state of the plasma, since it must in fact be observed while in this state and exhibits anomalous transport.

Since the resistive g-mode can be described within a fluid framework there are several reasons it is simpler to analyze than a microinstability such as the drift wave. First, the electron response is primarily hydrodynamic. Second, the resistive g-mode is a consequence of an imbalance of forces whereas the drift wave is a consequence of the introduction of inverse dissipation (Landau damping) into a marginally stable oscillation. Finally, the g-mode is dominantly electrostatic, and a description of the physics of pressure gradient-driven modes in the presence of multiple rational surfaces is simplified. The results may be of more general interest in the sense that the nonlinear evolution of

other dynamical systems may exhibit features similar to those discussed here.

In this chapter the simulation configuration and parameters used are presented. The results and interpretation for the regime where the growth rate is larger than the diamagnetic drift frequency are discussed. A theory for the saturation of the g-mode in the multiple rational surface case is outlined. The kinetic energy and pressure spectrum at saturation is compared with the nonlinear theory.

6.2 Simulation Configuration and Parameters

The model used in the previous chapter to study the g-mode localized about a single rational surface is extended to three dimensions and is shown in Fig. 6.1. The rational surface location and packing is varied by adjusting the shear strength, system length and mode numbers (m, n) . From the condition $k_{\parallel} = 0$, the rational surfaces are located at

$$x_{mn} = x_0 \pm \frac{n}{m} \left[\frac{L_s L_y}{L_z} \right] \quad (6.1)$$

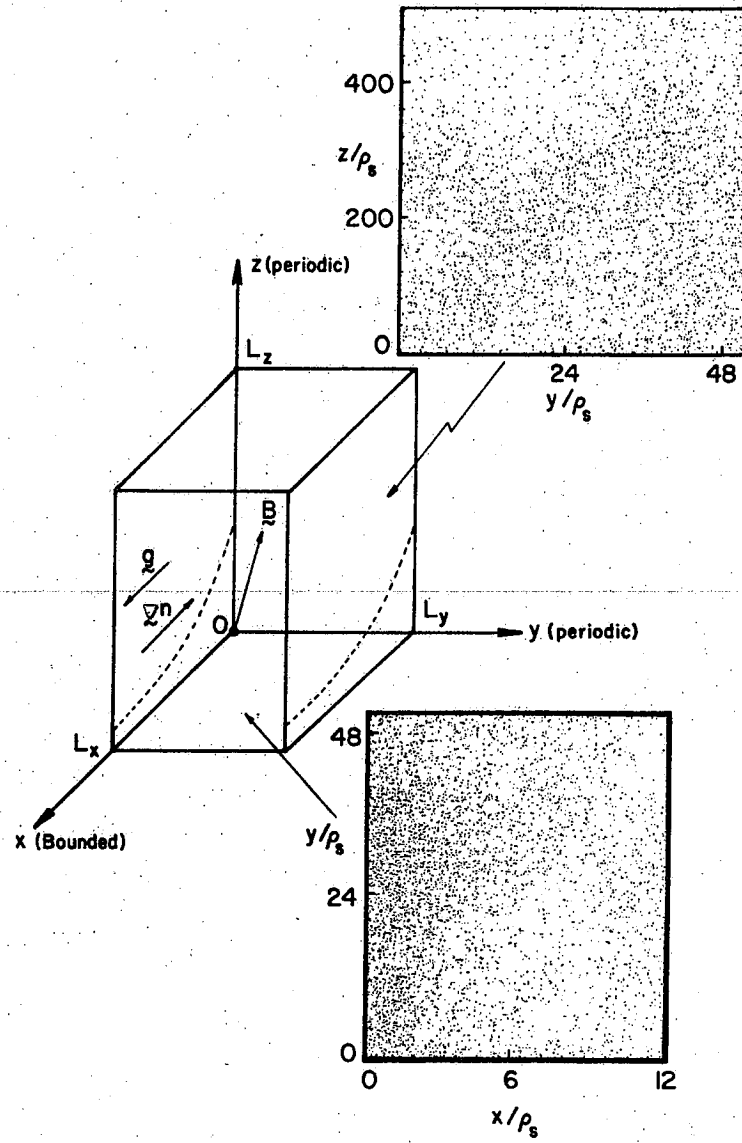


Fig. 6.1. Initial particle simulation configuration.

Typical parameters used are: $L_x \times L_y \times L_z = 32\Delta \times 128\Delta \times 1280\Delta$, particle size $a_x = 1.5\Delta$, $a_y = 1.5\Delta$, $a_z = 32\Delta$, $T_e/T_i = 1$, $m_i/m_e = 100$, $L_s/L_n = 28$, $L_n/L_c = 0.01$, $v_e/\omega_{pe}\Delta = 0.5$, $\omega_{ce}/\omega_{pe} = 2$, $\omega_*/\omega_{ci} = 0.043m$, $n_0 = 15$ particles/cell, $k_y\rho_s = 0.12m$, $m = 0, \pm 1, \dots, \pm 64$, $n = 0, \pm 1, \dots, \pm 8$, $\omega_{pe}\Delta t = 2$ and $v_{ei}/\omega_* = 465$. The rational surfaces are located at

$$x_{mn}/\rho_s = 6.4 \pm 8(n/m)$$

and Fig. 6.2 shows the position of each surface for a given (m,n) . The initial density profile is superimposed on the figure. The surfaces are more densely packed near $x_0/\rho_s = 6.4$ because more modes are retained in the y-direction than in the z-direction. The significance of arranging the rational surfaces in this pattern is that it ensures localized density profile flattening does not play a dominant role in the evolution of unstable modes.

The mode width is determined to be $\Delta_m = 7.7\rho_s m^{-1/3}$ from linear theory. This implies that there are approximately nineteen grid points to describe the low mode number eigenmodes ($m = 1$) and eight grid points

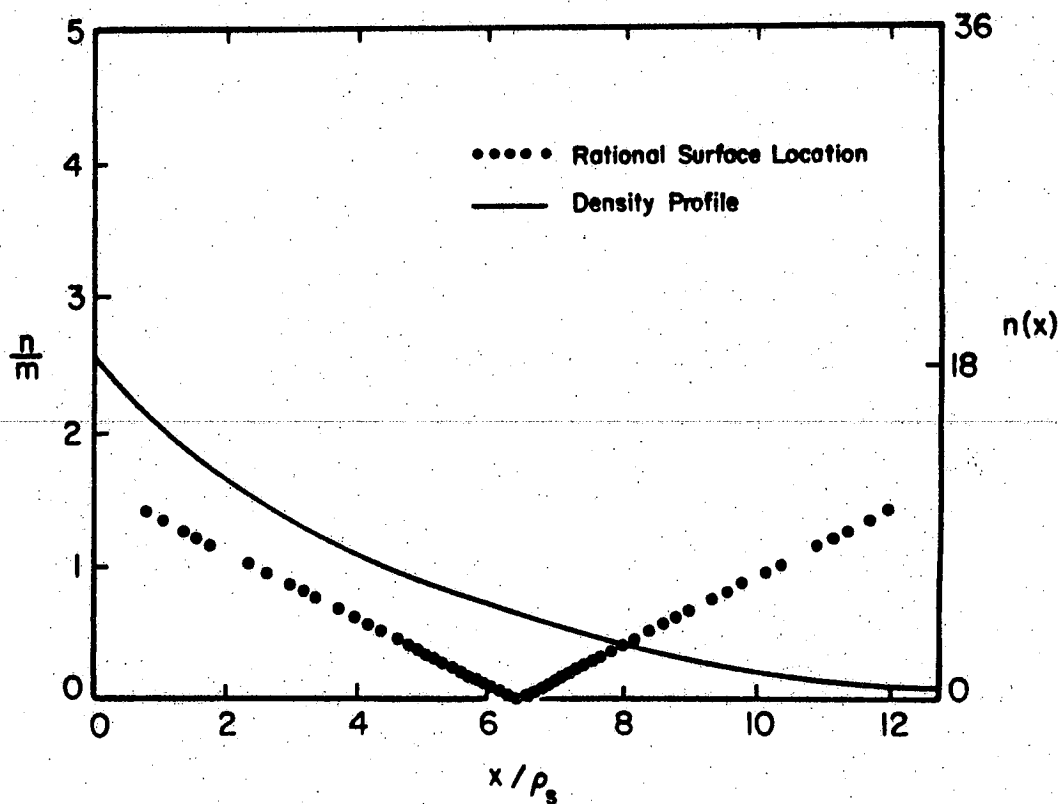


Fig. 6.2. Rational surface positions for each mode number (m,n) with density profile superimposed.

for the high mode numbers ($m = 10$). The finite particle size cutoff, $k_y a_y \simeq 1$, limits the highest mode number to be $m \simeq 16$. Since the mode widths are broad compared to the rational surface spacing there is strong overlap and eigenmode interaction at low fluctuation levels.

6.3 Simulation Results and Interpretation

The main emphasis of the presentation of the simulation results is the comparison between single and multiple rational surface configurations. The density profile evolution, mode energies and eigenmode structure are some of the diagnostics used to illustrate the differences.

For the parameters given in the previous section, the three dimensional simulation has been carried out from $\omega_{ci}t = 0$ to $\omega_{ci}t = 20$. Fig. 6.3 shows the time evolution of the electrostatic potential for different mode numbers (m,n) . Fig. 6.3a is a longer wavelength mode and Fig. 6.3b illustrates the shorter wavelength mode evolution. We note here that spatial averaging in the x-direction is done. Using a numerical solution to the eigenmode equation (5.15) the linear growth rates are

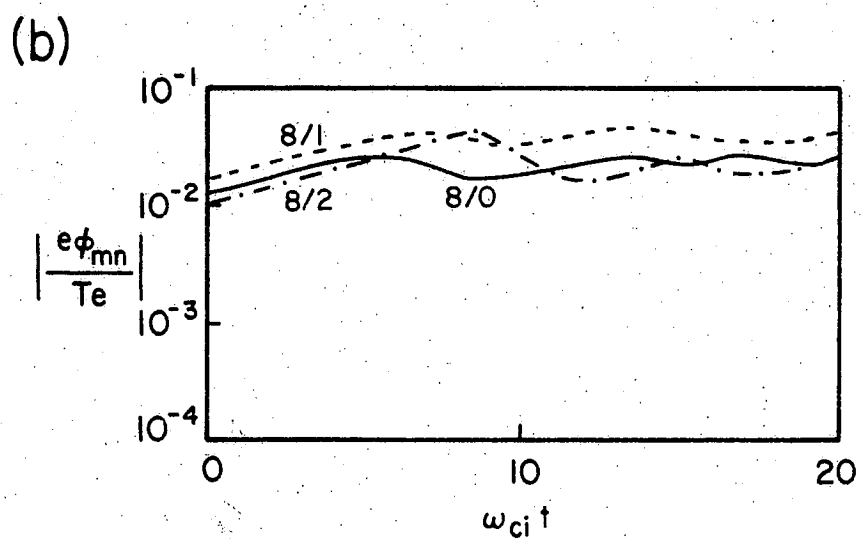
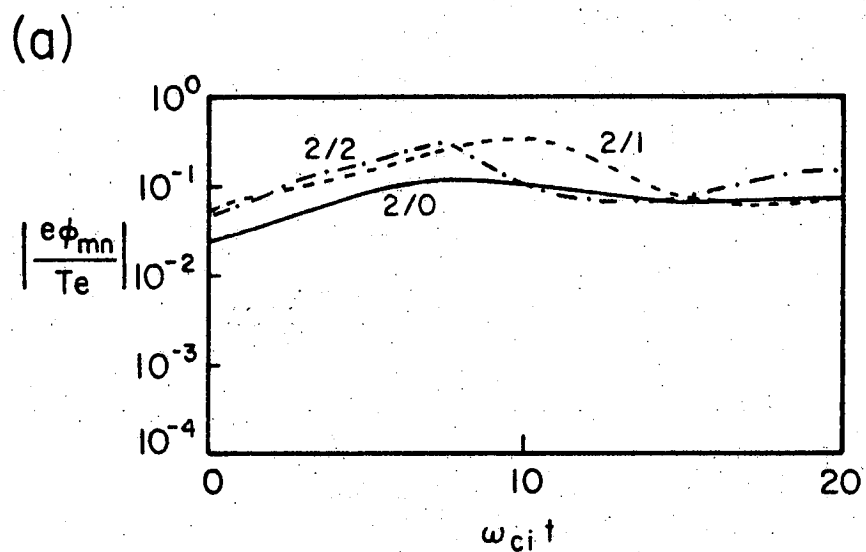
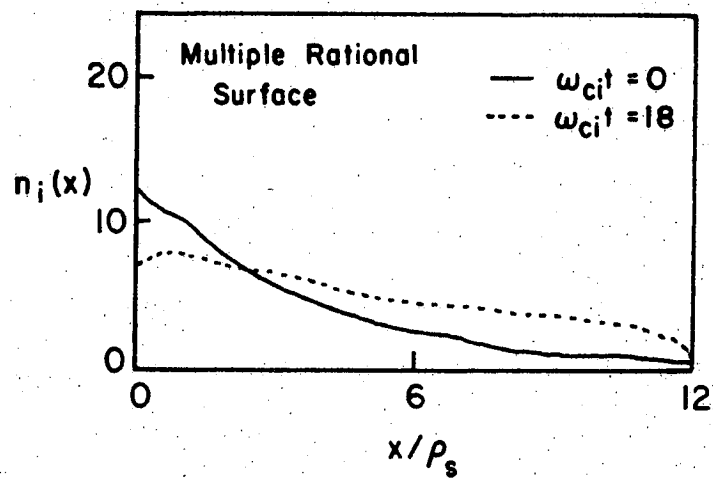


Fig. 6.3. Time evolution of modes (a) (2,n) and (b) (8,n), spatially-averaged.

observed in Fig. 6.3. The regime $\gamma \simeq \omega_*$ is considered, with the previously specified simulation parameters. Therefore, the linear growth rate dependence with wave-number is weak.

In Fig. 6.4 a comparison of the time evolution of the ion density profiles for the single and multiple rational surface configurations is made. The initial profile at $\omega_{ci}t = 0$ and the profile taken at $\omega_{ci}t = 18$, when the $m = 3$ mode saturates, is shown. Fig. 6.4b indicates that local density profile flattening over the width of the eigenmode occurs. This saturates the instability. Fig. 6.4a reveals that there is little evidence of localized profile flattening, however, a slight overall density profile change does occur. We note that the density gradient still exists at the time the long wavelength modes saturate. This can be seen in Fig. 6.5 where the spatially-averaged density is plotted versus time. The linear growth is indicated and the saturation occurs at $\omega_{ci}t = 8$ for the $m = 3$ mode and $\omega_{ci}t = 4$ for the $m = 9$ mode. There is a rise in the fluctuation amplitude of the shorter wavelength mode after the $m = 3$ mode has saturated. A theory for this saturation process is given in the next section.

(a)



(b)

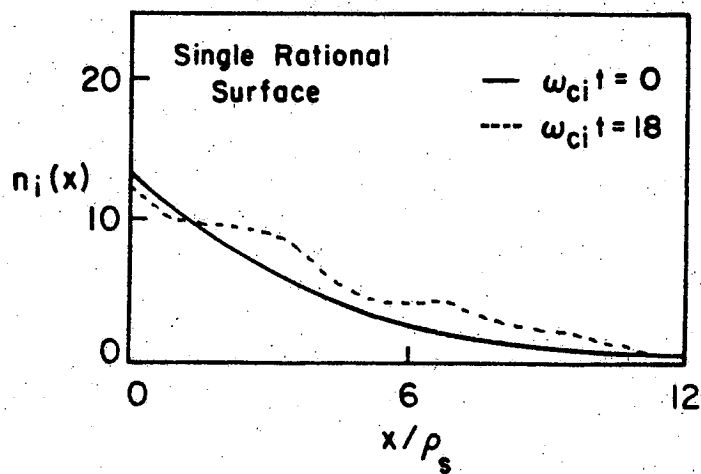
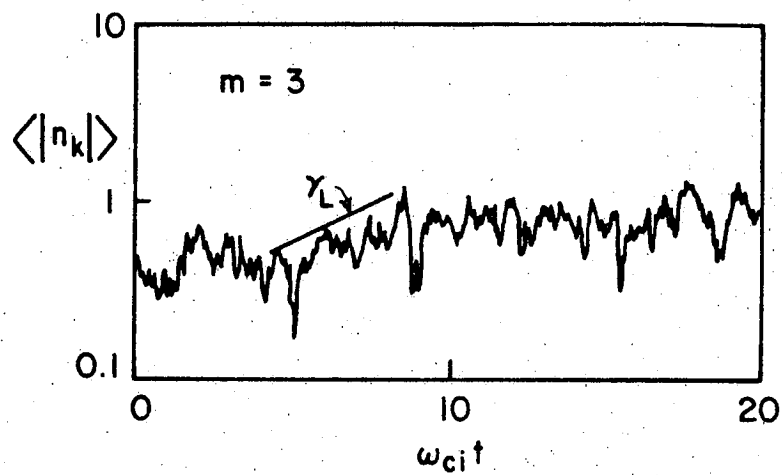


Fig. 6.4. Comparison between ion density profile evolution in (a) multiple rational surface and (b) single rational surface configurations.

(a)



(b)

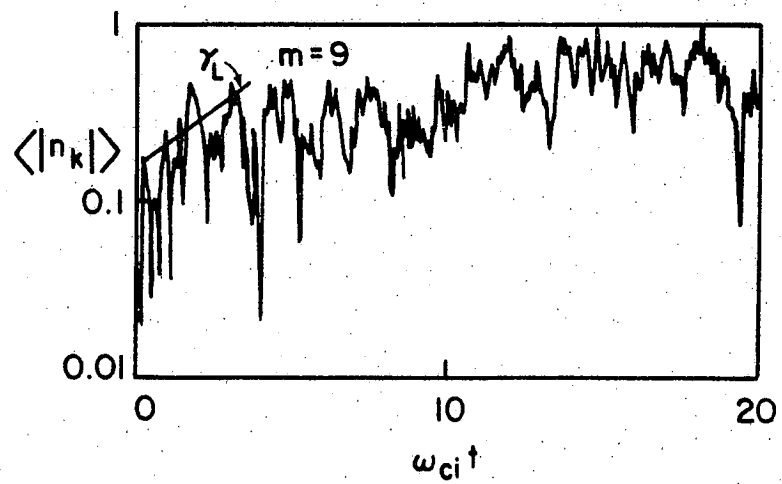


Fig. 6.5. Spatially averaged density evolution for (a) $m = 3$ mode and (b) $m = 9$ mode. γ_L refers to the linear growth rate of the mode number.

In order to further in the density profile, the spatial variation of test modes is considered. Fig. 6.6 shows the potential variation as a function of x at $\omega_{ci}t = 12$ and $\omega_{ci}t = 18$ for the (a) multiple and (b) single rational surface configuration. Fig. 6.6b indicates that spreading of the mode width, linearly in time, occurs as a result of the quasi-linear flattening process. In Fig. 6.6a the mode width shows little difference from its previous value. This implies that quasi-linear flattening of the density profile has no significant effect on the evolution of the test modes.

One other interesting result is the particle positions in the y - z plane shown in Fig. 6.7. Time steps $\omega_{ci}t = 0, 12$ and 18 were chosen. In the saturation phase one can observe local regions of enhanced particle density which persist until the end of the simulation run. The scale size of the regions corresponds to that of the dominant density fluctuation present at the particular time step.

6.4 Nonlinear Theory of the G-Mode

The physical picture and analytical model of saturation, given in the previous chapter, is inadequate

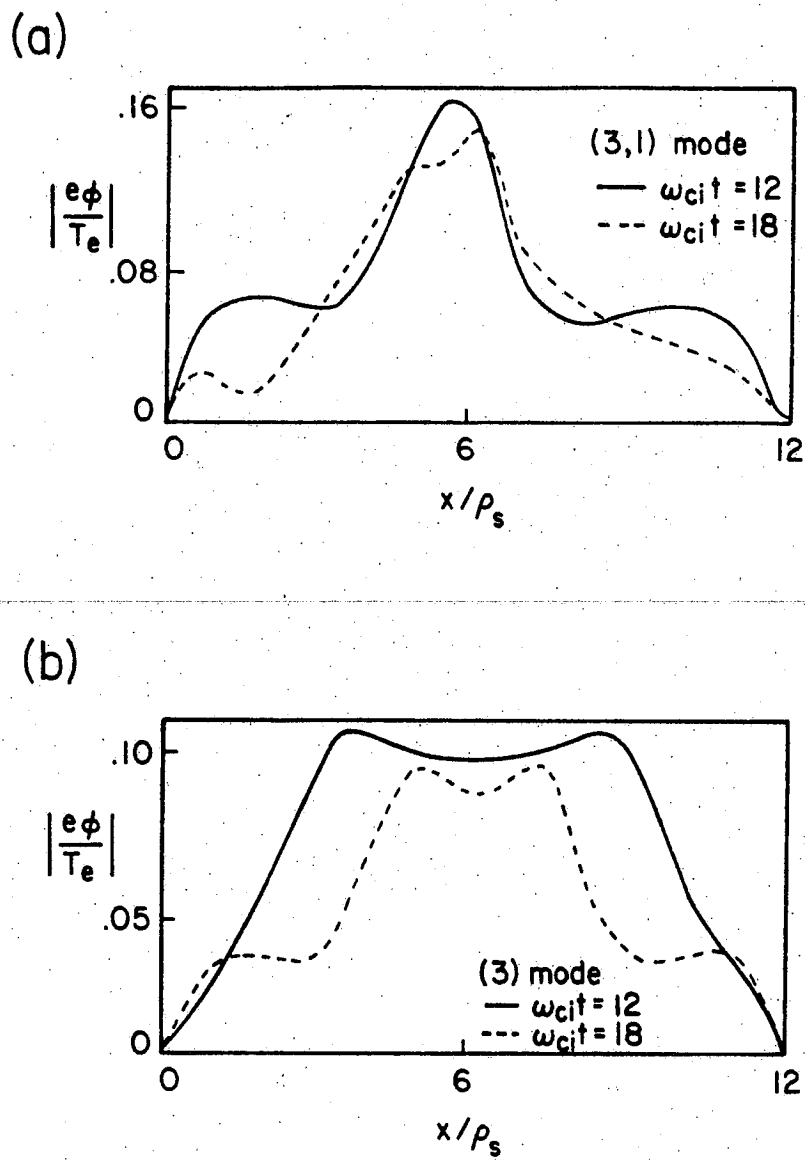


Fig. 6.6. Comparison between spatial mode evolution in (a) multiple rational surface and (b) single rational surface configurations.

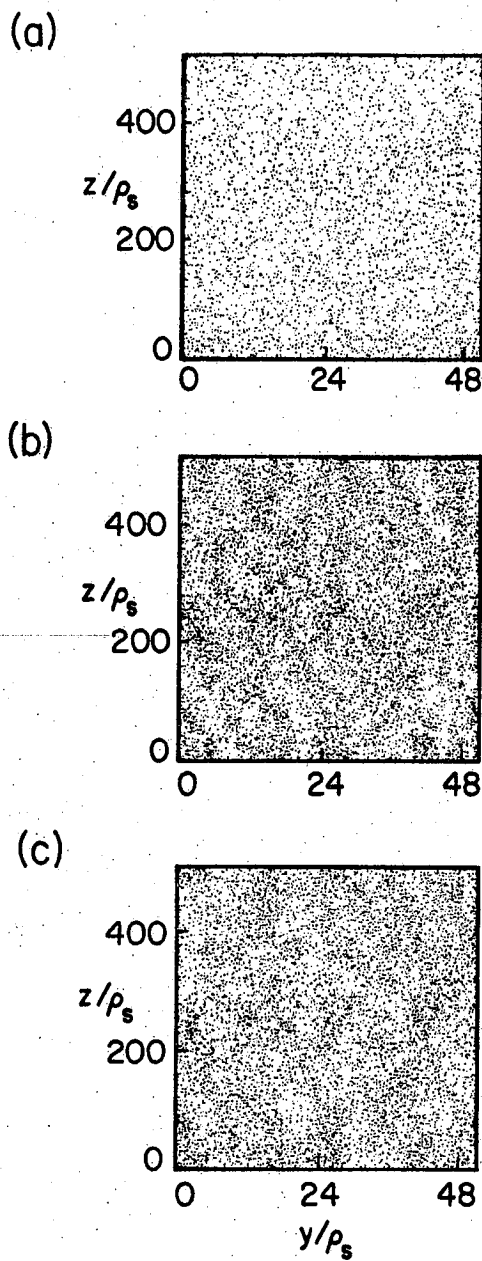


Fig. 6.7. Particle positions in y - z plane taken at (a) $\omega_{ci}t = 0$, (b) $\omega_{ci}t = 18$ and (c) $\omega_{ci}t = 20$.

for a description of the multiple rational surface case. The localized density profile evolution over the eigenmode width no longer is the dominant effect¹¹⁸ because a parcel of density convected a distance comparable to the eigenmode width exhibits a complex motion due to the presence of neighboring eigenmodes. The diffusion coefficient for turbulent convection must be evaluated so that it is consistent with the density profile evolution.

It is observed that the kinetic energy and density profile evolution exhibit differences in the saturated state. Since the mode width is a function of the linear growth rate the meaning of the mixing length estimate of saturation for the density, $\hat{n}_k/n_0 \simeq \Delta_k/L_n$, from the previous chapter, is unclear since $\gamma \rightarrow 0$. In this section a more precise understanding of the spatial (mixing length) and temporal (correlation time) scales at saturation is given. Comparisons with the simulation results of the previous section are made.

The nonlinear dynamics of resistive g-modes can be investigated using the electrostatic convection model based on the incompressible reduced MHD equations. With the addition of the equation for vorticity,

$\tilde{\nabla} \times \tilde{\mathbf{v}} = \tilde{\nabla}_\perp^2 \phi / B \hat{\mathbf{z}}$, to the density convection Eq. (5.23) it follows the basic equations are¹¹⁹

$$\frac{\partial n}{\partial t} + \frac{\tilde{\nabla} \phi \times \hat{\mathbf{z}}}{B} \cdot \tilde{\nabla}_\perp n = - \frac{\tilde{\nabla}_y \phi}{B} \frac{\partial \langle n \rangle}{\partial x} \quad (6.2a)$$

$$\begin{aligned} \frac{n_0}{B \omega_{ci}} \left[\frac{\partial}{\partial t} \tilde{\nabla}_\perp^2 \phi + \frac{\tilde{\nabla} \phi \times \hat{\mathbf{z}}}{B} \cdot \tilde{\nabla} \tilde{\nabla}_\perp^2 \phi \right] \\ = \frac{-1}{|\mathbf{e}| \eta} \tilde{\nabla}_\parallel^2 \phi - \kappa \tilde{\nabla}_y n \end{aligned} \quad (6.2b)$$

Here n is the perturbed density, ϕ the perturbed potential or velocity stream function and $\kappa \equiv g/\omega_{ci}$ is the curvature driving term. Linearizing the equations and solving the eigenmode equation in the limit $k_x \gg k_y$ gives the growth rate $\gamma = \eta^{1/3} (\kappa \partial \langle n \rangle / \partial x)^{2/3} (k_y L_S)^{2/3}$ and mode width $\Delta = \eta^{1/3} (\kappa \partial \langle n \rangle / \partial x)^{1/6} k_y^{-1/3} L_S^{2/3}$. This is the same result obtained in the previous chapter for the slow interchange mode in the $\gamma > \omega_*$ regime.

We consider the nonlinear evolution of the linearly unstable modes as part of a spectrum of multiple helicity (rational surface) turbulence in a sheared magnetic field. A set of renormalized equations for n_k and $\tilde{\nabla}_\perp^2 \phi_k$ which govern the evolution of the test modes can be written as:^{120, 121}

$$\frac{\partial n_k}{\partial t} - \frac{\partial}{\partial x} \left[D \frac{\partial n_k}{\partial x} \right] = - \frac{ik_y}{B} \frac{\partial \langle n \rangle}{\partial x} \phi_k \quad (6.3a)$$

$$\begin{aligned} \frac{\partial}{\partial t} (\nabla_{\perp}^2 \phi)_k - \frac{\partial}{\partial x} \left[D \frac{\partial}{\partial x} (\nabla_{\perp}^2 \phi)_k \right] + k_y^2 C_k \phi_k \\ = \frac{B\omega_{ci}}{|e|n_0} \frac{k_{\parallel}^2}{\eta} \phi_k - ik_y k_y \frac{n_k}{n_0} \end{aligned} \quad (6.3b)$$

where $k = (k_y, k_z)$. The turbulence diffusion coefficient is $D = \sum_{k'} k_y'^2 |\phi_{k'}|^2 / B^2 \Delta\omega_{k+k'}$, and the term $C_k = \sum_{k'} \langle (\nabla_{\perp}^2 \phi)^2 \rangle_{k'} / \Delta\omega_{k+k'}$, is a consequence of symmetrization which ensures that energy conservation is preserved in the renormalized theory.

Physically, the random convection of density by the turbulent fluctuations appears as a density diffusivity and the same D accounts for vorticity diffusion. From Eq. (6.3a) the diffusion coefficient, D , and non-linear mixing length in the saturated state ($\partial/\partial t \rightarrow 0$) can be obtained.

Since the saturation is dynamic the level can be obtained by a balance between the linear driving terms and terms which serve as an energy sink. This is more transparent if we write the kinetic energy,

$$E^K = \frac{1}{2} \int d^3x |\nabla_{\perp} \phi|^2, \text{ and } E^n = \frac{1}{2} \int d^3x |n|^2,$$

time evolution equations

$$\frac{\partial E^K}{\partial t} = - \int d^3x \sum_k \left[\frac{B\omega_{ci}}{en_0\eta} k_{\parallel}^2 |\phi_k|^2 - \frac{iB\omega_{ci}}{n_0} ik_y \phi_{-k} n_k \right] \quad (6.4a)$$

$$\frac{\partial E^n}{\partial t} = - \int d^3x \sum_k n_k^* \frac{ik_y \phi_k}{B} \frac{\partial \langle n \rangle}{\partial x} \quad (6.4b)$$

obtained from Eq. (6.2). Total energy balance requires that $\partial(E^K + E^n)/\partial t = 0$. We consider the saturation processes for the kinetic energy, E^K , and density, E^n , separately since they are independent.

First, consider the saturation of the kinetic energy, $\partial E^K/\partial t = 0$. From Eq. (6.4a) the resistive term damps the growth of the energy and opposes the curvature-density drive

$$-ik_y \phi_{-k} n_k \simeq \frac{k_{\parallel}^2}{\eta} |\phi_k|^2 \quad (6.5)$$

If we take

$$n_k \simeq \frac{-ik_y}{B} \frac{\partial \langle n \rangle}{\partial x} \frac{\phi_k}{(D/\Delta_k^2)}$$

from Eq. (6.3a) and substitute this into Eq. (6.5) one obtains

$$\frac{\kappa k_y^2}{B} \frac{\partial \langle n \rangle}{\partial x} \frac{|\phi_k|^2}{(D/\Delta_k^2)} \sim \frac{k_y^2 \Delta_k^2}{e\eta L_s^2} |\phi_k|^2 \quad (6.6)$$

Solving for D leads to

$$D = e\eta L_s^2 \frac{\kappa}{B} \frac{\partial \langle n \rangle}{\partial x} \quad (6.7)$$

At saturation, the asymptotic balance of vorticity diffusion and the resistive term in Eq. (6.3b) gives rise to a nonlinear mixing length

$$\Delta_k = \left[\frac{B\omega_{ci}}{n_0} \frac{k_y^2}{L_s^2 e\eta D} \right]^{-1/6} \quad (6.8)$$

Using the value of D in Eq. (6.7) which is necessary to maintain the curvature drive and the resistive term damping balance we obtain

$$\Delta_k = \eta^{1/3} k_y^{-1/3} L_s^{2/3} \kappa \frac{\partial \langle n \rangle}{\partial x} \quad (6.9)$$

which is equal to the linear mode width. It is easy to verify that $D = \gamma \Delta_k^2$ where γ is the linear growth rate.

Since

$$D = \sum_{k'} \frac{k_y'^2 |\phi_{k'}|^2}{B^2 \Delta\omega_{k+k'}} = \gamma_k \Delta_k^2 \quad (6.10)$$

and using the linear growth rate as the decorrelation rate, $\Delta\omega_{k+k'} \simeq \gamma_k$, the electrostatic potential fluctuation level for each mode is

$$\left[\frac{e\phi}{T_e} \right]_{\text{rms}} = \left[\frac{\gamma_k \Delta_k e B}{k_y T_e} \right] \quad (6.11)$$

The root mean square value is taken since a sum over k_z must be performed. This accounts for the modes centered on different rational surfaces which can interact with a given test mode.

In Fig. 6.8, the n -averaged value of $e\phi_m/T_e$ is obtained from the simulation results and compared with the theoretical estimate. The agreement is excellent for the large wavenumber regime and shows differences in the longest wavelength modes.

We note from Eq. (6.7) that the diffusion coefficient is independent of k . This means that the level of diffusion gives little insight into how the spectrum behaves. To estimate the density spectrum, n_k^2 , using this value of D we find

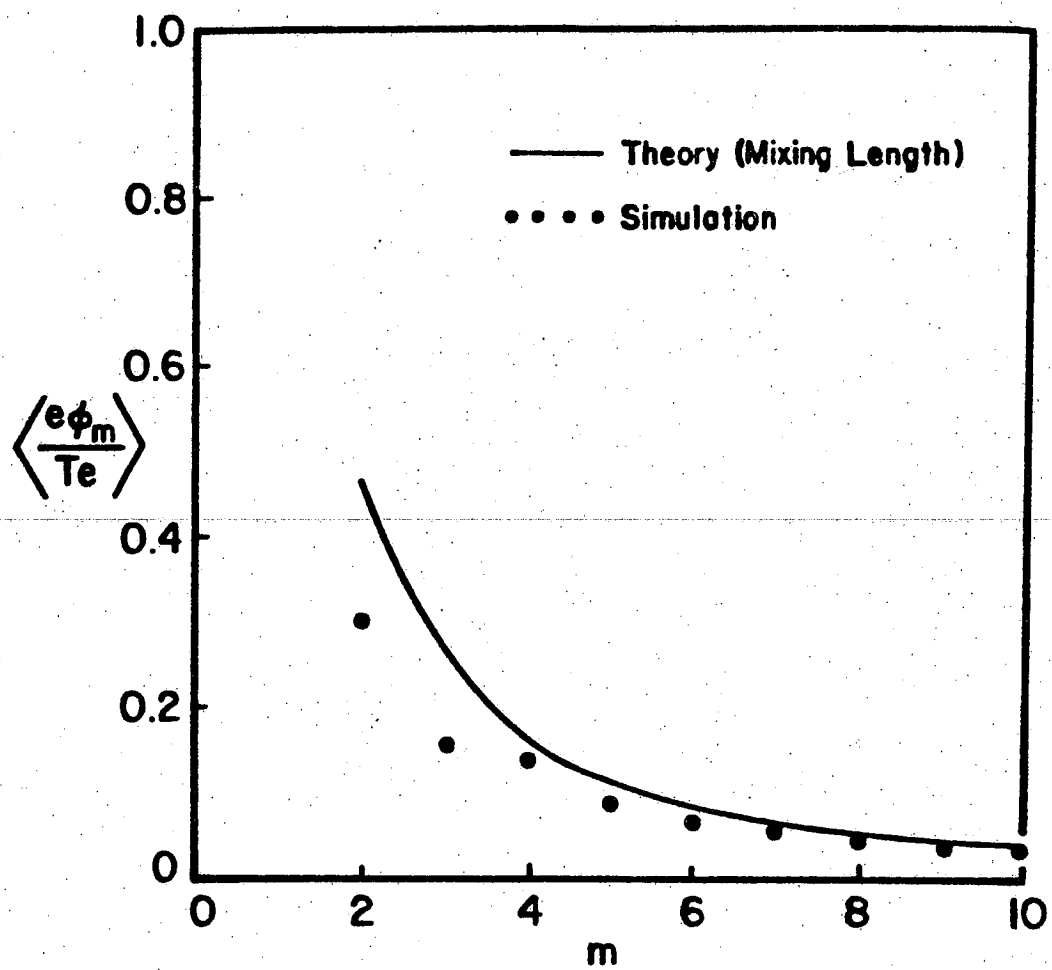


Fig. 6.8. Saturation levels for spatial and n -averaged electrostatic potential fluctuations versus mode number.

$$\frac{n_k^2}{\langle n \rangle^2} = \frac{\Delta_k^2}{L_n^2} \quad (6.12)$$

from Eq. (6.3a) and Eq. (6.11). Since $\Delta_k \propto k_y^{-1/3}$ the density spectrum $n_k^2 \propto k_y^{-2/3}$ and the spectrum depends weakly on k_y . Therefore, the density fluctuations are convected with the potential fluctuations. However, it is misleading to extract any information about the spectrum from this estimate since the diffusion has no wavenumber dependence. One must consider the two point density convection equation to obtain the correct spectral dependence, self-consistently.

From Eq. (6.4b) it is apparent that the density fluctuation energy cannot saturate unless collisional or thermal transport (perpendicular or parallel) is present. This is in the absence of localized quasi-linear profile flattening, i.e., $\partial \langle n \rangle / \partial x = 0$. Then

$$D_0 \int d^3x \left| \frac{\partial n}{\partial x} \right|^2 = - \int d^3x n v_x \frac{\partial \langle n \rangle}{\partial x} \quad (6.13)$$

where the left hand side is collisional dissipation at small scales and the right hand side represents density gradient relaxation due to convective ($E \times B$) motion.

For dynamic saturation a transfer or coupling term must be added to the left side of Eq. (6.13). This

term balances the density gradient term in the inertial range. At small scales the collisional dissipation term balances the gradient term. The saturation occurs when the long wavelength end of the density spectrum couples to the small scales through the inertial range.

To quantify this physical picture of the saturation of the density fluctuations we follow a standard two-point analysis of Eq. (6.2a). The two-point density convection equation is given by

$$\frac{\partial}{\partial t} \langle n(1)n(2) \rangle + T_{12} = - \left\langle \frac{\nabla_y \phi(1)}{B} n(2) \right\rangle \frac{\delta \langle n \rangle}{\delta x} \quad (6.14)$$

where

$$T_{12} = \left\langle \frac{\nabla_1 \phi(1) \times \hat{z}}{B} \cdot \nabla_1 n(1)n(2) \right\rangle + (1 \leftrightarrow 2)$$

The term, T_{12} , represents the turbulent scattering by the convective nonlinearity. The right hand side of Eq. (6.14) is the density gradient source of free energy for linear growth. It also contains incoherent emission effects, which are both needed for accurate small scale behavior. In the two-point analysis

$$T_{12} = D_- \frac{\partial^2}{\partial x_-^2} \langle n(1)n(2) \rangle \quad (6.15)$$

where D_- is the diffusion coefficient in the relative coordinate $x_- = x_1 - x_2$ and

$$D_- = 2D - D(1,2) - D(2,1) \quad (6.16)$$

where

$$D = \sum_{k'} \frac{k_y'^2 |\phi_{k'}|^2}{B^2 \Delta\omega_{k+k'}} \quad (6.16a)$$

and

$$D(1,2) = D(2,1) = \sum_{k'} \frac{\exp[ik_y y_- + ik_z z_-] k_y'^2 \langle \phi(x_1) \phi(x_2) \rangle}{B^2 \Delta\omega_{k+k'}} \quad (6.16b)$$

The diffusion coefficients $D(1,2)$ and $D(2,1)$ represent correlated diffusion whereas D represents uncorrelated diffusion.

The diffusion coefficient is given as

$$D_- = \sum_{k'} \frac{\langle v_x^2 \rangle_{k'}}{\Delta\omega_{k+k'}} (1 - \cos(k_y y_- + k_z z_-)) \quad (6.17)$$

which at small scales ($x_-, y_-, z_- \rightarrow 0$) becomes

$$D_- = D \left[\frac{x_-^2}{\Delta_0^2} + k_{0y}^2 y_-^2 + k_{0z}^2 z_-^2 \right] \quad (6.18)$$

$$= D (\tilde{k}_0 \cdot \tilde{x}_-)^2$$

The wavenumber, $k_{0x} \sim \Delta_0^{-1}$, in the x-direction represents the size of the small scale density 'clump.' When $k_0 x_- \gg 1$ the diffusion coefficient, D_- , is dominantly uncorrelated. When $k_0 x_- < 1$ the diffusion coefficient becomes correlated and D_- is given by Eq. (6.18).

In steady state, $\partial/\partial t \simeq 0$, and Eq. (6.14) becomes

$$D_- \frac{\partial^2}{\partial x_-^2} \langle \hat{n}(1) \hat{n}(2) \rangle \simeq \frac{\langle \nabla_y \phi(1) n(2) \rangle}{B} \frac{\partial \langle n \rangle}{\partial x} \quad (6.12)$$

In the limit $k_0 x_- < 1$, or at very small relative separation

$$\langle n^2 \rangle \simeq \tau_c \left\langle \frac{\nabla_y \phi}{B} n \right\rangle \frac{\partial \langle n \rangle}{\partial x} \quad (6.20)$$

where

$$\tau_c = \frac{1}{2Dk_{0x}^2} \ln \left[\frac{1}{k_{0x}^2 x_-^2 + k_{0y}^2 y_-^2 + k_{0z}^2 z_-^2} \right]$$

is the density clump lifetime.¹²² Integration over (x_-, y_-, z_-) leads to an expression for $\langle n_k^2 \rangle$. Averaging over the correlation length in x_- and Fourier transforming in (y_-, z_-) gives

$$\bar{\tau}_c = \frac{1}{2\pi} \int dy_- \exp[-ik_y y_-] \int dz_- \exp[-ik_z z_-] \frac{k_{0x}}{2} \int_{-k_{0x}}^{k_{0x}} dx_- \bar{\tau}_c \quad (6.21)$$

Since the density gradient source term has a weak wavenumber dependence at small separation

$$\langle n_k^2 \rangle = \left\langle \frac{\nabla_y \phi n}{B} \right\rangle \frac{\partial \langle n \rangle}{\partial x} \int_{-\infty}^{\infty} dk_z \bar{\tau}_c \quad (6.22)$$

and performing the integrals yields

$$\langle n_k^2 \rangle = \left\langle \frac{\nabla_y \phi n}{B} \right\rangle \frac{\partial \langle n \rangle}{\partial x} 2\pi \frac{k_{0y}}{k_y^2} \left[1 - J_0 \left[\frac{k_y}{k_{0y}} \right] \right] \quad (6.23)$$

In the small wavenumber (k_y/k_{0y}) regime, using the small argument expansion of the Bessel function, gives $\langle n_k^2 \rangle \simeq$ constant. For the intermediate region in wavenumber,

the inertial range,

$$\langle n_k^2 \rangle \propto k_y^{-2} \quad (6.24)$$

The spectrum predicted from the two-point theory is shown in Fig. 6.9 along with the simulation results. Also shown is the wavenumber dependence from the mixing length estimate, Eq. (6.12).

At smaller scales is the dissipation range. In this range ion viscosity and collisional dissipation become dominant. In the simulation these effects occur at wavelengths on the order of the particle size. Therefore, this provides the sink of energy for the unstable fluctuations.

We conclude this section with a comparison between the results presented here and from dimensional analysis of the reduced MHD equations.¹²³ The invariance properties of the reduced equations, given by Eq. (6.2), constrain the diffusion coefficient for the plasma. If the nature of the turbulence is known, in our case non-linear convection processes, further constraints on the diffusion coefficient are obtained.

Dimensional analysis of the reduced equations gives

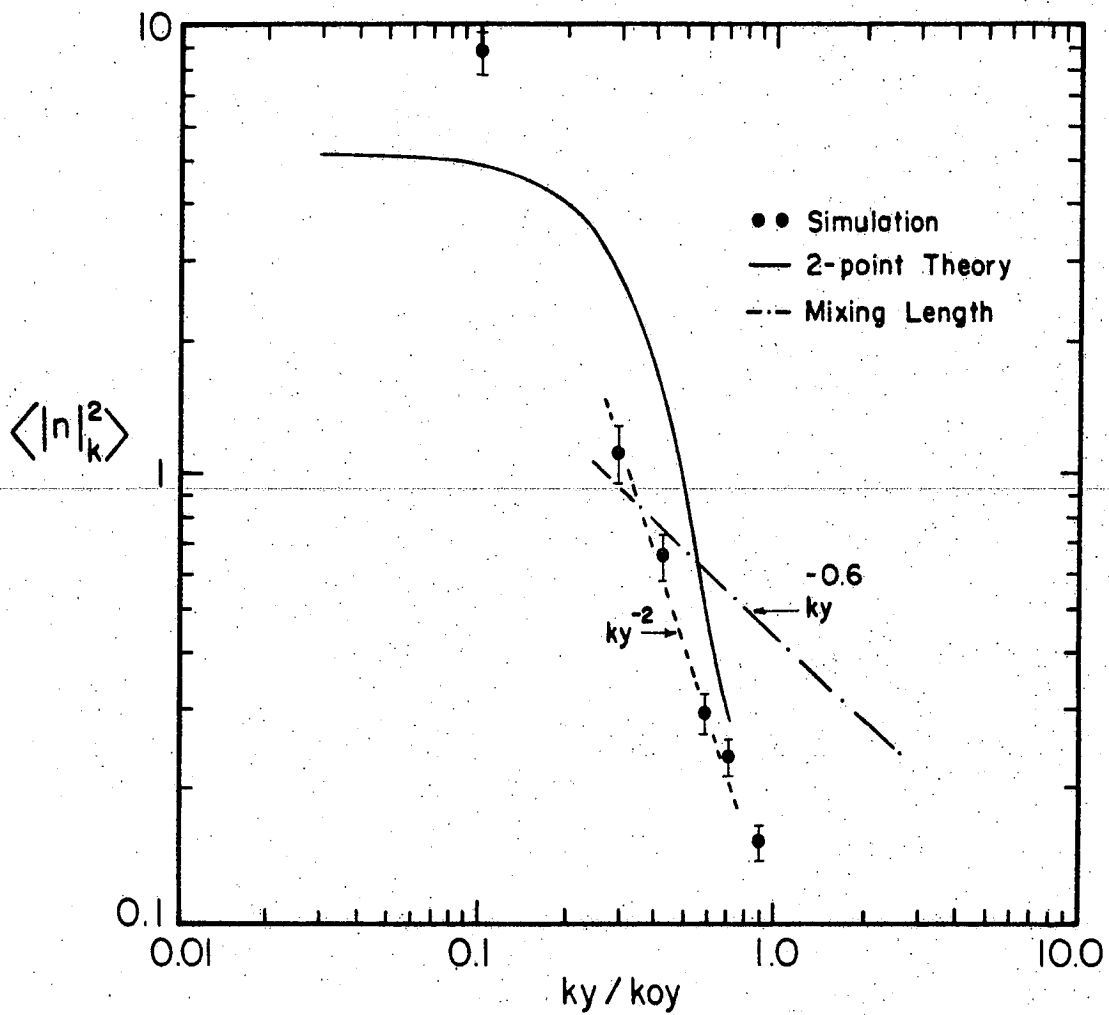


Fig. 6.9. Saturation levels for spatially-averaged density fluctuations versus mode number.

$$D = \alpha \epsilon \eta \frac{L_s^2}{B} \kappa \frac{\partial \langle n \rangle}{\partial x}, \quad \alpha = \text{constant} \quad (6.24)$$

for convective diffusion,¹²³ which agrees with Eq. (6.8). This expression for the diffusion coefficient has no k -dependence and therefore gives little insight into the dynamics of the k -spectrum. The reason for this is because the y and z -directions are translationally symmetric and hence no scale factors appear. The correlation length, which sets the scale in x , is specified by assuming a localized scale for the fluctuation.

This is in contrast to the analytic and computational results presented in this chapter. The spatial scales are not the same as is assumed in dimensional analysis arguments. The scale length in the x -direction is determined from theoretical considerations using two-point evolution equations. This gives an analytic form for the scale of the fluctuations in x . Furthermore, the $k_y - k_z$ interaction is important and can decouple the evolution of the density and potential fluctuations which in turn influences their spectral dependence.

C H A P T E R V I I

CONCLUSIONS AND REMARKS

In this dissertation two types of low frequency fluctuations, related to anomalous plasma losses in toroidal confinement devices, have been investigated. A particle simulation model, appropriate for investigating low frequency fluctuations, is outlined and the thermal spectrum of modes is rigorously tested for a homogeneous magnetized plasma.

The thermal spectrum of an inhomogeneous plasma, immersed in a sheared magnetic field is studied in detail with the particle simulation model. The fluctuation spectrum is dominated by stable drift wave eigenmodes, observed for the first time in computer simulation experiments, when the magnetic shear is strong ($L_s/L_n \lesssim 28$). For weaker magnetic shear localized, convective transient growths are observed before eigenmodes have developed. In certain cases the transient growths can modify the equilibrium density profile locally, at the electron resonance region. This subsequently changes the linear eigenmode structure.

An extension to three dimensions is made and the effects of a background microturbulence on the stable drift wave eigenmodes is considered. The orbital stochasticity of the electrons, induced by the drift modes centered about densely packed mode rational surfaces, is shown to affect the linear eigenmode stability. When a spectrum of wavenumbers, favorable for nonlinear instability, is allowed in the simulation, finite amplitude enhancements above the initial thermal level are observed. The stability of the fluctuations is dependent upon the temporal behavior of the diffusion coefficient in x . The results of this investigation indicate that a finite amplitude background of fluctuations can affect the stability of short wavelength drift modes. This can in turn produce the anomalous transport of particles and heat across the magnetic field. The inclusion of longer, more stable wavelength fluctuations in the simulation is shown to have a stabilizing influence on the shorter wavelength modes.

The second type of low frequency fluctuation under investigation is the resistive interchange (g) mode. This is an absolutely unstable fluctuation which is driven by the interaction between magnetic field curvature

and density gradients. Magnetic shear localizes the unstable interchange mode to the rational surface ($k_{\parallel} = 0$). It is found that the instability saturates when the density convects a distance comparable to the mode width in a growth time.

In three dimensions, when there is a strong overlap of the modes centered about different rational surfaces, the nonlinear convection processes become important. The nonlinear evolution of the modes and spectrum of electrostatic potential, as well as density, fluctuations at saturation is radically different from the single rational surface case. Nonlinear solutions of the density convection and vorticity evolution equations give some agreement with the results of the simulation study. In particular, the saturation amplitude of the fluctuations as a function of wavenumber. The conclusion drawn from this investigation is that convective nonlinearities must be taken into consideration when constructing a model of anomalous transport based on localized resistive interchange mode fluctuations. Extensions of this work to include finite diamagnetic drift frequency, as well as self-consistent electromagnetic effects, is currently being pursued.

R E F E R E N C E S

1. H. P. Furth, Nucl. Fusion, 15, 487 (1975).
2. C. M. Surko and R. E. Slusher, Science, 221, 817 (1983).
3. W. M. Tang, Nucl. Fusion, 18, 1089 (1978).
4. P. C. Liewer, Nucl. Fusion, to be published (1985).
5. W. Horton, Jr., Basic Plasma Physics II (ed. A. A. Galeev and R. N. Sudan, North Holland, 1985).
6. W. Horton and R. D. Estes, Nucl. Fusion, 19, 203 (1979).
7. J. A. Krommes, Suppl. Prog. Theor. Phys., 64, 137 (1978).
8. A. B. Rechester and M. N. Rosenbluth, Phys. Rev. Lett., 40, 38 (1978).
9. T. H. Stix, Nucl. Fusion, 18, 353 (1978).
10. B. V. Kadomtsev, Plasma Turbulence (Academic Press, New York, 1965).
11. L. D. Pearlstein and H. L. Berk, Phys. Rev. Lett., 28, 220 (1969).
12. D. W. Ross and S. M. Mahajan, Phys. Rev. Lett., 40, 324 (1978).
13. K. T. Tsang, P. J. Catto, J. C. Whitson and J. Smith, Phys. Rev. Lett., 40, 327 (1978).
14. S. P. Hirshman and K. Molvig, Phys. Rev. Lett., 42, 648 (1979).
15. C. Z. Cheng and L. Chen, Phys. Fluids, 23, 1770 (1980).

16. L. Chen, M. S. Chance, and C. Z. Cheng, Nucl. Fusion, 20, 901 (1980).
17. H. A. B. Bodin and A. A. Newton, Nucl. Fusion, 20, 1255 (1980).
18. K. V. Roberts and J. B. Taylor, Phys. Fluids, 8, 315 (1965).
19. H. P. Furth, J. Killeen and M. N. Rosenbluth, Phys. Fluids, 6, 459 (1963).
20. M. N. Rosenbluth and M. N. Bussac, Nucl. Fusion, 19, 489 (1979).
21. J. M. Finn, W. M. Manheimer and T. M. Antonsen, Phys. Fluids, 26, 962 (1983).
22. O. Buneman, Phys. Rev., 115, 503 (1959).
23. J. M. Dawson, Phys. Fluids, 5, 445 (1962).
24. A. B. Langdon, J. Comp. Phys., 30, 202 (1979).
25. J. Denavit, J. Comp. Phys., 42, 337 (1981).
26. A. Friedman, A. B. Langdon and B. I. Cohen, Comm. Plasma Phys. Controlled Fusion, 6, 225 (1981).
27. B. I. Cohen, A. B. Langdon and A. Friedman, J. Comp. Phys., 46, 15 (1982).
28. A. B. Langdon, B. I. Cohen and A. Friedman, J. Comp. Phys., 51, 107 (1983).
29. D. C. Barnes, T. Kamimura, J. N. Leboeuf and T. Tajima, J. Comp. Phys., 52, 480 (1983).
30. W. W. Lee, Phys. Fluids, 26, 556 (1983).
31. C. S. Gardner, Phys. Rev., 115, 791 (1959).
32. T. G. Northrop, Ann. Phys., 15, 79 (1961).
33. T. H. Johnson and J. Killeen, J. Comp. Phys. 23, 219 (1977).

34. C. Z. Cheng and H. Okuda, *J. Comp. Phys.*, 25, 133 (1977).
35. W. W. Lee and H. Okuda, *J. Comp. Phys.*, 26, 139 (1978).
36. O. Buneman, *J. Comp. Phys.*, 1, 517 (1967).
37. R. W. Hamming, Introduction to Applied Numerical Analysis (McGraw-Hill, New York, 1971).
38. C. K. Birdsall and A. B. Langdon, Plasma Physics via Computer Simulation (McGraw-Hill, New York, 1985).
39. J. W. Cooley and J. W. Tukey, *Math. Comput.*, 19, 297 (1965).
40. W. L. Krueer, J. M. Dawson and B. Rosen, *J. Comp. Phys.*, 13, 114 (1973).
41. V. K. Decyk and J. M. Dawson, *J. Comp. Phys.*, 30, 407 (1979).
42. O. Buneman, *J. Comp. Phys.*, 12, 124 (1973).
43. R. W. Hockney, Methods in Computational Physics, vol. 9 (ed. Alder, Fernbach and Rotenberg, Academic Press, New York, 1970).
44. H. Naitou, S. Tokuda and T. Kamimura, *J. Comp. Phys.*, 33, 86 (1979).
45. T. Kamimura, T. Wagner and J. M. Dawson, *Phys. Fluids*, 21, 1151 (1978).
46. S. Ichimaru, Basic Principles of Plasma Physics: A Statistical Approach (W. A. Benjamin Inc., Mass., 1973).
47. D. E. Baldwin and G. Rowlands, *Phys. Fluids*, 9, 2444 (1966).
48. H. Grad, *Physics Today*, 22, 34 (1969).

49. Y. L. Klimintovich, The Statistical Theory of Non-Equilibrium Processes in a Plasma (MIT Press, Cambridge, Mass., 1967).
50. R. Shanny, J. M. Dawson and J. M. Greene, *Phys. Fluids*, 10, 1281 (1967).
51. L. Spitzer, Jr., Physics of Fully Ionized Gases (Wiley Interscience Publishers Inc., New York, 1962).
52. T. A. Oliphant and C. W. Nielsen, *Phys. Fluids*, 11, 2103 (1970).
53. J. M. Dawson, *Rev. of Mod. Phys.*, 55, 403 (1983).
54. R. H. Berman, D. J. Tetreault and T. H. Dupree, *Phys. Fluids*, 26, 2437 (1983).
55. T. H. Dupree, C. E. Wagner and W. M. Manheimer, *Phys. Fluids*, 18, 1167 (1975).
56. N. Wax, Selected Papers on Noise and Stochastic Processes (Dover, New York, 1954).
57. C. Kittel, Elementary Statistical Physics (Wiley, New York, 1958).
58. P. B. Blackman and J. W. Tukey, The Measurement of Power Spectra (Dover, New York, 1958).
59. E. Parzen, Time Series Analysis Papers (Holden-Day, San Francisco, 1967).
60. J. P. Burg, Ph.D. Dissertation, Stanford University (1975).
61. V. K. Decyk, J. M. Dawson and G. J. Morales, *Phys. Fluids*, 22, 507 (1979).
62. V. Tserkovnikov, *Soviet Phys. JETP*, 5, 58 (1957).
63. N. Krall and M. N. Rosenbluth, *Phys. Fluids*, 8, 1488 (1965).
64. P. H. Rutherford and E. A. Frieman, *Phys. Fluids*, 10, 1007 (1967).

65. L. D. Pearlstein and H. L. Berk, Phys. Rev. Lett. 23, 220 (1969).
66. W. Manheimer, Phys. Fluids, 19, 335 (1976).
67. T. M. Antonsen, Phys. Rev. Lett., 41, 33 (1978).
68. Y. C. Lee and L. Chen, Phys. Rev. Lett., 42, 708 (1979).
69. F. L. Hinton and M. N. Rosenbluth, Phys. Fluids, 23, 528 (1980).
70. W. M. Nevins and L. Chen, Phys. Fluids, 23, 1973 (1980).
71. R. E. Waltz, W. Pfeiffer and R. R. Dominguez, Phys. Fluids, 23, 985 (1980).
72. W. W. Lee and H. Okuda, Phys. Rev. Lett., 36, 870 (1976).
73. W. W. Lee, Y. Y. Kuo and H. Okuda, Phys. Fluids, 21, 617 (1978).
74. W. W. Lee, W. M. Nevins, H. Okuda and R. B. White, Phys. Rev. Lett. 43, 347 (1979).
75. N. T. Gladd and W. Horton, Phys. Fluids, 16, 879 (1973).
76. D. W. Ross and S. M. Mahajan, Phys. Fluids, 22, 294 (1979).
77. R. D. Sydora, J. N. Leboeuf and T. Tajima, Phys. Fluids, 28, 528 (1985).
78. Y. Y. Lau and R. J. Briggs, Nucl. Fusion, 15, 103 (1975).
79. B. Coppi, G. Laval, R. Pellat and M. N. Rosenbluth, Nucl. Fusion, 6, 261 (1966).
80. C. M. Surko and R. E. Slusher, Phys. Rev. Lett., 37, 1747 (1976).

81. R. E. Slusher and C. M. Surko, Phys. Rev. Lett., 40, 400 (1978).
82. E. Mazzucato, Phys. Fluids, 21, 1063 (1978).
83. E. Mazzucato, Phys. Rev. Lett., 48, 1828 (1982).
84. S. J. Sweben, C. R. Menyuk and R. J. Taylor, Phys. Rev. Lett., 43, 1270 (1979).
85. C. Z. Cheng and L. Chen, Nucl. Fusion, 21, 403 (1981).
86. R. Marchand, N. T. Gladd and Y. C. Lee, Phys. Fluids, 25, 338 (1982).
87. T. H. Dupree, Phys. Fluids, 10, 1049 (1967).
88. P. Similon, Ph.D. Dissertation, Princeton University (1981).

89. P. H. Diamond and M. N. Rosenbluth, Phys. Fluids, 24, 1641 (1981).
90. P. H. Diamond and M. N. Rosenbluth, Institute for Fusion Studies Report No. IFSR-24 (1981).
91. S. P. Hirshman and P. H. Diamond, Institute for Fusion Studies Report No. IFSR-33 (1981).
92. P. W. Terry and P. H. Diamond, Statistical Physics and Chaos in Fusion Plasmas (ed. C. W. Horton, Jr. and L. E. Reichl, Wiley, New York, 1984).
93. C. O. Beasley, W. I. van Rij and K. Molvig, Phys. Fluids, 28, 271 (1985).
94. G. M. Zaslavskii and B. V. Chirikov, Sov. Phys. Uspekhi, 14, 549 (1972).
95. K. Molvig, J. P. Friedberg, R. Potok, S. P. Hirshman, J. C. Whitson and T. Tajima, Long Time Prediction in Dynamics (ed. C. W. Horton, Jr., Wiley, New York, 1983).

96. C. O. Beasley, K. Movig and W. I. van Rij, *Phys. Fluids*, 26, 678 (1983).
97. P. H. Diamond, M. N. Rosenbluth, S. P. Hirshman and J. R. Myra, *Fusion Energy-1981*, International Center for Theoretical Physics, Trieste, vol. 25, 1982.
98. B. Coppi, *Phys. Fluids*, 7, 1501 (1964).
99. B. Coppi, J. M. Greene and J. L. Johnson, *Nucl. Fusion*, 6, 101 (1966).
100. T. C. Hender and D. C. Robinson, *Comput. Phys. Comm.*, 24, 413 (1981).
101. J. A. A. Mirin, N. J. O'Neill, J. Killeen, R. J. Bonugli and M. J. Ellis, Lawrence Livermore National Laboratory Report No. LLNL-91823 (submitted to *Nucl. Fusion*, 1984).
-
102. D. D. Schnack, J. A. Killeen and R. A. Gerwin, *Nucl. Fusion*, 21, 1447 (1981).
103. T. C. Hender and D. C. Robinson, *Nucl. Fusion*, 21, 755 (1981).
104. T. C. Hender and D. C. Robinson, *Plasma Physics and Controlled Nuclear Fusion Research* (International Atomic Energy Agency, Vienna, 1983), vol. 3, p. 417.
105. Z. G. An and P. H. Diamond, *Sherwood Theory Meeting*, Arlington, Virginia, 1983, paper 2-523.
106. N. R. Ainsworth, T. Edington, W. Fletcher, C. A. Steed, D. R. Sweetman, E. M. Jones, M. F. Payne, A. C. Riviere, D. F. H. Start and T. N. Todd, *Plasma Physics and Controlled Nuclear Fusion Research* (International Atomic Energy Agency, Vienna, 1978), vol. 1, p. 745.
107. A. J. L. Venhage and D. C. Robinson, *Pulsed High Beta Plasma* (ed. D. E. Evans, Pergamon Press, Oxford, 1975).

108. D. Brotherton-Ratcliffe, C. G. Gimblett and I. H. Hutchinson (to be published, Nucl. Fusion, 1985).
109. B. A. Carreras (private communication).
110. A. B. Mikhailovskii, Theory of Plasma Instabilities, vol. 2, chap. 9 (Consultants Bureau, New York, 1974).
111. T. E. Stringer, Phys. Fluids, 10, 418 (1967).
112. T. E. Stringer, Phys. Fluids, 15, 125 (1975).
113. C. L. Chang, N. T. Gladd and C. S. Liu, University of Maryland Report No. UM-82-036 (1982).
114. W. M. Manheimer, Phys. Rev. Lett., 45, 1249 (1980).
115. H. Goede, D. Humanic and J. M. Dawson, Phys. Fluids, 26, 1812 (1983).
116. B. A. Carreras, P. H. Diamond, M. Murakami, J. L. Dunlap, J. D. Bell, H. R. Hicks, J. A. Holmes, E. A. Lazarus, V. K. Pare, P. Similon, C. E. Thomas, and R. M. Wieland, Phys. Rev. Lett., 50, 503 (1983).
117. B. A. Carreras, P. W. Gaffney, H. R. Hicks and J. D. Callen, Phys. Fluids, 25, 1231 (1982).
118. R. D. Sydora, J. N. Leboeuf, Z. G. An, P. H. Diamond and T. Tajima, Phys. Fluids, 28, 425 (1985).
119. H. R. Strauss, Phys. Fluids, 19, 134 (1976).
120. Z. G. An and P. H. Diamond, Proceedings of the Sixth U.S. Symposium on Compact Toroidal Research, Princeton Plasma Physics Laboratory, 1984.
121. Z. G. An, P. H. Diamond, R. D. Hazeltine, J. N. Leboeuf, M. N. Rosenbluth, R. D. Sydora, T. Tajima, B. A. Carreras, L. Garcia, T. C. Hender, H. R. Hicks, J. Holmes, V. E. Lynch and H. R. Strauss, Plasma Physics and Controlled Nuclear Fusion Research (International Atomic Energy Agency, London, England, 1984).

122. T. H. Dupree, *Phys. Fluids*, 15, 334 (1972).
123. J. W. Connor and J. B. Taylor, *Plasma Physics and Controlled Nuclear Fusion Research* (International Atomic Energy Agency, London, England, 1984).

V I T A

Richard Dwayne Sydora was born on August 20, 1958, in Vegreville, Alberta, Canada, the son of John Sydora and Alice Niemczyk-Sydora. After completing his high school education at Delnorte High School, Innisfree, Alberta, he entered the University of Alberta, Edmonton in the Fall of 1975. In 1979 he received the degree of Bachelor of Science with honors in applied mathematics. After graduation, he joined the Geophysical Institute at the University of Alaska, Fairbanks and worked as a research assistant under NASA on the fluorescent plasma tracer experiments in the aurora borealis. He was granted the degree of Master of Science in space physics in May, 1981. In September 1981, he entered the Graduate School of The University of Texas at Austin and has been employed by the Institute for Fusion Studies. He holds the position of Assistant Research Physicist in the Department of Physics, University of California, Los Angeles.

Permanent Address: Box 187
 Innisfree, Alberta
 Canada TOB 2G0